Magnetotelluric investigation in West Greenland - considering the polar electrojet, ocean and fjords

Lauritsen, Nynne Louise Berthou; Olsen, Nils; Junge, Andreas; Matzka, Jürgen

Publication date:
2016

Document Version
Publisher's PDF, also known as Version of record

Nynne Louise Berthou Lauritsen

Magnetotelluric investigation in West Greenland

Magnetotelluric investigation in West Greenland

- considering the polar electrojet, ocean and fjords

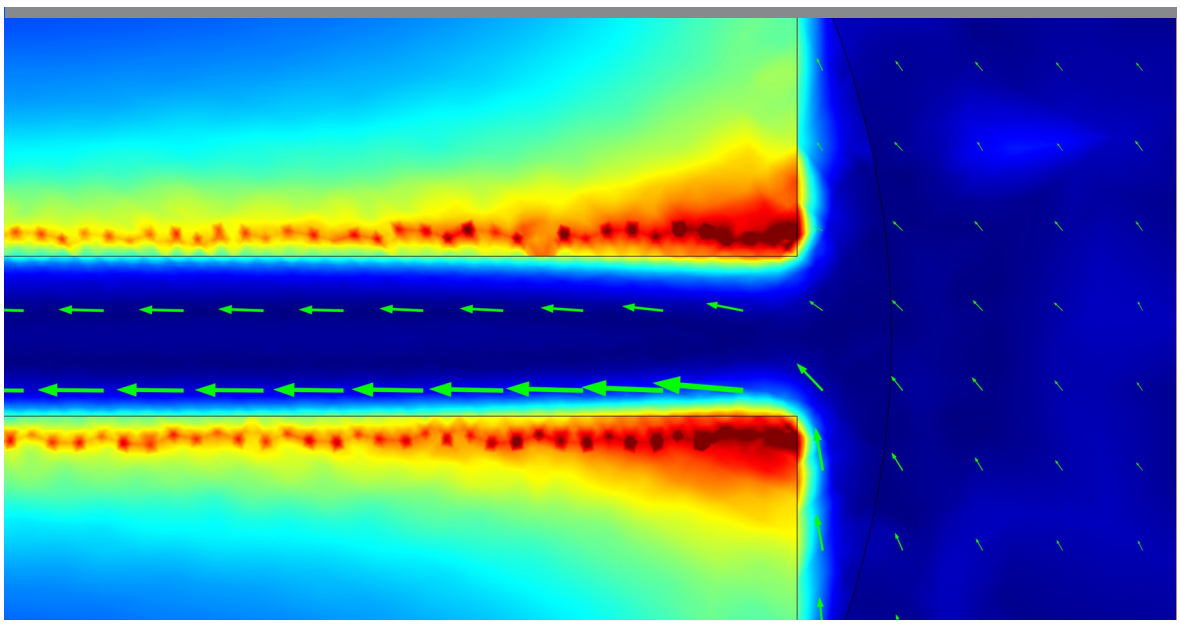

Nynne Louise Berthou Lauritsen
November 2016

DTU Space
National Space Institute

Magnetotelluric investigation in West Greenland

- considering the polar electrojet, ocean and fjords

Dissertation presented by

Nynne Louise Berthou Lauritsen

for the degree of Doctor of Philosophy to

DTU Space - National Space Institute
Technical University of Denmark
Kongens Lyngby, Denmark

November 2016

Supervisors

Prof. Nils Olsen
Geomagnetism, DTU Space
Technical University of Denmark
Denmark

Prof. Andreas Junge
Applied Geophysics, Institute of Geosciences
Goethe Universität Frankfurt am Main
Germany

Dr. Jürgen Matzka
Earth's magnetic field, Helmholtz Centre Potsdam
Deutsches GeoForschungsZentrum GFZ
Germany

Location

DTU Space
National Space Institute
Technical University of Denmark
Diplomvej 371
DK-2800 Kongens Lyngby
Tel (+45) 4525 9500

Ph.D. dissertation

ISBN: 978-87-91694-33-2

Acknowledgment

I would like to thank Nils Olsen for supervising me and introducing me to the world of geomagnetism, it has been an interesting and knowledgeable experience. At the same time I would like to thank Andreas Junge for taking my into the world of magnetotellurics, thank you for always taking your time for teaching and discussing with me when I needed it. I am grateful to Philip Hering, Marcel Cembrowski, Annika Rödder and Alex Löwer for all your help, when I had questions about MT, COMSOL, Matlab and for making me feel welcome in your group and your lives.

A great thanks shall go to all the people who have helped me through the thesis writing, assisting with proof reading of the manuscript and tea breaks when needed; Philip, Marcel, Alex, Anna, Livia, Sille, Joanna, Heidi, and my dear husband Magnus for all your support. And Maria, for being in the same situation as I at the same time, it made the last writing much more bearable and fun in your company. Thank you to the field work crew, Alexey Kuvshinov, Wolfgang Nitsch, Michael Skriver, Livia Kother for your assistance with collection of the data.

Last but not least, all my dear colleges in the Geomagnetism group for an always wonderful atmosphere and support.

Finally, I would like to thank The Danish Council for Independent Research | Natural Sciences (FNU) for funding this Ph.D. project, and to the GFZ instrument Pool (GIPP) for supporting the project with magnetotelluric fieldwork equipment (GIPP no. 201309).

Abstract

A magnetotelluric survey has been conducted in North West Greenland, with the purpose of investigating the subsurface. The results of two processing techniques are presented, a single station robust processing and a multiple station processing. The multiple station processing tries to eliminate data originating from other sources than the plane wave by removing incoherent noise between stations and selecting time periods from an eigenvalue criteria. It is successful for periods below 55 s, but has to undergo further investigation at longer periods. The two processing techniques show similar results, however the multiple station technique improves the data quality around 1 s compared to the single station technique. Different challenges are connected with the survey location, where ocean and fjord systems have a large impact on the transfer functions. A 3D model study of the impact of fjords on induction arrows is presented, illustrating the importance of including these in magnetotelluric modelling. This information is included in the 3D modelling of the magnetotelluric survey in Greenland, together with the bathymetry of the ocean. The modelling shows that the impact from the fjords and ocean heavily dominates the signal, making it difficult to differentiate any geology in the subsurface.

Resumé

Et magnetotellurisk feltarbejde er blevet udført i Nordvest Grønland, med formålet at undersøge geologien i undergrunden. Resultatet fra to forskellige databehandlingsteknikker er præsenteret, en enkelt stations robust databehandling og en fler stations databehandlingsteknik. Fler stations databehandlingsteknikken forsøger at fjerne data, som indeholder signal fra andre kilder end dem, som stammer fra den plane bølge ved at fjerne ikke korreleret støj mellem stationer og udvælge tidsperioder vha. et egenværdi kriterium. Teknikken virker for perioder mindre end 55 s, men skal undergå videre undersøgelser for længere perioder. De to teknikker viser tilsvarende resultater, men fler stations teknikken forbedrer data kvaliteten omkring 1 s sammenlignet med enkelt stations teknikken. Forskellige udfordringer er forbundet med feltarbejdets placering i Grønland, hvor havet og fjordene har en stor indflydelse på overførselsfunktionerne. Et 3D model studium er præsenteret, som viser fjordenes påvirkning af induktion vektorerne. Resultatet viser vigtigheden af at inkludere fjorde i magnetotellurisk modellering. Denne information er inkluderet i 3D modelleringen af det magnetotelluriske feltarbejde i Grønland, sammen med dybdemålingen af havet. Modelleringen viser, at påvirkningen fra fjordene og havet dominerer signalet, hvilket gør det problematisk at adskille dette signal fra signalet, der stammer fra geologien i undergrunden.

Contents

List of Figures

List of Tables

Abbreviations

AE-index	Auroral electrojet index
AG-AG-CL	Silver and chlorine electrodes
AMT	Audio magnetotelluric
CASTLE	Sensor box
Dst index	Disturbance storm time index
EEJ	Equatorial electrojet
EDL	Earth data logger
ELF	Extremely low frequency
EV-index	Eigenvalue index
FAC	Field-aligned currents
FFT	Fast Fourier transform
GIPP	Geophysical instrument pool Potsdam
K_p index	Planetary K-index, monitoring geomagnetic disturbance
LMT	Long period magnetotelluric
MT	Magnetotelluric
pc	Continuous pulsations
PEJ	Polar electrojet
pi	Irregular transient pulsations
Sq	Solar quiet
TE	Transverse electric
TM	Transverse magnetic
ULF	Ultra low frequency
VLF	Very low frequency

Chapter 1

Introduction

Greenland is an interesting area in geological terms, however, most investigations have been related to surface geology, which has been investigated thoroughly by the Geological Survey of Denmark and Greenland [2016]. The area where this project takes place, is located in North West Greenland, south of the town Aasiaat, in an interesting geological orogen named the Nagssugtoqidian, which has been studied for many years [e.g. Connelly and Mengel, 2000; Henriksen, 2008; Henriksen et al., 2009; Mengel et al., 1998; Ramberg, 1949; van Gool et al., 2002].

Onshore geophysical investigations of the subsurface in Greenland have, however been sparse [e.g. Forsberg, 1986]. Seismic studies has been carried out offshore all around Greenland, for example at the east coast [e.g. Dahl-Jensen et al., 1997; Hopper et al., 1998; Larsen and Jakobsdóttir, 1988], and in combination with gravity [e.g. Weigel et al., 1995]. Magnetotelluric investigations in Greenland have only been conducted in a few locations [Hautot and Tarits, 2016; Heincke et al., 2015; Kother, 2012]. Kother [2012] conducted a survey in 2010 in west Greenland near the town of Kangerlussuaq. They deployed five stations arranged from the fjord and inland towards the icecap, and created a 2D model of the subsurface resistivity, which suggest a low resistivity structure dipping SW-NE. Direction is changed approximately 64° from the result in the thesis, due to incorrect declination correction [Kother, 2016, personal communication]. Such a low resistivity is also detected in orogens of similar age in North America and Scandinavia [e.g. Jones, 1993; Rasmussen et al., 1987], and are suggested to be from the same orogen zone.

The Nagssugtoqidian orogen extends from the west coast 250 km to the east coast of Greenland where Heincke et al. [2015] conducted a magnetotelluric study. They deployed eight stations along the Sermilik Fjord in 2014, and performed a 2D magnetotelluric feasibility study to investigate how to plan magnetotelluric surveys in Greenland in the future, taking the difficult conditions into consideration. However, none of these projects have been published yet.

Hautot and Tarits [2016] performed magnetotelluric and gravity surveys in North West Greenland, on the Svartenhuk peninsula, with 21 magnetotelluric stations and 65 gravity measurement points. They performed a joint inversion, taking into account the ocean bathymetry, which resulted in density models constrained by the resistivity model.

The main objective of this project is to investigate the geological structures of the crust using the magnetotelluric method, in an area south of the town Aasiaat in North West Greenland. Greenland can be a challenging place for magnetotelluric, due to interference from ionospheric currents and the proximity of the ocean. This project tests the ability of a multiple station processing technique to select data with the least influence from the interfering currents in the ionosphere. The oceans influence on the data can be included when modelling the subsurface, and thereby determining its effect on the data. During this process it was discovered that fjords in the measuring area can influence the data significantly. A model study of these effects is therefore also included, which gives important information for the further modelling and future magnetotelluric field work.

Measuring areas located on islands or near to the coast experience an effect on the transfer functions that originates from the highly conductive ocean [e.g. Jones and Price, 1970; Parkinson, 1959]. Parkinson and Jones [1979] investigated different models to describe this ocean effect. The eddy currents flowing in the ocean are induced by the magnetic field. The ocean effect has been investigated in several publications, for example Menvielle et al. [1982] made a numerical study of the effect for different locations in the world. They show that it is possible to eliminate the ocean effect with a numerical model. The ocean effect is seen due to the high contrast to the resistive continental subsurface. Nolasco et al. [1998] also successfully removed the ocean effect using a thin sheet layer together with the bathymetry data. Santos et al. [2001] included a 3.5 km ocean layer in a 3D forward modelling and showed the importance of modelling the ocean effect, since it affects the transfer functions. In this case the ocean effect was important in periods larger than 100-300 s. In this project, the bathymetry of the ocean is included in the 3D forward modelling with a fixed depth, but with varying conductance to account for the true depth of the ocean.

Greenland is located beneath the auroral oval, a band approximately between 60° - 78° magnetic latitude. This band is an area that contains large non-uniform time-varying ionospheric currents. These currents can influence the magnetotelluric measurements and distort the transfer functions. Different approaches have been used to try to eliminate these effects when dealing with data from polar regions. Kother [2012] compared the magnetotelluric data to an index describing the disturbance of the global magnetic field, to discard time periods where the magnetic field where disturbed. Others e.g. Garcia et al. [1997], have tested robust processing vs. non-robust processing techniques on data from Canada and concluded that robust processing can considerably reduce the effects of the non-uniform currents if the affected data is not the dominating part of the data set. Viljanen et al. [1993] investigated the possibility to remove distortion from a polar electrojet through the use of averaging of data. They used two different synthetic models for the polar electrojet and subsurface. The averaging can reduce the distortion, however not enough to avoid distortion. They conclude that averaging as a method of removing distortion created by a polar electrojet is not a sufficient technique in polar regions. Jones and Spratt [2002] used the vertical magnetic field variations to model the subsurface for a site beneath the auroral oval. They divided the data into two selections for processing. First, all data was included in a robust processing and secondly, only data where the solar activity was low were included, which were 70% of the data. These two different data selections resulted in different models of the subsurface, where the 30% data which was sorted out, corresponded to the response of a 3000 km wavelength ionospheric source. In this situation the robust processing

failed to describe the subsurface when including all data, so caution must be taken when measuring in the polar regions.

Several others have tried to model the effect of the polar electrojet, by creating different models of the electrojet itself. Osipova et al. [1989] made a model of a stationary electrojet to calculate its effect on a resistivity model, where their results showed that for periods less than 15 min (900 s) the results are roughly independent of the electrojet. Pirjola [1992] present a theoretical model of the polar electrojet to examine the distortion on the transfer functions. He finds that above 1 min there are distortion effects in the plane wave assumption. It is difficult to set up a model of the polar electrojet, since changes in the parameters clearly affects the transfer function, so accurate models are needed.
In the summer of 1998, a large scale magnetotelluric and geomagnetic deep sounding project was conducted to map the deep crust and upper mantle structures of the Baltic Shield, The Baltic Electromagnetic Array Research. Several subprojects have been conducted [e.g. Hjelt et al., 2006; Korja et al., 2002; Lahti et al., 2005; Sokolova et al., 2007; Varentsov et al., 2003], where Engels et al. [2002] investigated the influence from a polar electrojet on magnetotelluric data, using a current loop as a source model. They concluded that the source field effects on the transfer functions are complicated and very difficult to predict.

All these projects agree that it is a complicated effect the polar electrojet can have on the transfer functions. And it is difficult to remove the effect at longer periods above 100 s. Some of the methods mentioned here reduce the effect, but they do not remove it. The multiple station processing used in this project tries to remove incoherent noise between stations. If the stations are at a considerable distance the polar electrojet would affect them differently and its effect might therefore be possible to remove, if there is enough available data. However, this needs to be tested in order to confirm.

During this project it was discovered that narrow fjords can have a large effect on the transfer functions, similar to the ocean effect. The currents induced in the ocean are channelled into the fjords and enhanced. The effect on the transfer functions can be considerable and are therefore also necessary to include in the modelling.

Thesis outline

Chapter 2 explains the different external current systems that contributes to Earth's magnetic field, and which are the sources of the magnetotelluric method. Chapter 3 contains the theory behind the magnetotelluric method. Chapter 4 introduces the measurements area with the geological background, and the field work. The processing software used in this project is presented in chapter 5, where the signal analysis necessary and processing techniques are explained. Chapter 6 presents the processing results and possible descriptions hereof. The different methods and results are compared with each other. Chapter 7 illustrates a model study of the impact fjords can have on induction arrows together with a forward modelling of the processing results from chapter 6. Chapter 8 sums up the conclusions of the project and discuss the future outlook of magnetotellurics in Greenland.

Chapter 2

Natural sources

The magnetotelluric method used in this project is a passive electromagnetic method which uses the natural variations of Earth's magnetic field to determine the electrical conductivity of the subsurface. This chapter introduces the different external sources that are responsible for these variations, together with an introduction to the magnetotelluric assumption and the polar electrojet, which is a source that can violate the magnetotelluric assumption.

Several sources contribute to the Earth's magnetic field. The location of these sources stretches deep within the Earth and out into the magnetosphere. It is common practise to divid them into internal and external sources, where internal sources originates from the core and crustal field, and the external sources covers the ionospheric and magnetospheric current systems. The main part of the magnetic field is generated in the liquid outer core, by a self-sustaining dynamo of conducting liquid iron. Outside the Earth, this field would approximate the magnetic field of a simple bar magnet, however, secondary sources distort the field. In the crust, the main core field magnetise susceptible rocks, which generates small variation in the magnetic field [McPherron, 1991].

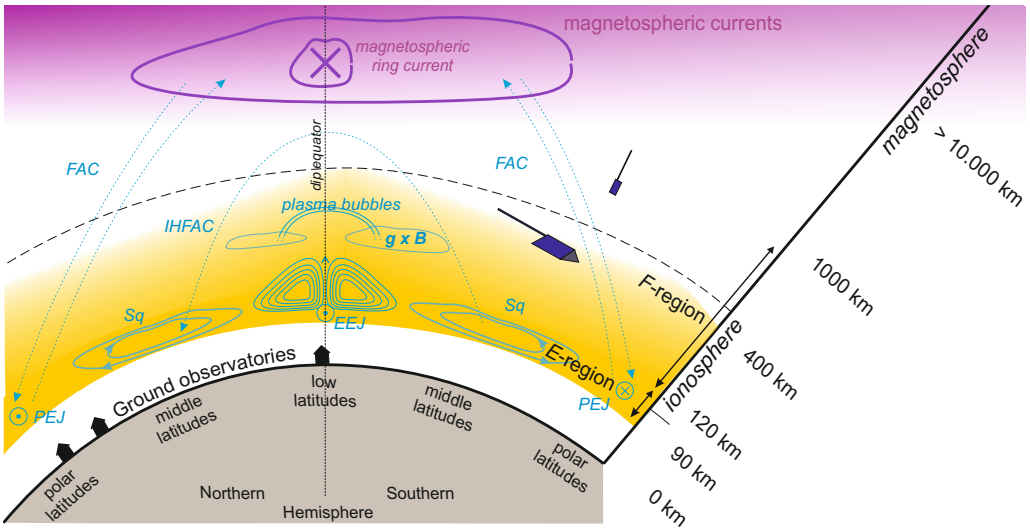

Figure 2.1: External sources of Earth's magnetic field [Olsen and Stolle, 2016]

The external sources are illustrated in Fig. 2.1, which include the magnetospheric ring current, solar quiet (Sq) variation, equatorial electrojet, polar electrojet and atmospheric variations [Olsen, 2007], and will be explained in this chapter.

When Earth's magnetic field interacts with the solar wind, it becomes complex. During certain conditions particles in the solar wind can enter the magnetosphere and ionosphere, generating electrical currents, which in turn generates magnetic fields. During times of strong solar wind with high particle density and velocity, these currents become large and can give rise to magnetic storms. The signature of magnetic storms in measurements at the surface and in low Earth orbit is characterised by a decrease in the horizontal component of the magnetic field. The particles that have entered the magnetosphere become trapped between the magnetic field lines and drifts around the Earth creating the magnetospheric ring current at a distance of a few Earth radii. This ring current produces a magnetic field, which at the surface will have a direction opposite the magnetic field from the core, hence a depression in the horizontal component of Earth's magnetic field. Magnetic storms can last for several days before the magnetic field returns to a normal state and can generate variations larger than 300 nT in size [Baumjohann and Treumann, 2012].

Besides entering the magnetospheric ring current, the particles can accumulate in the magnetotail. Eventually this can result in an unstable configuration with a sudden release of particles into the ionosphere in the polar regions. This phenomenon is called a substorm. When the particles enter the ionosphere they will generate a substorm electrojet, a polar electrojet (PEJ), flowing horizontally in the ionosphere. It is a strong east-west current located approximately at a height of 100 km. A substorm can last up to a few hours with large variation up to 1000 nT or even 3000 nT during magnetic storms [Baumjohann and Treumann, 2012]. A magnetic storm is not needed for a substorm to occur, but substorms will occur during a magnetic storm.

During day time, the solar radiation ionises the neutral gas in the ionosphere, which leads to increased conductivity. The neutral winds moving in the ionosphere drags the ions along with them, but not the electrons. This separation generates electric currents, for example the Sq current system [Alken et al., 2011; Maus and Lühr, 2006]. This system consists of two current vortexes, one on the northern hemisphere and one on the southern hemisphere, see Fig. 2.2. They rotate opposite each other due to the rotation of the Earth, with their centers located at local noon in the mid-latitudes [Schmucker, 1985]. These current systems are always present during local daytime with magnitude of 20-50 nT. During night time, the conductivity decrease to almost zero and the currents subside. Their contribution is best detected during quiet magnetic time, where the magnetic field is least disturbed, hence the name solar quiet variation.

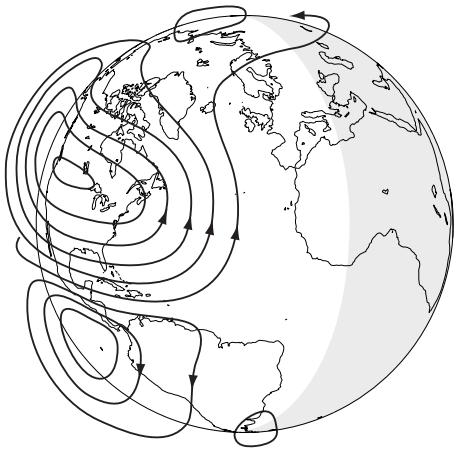

Figure 2.2: Sq current system [Viljanen, 2012]. The arrows indicate the direction of the currents.

At the geomagnetic dip equator, where the two current systems of the Sq variation meet, an eastward electrojet is flowing. It is a current band called the equatorial electrojet (EEJ), spanning a few degrees around the dip equator and the magnitude of this magnetic field can be up to five times stronger than the Sq variations [Olsen, 2007; Winch, 2007]. As the Sq current system is limited to the sunlit side of the Earth, so is the equatorial electrojet.

Hydromagnetic waves, such as Ultra Low Frequency (ULF) waves, are generated in the solar wind and magnetosphere. They consist of several classes of continuous and irregular pulsations within periods of 0.2 - 150 s. An example is when the waves propagate through the magnetosphere, which is connected to the ionosphere through field lines, and the field lines then resonate creating currents often seen as sinusoidal variations in the magnetic field [Viljanen, 2012].

All variations mentioned up until now have periods > 1 s, except ULF's which have periods both below and above 1 s. Variations with a period < 1 s originates in meteorological activity in the atmosphere. Global lightning and lightning discharges result in Schumann resonances and extremely low frequency (ELF) transients, which resonate in the cavity between the Earth and the ionosphere, globally around the Earth [Viljanen, 2012]. They produce variations with a magnitude less than 1 nT and can have a period down to 10^{-5} s.

Tab. 2.1 presents all the different magnetic variations belonging to the external sources of Earth's magnetic field, with their periods, amplitudes and possible penetration depths with electromagnetic induction [Olsen, 2007].

Type of variation	Symbol	Typical period	Typical amplitude	Typical penetration depth
Solar cycle variations		11 years	10–20 nT	>2000 km
Annual variation		12 months	5 nT	1500–2000 km
Semiannual variation		6 months	5 nT	
Storm-time variation	Dst	Hours to weeks	50–500 nT	300–1000 km
Regular daily variation				
At midlatitudes	Sq	24 h and harmonics	20–50 nT	300–600 km
At low latitudes	EEJ		50–100 nT	
Substorms	DP	10 min to 2 h	100 nT (1000 nT at p.l.)	100–300 km
Pulsations (=Ultra low frequency waves)	ULF	0.2–600 s		20–100 km
regular	pc	150–600 s (pc5)	10 nT (100 nT at p.l.)	
continuous		45–150 s (pc4)	2 nT	
pulsations		5–45 s (pc2,3)	0.5 nT	
		0.2–5 s (pc1)	0.1 nT	
Irregular transient pulsations	pi	1–150 s	1 nT	
Extreme low-frequency waves	ELF sferics	1/5–1/1000 s	<0.1 nT	Tens of meters-kilometers
Schumann resonance oscillations		1/8 s	<0.1 nT	
Very low-frequency waves, whistlers	VLF	10^{-5}–10^{-3} s		Few meters-tens of meters

Note: If amplitude depends significantly on latitude, values are also given for polar latitudes (p.l., dipole latitude >65°).

Table 2.1: Geomagnetic variations from Olsen [2007] (modified after Schmucker [1985])

The strength of the solar wind varies with the solar cycle with a period of 11 years. Due to the close connection to the solar wind, the amount of magnetic storms correlates well with the solar cycle [Viljanen, 2012], but with a slight shift such that the highest number of storms occur during the early descending phase of the solar cycle. An example is shown in Fig. 2.3 where a monthly magnetic storm analysis is shown, based on a time span between 1935 and 2009.

The magnetic field is measured at magnetometer stations around the globe, where they measure the local variation in the three components b_x, b_y and b_z. For a global view of the disturbance in Earth's magnetic field, different indices have been derived, e.g.

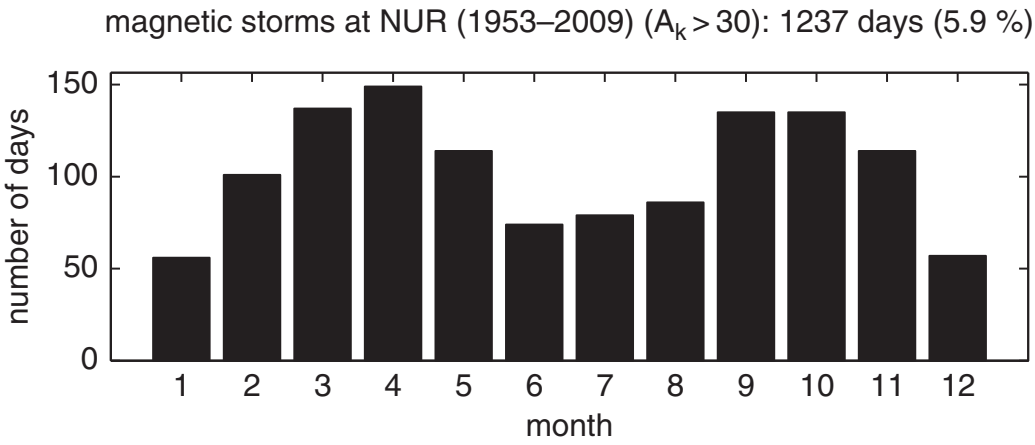

Figure 2.3: Monthly distribution of magnetically stormy days (activity index $A_k > 30$), measured between 1935 and 2009 at Nurmijärvi observatory in Finland [Viljanen, 2012].

Dst, K_p and *AE* index. The *Dst* index, the disturbance storm time index [Sugiura, 1964], is derived from four observatories located at low latitudes, around 20° - 30° from the geomagnetic dip equator. It is a measure of the magnetic field strength of the magnetospheric ring current, and is given as an hourly mean of the horizontal magnetic field. Since the magnetospheric ring current is flowing westward, the *Dst* index is often negative. The World Data Center for Geomagnetism, Kyoto [2016] is the provider of the *Dst* index.

K_p index, the planetary K-index [Menvielle and Berthelier, 1991], is derived from 13 magnetic observatories, located in the subauroral region within 38° to 60° or -35°to -43° latitude. The index is ranging from 0 (low activity) - 9 (high activity) on a quasi logarithmic scale and is derived from the horizontal components for a three hour interval. In each time interval, the maximum magnetic fluctuation is calculated and the quiet day variation is removed. By calculating a weighted average of these fluctuations, removing annual cycles of the daily variation from the local observatories, the K_p index is derived. The result gives an indication of the geomagnetic activity. K_p index is derived and accessible at GFZ - German Research Centre for Geosciences [2016].

The Auroral Electrojet index, called the *AE* index [Davis and Sugiura, 1966], is derived for each minute from the horizontal component of 10-13 observatories located in the polar regions, between 65° - 70°. It illustrates the highest magnetic fluctuation between the observatories, and thus the polar electrojets activity. It is derived at the World Data Center for Geomagnetism, Kyoto [2016].

This section has covered the external variations of Earth's magnetic field, more information can be found in the literature e.g. Chapman and Bartels [1940a,b]; Gubbins and Herrero-Bervera [2007]; Jacobs [1991a,b].

2.1 Magnetotelluric assumption

The magnetotelluric method (MT) investigates the electrical conductivity of the subsurface with the use of natural variations of Earth's magnetic field. The method is based on the assumption that the source fields are remote fields which can be treated as a quasi-stationary plane wave propagating vertical downward towards the Earth. The

assumption holds, if the lateral extension of the source field is considerable larger than the skin depth of the measuring frequency [Cagniard, 1953; Simpson and Bahr, 2005]. The curvature of the Earth will not affect the plane wave assumption for periods less than 1 day, therefore even with long period magnetotelluric data an assumption of a flat Earth and thereby a cartesian coordinate system is valid [Simpson and Bahr, 2005]. Magnetotelluric measurements are divided into two groups depending on the origin of the sources. Audio magnetotelluric (AMT) investigates shallow layers of the Earth and utilises the natural sources with a period less than 1 s down to 10^{-4} s, which are generated by global thunderstorms and lightning activity [Garcia and Jones, 2002]. Natural sources with a period longer than 1 s, which originates from the solar wind interaction with Earth's magnetic field, are used for the long period magnetotelluric (LMT) which can measure up to a period of 10^{5} s. In magnetotelluric, the magnetic fields of the natural sources are measured, simultaneously with the electric currents that the magnetic fields are inducing in the Earth. Experience has shown that magnetotelluric observations recorded over a long time period can compensate for non-homogeneous source field effects, which might occur, in such a way that the plane wave assumption is still valid. This is generally true when measuring at mid-latitudes, but at high or low latitudes the source field effects cannot be removed in this manner. The advantages of the plane wave assumption is that the transfer functions between the magnetic and electric fields are time invariant, meaning they are constant regardless of when the electric and magnetic fields were measured [Simpson and Bahr, 2005]. The period band around 1 Hz is called the dead band, because the power spectrum of the natural sources are at a minimum, see Fig. 2.4. This is the period band where the sources of AMT and LMT reach their boundary. Measurements taken in this period band often result in magnetotelluric response functions with reduced quality, because of the reduced energy present. A similar area is present for AMT at 1-5 kHz, called the AMT dead band [Viljanen, 2012].

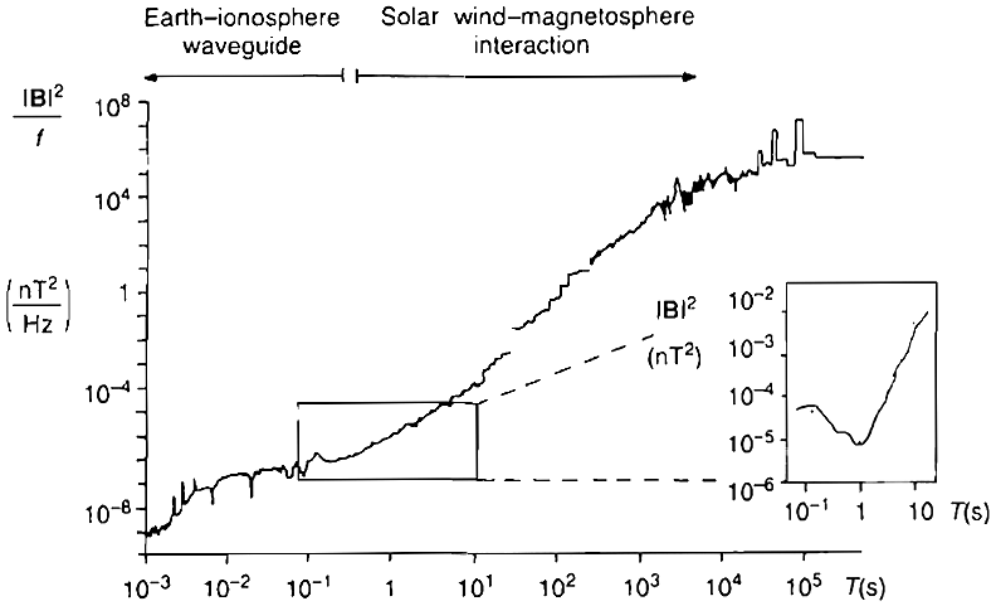

Figure 2.4: Power spectrum of the magnetotelluric sources from Simpson and Bahr [2005] modified from Junge [1994]. The small window illustrate the dead band around 1 Hz.

2.2 The polar electrojet

At polar latitudes, the plane wave assumption in magnetotelluric is not always valid and caution has to be taken when interpreting the transfer functions. The reason is a non-homogeneous source field in the ionosphere, called the polar electrojet. It is a strong east - west current system located at a height of 100 km, and due to its close location to the surface it produces the largest ground based magnetic disturbances observed [Baumjohann and Treumann, 2012]. The polar electrojet (also called auroral electrojet) consists of two parts. One, an always present current system consisting of an eastward and westward electrojet running from the day side towards midnight, with an approximately stationary position and with small variations, called convection electrojets, a sketch is displayed in Fig. 2.5 left figure. Up to a substorm, the amount

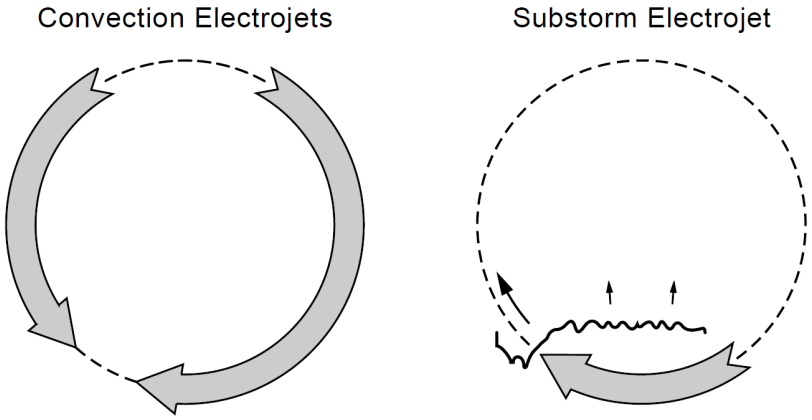

Figure 2.5: The two electrojet systems, seen from the pole and down towards the surface. Noon is up and midnight is down [Baumjohann and Treumann, 2012]. **Left:** The convection electrojets. **Right:** Electrojet enhancement present during substorms.

of particles in the magnetosphere is significantly increased, and there is a build up of particles in the magnetotail. These particles are released from the tail and injected into the ionosphere at polar latitudes with high velocity. Besides enhancing the convection electrojets, this unloading of particles into the ionosphere leads to the formation of a substorm electrojet [Baumjohann and Treumann, 2012], the second part of the polar electrojet, see sketch in Fig. 2.5 right figure, which is an electrojet that enhances the westward convection electrojet. A substorm lasts normally a few hours, but during magnetic storms several substorms can occur and begin before the previous substorm has ended, thus prolonging the time with the strong currents.

These substorm electrojets can give large disturbances in magnetotelluric measurements, if the site is located in its close vicinity. Fig. 2.6 is a simple illustration of a line current in the ionosphere, representing the polar electrojet, and the effects it will have on sites on the surface. If the electrojet would be stationary in space and strength, the effect on the sites would always be the same on the individual sites 1, 2 and 3. However, the strength of the electrojet is constantly changing, and during a substorm the electrojet moves southward and northward in its different phases before ending. To illustrate this, imagine the sites in Fig. 2.6 are not three different sites, but the same site at three different times. This is a more complex situation, where the magnetic field from the electrojet is changing over time, and if the movement and size of the electrojet

is not known, it is difficult to distinguish the magnetic field originating from the electrojet, from the magnetic field generated by the other magnetotelluric sources. If transfer functions are calculated from a magnetic field with an electrojet present, they will not only represent the subsurface, but also the electrojet. Different approaches can be used to account for this situation, e.g. model the electrojet to estimate the magnetic field it produces [e.g. Engels et al., 2002; Osipova et al., 1989; Pirjola, 1992], or select time periods where the electrojet is not present [e.g. Garcia et al., 1997; Viljanen, 1996], but it is a very complex situation which is not always resolved.

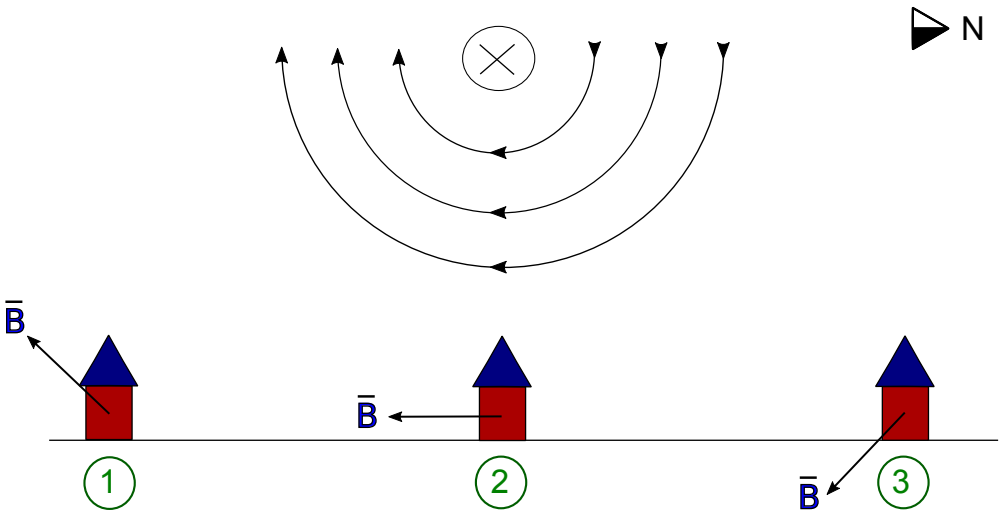

Figure 2.6: Simple illustration of a current running westward in the ionosphere and how the corresponding magnetic field will be at three locations or at one location at three different times.

Chapter 3

Magnetotelluric

The magnetotelluric method is a passive exploration technique that utilises natural variations in the Earth's magnetic field as a source to investigate the electrical resistivity distribution in the Earth. The method was proposed by Cagniard [1953] in France and Tikhonov [1950] in USSR, independently of each other in the middle of the 20th century. They discovered that simultaneous measurements of the electric and magnetic field variations can be used to estimate the penetration depth of electromagnetic fields in the subsurface. Prior to Cagniard [1953] and Tikhonov [1950], other researchers made discoveries related to the method e.g. Kato and Kikuchi [1950a,b] and Rikitake [1951], who discovered that the amplitude of the ratio of the electric and magnetic field, E/B, and the phase changes with period.
In the following chapter, the basic principles behind the magnetotelluric method are introduced, including the magnetotelluric transfer functions and the effect sources of different spatial geometry can have on transfer functions and the magnetotelluric assumption. The following calculations can be found in e.g. Chave and Weidelt [2012]; Keller and Frischknecht [1966]; Schmucker and Weidelt [1975]; Simpson and Bahr [2005]; Telford et al. [1990] if not otherwise stated.

The magnetotelluric method builds upon Maxwell's equations, which describe the relation between the electric, $\mathbf{E}$, and magnetic, $\mathbf{B}$, field. The general description is shown in eqn. 3.1.

$$\begin{aligned} \nabla \cdot \mathbf{E} &= \frac{1}{\epsilon_0} q \\ \nabla \times \mathbf{E} &= -\frac{\partial \mathbf{B}}{\partial t} \\ \nabla \cdot \mathbf{B} &= 0 \\ \nabla \times \mathbf{B} &= \mu_0 \mathbf{J} + \mu_0 \epsilon_0 \frac{\partial \mathbf{E}}{\partial t} \end{aligned} \tag{3.1}$$

where q is the electric charge density, $\mathbf{J}$ is the current density, μ_0 and ϵ_0 are the permeability and permittivity of free space, respectively.
There are two types of charges and currents, free and bound. Bound charges occur inside atoms and molecules that have been polarised. Free charges, however, are electrons or ions which can move independently of a molecule, for example inside metals or in free space. On a macroscopic scale the bound charges and currents are negligible

compared to the free, and Maxwell's equations can be reformulated

$$\nabla \cdot \mathfrak{D} = q_e \tag{3.2}$$

$$\nabla \times \mathbf{E} = -\frac{\partial \mathbf{B}}{\partial t} \tag{3.3}$$

$$\nabla \cdot \mathbf{B} = 0 \tag{3.4}$$

$$\nabla \times \mathbf{H} = \mathbf{J}_e + \frac{\partial \mathfrak{D}}{\partial t} \tag{3.5}$$

where $\mathfrak{D}$ is the electric displacement, q_e is the electric charge density of the free charges, $\mathbf{H}$ is the magnetic field strength and $\mathbf{J}_e$ is the electric current density of the free currents [Chave and Weidelt, 2012; Griffiths, 1999]. Within other research fields, $\mathbf{B}$ is usually denoted as the magnetic induction and $\mathbf{H}$ as the magnetic field. However, within geomagnetism $\mathbf{B}$ is often called the magnetic field.
The displacement $\mathfrak{D}$ and the magnetic field strength $\mathbf{H}$ can be expressed by $\mathbf{E}$ and $\mathbf{B}$, respectively

$$\mathfrak{D} = \epsilon \mathbf{E} \tag{3.6}$$

$$\mathbf{H} = \frac{1}{\mu}\mathbf{B} \tag{3.7}$$

where μ and ϵ are the permeability and permittivity of the medium. In magnetotellurics, the variations in μ and ϵ are considered negligible compared to bulk rock conductivities, μ and ϵ are therefore set as the value of free space, $\mu = \mu_0$ and $\epsilon = \epsilon_0$. In a medium, with isotropic conductivity, $\mathbf{E}$ produces a current density $\mathbf{J}$, with the relation through Ohm's law

$$\mathbf{J} = \sigma \mathbf{E} \tag{3.8}$$

where $\sigma = \frac{1}{\rho}$ is the conductivity, the reciprocal of the resistivity, ρ.

When studying the Earth, an external time varying magnetic field $\mathbf{B}$ induces an electric field $\mathbf{E}$ in the subsurface, which in turn produces a secondary magnetic field, as given by Maxwell's equations. From these equations it is possible to derive a diffusion equation, which gives information about the conductivity distribution of the Earth. Focusing first on the derivation for the electric field **E**, eqn. 3.3 is combined with 3.7, and eqn. 3.5 is combined with eqn. 3.6 and eqn. 3.8 to give

$$\nabla \times \mathbf{E} = -\mu_0 \frac{\partial \mathbf{H}}{\partial t} \tag{3.9}$$

$$\nabla \times \mathbf{H} = \sigma \mathbf{E} + \epsilon_0 \frac{\partial \mathbf{E}}{\partial t} \ . \tag{3.10}$$

By combining eqn. 3.9 and 3.10 and using the vector calculus identity $\nabla \times (\nabla \times \mathbf{v}) = \nabla(\nabla \cdot \mathbf{v}) - \nabla^2 \mathbf{v}$ ($\mathbf{v}$ is any vector), and eqn. 3.6 with the assumption that the electric field is divergence free, $\nabla \cdot \mathbf{E} = 0$, the telegraph equation for the electric field is given as

$$\nabla^2 \mathbf{E} = \mu_0 \Big(\sigma \frac{\partial \mathbf{E}}{\partial t} + \epsilon_0 \frac{\partial^2 \mathbf{E}}{\partial t^2} \Big) \ . \tag{3.11}$$

Similar calculations can be performed for the magnetic field **B**, combining eqn. 3.5, eqn. 3.8 and eqn. 3.6 and taking the curl of the result yields

$$\nabla \times (\nabla \times \mathbf{H}) = \nabla \times \Big(\sigma \mathbf{E} + \epsilon \frac{\partial \mathbf{E}}{\partial t} \Big) \ . \tag{3.12}$$

With the use of the vector calculus identity as used for the electric field together with eqn. 3.4, eqn. 3.3 and eqn. 3.7, the telegraph equation for the magnetic field is

$$\nabla^2\mathbf{B} = \mu_0\Big(\sigma\frac{\partial\mathbf{B}}{\partial t} + \epsilon_0\frac{\partial^2\mathbf{B}}{\partial t^2}\Big) \ . \tag{3.13}$$

Assuming the fields have a harmonic dependency $e^{i\omega t}$, where $\omega = 2\pi f$ is the angular frequency, the telegraph equation for $\mathbf{E}$ and $\mathbf{B}$ become

$$\begin{aligned}\nabla^2\mathbf{E} &= \mu_0\sigma\Big(i\omega - \frac{\omega^2\epsilon}{\sigma}\Big)\mathbf{E} \\ \nabla^2\mathbf{B} &= \mu_0\sigma\Big(i\omega - \frac{\omega^2\epsilon}{\sigma}\Big)\mathbf{B} \ .\end{aligned} \tag{3.14}$$

The expression $-\frac{\omega^2\epsilon}{\sigma}$ originates from displacement processes and can be neglected, within the magnetotelluric frequency span, compared to the diffusion processes, $i\omega$, in the Earth. Examples of the difference in magnitude of the two processes are listed in Tab. 3.1 for three different resistivities. For short periods (high frequencies) and low resistivity, the magnitude of the two processes will be similar, and the assumption that displacement processes can be neglected is invalid.

Frequency f [Hz]	Diffusion processes: $\lvert i\omega\mu_0\sigma\rvert$ $[m^{-2}]$			Displacement processes: $\lvert\omega^2\epsilon\mu_0\rvert$ $[m^{-2}]$
	$10\ \Omega m$	$100\ \Omega m$	$1000\ \Omega m$	
10^{-3}	10^{-8}	10^{-7}	10^{-6}	10^{-15}
1	10^{-5}	10^{-4}	10^{-3}	10^{-9}
$10^{\ 3}$	10^{-2}	10^{-1}	1	10^{-3}

Table 3.1: Approximative magnitude of diffusion processes and displacement processes, with three different subsurface resitivities.

For most situations within the magnetotelluric frequency band, $10^{-5} - 10^4$ Hz, the assumption $|i\omega| \gg |\frac{\omega^2\epsilon}{\sigma}|$ is valid and displacement processes can be neglected. This changes eqn. 3.14 to a diffusion equation

$$\begin{aligned}\nabla^2\mathbf{E} &= i\omega\mu_0\sigma\mathbf{E} \\ \nabla^2\mathbf{B} &= i\omega\mu_0\sigma\mathbf{B} \ .\end{aligned} \tag{3.15}$$

With the different assumptions taken in magnetotellurics, Maxwell's equations can be presented in a simpler form

$$\nabla\cdot\mathbf{E} = \frac{q_e}{\epsilon_0} \tag{3.16}$$

$$\nabla\cdot\mathbf{B} = 0 \tag{3.17}$$

$$\nabla\times\mathbf{E} = -\frac{\partial\mathbf{B}}{\partial t} \tag{3.18}$$

$$\nabla\times\mathbf{B} = \mu_0\mathbf{J} \tag{3.19}$$

In addition to the harmonic dependency $e^{i\omega t}$ in time, we assume a harmonic dependency in space representing a travelling plane wave: $e^{i(\omega t - k_x x - k_y y)}$. A solution of eqn. 3.15 is

$$\mathbf{E} = \mathbf{E}_1 \; e^{k_z z} \; e^{i(\omega t - (k_x x + k_y y))} + \mathbf{E}_2 \; e^{-k_z z} \; e^{i(\omega t - (k_x x + k_y y))} \tag{3.20}$$

$$\mathbf{B} = \mathbf{B}_1 \; e^{k_z z} \; e^{i(\omega t - (k_x x + k_y y))} + \mathbf{B}_2 \; e^{-k_z z} \; e^{i(\omega t - (k_x x + k_y y))} \tag{3.21}$$

if the conductivity of the Earth is only dependent on the depth, $\sigma = \sigma(z)$. $\mathbf{E}_1$, $\mathbf{E}_2$, $\mathbf{B}_1$ and $\mathbf{B}_2$ represent the amplitudes of the different waves. The second term on the right hand side of eqn. 3.20 and 3.21 describes a wave moving in the opposite direction than the first term, however, since the Earth only dissipates or absorbs electromagnetic energy and does not generate it, $\mathbf{E}_2 = 0$ and $\mathbf{B}_2 = 0$ for $z \to R_E$ (radius of the Earth) and the term vanishes. The harmonic oscillation in the x and y direction is represented by the wave number $k = \sqrt{k_x^2 + k_y^2}$, where k_x and k_y are the wave number in the x and y direction, respectively. With this representation of the fields, $\nabla^2\mathbf{E}$ yields

$$\nabla^2\mathbf{E} = k_z^2\mathbf{E} - k_x^2\mathbf{E} - k_y^2\mathbf{E} \tag{3.22}$$

which is equal to eqn. 3.15. Since $\frac{\partial^2\mathbf{E}}{\partial z^2} = k_z^2\mathbf{E}$, the diffusion equation can be written as

$$\frac{\partial^2\mathbf{E}}{\partial z^2} = (i\omega\mu_0\sigma + k^2)\mathbf{E} = K^2\mathbf{E} \tag{3.23}$$

where $K = \sqrt{i\omega\mu_0\sigma + k^2}$ is the complex vertical wavenumber. Similar solution is valid for the magnetic field

$$\frac{\partial^2\mathbf{B}}{\partial z^2} = (i\omega\mu_0\sigma + k^2)\mathbf{B} = K^2\mathbf{B} \; . \tag{3.24}$$

Homogeneous half space

The simplest subsurface model is a homogeneous half space, which consists of an uniform, homogeneous subsurface with a constant electrical conductivity, σ. In such a model, a relation can be presented, between the frequency of the signal and the depth in the subsurface it describes.

The inverse of K is referred to as the Schmucker-Weidelt transfer function [Schmucker, 1973; Weidelt, 1972], $C = \frac{1}{K}$, which is the complex penetration depth, dependent on frequency. C describes a linear relationship between the electric and magnetic fields. For example for a 1D subsurface model, from Maxwell's eqn. 3.3 and eqn. 3.23

$$\frac{\partial E_x}{\partial z} = -\frac{\partial B_y}{\partial t} = -i\omega B_y = -KE_x \tag{3.25}$$

in a coordinate system with x directed towards magnetic north, y towards east and z positively downwards. Therefore, C can be calculated from the orthogonal components of E and B

$$C = \frac{E_x}{i\omega B_y} \qquad\qquad C = -\frac{E_y}{i\omega B_x} \tag{3.26}$$

The real part of C, $\Re(C)$, gives an indication of which depth a signal with a certain frequency is describing

$$\delta = \Re(C) = \frac{1}{\Re(K)} = \sqrt{\frac{2}{\mu_0\sigma\omega}} \tag{3.27}$$

this is referred to as the skin depth, or penetration depth. The relation between the two penetration depths, C and δ, is

$$C = \frac{1}{\sqrt{i\omega\mu_0\sigma + k^2}} = \frac{1}{\sqrt{\frac{2i}{\delta^2} + k^2}} = \frac{1}{k\sqrt{\frac{2i}{\delta^2 k^2} + 1}} \tag{3.28}$$

If $\delta^2 k^2 \gg 1$, $C = \frac{1}{k}$ and the transfer function depends only on the wave number k of the source. C is not affected by the conductivity of the subsurface or the frequency. However, if $\delta^2 k^2 \ll 1$, C only depends on the skin depth

$$C = \frac{1}{k\sqrt{\frac{2i}{\delta^2 k^2}}} = \frac{1-i}{2}\delta \ . \tag{3.29}$$

as if the source is a plane wave, $k = 0$. The imaginary part of K results in an attenuation of the electromagnetic wave, by a factor of $1/e$ at skin depth. This implies the electromagnetic field is only affected by the layers above the skin depth and unaffected by the layers below.
The C response is a transfer function that describes the subsurface in 1D situations. However, in magnetotelluric, the relation between the electric and magnetic fields are often given through the impedance tensor $\mathbf{Z}$, which contains the ratios of the electric and magnetic fields

$$\begin{pmatrix} E_x \\ E_y \end{pmatrix} = \begin{pmatrix} Z_{xx} & Z_{xy} \\ Z_{yx} & Z_{yy} \end{pmatrix} \begin{pmatrix} B_x \\ B_y \end{pmatrix} \tag{3.30}$$

where

$$Z_{xy} = \frac{E_x}{B_y} = i\omega C_{xy} \qquad\qquad Z_{yx} = \frac{E_y}{B_x} = -i\omega C_{yx} \tag{3.31}$$

which is often used for visualising the response. For a 1D subsurface, $Z = Z_{xy} = -Z_{yx}$ and thereby $C = C_{xy} = C_{yx}$ as eqn. 3.26. Since the impedance tensor element is a complex value, it is possible to calculate the phase ϕ between the electric and magnetic field, and the magnitude of the response is given as the apparent resistivity ρ_a

$$\rho_{a,xy} = \frac{\mu_0}{\omega}|Z_{xy}(\omega)|^2 = \mu_0\omega|C_{xy}(\omega)|^2 \tag{3.32}$$

$$\phi_{xy} = \tan^{-1}\left(\frac{\Im(Z_{xy})}{\Re(Z_{xy})}\right) \ . \tag{3.33}$$

The phase ϕ_{xy} describes the delay between the electric field E_x and magnetic field B_y, which in a homogeneous half space will be at a constant $45°$, because the magnetic field consist of both a primary (external) and a secondary (internal) field and will shift the phase compared to the electric field. The apparent resistivity ρ_a is the resistivity of the subsurface, as measured if it was a homogeneous half space.

Layered half space

Until now, the focus has been on a homogeneous half space, however, the subsurface can often better be approximated with a layered half space. The solution to the diffusion equations contain both terms as in eqn. 3.20 and 3.21, because $E_2 \neq 0$ since the

subsurface layers have a limited thickness, and can be displayed in terms of the complex vertical wave number $K_n = \sqrt{i\omega\mu_0\sigma_n + k^2}$

$$\mathbf{E}_n = \mathbf{E}_{1,n}e^{i\omega t}e^{-K_n z_n} + \mathbf{E}_{2,n}e^{i\omega t}e^{K_n z_n} \tag{3.34}$$

where n is the layer number counted from the surface and downwards. $n = N$ is the deepest layer, which is a homogeneous half space. Beginning with the homogeneous half space at $n = N$, the Schmucker-Weidelt transfer function C is calculated as

$$C_N = \frac{1}{K_N} = \frac{E_{x,N}}{i\omega B_{y,N}} \tag{3.35}$$

as in eqn. 3.26. $B_{y,n}$ can be expressed in terms of K_n and $E_{x,n}$ with the use of eqn. 3.25

$$B_{y,n} = \frac{K_n}{i\omega}(E_{1,xn}e^{i\omega t}e^{-K_n z_n} - E_{2,xn}e^{i\omega t}e^{K_n z_n}) \ . \tag{3.36}$$

It is possible to calculate the transfer function of the layered subsurface by calculating the transfer function at the top of the n'th layer if the transfer function of the $(n+1)$'th layer is known, and iterate from the deepest layer to the surface. This procedure is called Waits recursion formula [Wait, 1954]. C_n can be determined from eqn. 3.26

$$C_n(z_n) = \frac{1}{K_n}\frac{E_{1,xn}e^{i\omega t}e^{-K_n z_n} + E_{2,xn}e^{i\omega t}e^{K_n z_n}}{E_{1,xn}e^{i\omega t}e^{-K_n z_n} - E_{2,xn}e^{i\omega t}e^{K_n z_n}} \ . \tag{3.37}$$

By calculating a similar equation for layer $(n-1)$ and rearranging eqn. 3.37, the transfer function of layer $(n-1)$ can be calculated, with the information that the field components of $\mathbf{E}$ and $\mathbf{B}$ are continuous at the boundary between the layers

$$C_n(z_{n-1}) = \frac{1}{K_n}\frac{K_n C_n(z_n) + \tanh(K_n d_n))}{(1 + K_n C_n(z_n)\tanh(K_n d_n))} \tag{3.38}$$

where $d_n = z_n - z_{n-1}$ is the thickness of layer n. By iterating from the deepest layer with C_N and upwards until the surface layer, it is possible to obtain the transfer function for the layered half space.

The apparent resistivity and phase is calculated from eqn. 3.32 and 3.33, however in a subsurface with a layered half space, the phase is not constant. It changes with frequency, which is an indication of a transition between regions in the subsurface with different resistivities. For transitions from low to high resistivity, in a 1D subsurface, the phase will decrease below 45° and for transitions from high to low resistivity, the phase will increase above 45°.
The phase and apparent resistivity are often displayed as a function of frequency or period. The period is a relative measure of the depth, through the skin depth in eqn. 3.27, since long periods penetrates deeper into the subsurface, however absolute values cannot be determined unless the subsurface is a homogeneous half space.

An example of the response of a three layered half space, is displayed in Fig. 3.1, where the phase begins at 45°, then decreases below 45° when the resistivity is increasing, and when the resistivity changes again to a lower value, the phase is above 45°. When the subsurface is non-1D, the response is more difficult to interpret.

The phase ϕ expresses the phase delay between the electric and magnetic field, and is not independent of the apparent resistivity. ϕ can be predicted from ρ_a through the

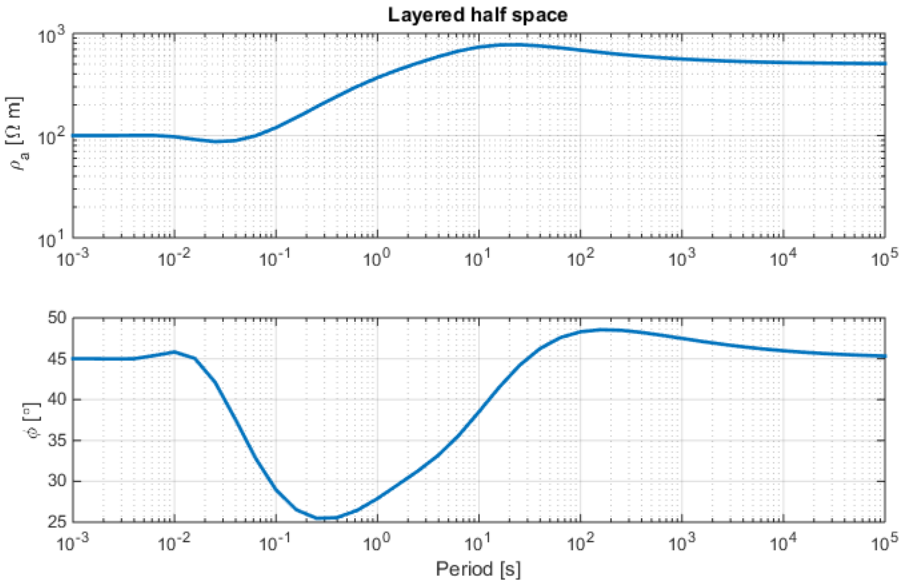

Figure 3.1: Phase and apparent resistivity of layered half space, with transitions depths at 1 km and 50 km and resistivities of $100\ \Omega m$, $1000\ \Omega m$ and $500\ \Omega m$.

Kramers-Kroenig relation [Weidelt, 1972]

$$\phi(\omega) = \frac{\pi}{4} - \frac{\omega}{\pi}\int_0^\infty \log\frac{\rho_a(x)}{\rho_0}\frac{1}{x^2-\omega^2}\,\mathrm{d}x\ . \tag{3.39}$$

For a layered subsurface the $\rho^* - z^*$ transformation [Schmucker, 1987] can be used to estimate the resistivity of the underlying homogeneous half space ρ^* from the phase $\phi(\omega)$

$$\begin{aligned} \rho^* &= \rho_a\ 2\cos^2(\phi(\omega)) && \phi(\omega) > 45^\circ \\ \rho^* &= \rho_a\ 1/(2\sin^2(\phi(\omega))) && \phi(\omega) < 45^\circ \end{aligned} \tag{3.40}$$

ρ_a are here the apparent resistivity of the overlaying layer. The shape of the resistivity can be indicated from $\phi(\omega)$, but not necessarily the absolute value, if galvanic distortion is present, see section 3.2, which is distortion caused by small scale anomalies near the surface.

Multidimensional subsurface

In a multidimensional subsurface, the conductivity changes in two or three dimensions. Since the current density is conserved across a discontinuity, the electric field is not continuous, since the conductivity is varying in space $\sigma = \sigma(x, y, z)$ in a multidimensional subsurface. This means that $\nabla \cdot \mathbf{E} \neq 0$ as in the situation with σ only varying with depth, $\sigma(z)$, but $\nabla \cdot (\sigma\mathbf{E}) = 0$, since there have to be conservation of current across a discontinuity.

$$\nabla \cdot (\sigma\mathbf{E}) = \sigma\nabla\cdot\mathbf{E} + \mathbf{E}\nabla\sigma = 0 \tag{3.41}$$

$$\nabla\cdot\mathbf{E} = -\frac{1}{\sigma}\mathbf{E}\nabla\sigma\ . \tag{3.42}$$

Due to this change, the diffusions equations in eqn. 3.15 have to be modified. The electric diffusions equation in a multidimensional subsurface is calculated from eqn. 3.9, 3.10 and the vector identity $\nabla \times (\nabla \times \mathbf{v}) = \nabla(\nabla \cdot \mathbf{v}) - \nabla^2\mathbf{v}$, as previously.

$$\nabla \times (\nabla \times \mathbf{E}) = -i\omega\mu_0\sigma\mathbf{E} \tag{3.43}$$

$$\nabla(\nabla \cdot \mathbf{E}) - \nabla^2\mathbf{E} = -i\omega\mu_0\sigma\mathbf{E} \tag{3.44}$$

where the assumption of no displacement processes are still valid. However, the equation differs because $\nabla \cdot \mathbf{E} \neq 0$, resulting in

$$\boxed{\nabla^2\mathbf{E} = i\omega\mu_0\sigma\mathbf{E} - \nabla(\frac{1}{\sigma}\mathbf{E}\nabla\sigma)} \tag{3.45}$$

by combining eqn. 3.44 and 3.42. For the magnetic field, the vector identity $\nabla \times (\psi\mathbf{v} = \psi(\nabla \times \mathbf{v}) + \nabla\psi \times \mathbf{v}$ (ψ is a scalar), eqn. 3.46 is used together with eqn. 3.18 and the solution for $\mathbf{B}$, eqn. 3.21

$$\nabla \times (\sigma\mathbf{E}) = \sigma\nabla \times \mathbf{E} - \mathbf{E} \times \nabla\sigma \tag{3.46}$$

$$= -i\omega\sigma\mathbf{B} - \mathbf{E} \times \nabla\sigma \ . \tag{3.47}$$

The left hand side can be rewritten in terms of $\mathbf{B}$, from eqn. 3.19 and 3.8, with no displacement processes.

$$\nabla \times \mathbf{B} = \mu_0\mathbf{J} = \mu_0\sigma\mathbf{E} \tag{3.48}$$

$$\nabla \times (\nabla \times \mathbf{B}) = \mu_0\nabla \times (\sigma\mathbf{E}) \ . \tag{3.49}$$

With the use of the vector identity $\nabla \times (\nabla \times \mathbf{v}) = \nabla(\nabla \cdot \mathbf{v}) - \nabla^2\mathbf{v}$ together with eqn. 3.17

$$-\nabla^2\mathbf{B} = \mu_0(\nabla \times \sigma\mathbf{E}) \tag{3.50}$$

which together with eqn. 3.46 and eqn. 3.48 returns the modified diffusion equation for the magnetic field

$$\nabla^2\mathbf{B} = i\omega\mu_0\sigma\mathbf{B} - \mu_0(\mathbf{E} \times \nabla\sigma) \tag{3.51}$$

$$\boxed{\nabla^2\mathbf{B} = i\omega\mu_0\sigma\mathbf{B} + \frac{1}{\sigma}(\nabla \times \mathbf{B}) \times \sigma} \ . \tag{3.52}$$

Solutions for these modified diffusions equations cannot be estimated analytically, but can be found numerically with the use of e.g. Finite Difference, Finite Element or Finite Volume methods.

For a 2D subsurface where the conductivity is changing only in one horizontal direction, for instance only in y direction, the impedance tensor relation in eqn. 3.30 can be simplified. For example if the subsurface contains a discontinuity, such as a fault line in Fig. 3.2, the current density must be conserved across a boundary, therefore if the conductivity changes the electric field must also change

$$J_y = \sigma_1 E_{y,1} = \sigma_2 E_{y,2} \ . \tag{3.53}$$

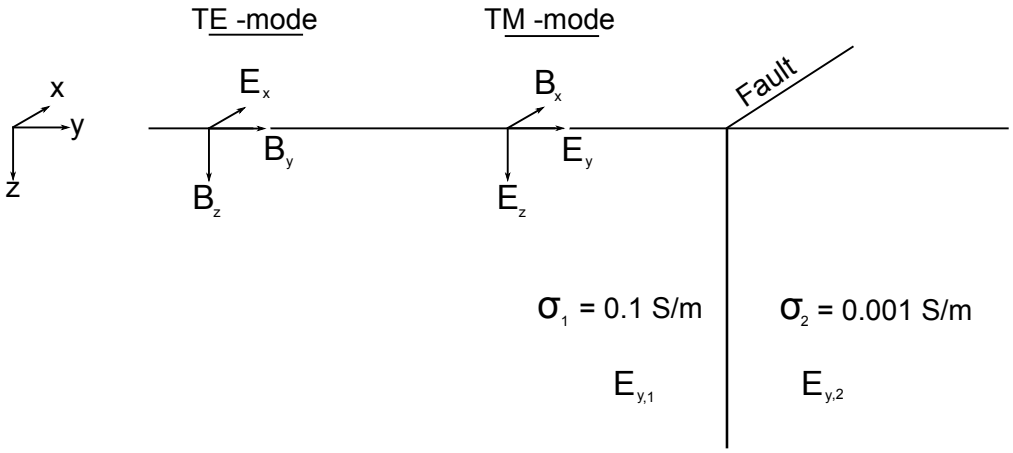

Figure 3.2: Simple 2D model with a fault line, showing the corresponding fields for TE and TM mode. Redrawn from Simpson and Bahr [2005].

Ideally the electric and magnetic fields are orthogonal on each other, which means the electric field E_x only will produce a magnetic field in the y-direction B_y. Therefore can eqn. 3.4 and eqn. 3.5 be decoupled and divided into two groups, *transverse electric* (TE mode) and *transverse magnetic* (TM mode), see eqn. 3.54. The TE-mode describes the electric currents flowing along the strike direction, the fault in Fig. 3.2, with the fields E_x, B_y, B_z and the TM-mode describes the currents flowing across the strike direction, with the fields B_x, E_y, E_z.

TE-mode	**TM-mode**
$\frac{\partial E_x}{\partial y} = \frac{\partial B_z}{\partial t} = i\omega B_z$	$\frac{\partial B_x}{\partial y} = \mu_0 \sigma E_z$
$\frac{\partial E_x}{\partial z} = \frac{\partial B_y}{\partial t} = -i\omega B_y$	$-\frac{\partial B_x}{\partial z} = \mu_0 \sigma E_y$
$\frac{\partial B_z}{\partial y} - \frac{\partial B_y}{\partial z} = \mu_0 \sigma E_x$	$\frac{\partial E_z}{\partial y} - \frac{\partial E_y}{\partial z} = i\omega B_x$.

(3.54)

To decouple the impedance tensor, it has to be rotated into the strike direction

$$\mathbf{R_z E} = \mathbf{R_z Z R_z^{-1}}\ \mathbf{R_z B} \tag{3.55}$$

with the rotation matrix $\mathbf{R_z}$

$$\mathbf{R_z} = \begin{pmatrix} \cos\theta & \sin\theta \\ -\sin\theta & \cos\theta \end{pmatrix} \tag{3.56}$$

where θ is the rotation angle into the strike direction. By this rotation $Z_{xx} = Z_{yy} = 0$ and only Z_{xy} and Z_{yx} will contain the information from the TE and TM mode, respectively. With real measurement data, the rotation angle can be estimated by minimizing $|Z_{xx}|^2 + |Z_{yy}|^2$ [Engels, 1997; Swift, 1967]

$$\theta = \frac{1}{4} \tan^{-1} \left(\frac{2\Re(Z_{xy} + Z_{yx})(Z_{xx} - Z_{yy})}{|Z_{xx} - Z_{yy}|^2 - |Z_{xy} - Z_{yx}|^2} \right) \tag{3.57}$$

however, there is a 90° ambiguity in the direction.
The resistivities, ρ_{yx} and ρ_{xy}, will not be identical as in the 1D case, since the electromagnetic fields change because of the fault. ρ_{xy} and ϕ_{xy} are the TE mode which will not detect the fault, however the TM mode, ρ_{yx} and ϕ_{yx}, include the electric field, E_y, which is discontinuous across the fault. Charges are accumulated along the boundary, which is detected in the TM mode. Therefore, is TM mode more sensitive to interfaces. The TE mode is instead more sensitive to conductors along strike, and deep structures where TM mode detects near surfaces structures better [e.g. Berdichevsky et al., 1998]. The two modes complement each other with their different sensitivities. Conductive structures are better detected by TM mode, and resistive structures by the TE mode [e.g. Berdichevsky et al., 1998].

The TE mode contains a vertical magnetic field B_z, which is generated by lateral conductivity gradients, if the source field is a plane wave. By combining the information in the different magnetic field components it is possible to detect lateral conductivity contrasts. This is calculated through the transfer function $\mathbf{T}$, often referred to as the tipper

$$B_z = \begin{pmatrix} T_{xz} & T_{yz} \end{pmatrix} \begin{pmatrix} B_x \\ B_y \end{pmatrix} \ . \tag{3.58}$$

Vector representations of $\mathbf{T}$ are divided into a real vector, $(\Re(T_{xz}),\Re(T_{yz}))$, and an imaginary vector, $(\Im(T_{xz}),\Im(T_{yz}))$, which are often referred to as tipper vectors or induction arrows. An example of the real induction arrows behaviour across a 2D structure with a lateral boundary, is illustrated in Fig. 3.3. There are two common illustrations

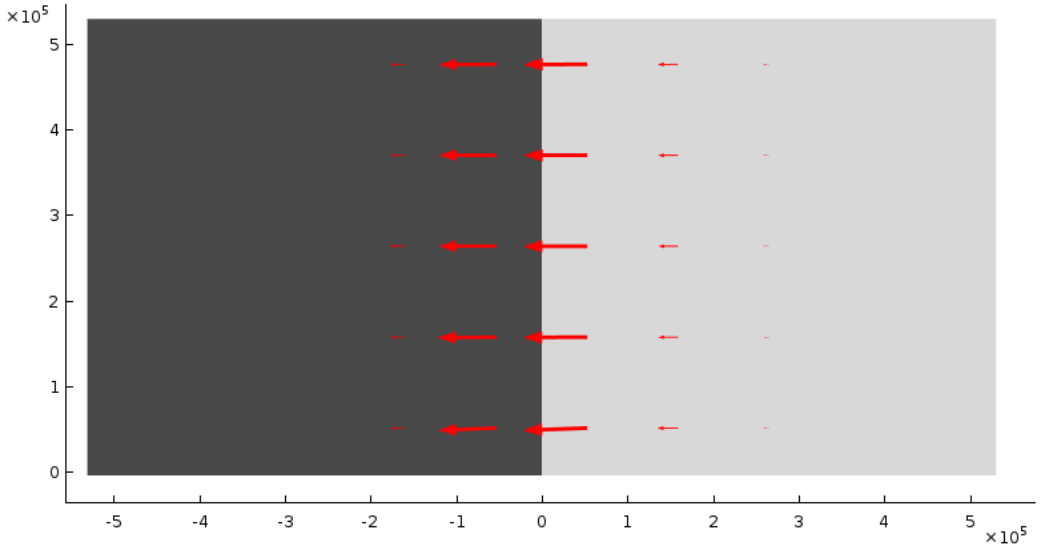

Figure 3.3: Real part of the induction arrows across a lateral boundary, with high resistivity $(500\ \Omega m)$ in the light grey area and low resistivity $(10\ \Omega m)$ in the dark grey area.

of the arrows, the Wiese convention where the real induction arrows points away from conductive material [Wiese, 1962], which is the used convention in Fig. 3.3, and the Parkinson convention, where the induction arrows point towards conductive material [Parkinson, 1959].
The induction arrows are a good dimensionality indicator. For a 1D subsurface no induction arrows exists because the contribution from the vertical magnetic field B_z of

the plane wave, will be zero. A 2D subsurface will produce a vertical magnetic field B_z, therefore can induction arrows be calculated, as seen in Fig. 3.3. It is important to notice that the induction arrows to the right of the boundary show the same direction and size as the arrows to the left of the boundary. If the induction arrows are varying greatly between periods, the subsurface is likely 3D [Ritter, 2007].

In a 3D subsurface, a decoupling is not possible since there will be changing electric fields in both E_x and E_y, so the impedance tensor is calculated from the general eqn. 3.30. It can be difficult to interpret 3D responses, since there will be several depth information contained in the response. It is advisable, if possible, to have additional information from other geophysical and geological information when analysing the responses.

Dimensionality

$$\begin{pmatrix} E_x \\ E_y \end{pmatrix} = \begin{pmatrix} Z_{xx} & Z_{xy} \\ Z_{yx} & Z_{yy} \end{pmatrix} \begin{pmatrix} B_x \\ B_y \end{pmatrix} \tag{3.59}$$

The impedance tensor contains information about the dimensionality and direction of the conductivity structure of the subsurface. When the subsurface is 1D, the conductivity only changes with depth and the diagonal elements of the impedance tensor are zero, while the off-diagonal elements have opposite signs, but equal magnitude.

$$\text{1D subsurface:} \qquad \begin{aligned} Z_{xx} &= \quad Z_{yy} = 0 \\ Z_{xy} &= -Z_{yx} \end{aligned} \quad . \tag{3.60}$$

If the subsurface is 2D, the conductivity varies both with depth and in one horizontal direction, x or y. Then the diagonal elements will have an equal magnitude, but different sign, and the off-diagonal elements will differ from each other.

$$\text{2D subsurface:} \qquad \begin{aligned} Z_{xx} &= -Z_{yy} \\ Z_{xy} &\neq \quad Z_{yx} \end{aligned} \quad . \tag{3.61}$$

The impedance tensor can be rotated into the strike direction of the subsurface, with eqn. 3.55. Then the diagonal elements will become zero, $Z_{xx} = Z_{yy} = 0$, and the decoupling into the TE and TM mode, eqn. 3.54, can be performed.
In a 3D subsurface the conductivity varies in three directions, depth and the two horizontal directions, and all the impedance tensor elements will differ and be non-zero.

$$\text{3D subsurface:} \qquad \begin{aligned} Z_{xx} &\neq \quad Z_{yy} \neq 0 \\ Z_{xy} &\neq \quad Z_{yx} \neq 0 \end{aligned} \quad . \tag{3.62}$$

In practise, it can be difficult to obtain a direction where the diagonal elements are exactly zero. This might be due to noise in the data, galvanic distortion or simply because the subsurface is 3D. For very shallow depths, very short periods, the subsurface should in general look 1D, an example is illustrate in sec. 3.2 where the concept of galvanic distortion is described.

3.1 Source fields effects

Until now, the basic equations related to the magnetotelluric method have been presented for different subsurfaces. However, the most important assumption in the magnetotelluric method is related to the geometry of the source field. The method relies on the assumption of $\delta^2 k^2 \ll 1$ $(k = 0)$, so C is only dependent on the subsurface and not affected by the geometry of the exiting sources. This is valid at mid-latitudes, but is not always valid at high or low latitudes when a spatially small source, such as the equatorial or polar electrojet, is present. The effect on the apparent resistivity and phase of the impedance tensor, ρ_a and ϕ, can be significant. Fig. 3.4 illustrates the real and imaginary parts of the impedance tensor together with ρ_a and ϕ for varying spatial scale k of the exiting sources, with a subsurface as a homogeneous half space with resistivity $\rho = 100\ \Omega m$.

The light blue colour represents $k = 0$, which is the response of a vertical incident plane wave, the assumption of the magnetotelluric method. For a homogeneous half space the phase response from the subsurface will always be $45°$. Depending on which period is in focus the ρ_a and ϕ will deviate from $k = 0$. For $k = 2\pi/1km^{-1}$, the phase is $45°$ higher for periods longer than $10^{-2}\ s$, and the apparent resistivity will drop linearly downwards from the true resistivity at a period of $10^{-3}\ s$. This response does not describe the subsurface, but only the source field. If the geometry of the source field expands, $k \to 0$, the starting period of where the response deviates from the plane wave response is moved to higher periods.
For a layered half space, see Fig. 3.5, similar patterns are visible. If the source field has a small geometry, k is large, there are no response from the subsurface only from the source field. However, when increasing the geometry of the source the response contains more information about the subsurface and the curves in Fig. 3.5 follow the response of $k = 0$ for longer periods.
The assumption of $k = 0$ are therefore important for the magnetotelluric method to work. If there are source fields present which have higher k, it will not be possible to separate the response of the subsurface from the response of the source field, with the magnetotelluric method. In situations where the source field is not always present, a selection can be made for the time periods where the response of source field is zero. Then the assumption of $k = 0$ is valid again.

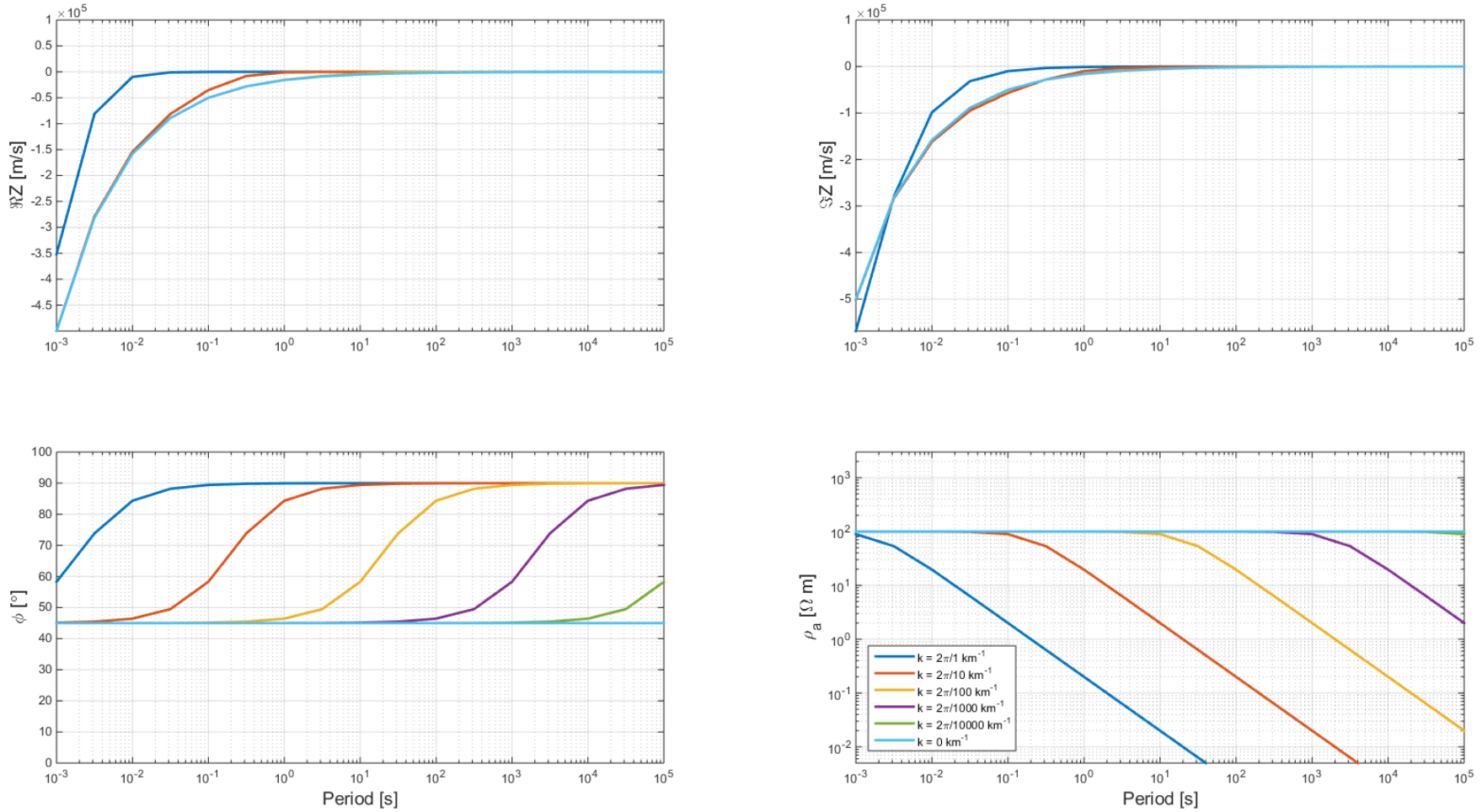

Figure 3.4: The responses of a homogeneous half space with resistivity of $100\ \Omega m$ for various values of k. **Top left:** Real part of impedance tensor. **Top right:** Imaginary part of impedance tensor. **Bottom left:** Phase ϕ. **Bottom right:** Magnitude ρ_a.

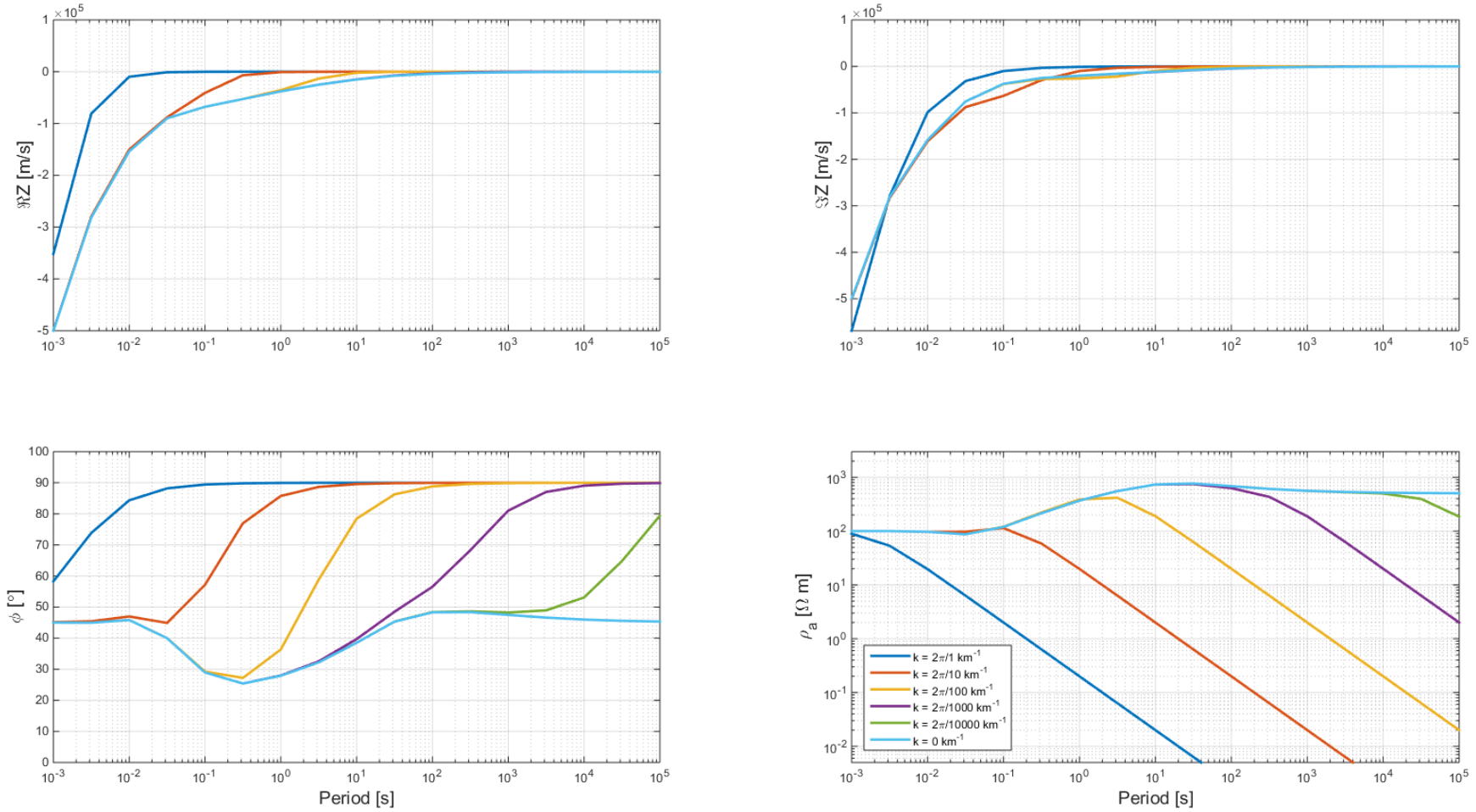

Figure 3.5: The responses of a layered half space with three layer, with boundaries at 1 km and 50 km and resistivity of $100\ \Omega m$, $1000\ \Omega m$ and $500\ \Omega m$, for varying values of k. **Top left:** Real part of impedance tensor. **Top right:** Imaginary part of impedance tensor. **Bottom left:** Phase ϕ. **Bottom right:** Magnitude ρ_a.

3.2 Galvanic distortion

The impedance tensor is often visualised through the apparent resistivity and phase, as described previously. However, the apparent resistivity can be distorted by small scale near surface conductivity anomalies, if the skin depth is significantly larger than the dimensions of the small anomaly [Groom and Bahr, 1992; Simpson and Bahr, 2005]. This is referred to as galvanic distortion or static shift. The distortion influences the measured electric field and distorts the corresponding impedance tensor. Fig. 3.6 illustrates at which depth such a distortion occurs. The background subsurface is uniform with resistivity ρ_2 embedded with a small anomaly with a different resistivity ρ_1. The four red half spheres A, B, C and D, represents the skin depth of four frequencies.

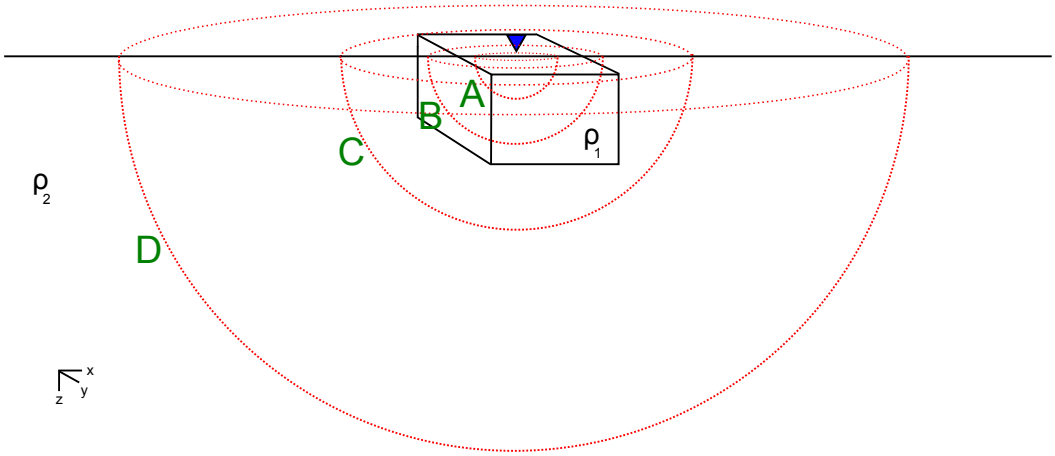

Figure 3.6: The figure illustrates a subsurface with an anomaly located beneath the MT station (blue triangle). The red circles A, B, C and D, represents the skin depth of four frequencies. Redrawn from Simpson and Bahr [2005].

With a frequency representing the skin depth boundary of sphere A, the subsurface will appear 1D, since the skin depth is contained within the anomaly and the frequency will only contain information about layers above the skin depth and none below. At the boundary of sphere B, the skin depth reaches beyond the anomaly in the x-direction, but is contained inside the anomaly in the y- and z-direction. In this situation the subsurface will appear 2D. At the boundary of sphere C, the skin depth reaches beyond the anomaly in all three directions, which yields a 3D subsurface. When going further at the boundary D, the skin depth will be significantly larger than the anomaly, and build up of charges along the boundaries of the anomaly leads to galvanic distortion interfering with the measured response [Simpson and Bahr, 2005].

The electric field measured when the anomaly is present, $\mathbf{E}$, will be comprised of the regional electric field (when the anomaly is not present), $\mathbf{E}_R$, and a distortion tensor, $\mathbf{D}$ [Weidelt and Chave, 2012]

$$\mathbf{E} = \mathbf{D}\mathbf{E}_R \ . \tag{3.63}$$

The model is based on the assumption that the distortion is caused by galvanic deflection and not induction, and thus is independent of frequency. The galvanic deflection occurs at conductivity boundaries where charges will build up and create an electric field

[Chave and Weidelt, 2012]. The distortion tensor, $\mathbf{D}$, is therefore assumed to be real and frequency independent, hence $\mathbf{E}$ and $\mathbf{E}_R$ will have the same phase, but different magnitude and direction [Weidelt and Chave, 2012]. The magnetic field is, however, assumed to have a distortion which can be neglected, $\mathbf{B} = \mathbf{B}_R$. With a distorted electric field, the impedance tensor will therefore also be distorted

$$\begin{aligned} \mathbf{E} &= \mathbf{D}\mathbf{E}_R = \mathbf{D}(\mathbf{Z}_R\mathbf{B}_R) = (\mathbf{D}\mathbf{Z}_R)\mathbf{B} \\ \mathbf{Z} &= \mathbf{D}\mathbf{Z}_R \ . \end{aligned} \tag{3.64}$$

The apparent resistivity calculated from the distorted impedance tensor, eqn. 3.32, will also be distorted, since it contains the absolute value of an impedance tensor elements. However, the phase, eqn. 3.33, will not be affected by the distortion, since the impedance element is divided into the imaginary and real part, and since the distortion tensor is a real tensor, the phase will be unchanged. More calculations and investigations into the galvanic distortion problem are available in e.g. Bahr [1988]; Groom and Bahr [1992]; Jones [2012]. To avoid distortion effects when evaluating the data, the phase tensor is a good supplement, because the distortion tensor is eliminated, see section 3.3.

3.3 Phase tensor

The phase relationship of $\mathbf{Z}$ can also be visualised through a tensor. It has the advantage that, no additional information about the dimensionality of the subsurface is needed and it is not affected by near-surface heterogeneities producing galvanic distortion, as the apparent resistivity of $\mathbf{Z}$ is. All further descriptions in this section can be found in Caldwell et al. [2004] and Booker [2014].

$$\mathbf{\Phi} = \mathbf{X}^{-1}\mathbf{Y} = \begin{bmatrix} \phi_{xx} & \phi_{xy} \\ \phi_{yx} & \phi_{yy} \end{bmatrix} \ . \tag{3.65}$$

The phase tensor, $\mathbf{\Phi}$, is calculated from $\mathbf{X}$ and $\mathbf{Y}$ which are the real part and imaginary part of $\mathbf{Z}$, respectively.

$$\mathbf{Z} = \mathbf{X} + i\mathbf{Y} \ . \tag{3.66}$$

If near-surface heterogeneities are present in the subsurface the electric field measured will be distorted and will deviate from the true electric field of the region. The impedance tensor is calculated directly from the electric field, and will therefore also contain the contribution from the distortion, see eqn. 3.64. The regional electric field, $\mathbf{E}_R$, would be the measured electric field if no near-surface heterogeneities were present to distort the field. However, the phase tensor can describe the regional contribution, unaffected by the distortion, see eqn. 3.67. This is seen by combining eqn. 3.64, eqn. 3.66 and 3.65.

$$\begin{aligned} \mathbf{\Phi} &= \mathbf{X}^{-1}\mathbf{Y} \\ &= (\mathbf{D}\mathbf{X}_R)^{-1}(\mathbf{D}\mathbf{Y}_R) \\ &= \mathbf{X}_R^{-1}\mathbf{D}^{-1}\mathbf{D}\mathbf{Y}_R = \mathbf{X}_R^{-1}\mathbf{Y}_R \\ &= \mathbf{\Phi}_R \ . \end{aligned} \tag{3.67}$$

The individual phase tensor elements can be calculated from the real and imaginary components of $\mathbf{Z}$ in the following manner

$$\mathbf{\Phi} = \begin{bmatrix} \Phi_{11} & \Phi_{12} \\ \Phi_{21} & \Phi_{22} \end{bmatrix} = \frac{1}{det(\mathbf{X})} \begin{bmatrix} X_{22}Y_{11} - X_{12}Y_{21} & X_{22}Y_{12} - X_{12}Y_{22} \\ X_{11}Y_{21} - X_{21}Y_{11} & X_{11}Y_{22} - X_{21}Y_{12} \end{bmatrix} \tag{3.68}$$

with the determinant being $det(\mathbf{X}) = X_{11}X_{22} - X_{21}X_{12}$. The characteristics of the phase tensor can be expressed by three coordinate invariants, the trace, determinant and skew, see eqn. 3.69.

$$\begin{aligned} tr(\mathbf{\Phi}) &= \Phi_{11} + \Phi_{22} \\ sk(\mathbf{\Phi}) &= \Phi_{12} - \Phi_{21} \\ det(\mathbf{\Phi}) &= \Phi_{11}\Phi_{22} - \Phi_{12}\Phi_{21} \ . \end{aligned} \tag{3.69}$$

When visualising the phase tensor four values are used, the minimum phase, the maximum phase, the skew angle and the angle α which gives a measure of the phase tensor dependency on the coordinate system.

$$\begin{aligned} \Phi_{min} &= (\Phi_1^2 + \Phi_3^2)^{\frac{1}{2}} - (\Phi_1^2 + \Phi_3^2 - \Phi_2^2)^{\frac{1}{2}} \\ \Phi_{max} &= (\Phi_1^2 + \Phi_3^2)^{\frac{1}{2}} + (\Phi_1^2 + \Phi_3^2 - \Phi_2^2)^{\frac{1}{2}} \end{aligned} \tag{3.70}$$

where

$$\Phi_1 = tr(\mathbf{\Phi})/2 \qquad \Phi_2 = det(\mathbf{\Phi})^{\frac{1}{2}} \qquad \Phi_3 = sk(\mathbf{\Phi})/2 \ . \tag{3.71}$$

The angle α and the skew angle β are both calculated from the skew and the trace

$$\alpha = \frac{1}{2}\tan^{-1}\left(\frac{\Phi_{12} + \Phi_{21}}{\Phi_{11} - \Phi_{22}}\right) \qquad \beta = \frac{1}{2}\tan^{-1}\left(\frac{\Phi_{12} - \Phi_{21}}{\Phi_{11} + \Phi_{22}}\right) \ . \tag{3.72}$$

$\alpha - \beta$ describes the direction of the phase tensor. With these four values (Φ_{min}, Φ_{max}, α and β) it is possible to completely represent the phase tensor, as seen in eqn. 3.73.

$$\mathbf{\Phi} = \mathbf{R}^T(\alpha - \beta) \begin{bmatrix} \Phi_{max} & 0 \\ 0 & \Phi_{min} \end{bmatrix} \mathbf{R}(\alpha - \beta) \tag{3.73}$$

with $\mathbf{R}$ as the rotation matrix

$$\mathbf{R}(\alpha - \beta) = \begin{bmatrix} \cos(\alpha - \beta) & \sin(\alpha - \beta) \\ -\sin(\alpha - \beta) & \cos(\alpha - \beta) \end{bmatrix} \ . \tag{3.74}$$

The visible representation is shown in Fig. 3.7. The three values, Φ_{min}, Φ_{max} and β, are independent of the coordinate system, whereas α is not since it describe the dependency on the coordinate system.

The phase tensor also contains information about the regional subsurface dimensionality. In a 1D Earth the length of Φ_{min} and Φ_{max} are equal, so the ellipse shown in Fig. 3.7 will become a circle. There will be no preferred direction of the circle, because α becomes undefined. In a 2D Earth the regional strike will determine the direction of the ellipse axes, either Φ_{min} or Φ_{max} will be along strike, however to determine which, additional information from the induction arrows has to be taken into account. For example, the induction arrows have the advantage of pointing away from strike and

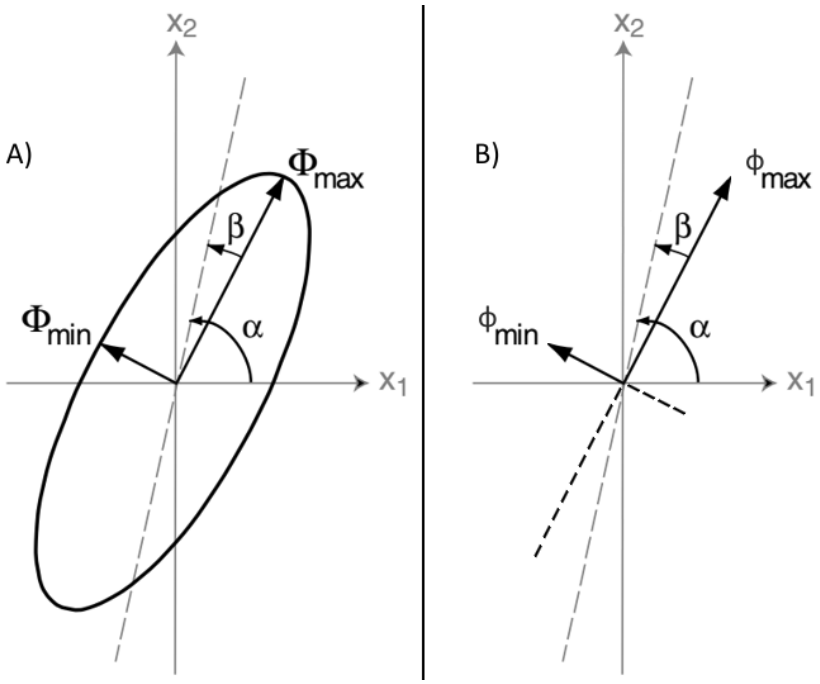

Figure 3.7: Phase tensor illustration. **Left (A)** Original illustration in ellipses form by Caldwell et al. [2004] redrawn by Löwer [2014], with Φ_{min} and Φ_{max} expressed as the length of the ellipse axes. $\alpha - \beta$ orientate the axes in the correct direction. **Right (B)** Phase tensor represented as a bar diagram with ϕ_{min} and ϕ_{max} expressed as the length of the ellipse axes, where $\phi_{min} = arctan(\Phi_{min})$ and $\phi_{max} = arctan(\Phi_{max})$. The axes can be coloured with the value of ϕ_{min} and ϕ_{max} for better visualisation. Figure redrawn by Löwer [2014] from Häuserer [2010].

can reveal which phase is which. The skew angle β must also be zero together with a constant Φ_{max} axis, in a range of periods, to establish that the subsurface is 2D [Caldwell et al., 2004]. If the length of the axes are different from each other and the skew is different from zero $\beta \neq 0$, the subsurface is 3D. The direction of Φ_{max} is given by the angle $(\alpha - \beta)$.

In this project the notation of Häuserer [2010] is used, which is illustrated in Fig. 3.7 left figure. Here the axes are given by the phases, $\phi_{max} = \arctan(\Phi_{max})$ and $\phi_{min} = \arctan(\Phi_{min})$, and β and α are identical to the notation by Caldwell et al. [2004].

Chapter 4

Data collection

This chapter provides a short introduction to the geological background of the field campaign, the measurements, and the instruments used during the field work.

4.1 Geological area

West Greenland consists of different interesting geological areas, which can be divided in to three large zones. Most of the northern part is included in the Rinkian fold belt, where its southern border meets the Nagssugtoqidian orogen in the Disco Bay area. The Nagssugtoqidian orogen is a narrower belt crossing from the west to the east of Greenland. Its southern border meets the Archean craton which is the third of the large zones, see Fig. 4.1.

Figure 4.1: Simple map showing the different Archaean and Palaeoproterozoic zones of Greenland. Map from Henriksen et al. [2009]

The Nagssugtoqidian orogen is the geological area in which the magnetotelluric field campaign of this project took place. It was created in the Palaeoproterozoic period, 1.9 Ga ago, and consists of modified and reworked Archaean rock (gneiss) folded together with sediments. The gneisses are often visible as exposed east-west striking bands in the area between the towns of Aasiaat and Kangerlussuaq, see Fig. 4.2. An orogen is a wide area of highly reworked rocks, which is created during lithospheric plate collisions. Originally, West Greenland consisted of two Archaean cratonic blocks that divided and separated from each other, creating a rift which over time filled with water and Archaean sediments. Once the spreading of the cratonic blocks ceased, the northern block moved back towards the southern block and trusted over it in a colli-

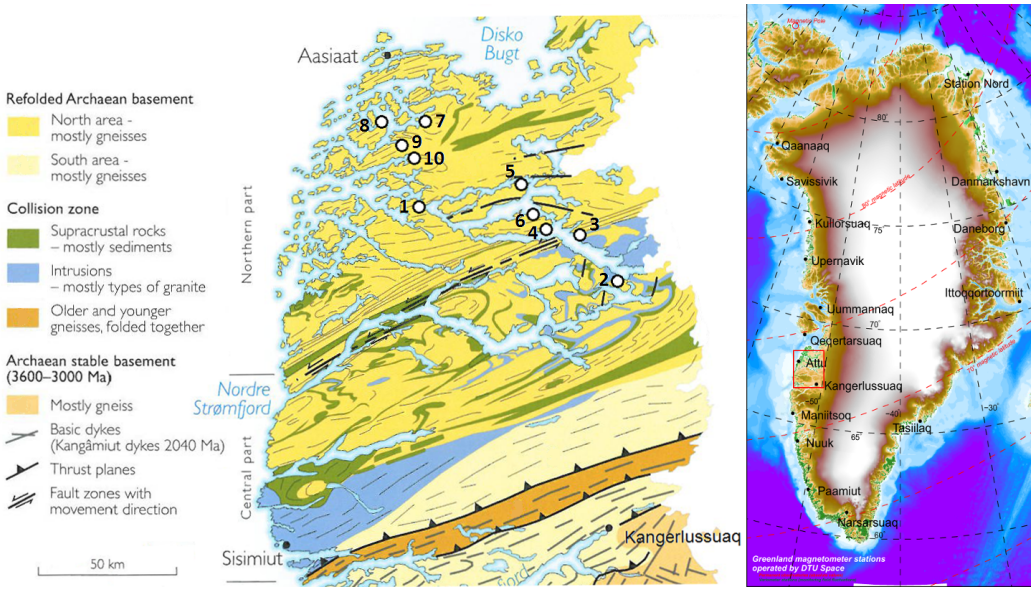

Figure 4.2: **Left** Geological map modified from J.A.M. van Gool in Henriksen [2008]. The white circles indicates the location of the magnetotelluric stations. **Right** Map of the permanent DTU Space magnetometer stations in black dots. The red square indicates the location of the geological map.

sion, which mixed the deposited sediments with Archaean rock of the craton [Bridgwater et al., 1990; Henriksen, 2008; Mengel et al., 1998].

The Nagssuqtoqidian fold belt in Greenland is believed to be connected with similar geology present in both North-America and North-east Europe, through the supercontinent 'Nuna', see Fig. 4.3. Nuna or Columbia as it is also called, existed 1.8 to 1.3 Ga ago where Laurentia (North America) including Greenland was connected to Baltica in a proposed configuration by Johansson [2009], see Fig. 4.3. The Nagssugtuqidian fold belt crossing Greenland is continuing to the west into Canada, possible connected to the Trans-Hudson, and to the east into Fennoscandia.

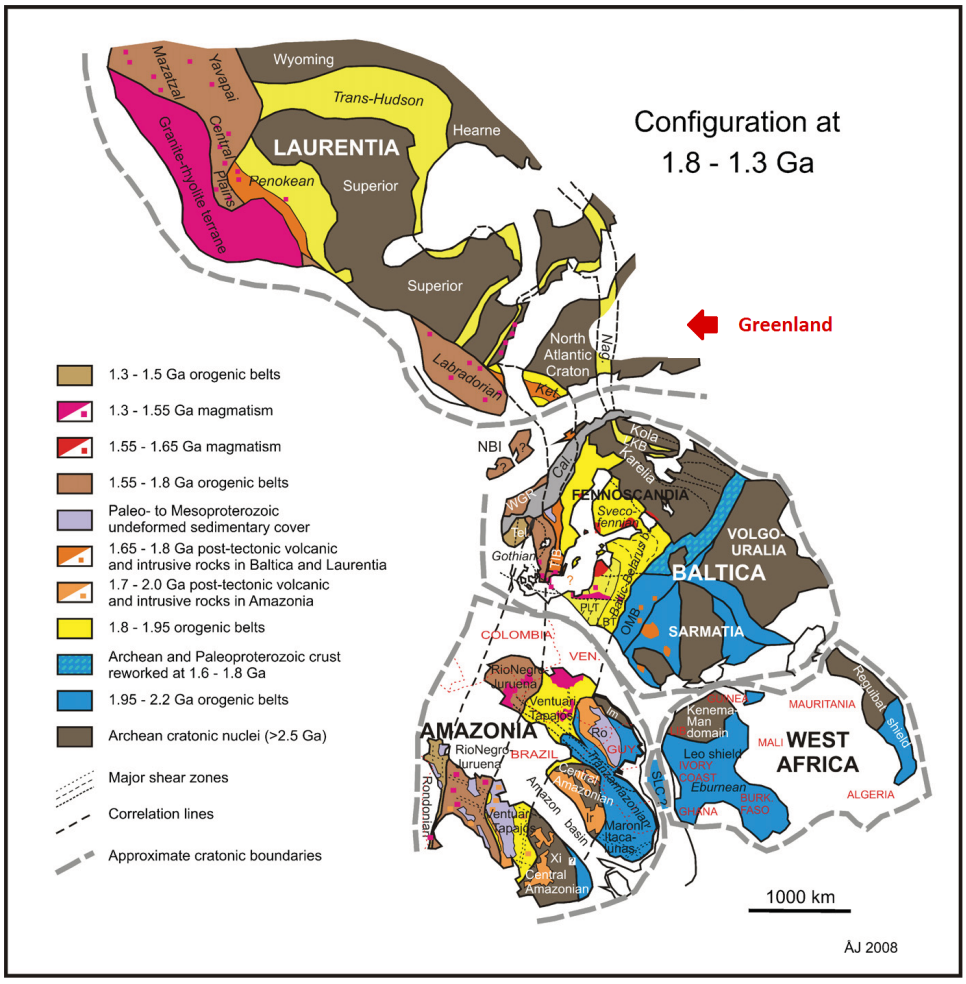

Figure 4.3: Proposed fit of the Nuna continent in the period 1.8 - 1.3 Ga ago. The yellow belt crossing Greenland is the Nagssugtoqidian fold belt. Modified from Johansson [2009].

4.2 Measurements

The magnetotelluric survey was carried out in the summer of 2013 (august to september), with 10 stations on a profile of approximately 100 km. The stations were placed alongside the shoreline of the Arfersiorfik fjord which are placed south of the town Aasiaat, see Fig. 4.2. The deployment was done from a boat and carried inland to the desired location, approximately 50 meters from the water. Exact coordinates and electrode distances of each station can be seen in Tab. 4.1.

The stations were set up to measure for one month with a sampling rate of 0.1 s. However, several of the stations did not contain usable data for the whole time, see Fig. 4.4. Data gaps were either caused by cloudy weather leading to insufficient recharge of solar panels, or, as for most stations, caused by foxes destroying the cables.

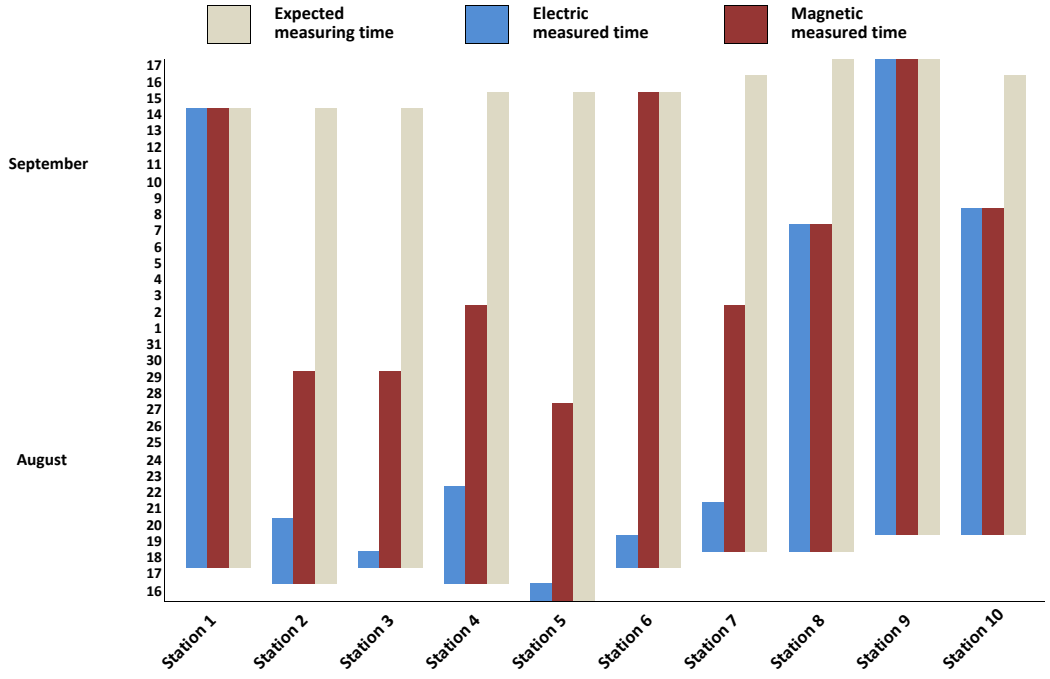

Figure 4.4: Measuring time for each station. Grey represents the expected time measured at set up. Blue represents the actual time measured for the electric field and red represents the actual time measured for the magnetic field.

Station	N coordinate	W coordinate	Dist. N-S [m]	Dist. E-W [m]
1	68° 10,789'	52° 32,686'	60	60
2	67° 53,984'	50° 38,061'	60	60
3	68° 03,765'	50° 58,528'	60	60
4	68° 06,749'	51° 14,688'	60	60
5	68° 15,133'	51° 31,156'	60	60
6	68° 08,687'	51° 25,117'	60	60
7	68° 27,972'	52° 26,686'	60	61
8	68° 28,277'	52° 55,365'	61	60
9	68° 23,528'	52° 42,689'	60	60
10	68° 18,237'	52° 44,639'	60	60

Table 4.1: GPS coordinates and electrode distances at the stations.

4.3 Instruments

The survey consisted of 10 long period magnetotelluric stations, with both magnetic and electric measurements. The instruments were borrowed from the GFZ Geophysical Instrument Pool Potsdam [GFZ GIPP, 2015]. The set-up of a station consisted of 1 EDL (Earth Data Logger) for recording of the collected measurements, 1 Geomagnet fluxgate magnetometer for measuring variations in the magnetic field and 5 AG-AG-CL non-polarised electrodes to measure the electrical current, see Fig. 4.5. Each station was powered by two large batteries which were recharged by solar panels.

Figure 4.5: Earth Data Logger (EDL), CASTLE sensor box, Geomagnet fluxgate magnetometer, and AG-AG-CL electrodes. Equipment and figures from GFZ GIPP [2015]

The stations were set up as a cross with one electrode in the center and four 30 m away towards the four magnetic directions, see Fig. 4.6. The electrodes were connected to the EDL through the CASTLE sensor box, and the magnetometer was connected directly to the EDL. The CASTLE sensor box provides the interface in which it is possible to use the EDL to record the information from the electrodes.

The electrodes are non-polarised electrodes, which measure the potential difference between the two electrodes in the North-South direction (e_x component) and in the East-West direction (e_y component), with a ground electrode in the middle. The electrodes are placed approximately 30 cm below the surface to protect from temperature variations. A good contact between the electrode and the soil is important to measure the correct potential. To ensure this we used bentonite mixed in water. The Geomagnet magnetometer is a three component (b_x, b_y and b_z) variometer, which means that the main magnetic field has been removed, so it measures the variations of the magnetic field. The sensor inside the magnetometer was orientated towards magnetic north and was also placed 30 cm under the surface to protect it from wind and temperature which can alter the orientation of the sensors.

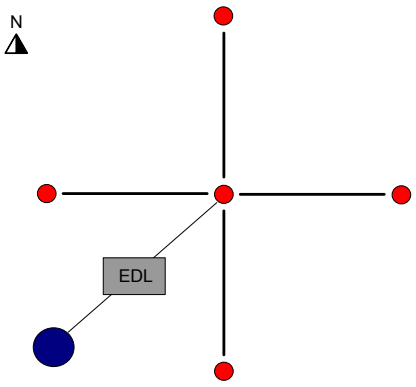

Figure 4.6: Station setup: Red marks illustrates electrodes, the blue mark illustrate the magnetometer, and the grey box illustrates the data logger. The station set up is orientated towards magnetic north.

Chapter 5

Data processing

This chapter addresses the different steps of the signal analysis (filtering, time-frequency transformation etc.) and the processing techniques. The commercial software package MATLAB [R2014b, 2015] has been used for programming and processing. The MATLAB scripts used for the signal analysis and processing have been written primarily by Frankfurt University and the multiple station processing scheme (EGstart) by Hering [2015] and modified for this project by me and Philip Hering. It builds on an eigenvalue decomposition method from Egbert [1997] and is also presented in Hering et al. [2015]. FMTtools, also developed at Frankfurt University, is a standard robust processing software which is described in more detail in Löwer [2014] and Häuserer [2010]. Calculations and more explanation regarding signal analysis can be found in [e.g. Chatfield, 2004; Priestley, 1981; Simpson and Bahr, 2005].

5.1 Signal analysis

The raw data collected with the field work instruments, sec. 4, are recorded as discrete time series, and before processing, the time series have to be prepared, thus transferred from time domain into frequency domain. The time series consist of information in a large span of frequencies. However, the analysis is often performed on a specific frequency band of interest. The information in this frequency band can be separated from the rest of the information by applying a bandpass filter to the time series.

Besides filtering, a visual inspection of the time series is important. It can reveal abnormal behaviour, e.g. abrupt jumps in amplitude or a missing signal, where the cause of this behaviour has to be investigated before proceeding. It can also reveal a time shift in the time series between stations, which can be corrected.

The last step in the preparation is to transform the time series into the frequency domain, which is performed with a Fast Fourier Transform (FFT), where the information in the time series is decomposed into a frequency spectrum. In the further processing, data will only be analysed in the frequency domain. The described preparations will be discussed in more detail in the following section.

5.1.1 Filtering

Filtering is used to isolate a specific frequency band as mentioned previously. This is useful to get rid of frequencies outside the frequency band of interest, which could negatively affect the afterwards calculated transfer functions. The filtering is performed with the MATLAB library function *filtfilt.m*, using a Butterworth filter, which is designed to attenuate a signal with a value of $[order] \cdot 20$ dB per decade. It involves a bandpass filter, which consists of a low pass filter of $order = 3$ and a high pass filter of $order = 6$ [Hering, 2015; Löwer, 2014]. The filters allow signals in the time series from frequencies

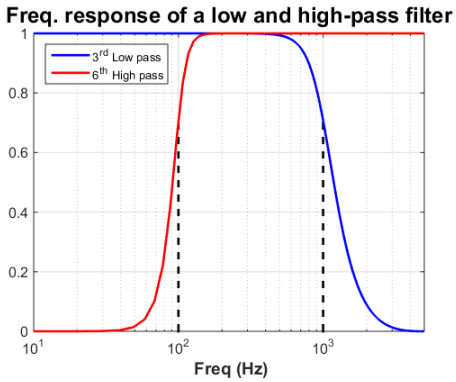

Figure 5.1: Butterworth band pass filter consisting of a low and high pass filter, with cut off frequencies at 1000 and 100 Hz, respectively.

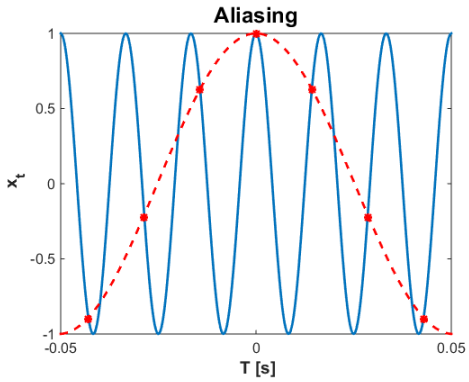

Figure 5.2: Aliasing of a 60 Hz signal (blue) sampled at 70 Hz (red dots). The red line is the artificial signal due to the 70 Hz undersampling.

which are above (high pass) and below (low pass) the cut-off frequencies. An example is illustrated in Fig. 5.1. If the time series contain frequencies higher than the Nyquist frequency, $f_{Ny} = \frac{f_s}{2}$ where f_s is the sampling frequency, problems with aliasing will occur. The Nyquist frequency is the maximum frequency for which a signal, recorded with a given sampling rate, can be reconstructed without causing artificial signals. An example of aliasing is illustrated in Fig. 5.2. The blue curve is the original signal, which cannot be reconstructed with the given sampling frequency of 70 Hz (red dots) and which causes artificial signals within the time series (red line). To avoid this situation, the measurement instruments contain analogue anti-aliasing filters (low pass) which remove signals higher than f_{Ny} already during recording. The measurements presented in this thesis, were collected at a sampling frequency, f_s, of 10 Hz, and the cut-off frequency of the low pass filter was set to $\frac{f_s}{4}$ or 1 Hz, depending on the processing technique, to insure the Fourier spectrum is zero at frequencies higher than the Nyquist frequency [e.g. Priestley, 1981]. The lowest possible resolved frequency is the frequency which completes one oscillation within the length of the time series, $f = \frac{2\pi}{L}$, where L is the length of the time series.

5.1.2 Time shift

A time shift between stations, which were supposed to be measured simultaneously, can cause problems in the processing later on. For single station processing, it will not affect the resulting transfer functions, since each station is processed independently. However, as soon as the results are compared with other data, for example data from other stations, satellite data or observatory data, the time shift will affect the results. Especially when using the multiple station processing, it is of crucial importance that the time series from individual stations are perfectly synchronous. Otherwise the processing scheme will not be able to separate out signal from incoherent noise.

To investigate if there is a time shift between two time series, the coherence between the magnetic fields is a good indicator, since magnetic fields measured at stations in vicinity of each other are comparable, however not identical. The coherence is a value between 0 and 1, with 1 meaning highest coherence.

$$w_{12} = \frac{|\langle B_{x,1} B^*_{x,2} \rangle|^2}{|B_{x,1}|^2 |B_{x,2}|^2} \tag{5.1}$$

with $\langle B_{x,1} B^*_{x,2} \rangle$ being the cross spectra of B_x between the two stations and $|B_{x,1}|^2 = \langle B_{x,1} B^*_{x,1} \rangle$ and $|B_{x,2}|^2 = \langle B_{x,2} B^*_{x,2} \rangle$ are the auto spectra of B_x for station 1 and 2, respectively. Calculation of the spectra are discussed in sec. 5.1.4. This investigation has been performed with all stations presented in this project. In Fig. 5.3 time series of station 8 and 10 are compared with each other. The top right figure shows the two time series of B_x in their original measured state. The time shift is clearly visible in this example. However, when transforming the time series into the frequency domain and calculating the coherence, the exact time shift can be obtained. For this purpose one

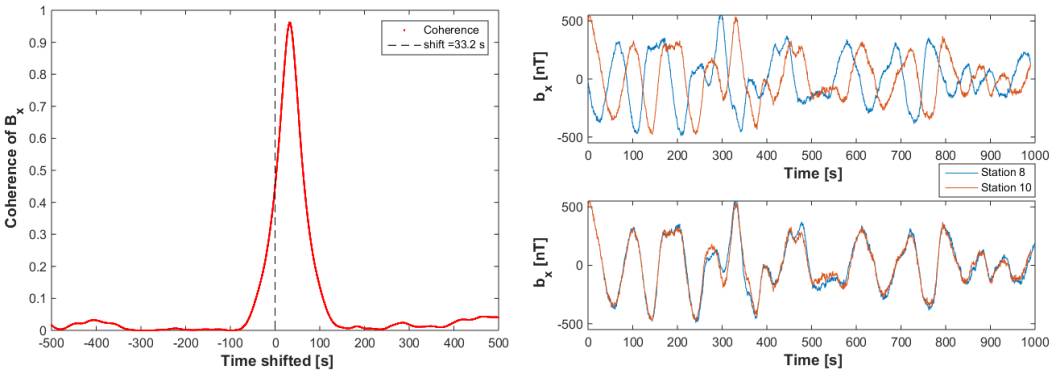

Figure 5.3: **Left:** Coherence between b_x time series of station 8 and station 10, when the time series of station 8 is shifted with respect to station 10. **Top Right:** The time series of station 8 and 10 before time shift correction. **Bottom Right:** The time series of station 8 and 10 after the time shift correction

time series is shifted stepwise against the second one. At each step the coherence is calculated and the result is plotted in dependence of the time shift, Fig. 5.3 left figure. The coherence curve in Fig. 5.3 shows that there is a time shift of 32.2 s between station 8 and station 10. This time shift correction is applied to one of the time series, as illustrated in Fig. 5.3 bottom right figure.

5.1.3 Fast Fourier Transform

The time series have to be transformed from time domain into frequency domain. The transformation is performed with MATLAB's library function *fft.m*, which calculates a discrete Fourier transform with the use of a fast Fourier transform algorithm, where the energy of each frequency is preserved. The discrete Fourier transform is used because the data is collected at a certain sampling frequency, f_s, and is therefore not a continuous time series. The fast Fourier transform of a discrete time series, x_t, takes the form,

$$\widetilde{X}(m) = \sum_{n=0}^{N-1} x_t e^{-\frac{2\pi i m t}{N}}, \qquad 0 \leq m \leq N-1 \tag{5.2}$$

where $\widetilde{X}$ contains the complex Fourier coefficients resulting from a time series with a length of N data points. Only the first half of $\widetilde{X}$, the $\widetilde{X}(1) - \widetilde{X}(N/2-1)$ coefficients, is used since the other half of $\widetilde{X}$ is the mirror spectrum of the first.
The highest possible frequency, for which the coefficients are calculated, is the Nyquist frequency [Chatfield, 2004], as mentioned in sec. 5.1.1. The resolution of the frequency range depends on the length of the time series, N, and the sampling frequency, f_s, and is calculated as follows, $\Delta f = \frac{f_s}{N}$.
The longer the time series, the higher is the resolution of the frequency range. The frequency range will be from DC, $0\ Hz$, until the Nyquist frequency, f_{Ny}, with the resolution, Δf, as spacing.
The FFT is performed on a finite set of data points, where the endpoints are interpreted as if they were connected, so the time series span one cycle. If the endpoints are discontinuous, the FFT will contain high artificial frequencies, which are not actually present in the time series, but are created due to the discontinuity. To avoid this, a window function is applied to the time series, which ensures that the endpoints are both 0 and therefore continuous. A Tukey window is an example of such a window function. It smooths the edges of the time series with a cosine going from 1 to 0. Fig. 5.4 illustrates the effect of such a window. The black line is the Tukey window, which is 1 in the central part of the window and goes to 0 at the borders. The blue line is a synthetic signal, which is attenuated by the Tukey window, resulting in a signal illustrated by the red line.

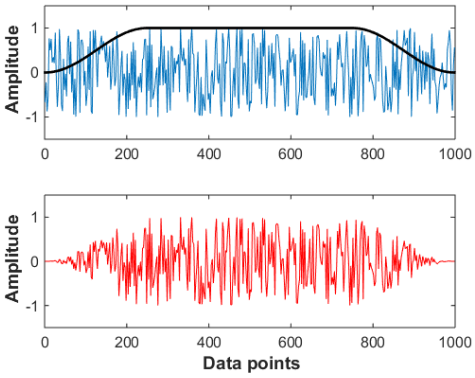

Figure 5.4: **Top:** Artificial signal (blue) and a Tukey window (black). **Bottom:** Tukey window applied to the signal.

During the evaluation of the frequencies, target frequencies are used instead of the $\frac{N}{2}$ Fourier coefficients calculated with the FFT. A target frequency is a frequency of interest. It can be a single frequency or an average of a frequency band. The latter is used in this project. Averaging over a frequency band is valid, because transfer functions are changing slowly with depth and frequencies directly adjacent to each other produce similar transfer functions [Junge, 1992]. With this adjustment, a few target frequencies per decade, spaced equally on a logarithmic scale, will be available for the data analysis. In the processing techniques explained later on, FMTtools uses 5

target frequencies per decade [Löwer, 2014], and the multiple station processing EGstart uses 6 target frequencies per decade [Hering, 2015].

5.1.4 Cross- and Auto powers

Cross- and auto powers (spectra), describe the distribution of energy in the spectra of a times series. The auto power is the squared power of a single time series, whereas the cross power describes the power of the correlation between two time series

Auto spectra:
$$\widetilde{X}\widetilde{X}^* = |\widetilde{X}|^2 = \left| \sum_{n=0}^{N-1} x_t e^{-\frac{2\pi i m t}{N}} \right|^2 \tag{5.3}$$

Cross spectra:
$$\widetilde{X}\widetilde{Y}^* = \sum_{n=0}^{N-1} x_t e^{-\frac{2\pi i m t}{N}} \cdot \sum_{n=0}^{N-1} y_t e^{-\frac{2\pi i m t}{N}} \tag{5.4}$$

where $\widetilde{X}$ and $\widetilde{Y}$ are the Fourier coefficients of the discrete time series x_t and y_t, as given in eqn. 5.2. For an averaged frequency range, denoted by $\langle\ \rangle$, the cross and auto powers can be calculated from the single Fourier coefficients as follows:

$$\langle XX^* \rangle = \frac{1}{M} \sum_{\nu_1}^{\nu_M} |\widetilde{X}|^2 \tag{5.5}$$

$$\langle XY^* \rangle = \frac{1}{M} \sum_{\nu_1}^{\nu_M} \widetilde{X}\widetilde{Y}^* \tag{5.6}$$

where ν_1 is the first frequency within the frequency band, and ν_M the last. M is the number of frequencies in the frequency band. In magnetotellurics, X and Y are the different electric and magnetic components in frequency domain, E_x, E_y, B_x, B_y, or B_z. X^* is the complex conjugate of X.

5.2 Processing techniques

The transfer function relation of the impedance tensor, displayed in eqn. 3.30 in chap. 3, is valid as long as the data is completely noise free and the plane wave assumption is fulfilled. However, in real measurements this is far from true. The data will always contain measurement noise and the plane wave assumption is only an approximation. Therefore eqn. 3.30 will become inexact. However, there are different methods which help estimating the transfer functions. Here three methods are presented: bivariate regression, robust estimation and multivariate statistical estimation. In practice bivariate and multivariate estimation are often combined with robust methods.

In this project, the single station processing (FMTtools) uses bivariate regression with the assumption that the noise is electrical together with robust processing. The multiple station processing (EGstart) uses the multivariate statistical estimation, which has similar elements to the remote reference method. The method detects incoherent noise parts within the channels from two or more stations. More details of the processing software will be explained in sec. 5.3.

5.2.1 Bivariate regression

Since the time series often contain incoherent noise which will have a negative effect on the calculation of the transfer functions, it is possible to estimate $\mathbf{Z}$ with a statistical method.
The representation of the impedance tensor in eqn. 3.30 can be displayed as

$$\begin{aligned} E_x &= Z_{xx}B_x + Z_{xy}B_y \\ E_y &= Z_{yx}B_x + Z_{yy}B_y \ . \end{aligned} \tag{5.7}$$

However, when the time series contain incoherent noise, an additional value δZ must be added to eqn. 5.7. For example, if the noise is located in the electrical component, δZ will be on the right hand side of eqn. 5.7

$$\begin{aligned} E_x &= Z_{xx}B_x + Z_{xy}B_y + \delta Z \\ E_y &= Z_{yx}B_x + Z_{yy}B_y + \delta Z \ . \end{aligned} \tag{5.8}$$

If the noise is magnetic, the value δZ will be located on the left hand side of eqn. 5.7. Whether the noise in $\mathbf{Z}$ is magnetic or electric, it is assumed to be normally distributed. The standard approach is a least square method, which minimises the squared residuals of the cross and auto spectra, by averaging over a frequency band or by stacking the same frequency from different time intervals. Due to this averaging the noise will vanish, since it is randomly distributed, and the signal will be enhanced. If the noise is not confined to either magnetic or electric noise as assumed, the noise is amplified in the auto spectra, and the transfer functions will be biased. This is also the case if the noise is assumed to be electric, but is in fact magnetic.
To estimate the elements of $\mathbf{Z}$ including noise, the cross and auto spectra are used, which can be found by multiplying eqn. 5.8 with the complex conjugates of the magnetic and electric spectra, see sec. 5.1.4, e.g. $\langle E_x E_x^* \rangle = Z_{xx}\langle B_x E_x^* \rangle + Z_{xy}\langle B_y E_x^* \rangle$. The $\langle\ \rangle$ represent the averaging over frequencies. Using all eight cross powers, combinations of E_x and E_y with E_x, E_y, B_x, and B_y, it is possible to find an expression for each of the four components of $\mathbf{Z}$. For example for Z_{xy}

$$Z_{xy} = \frac{\langle E_x B_y^* \rangle \langle B_x B_x^* \rangle - \langle E_x B_x^* \rangle \langle B_x B_y^* \rangle}{\langle B_x B_x^* \rangle \langle B_y B_y^* \rangle - |\langle B_x B_y^* \rangle|^2} \ . \tag{5.9}$$

The elements of the tipper, $\mathbf{T}$, are estimated similarly

$$T_x = \frac{\langle B_z B_x^* \rangle \langle B_y B_y^* \rangle - \langle B_z B_y^* \rangle \langle B_y B_x^* \rangle}{\langle B_x B_x^* \rangle \langle B_y B_y^* \rangle - |\langle B_x B_y^* \rangle|^2} \tag{5.10}$$

The elements of of Z_{xx}, Z_{yx}, Z_{yy} and T_y are shown in app. A.1.

A way to avoid bias due to noise in the magnetic channels is to use a remote reference station. The magnetic field is an external field, see sec. 2, which is assumed to be homogeneous and similar over large distances. By setting up a magnetic station several kilometres away from the local measurement site, the local noise at the two stations should be incoherent and therefore removable. Nevertheless, if the noise in the magnetic channels is coherent between local and remote site, the remote reference method will fail. The necessary distance to the reference station depends on the noise source, the frequency range and the subsurface conductivity [Simpson and Bahr, 2005].

5.2.2 Robust estimation

The bivariate regression mentioned in sec. 5.2.1 is often combined with robust estimation. Robust algorithms sort the data with respect to different criteria. An example is from Egbert and Booker [1986], who uses least squares methods and a weighting scheme to remove outliers in an otherwise well behaved data set. The weighting scheme depends on a function (e.g. a regression M-estimate [Huber, 1981]) which iteratively calculates weights for each data point. The residuals of all data points are compared to a Gaussian error distribution, and residuals that deviate from it are classified as outliers.

In another robust approach, which is used in the processing software FMTtools, the time series are divided into time intervals with a fixed number of data points, sorted via a selected weighting criteria and hereafter Fourier transformed. The length of the intervals depends on the evaluated frequencies.
Here, it is important to find appropriate weighting criteria for selecting the best time intervals. A good criterion could for example be the coherence, which gives a measure of the correlation between two time series. The coherence between two signals is given in eqn. 5.11 through the cross and auto spectra of the time series [e.g. Chatfield, 2004]. Eqn. 5.11 is the general representation of eqn. 5.1.

$$w_{ab}^2 = \frac{|\langle a\ b^* \rangle|^2}{\langle a\ a^* \rangle \langle b\ b^* \rangle} \tag{5.11}$$

where a and b represent the electric and magnetic field components.
However, in some situations the coherence might be high between two signals because they both have a high coherence with a third signal, c, and not because the two signals are similar. In this situation it is better to use the partial coherence, which measures the coherence between the two signals after the influence of the third signal has been removed [e.g. Priestley, 1981]

$$W_{ab(c)} = \frac{w_{ab} - w_{ac} w_{cb}}{\sqrt{(1 - |w_{ac}|^2)(1 - |w_{cb}|^2)}} \ . \tag{5.12}$$

With the weighting criteria of the partial coherence, the impedance tensor elements can be calculated, by including the weights in eqn. 5.9 if a mean estimator is used, see eqn. 5.13. Then, for each target frequency, the weighted transfer functions from al time intervals can be combined in one single transfer function.

$$Z_{xy,q} = \frac{\langle \langle E_x B_y^* \rangle \langle B_x B_x^* \rangle \cdot W_{xy(x)} \rangle_q - \langle \langle E_x B_x^* \rangle \langle B_x B_y^* \rangle \cdot W_{xy(x)} \rangle_q}{\langle \langle B_x B_x^* \rangle \langle B_y B_y^* \rangle \cdot W_{xy(x)} \rangle_q - |\langle \langle B_x B_y^* \rangle|^2 \cdot W_{xy(x)} \rangle_q} \ . \tag{5.13}$$

If a median estimator is used, the weighting criteria is used to select the time intervals which have a partial coherence above a certain value.
The three components which are necessary to calculate the coherence for the impedance tensor elements, are displayed in Tab. 5.1. The weighting is performed on each time interval, q, and for each target frequency individually.
The median estimator is described in Häuserer [2010] and is calculated separately for the real and imaginary parts and combined in the resulting impedance tensor elements afterwards

$$\begin{aligned} \Re(Z_{xy}) &= med_k(\Re(Z_{xy,k})) \\ \Im(Z_{xy}) &= med_k(\Im(Z_{xy,k})) \\ Z_{xy} &= \Re(Z_{xy}) + i\Im(Z_{xy}) \ . \end{aligned} \tag{5.14}$$

Impedance elements	Input signal a	Output signal b	Third signal c
Z_{xx}	E_x	B_x	B_y
Z_{xy}	E_x	B_y	B_x
Z_{yx}	E_y	B_x	B_y
Z_{yy}	E_y	B_y	B_x

Table 5.1: Indices for the squared and partial coherencies when calculating the impedance tensor elements [Löwer, 2014]

The median estimator is insensitive to outliers, which will ensure a higher quality of the transfer functions since poor quality data will not affect the results [Löwer, 2014].
The confidence level of the transfer functions can be calculated from the absolute deviation of the errors [Häuserer, 2010]. The calculation is divided into the real and imaginary part, in the same way as in eqn. 5.14

$$\begin{aligned} \delta Z_{xy}(\Re) = &\quad 1.483 \cdot med(|\Re(Z_{xy,k}) - \Re(Z_{xy})|) \\ \delta Z_{xy}(\Im) = &\quad 1.483 \cdot med(|\Im(Z_{xy,k}) - \Im(Z_{xy})|) \ . \end{aligned} \tag{5.15}$$

The median is calculated for the differences between the transfer functions of a single time interval and the averaged transfer function. The largest value of $\delta Z_{xy}(\Re)$ or $\delta Z_{xy}(\Im)$, is used for the value δZ_{xy}^{max}, which determines the error δZ_{xy}.

$$\delta Z_{xy} = \frac{1.96 \cdot \delta Z_{xy}^{max}}{\sqrt{n_q}} \tag{5.16}$$

where n_q is the number of time intervals used in the calculation of the median transfer function [Löwer, 2014].

5.2.3 Multivariate statistical estimation

This processing scheme, used in EGstart, is based on a multivariate statistical estimation [Egbert, 1997], and uses electric and magnetic channels from two or more stations to detect and exclude incoherent noise from the data. The idea is to solve a generalised eigenvalue problem and to isolate the signal only originating from the sources fields.
As in the previous section, the time series are divided into time intervals and the calculated estimates are computed independently for each interval and each target frequency. The data vector in the frequency domain can be expressed as

$$\boldsymbol{X}_i = \begin{pmatrix} \boldsymbol{B}_{1i} \\ \boldsymbol{E}_{1i} \\ - \\ \vdots \\ - \\ \boldsymbol{B}_{Ji} \\ \boldsymbol{E}_{Ji} \end{pmatrix} = \begin{pmatrix} \boldsymbol{\eta}_{11} \\ \boldsymbol{\zeta}_{11} \\ - \\ \vdots \\ - \\ \boldsymbol{\eta}_{J1} \\ \boldsymbol{\zeta}_{J1} \end{pmatrix} \beta_{1i} + \begin{pmatrix} \boldsymbol{\eta}_{12} \\ \boldsymbol{\zeta}_{12} \\ - \\ \vdots \\ - \\ \boldsymbol{\eta}_{J2} \\ \boldsymbol{\zeta}_{J2} \end{pmatrix} \beta_{2i} + \boldsymbol{\epsilon}_i = \boldsymbol{U}\boldsymbol{\beta}_i + \boldsymbol{\epsilon}_i \tag{5.17}$$

where B_{ji} and E_{ji} are the magnetic and electric Fourier coefficients for the i'th time segment for station j, respectively. β_{1i} and β_{2i} refer to the two polarizations resulting

from the natural source fields, and $\boldsymbol{\eta}$ and $\boldsymbol{\zeta}$ are the Fourier coefficients of the electric and magnetic fields referred to these polarisations. ϵ_i contains the incoherent noise parts, however if coherent noise is present, eqn. 5.17 must be modified

$$\boldsymbol{X}_i = \boldsymbol{U}\boldsymbol{\beta}_i + \boldsymbol{V}\boldsymbol{\gamma}_i + \boldsymbol{\epsilon}_i = \begin{bmatrix} \boldsymbol{U} & \boldsymbol{V} \end{bmatrix} \begin{bmatrix} \boldsymbol{\beta}_i \\ \boldsymbol{\gamma}_i \end{bmatrix} + \boldsymbol{\epsilon}_i = \boldsymbol{P}\boldsymbol{\alpha}_i + \boldsymbol{\epsilon}_i \tag{5.18}$$

where $\boldsymbol{V}$ contains coherent noise resulting from the sources. As coherent noise $\boldsymbol{V}$ and signal $\boldsymbol{U}$ cannot easily be distinguished in practice, the latter is attributed to the signal (summarized in $\boldsymbol{P}$). Hence, the method is useful to estimate the level of incoherent noise, but is not suitable to separate coherent noise from data. Nevertheless, it can give hints of influences from coherent noise sources, when looking at the number of dominant eigenvalues. To estimate the matrix $\boldsymbol{U}$, a spectral density matrix, containing all possible cross and auto spectra from all measured data channels, has to be calculated. The number of stations included in the method has to be two or more, and has no upper limit, only computer power limitations.

$$\boldsymbol{S} = \begin{bmatrix} \langle B_{x1,i} \cdot B^*_{x1,i} \rangle & \langle B_{y1,i} \cdot B^*_{x1,i} \rangle & \cdots & \langle E_{xK,i} \cdot B^*_{x1,i} \rangle & \langle E_{yK,i} \cdot B^*_{x1,i} \rangle \\ \langle B_{x1,i} \cdot B^*_{y1,i} \rangle & \langle B_{y1,i} \cdot B^*_{y1,i} \rangle & & \langle E_{xK,i} \cdot B^*_{y1,i} \rangle & \langle E_{yK,i} \cdot B^*_{y1,i} \rangle \\ \vdots & & \ddots & & \vdots \\ \langle B_{x1,i} \cdot E^*_{xK,i} \rangle & \langle B_{y1,i} \cdot E^*_{xK,i} \rangle & & \langle E_{xK,i} \cdot E^*_{xK,i} \rangle & \langle E_{yK,i} \cdot E^*_{xK,i} \rangle \\ \langle B_{x1,i} \cdot E^*_{yK,i} \rangle & \langle B_{y1,i} \cdot E^*_{yK,i} \rangle & \cdots & \langle E_{xK,i} \cdot E^*_{yK,i} \rangle & \langle E_{yK,i} \cdot E^*_{yK,i} \rangle \end{bmatrix} . \tag{5.19}$$

The matrix $\boldsymbol{S}$, has the dimension $K \times K$, where K is the number of electric and magnetic components from all stations in total. Besides $\boldsymbol{S}$, it is essential to estimate a noise covariance matrix $\boldsymbol{N}$, in order to determine the incoherent noise level in each component. Coherent noise is allowed between the field components at each station, and multiple linear regressions can be performed such that each of the 5 components of a station is predicted by the (K-5) components of the remaining sites. Afterwards, the resulting variance and covariance of the residuals define a covariance matrix for each site, which can be summarised in a block diagonal matrix [Hering et al., 2015].

$$\boldsymbol{N} = \begin{bmatrix} \sigma^2_1 & \sigma^2_{1,2} & \sigma^2_{1,3} & \cdots & 0 & 0 & 0 \\ \sigma^2_{2,1} & \sigma^2_2 & \sigma^2_{2,3} & & 0 & 0 & 0 \\ \sigma^2_{3,1} & \sigma^2_3 & \sigma^2_{3,3} & & 0 & 0 & 0 \\ & \vdots & & \ddots & & \vdots & \\ 0 & 0 & 0 & & \sigma^2_{K-1,K-2} & \sigma^2_{K-1} & \sigma^2_{K-1,K} \\ 0 & 0 & 0 & \cdots & \sigma^2_{K,K-2} & \sigma^2_{K-1} & \sigma^2_K \end{bmatrix} . \tag{5.20}$$

This will take into account both, noise being incoherent between stations and noise being coherent between the channels of a single station, but not noise which is coherent between all stations [Hering et al., 2015].

The spectral density matrix is then normalised by the noise covariance matrix, and an eigenvalue problem can be formulated

$$\boldsymbol{S}\boldsymbol{v} = \lambda \boldsymbol{N}\boldsymbol{v} \tag{5.21}$$

where λ contains the eigenvalues and $\boldsymbol{v}$ represents the corresponding eigenvectors. The signal $\boldsymbol{U}$ can be calculated from the eigenvectors belonging to the two largest eigenvalues, which are significantly larger than 1, represented as $\boldsymbol{v'}$

$$\boldsymbol{U} = \boldsymbol{N}^{\frac{1}{2}} \boldsymbol{v'} (\boldsymbol{v'} \boldsymbol{N}^{-1} \boldsymbol{v'})^{-1} . \tag{5.22}$$

Ideally, the signal $\boldsymbol{U}$ only consists of Fourier coefficients that represent the electric and magnetic components originating from the uniform plane wave, which means there are two large eigenvalues and the rest are significantly lower. If there are more than two dominating eigenvalues, the number of independent source field polarisations exceeds the case of an exclusively plane natural source field and additional sources have to be considered (referred to as coherent noise).
From the signal matrix, the transfer functions can be estimated as follows

$$\boldsymbol{Z}_j = \begin{bmatrix} \zeta_{xj1} & \zeta_{xj2} \\ \zeta_{yj1} & \zeta_{yj2} \end{bmatrix} \begin{bmatrix} \eta_{xj1} & \eta_{xj2} \\ \eta_{yj1} & \eta_{yj2} \end{bmatrix}^{-1} \tag{5.23}$$

here ζ represents the magnetic and η the electric contribution from $\boldsymbol{U}$ with the corresponding x and y components. The indices 1 and 2 refer to the two polarisations of the natural source field, which is visible as the two dominating eigenvalues.

5.3 Processing software

In this project, two different processing approaches have been used to estimate the transfer functions. A single station processing *FMTtools*, which builds on robust estimations to remove outliers, and a multiple station processing *EGstart*, which uses a noise covariance matrix to remove incoherent noise parts. Fig. 5.5 illustrates the single processing steps for both methods. Specific details, individual for each technique, will be explained in the following section.

5.3.1 Single station processing - FMTtools

FMTtools is a robust processing software developed at Frankfurt University [Häuserer, 2010; Löwer, 2014]. It processes the time series of each station independently. In order to reduce the computational time of the processing, the time series are decimated with a factor of 10, 100 and 1000. This will not affect the results, as long as the evaluated frequencies are adjusted to be lower than the new Nyquist frequency, $\frac{f_s}{2}$. The time series in this project were collected at a sampling frequency of 10 Hz, which is equal to a sampling period of 0.1 s, the reciprocal of the frequency, $T = \frac{1}{f}$. It is convenient to use the period terminology since the evaluated frequencies are low. Tab. 5.2 shows the four different sampling rates, the original and the three decimated, with their corresponding cut off frequencies. The first time series with a sampling period of 0.1 s, is the original time series. The three next, are the decimated time series, where the last time series with a sampling period of 100 s is only used for stations where the original time series is long enough. The length is dependent on how many time intervals the time series contain. Each time series is divided into time intervals of 1000 data points, with an overlap of 500 data points. There must be 5 or more time intervals in a time series for the processing to succeed. For a sampling period of 100 s, the length of the time series must be longer than 3.5 days.

All time intervals are independently transformed with the FFT and calibrated with the frequency dependent transfer functions of the measurement instruments. The Fourier coefficients are hereafter summarized in different target periods, with 5 target periods per decade. In Tab. 5.3 the used target periods and their period range are displayed.

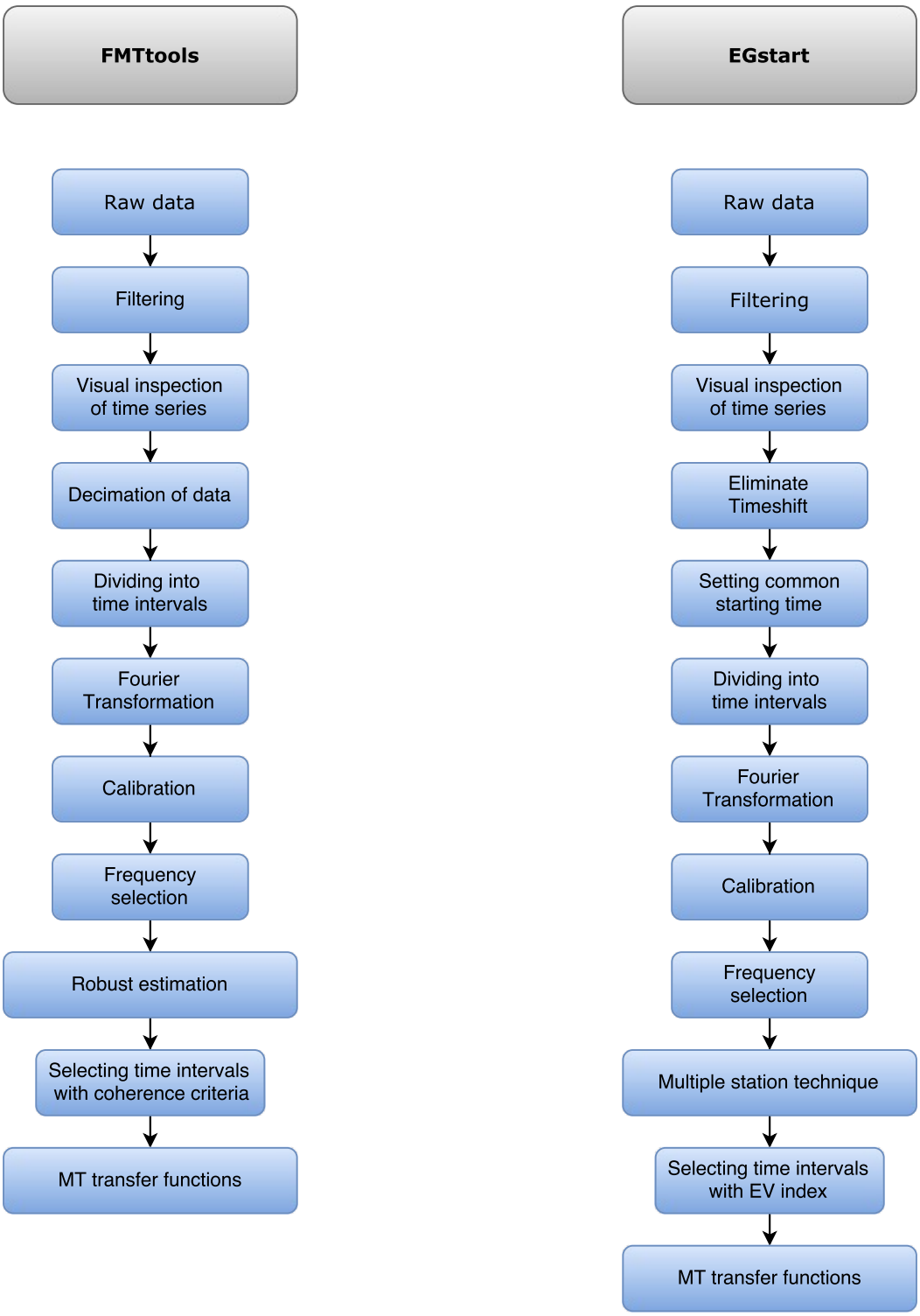

Figure 5.5: Flowchart of the steps in processing of MT data. **Left** The steps taken in the bivariate robust processing technique, FMTtools. **Right** The steps taken in the multivariate processing technique, EGstart.

Sampling period [s] T_s	Low pass cut off period [s] $200 \cdot T_s$	High pass cut off period [s] $4 \cdot T_s$
0.1	20	0.4
1	200	4
10	2000	40
100	20000	400

Table 5.2: Cut off period for the different time series after decimation.

Sampling period [s]	Target period [s]	Period range [s]
0.1	6.25	$5.00 - 8.333$
	4.0	$3.125 - 5.555$
	2.5	$1.961 - 3.448$
	1.5625	$1.219 - 2.174$
	1.0	$0.769 - 1.429$
1	62.5	$50 - 83.33$
	40.0	$31.25 - 55.55$
	25.0	$19.61 - 34.48$
	15.625	$12.19 - 21.74$
	10.0	$7.69 - 14.29$
10	625	$500 - 833.3$
	400	$312.5 - 555.5$
	250	$196.1 - 344.8$
	156.25	$121.9 - 217.4$
	100	$76.9 - 142.9$
100	6250	$5000 - 8333$
	4000	$3125 - 5555$
	2500	$1961 - 3448$
	1562.5	$1219 - 2174$
	1000	$769 - 2174$

Table 5.3: Target periods for each of the time series, original and decimated.

FMTtools uses a robust processing, see sec. 5.2.2, which is insensitive to outliers and select time intervals for the calculation of the transfer functions. The intervals are sorted by the partial coherence, however, only time intervals with a partial coherence above 0.6 are included [Löwer, 2014]. From this selection the time intervals with the 10% highest partial coherences are used to calculate the transfer functions. If less than five intervals are selected with these criteria, the best five intervals out of all the intervals are used instead [Löwer, 2014].

The transfer functions of the selected time intervals are calculated with bivariate regression and the assumption that the noise is electric, see sec. 5.2.1. Hereafter, the final transfer functions are estimated with the median estimator in sec. 5.2.2.

5.3.2 Multiple station processing - EGstart

EGstart uses a multivariate statistical estimation by Egbert [1997] to detect and exclude incoherent noise, see sec. 5.2.3, which is different from FMTtools that uses single station processing. However, besides the processing being different the filter settings are also slightly different. The cut off periods are selected manually, within the criteria in sec. 5.1.1, and the evaluated period range lies between 0.9 of the low pass cut off period and 1.5 of the high pass cut off period. For example with cut off periods of 1 s and 80 s, the target periods are as displayed in Tab. 5.4

Sampling period [s]	Target period [s]	Period range [s]
0.1	55.2145	46.4159 – 68.1292
	37.6172	31.6228 – 46.4159
	25.6283	21.5443 – 31.6228
	17.4604	14.6780 – 21.5443
	11.8956	10 – 14.6780
	8.1044	6.8129 – 10
	5.5215	4.6416 – 6.8129
	3.7617	3.1623 – 4.6416
	2.5628	2.1544 – 3.1623
	1.7460	1.4678 – 2.1544
	1.1896	1 – 1.4678

Table 5.4: Example of target periods with cut off periods 1 s and 80 s.

The length of the time series from the stations are all edited to have the same start and end time. Therefore, only the parts of the time series which overlap for all stations are included in the processing. The start time is determined by the station which started recording latest, and the end time is determined by the shortest time series. Hereafter, the processing is performed on individual time intervals within the entire time series. The length of these intervals is set manually, depending on which resolution is needed and which periods have to be evaluated. With a short length of the time intervals, there are many time intervals from which to choose good data. However, the lower the

evaluated period range is the shorter the time intervals have to be. For long periods the time intervals have to be longer and only a few intervals will be available in the time series. To ensure the best resolution for all periods, it is possible to change the length of the time intervals depending on which period is evaluated.
When the time intervals and periods are chosen, the multivariate processing is performed for each of them. It is possible to include a robust procedure, which estimates the noise covariance matrix by iteratively down weighting outliers in the residuals, however this was not used in this project. The time intervals are selected differently than in FMTtools. Here it is the eigenvalues calculated in the multivariate processing which determines the selection. An eigenvalue index (EV-index) is calculated for each time window at each period [Hering, 2015]

$$\text{EV-index} = \frac{|\lambda_2|}{|\lambda_3|} - |\lambda_3|^2 \tag{5.24}$$

where the ratio between the second largest eigenvalue and the third largest should be as large as possible, and at the same time the value of the third eigenvalue should be as small as possible. The transfer functions are calculated for each time intervals, from the two dominating eigenvalues, as given in eqn. 5.23, and a weighted median is calculated from the 20% best time intervals, determined by the EV-index.

Chapter 6

Data analysis and discussion

The transfer functions calculated with the two processing softwares FMTtools and EGstart presented in sec. 5, are analysed and evaluated in this chapter. FMTtools estimates the transfer functions of each station individually with robust processing and bivariate regression. The transfer functions are compared with the AE and Kp index to establish possible variation patterns, and they are displayed without further selection than the initial. EGstart estimates the transfer functions of multiple stations by calculating the different eigenvectors estimated from the time series. These corresponding eigenvalues are used for the selection of data from which the final transfer functions are calculated. The transfer functions presented are the real and imaginary elements of Z, apparent resistivities and impedance phase, induction arrows and phase tensors.

6.1 Single station processing results

The magnetotelluric method builds on the assumption that the source field is a plane wave and therefore the transfer functions are time invariant, as discussed in sec. 2.1. This has to be verified in the calculated transfer functions from FMTtools to ensure a correct analysis. For this purpose, the impedance tensor element Z_{yx} is displayed separately in its real and imaginary parts to visualise if there is a time dependency in the data. An example for station 8 is shown in Fig. 6.1 - 6.4, for two target periods 1 s and 10 s. In app. B.1, Z_{yx} is displayed at additional periods, for stations 8 and 10. The figures illustrate the average impedance tensor element for each hour of the time series, calculated as the average of the cross and auto spectra, which the impedance tensor element consist of, see app. A.1. At 1 s the impedance element has small variations, where both the real and imaginary parts have similar values within approximately $\pm$ 0.05 m/s in all hour intervals, with the exception of a few outliers. At 10 s, the variations in Z_{yx} illustrate that the values are not constant over time. This is also the general impression in the other impedance elements, seen in app. B.1. There is a polarity in the values, where data before 12 UT are similar, and data after 12 UT are similar. This is a rough description with variations. The values of a single day varies with the time of day, however there are also variations between the different days. The values range from 0 – 1.5 m/s for real values and from 0 – -1.2 m/s for imaginary. At 100 s periods the variations become smaller in magnitude, see app. B.1, and almost vanishes.

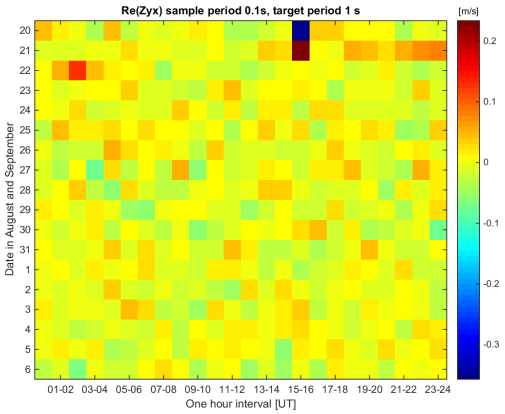

Figure 6.1: $\Re(Z_{yx})$ for station 8 at period 1 s. The y axis is the date in August and September of the measurement, the x axis is divided into one hour intervals from 00-24 UT.

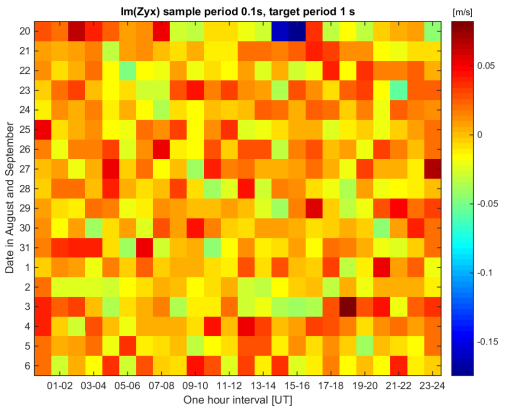

Figure 6.2: $\Im(Z_{yx})$ for station 8 at period 1 s. The y axis is the date in August and September of the measurement, the x axis is divided into one hour intervals from 00-24 UT.

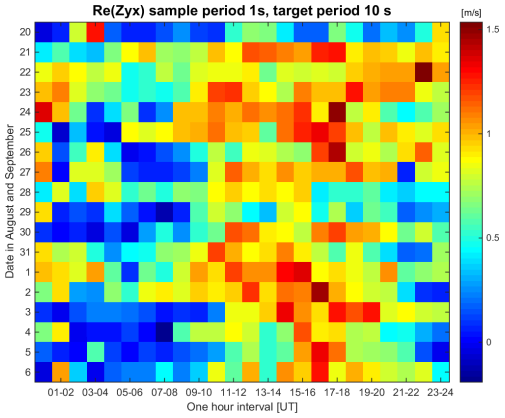

Figure 6.3: $\Re(Z_{yx})$ for station 8 at period 10 s. The y axis is the date in August and September of the measurement, the x axis is divided into one hour intervals from 00-24 UT.

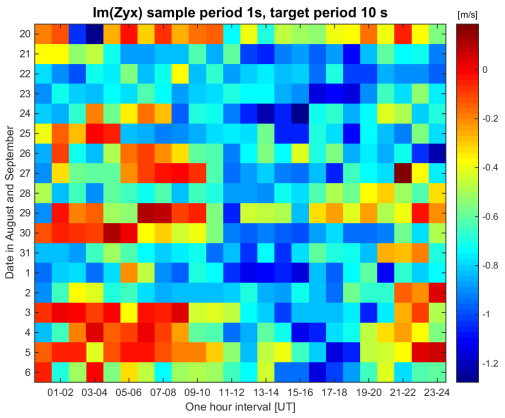

Figure 6.4: $\Im(Z_{yx})$ for station 8 at period 10 s. The y axis is the date in August and September of the measurement, the x axis is divided into one hour intervals from 00-24 UT.

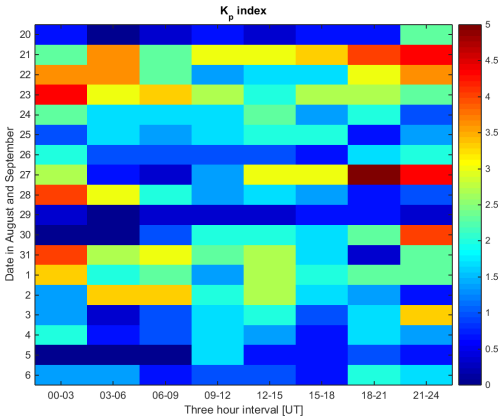

Figure 6.5: Kp index in three hour intervals in the measuring time of August and September. Data provided by GFZ - German Research Centre for Geosciences [2016].

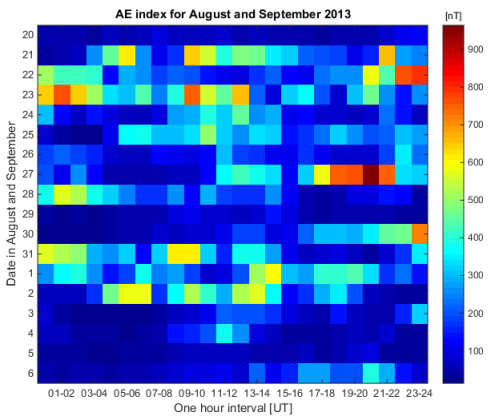

Figure 6.6: AE index for each hour of the day in the measuring time of August and September. Data provided by World Data Center for Geomagnetism, Kyoto [2016].

Due to these variation in the impedance elements, which likely is caused by source variations, a selection of data should be made. Different selections can be made, for example, only daytime data [e.g. Garcia et al., 1997], quiet time events in time intervals [e.g. Viljanen, 1996] or selecting from the K_p index [e.g. Kother, 2012]. I chose to test if a selection was possible with either the K_p index or the AE index, see sec. 2 for description. Fig. 6.5 illustrates the K_p index in 3 hour intervals for the measurement time of station 8. The activity varies between $0-5$, where the values are highest around midnight and on specific days, which is a different pattern than seen in the impedance element of station 8. Kother [2012] made a selection where half days with an average of 2.5 were selected and the rest discarded. However, their results had a similar pattern as the change in the K_p index. In our situation, such a selection from the K_p index would not secure quiet data since the pattern in the K_p index is different from the pattern in the impedance element. Comparing with the AE index, which is an auroral activity index, could be better. However, as seen in Fig. 6.6, the AE index has specific days with high activity > 200 nT, as the K_p index, and not the pattern as seen in the impedance elements. A selection from the AE index will also not remove disturbed data. Since selection from neither the K_p or AE index was possible, we decided to abandon visual inspection techniques and instead try the multiple station processing technique, which uses an eigenvalue selection, see sec. 6.2.

However, if a visual inspection should be tested, a selection of daytime data might be better suited. The variation in Z_{yx} during the day are very distinct if looking at averaged hourly value during the measurement period, at 10 s, see Fig. 6.8. At other periods the variation can be different than purely day and night time variations, and data for each period should be selected carefully.

Description of transfer functions

The transfer functions for all stations, without selection, are displayed as the apparent resistivity and phase in Fig. 6.10 - 6.17, the induction arrows in Fig. 6.18 and 6.19 and

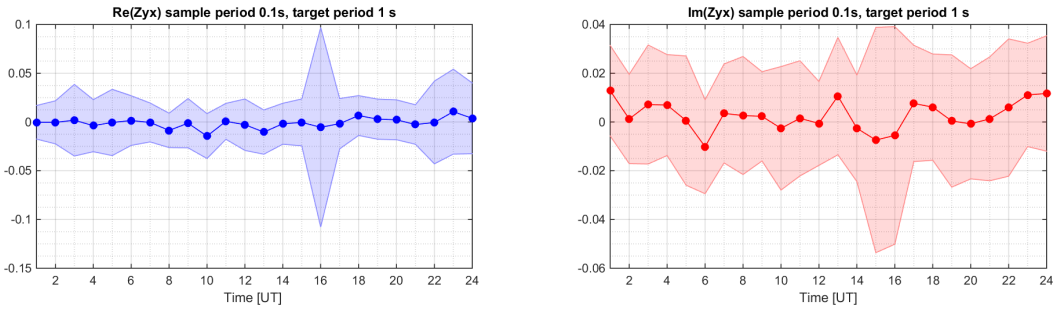

Figure 6.7: The mean hour value of Z_{yx} at 1 s, for station 8. Shaded areas represent the standard deviation range. **Left** Real part, **Right** Imaginary part.

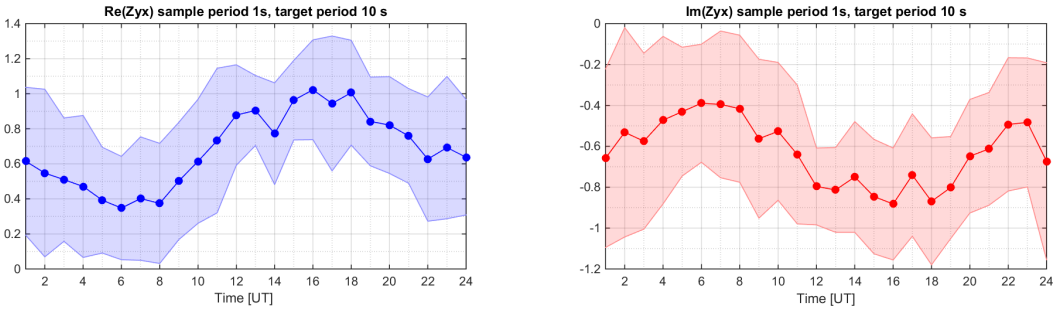

Figure 6.8: The mean hour value of Z_{yx} at 10 s, for station 8. Shaded areas represent the standard deviation range. **Left** Real part, **Right** Imaginary part.

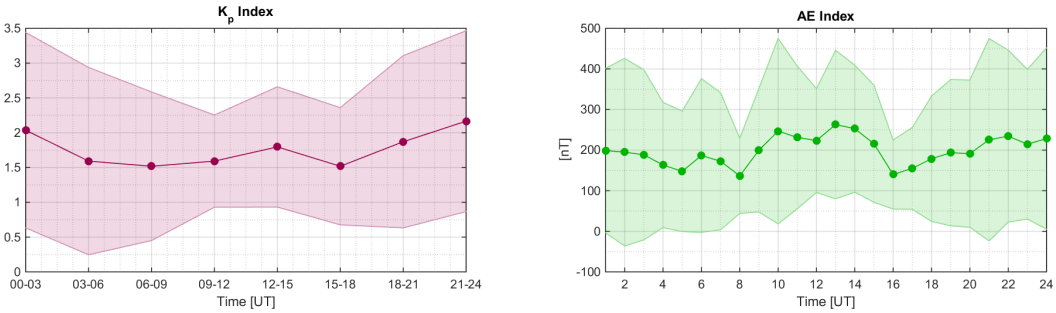

Figure 6.9: The mean hour value of K_p and AE index. Shaded areas represent the standard deviation range.

the phase tensor in Fig. 6.20, with the period range displayed on a logarithmic scale. The apparent resistivity and phase are displayed as the off diagonal elements of the impedance tensor, however in the geomagnetic reference frame, which at the location in Greenland has an average declination of 32° W at the time of measuring [National Geophysical Data Center, 2016]. The induction arrows and the phase tensors have been rotated into the geographical coordinate system for a better interpretation when comparing with surface geology and ocean. The behaviour of the transfer functions at each station will be described, however no conclusions on the geology will be made from these transfer functions, since no selection criterion has been imposed on the data, and it is unsure if the transfer functions illustrate the subsurface or an ionospheric polar electrojet.

At station 1, apparent resistivity is increasing from period $10^{0.5}-10^{1}$ s for both $\rho_{a\ (e_x,b_y)}$ and $\rho_{a\ (e_y,b_x)}$, and decreasing slightly at 10^{1} s and longer periods. $\phi_{(e_x,b_y)}$ is increasing from 10° at $10^{0.5}$ s to 55° at 10^{2} s, hereafter it is stable until $10^{2.6}$ s where it increases again and ends with a steeper decrease after $10^{3.5}$ s. $\phi_{(e_y,b_x)}$ is instead almost stable in the whole period range with a slight decrease in the beginning. A parallel split between $\rho_{a(e_x,b_y)}$ and $\rho_{a(e_y,b_x)}$ which is not present in the phase, can indicate the presence of static shift [Simpson and Bahr, 2005]. When there is a split between the phases, it indicates that the subsurface is multidimensional.

Station 2 has a split between the apparent resistivities which increases with period while the values decrease. The phases are behaving opposite the resistivities in the low periods, with increasing values until $10^{1.6}$ s, where after it is approximately stable at the same value, however different for each phase.

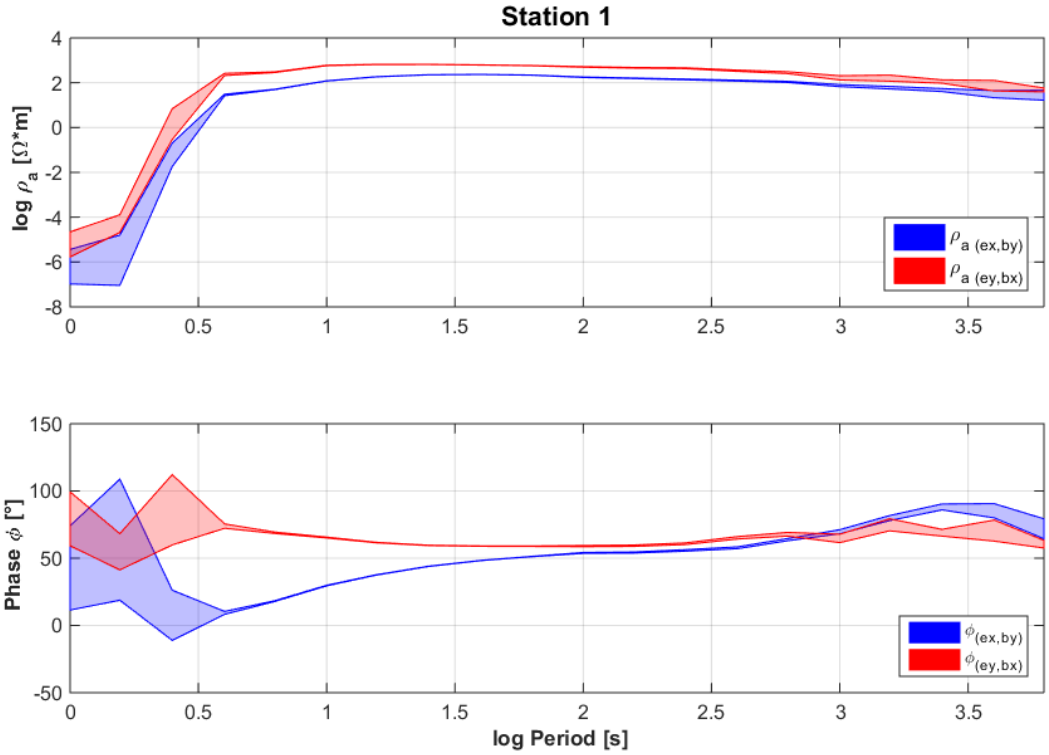

Figure 6.10: Apparent resistivity and phase - Station 1

At station 3, $\rho_{a\ (e_x,b_y)}$ has a higher value than $\rho_{a\ (e_y,b_x)}$, and is stable around $10^{2}\ \Omega m$,

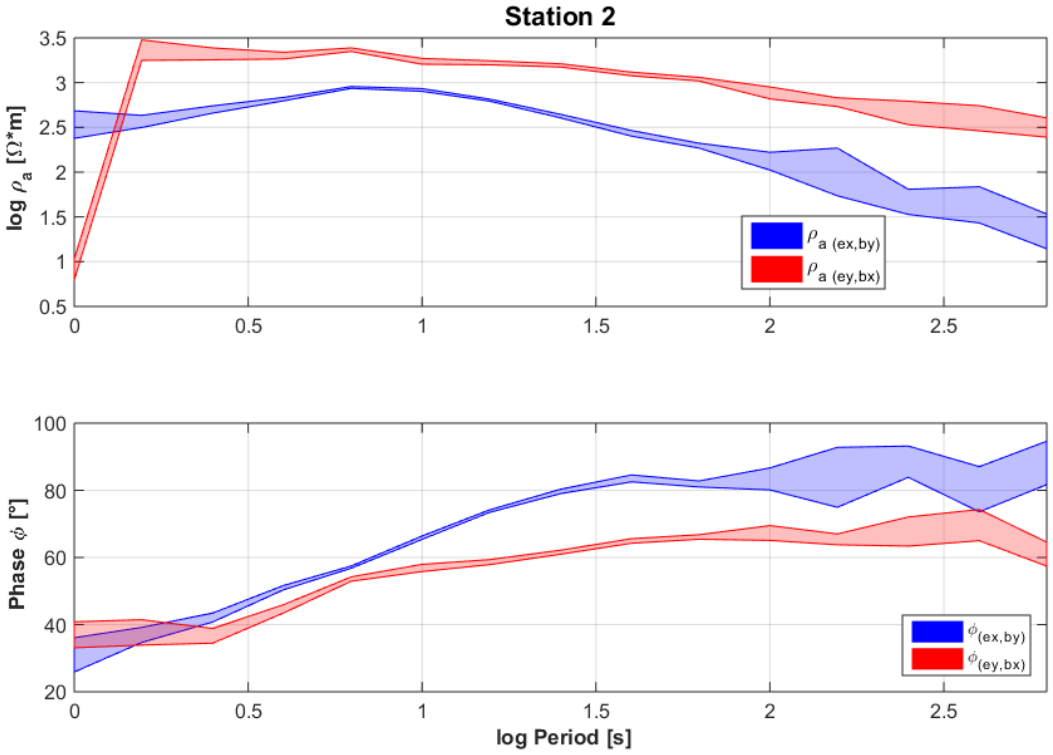

Figure 6.11: Apparent resistivity and phase - Station 2

with small variations. $\rho_{a\ (e_y,b_x)}$ is slowly increasing from $10^{0.2}\ \Omega m$ to $10^{1.2}\ \Omega m$. The phases are also split in the whole period range with a constant linear increase.

The impedance tensor was not calculated at station 4 and 5, due to missing electrical measurements.

Station 6 has a similar split in the resistivities as the rest of the stations, with $\rho_{a\ (e_x,b_y)}$ as the highest. It increases in the low periods up to $10^{1.1}$ s, where after it levels out. The phases at this station are not split as the previous, instead $\phi_{(e_y,b_x)}$ is slightly higher than $\phi_{(e_x,b_y)}$ in the low periods until $10^{1.2}$ s, where they follow each other around 50°. Hereafter they are stable with a slight increase until $10^{2.4}$ s where $\phi_{(e_y,b_x)}$ decreases and $\phi_{(e_x,b_y)}$ increases for the last to target periods.

The resistivities at station 7 have a split between them, which is not present in the phases, which can indicate static shift. $\rho_{a\ (e_x,b_y)}$ has a stable resistivity between 10^1 and $10^{1.5}\ \Omega m$ during the whole period range. $\rho_{a\ (e_y,b_x)}$ has more variation between $10^{2.5} - 10^{3.5}\ \Omega m$, it decreases from $10^{0.6} - 10^1$ s and increases from $10^1 - 10^{1.4}$ s. Hereafter it slowly decreases for the rest of the periods. The phases are stable around 50°, until $10^{2.2}$ s where $\phi_{(e_y,b_x)}$ increases and $\phi_{(e_x,b_y)}$ remains at the same level.

Similar to station 7, station 8 has a split between the resistivities, however with different values and the highest resistivity is $\rho_{a\ (e_x,b_y)}$. In the low periods the split is approximately on $10^1\ \Omega m$, which increases with period to $10^{3.5}\ \Omega m$. $\rho_{a\ (e_x,b_y)}$ has the highest values and the smallest decrease over the period range, whereas $\rho_{a\ (e_y,b_x)}$ has a steeper decrease with a little increase at $10^{3.2}$ s. The phases have a different behaviour than the resistivities. $\phi_{(e_x,b_y)}$ has a slight oscillation between 50° – 90° with one minimum at $10^{2.1}$ s and two maxima at $10^{0.6}$ s and $10^{3.4}$ s. $\phi_{(e_y,b_x)}$ increases from 60° to 90° at

$10^{2.8}$ Ωm, where after it has a steep decrease until 20°.

At station 9, $\rho_{(e_x,b_y)}$ is approximately stable around 10^2 Ωm for all periods, where $\rho_{(e_y,b_x)}$ has a steep increase from $10^{0.5} - 10^{1.2}$ s. It is stable until $10^{2.6}$ s where a short decrease occurs and then a slow increase for the rest of the period range. $\rho_{(e_y,b_x)}$ never reaches the level of $\rho_{(e_x,b_y)}$. The phase behaves differently, with $\phi_{(e_x,b_y)}$ stable around 50° with a slight increase at long periods. $\phi_{(e_y,b_x)}$ has a constant increase in the whole period range, from approximately -50° to 150°.

The apparent resistivities at station 10 follow each other, with a little split, in the low period with a small increase until 10^1 s where after they decrease. At $10^{2.6}$ s the split has demised, but they still have a similar decrease following each other within the error margins. The phases behave differently, with $\phi_{(e_x,b_y)}$ stable at 60° until $10^{2.5}$ s where it increases up until $10^{3.4}$ s and then decreases. $\phi_{(e_y,b_x)}$ begins with an increase from $10^{0.5} - 10^{2.6}$ s between 20° and 70°. Hereafter it is approximately stable around 70° until $10^{3.2}$ s and then decreases.

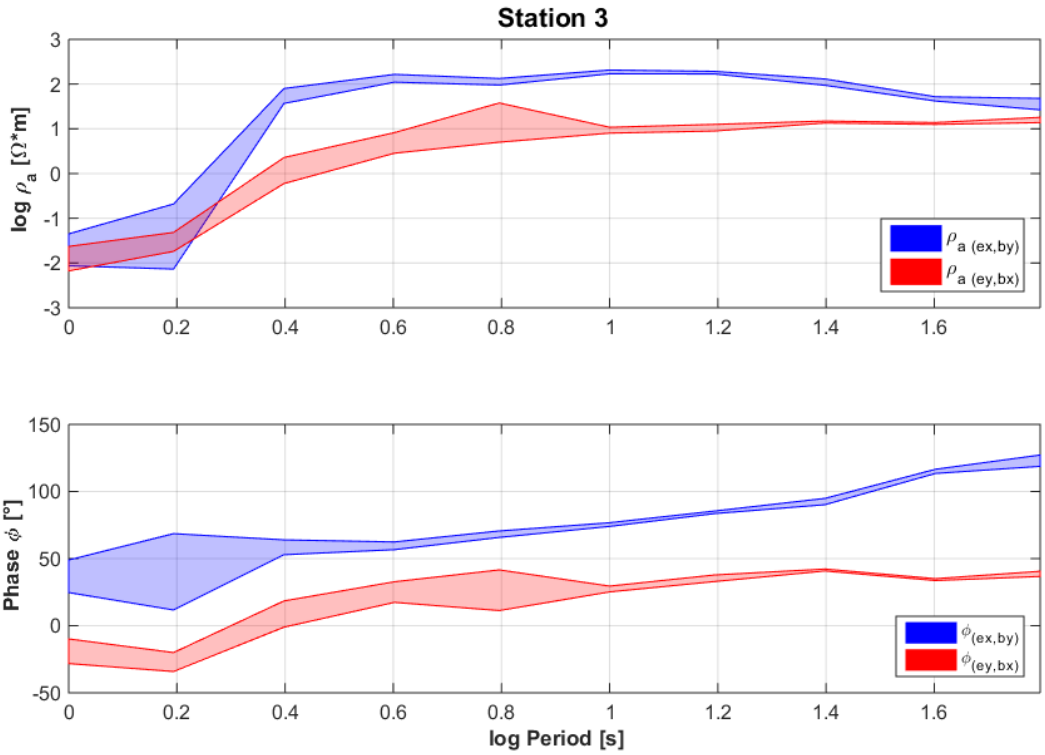

Figure 6.12: Apparent resistivity and phase - Station 3

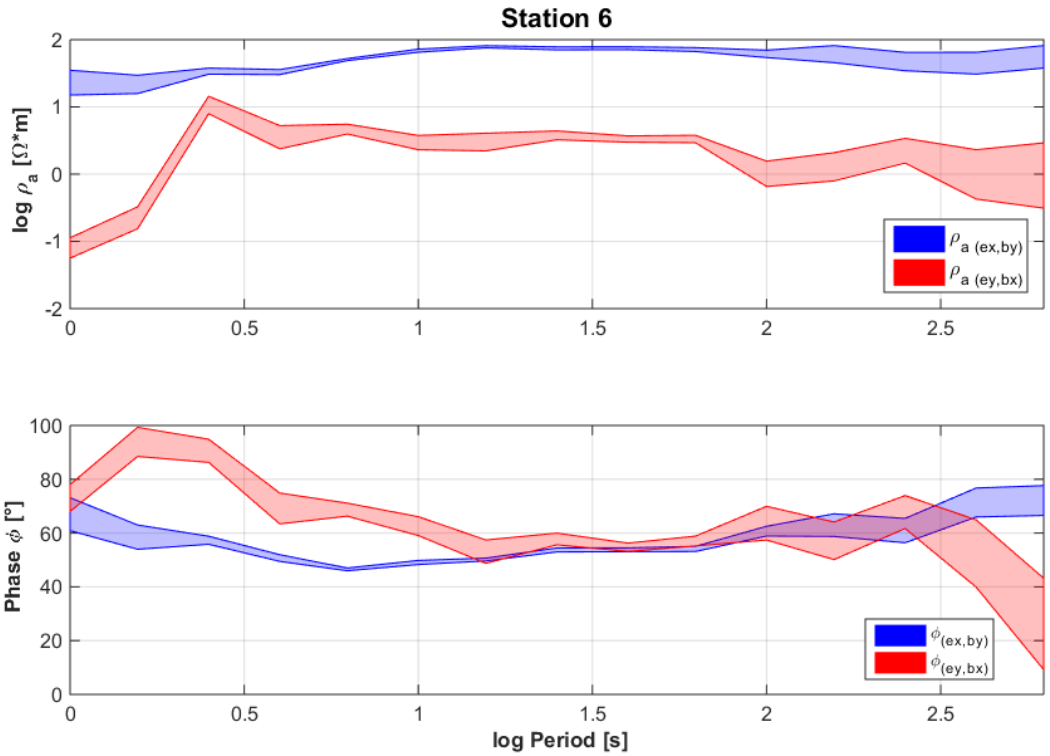

Figure 6.13: Apparent resistivity and phase - Station 6

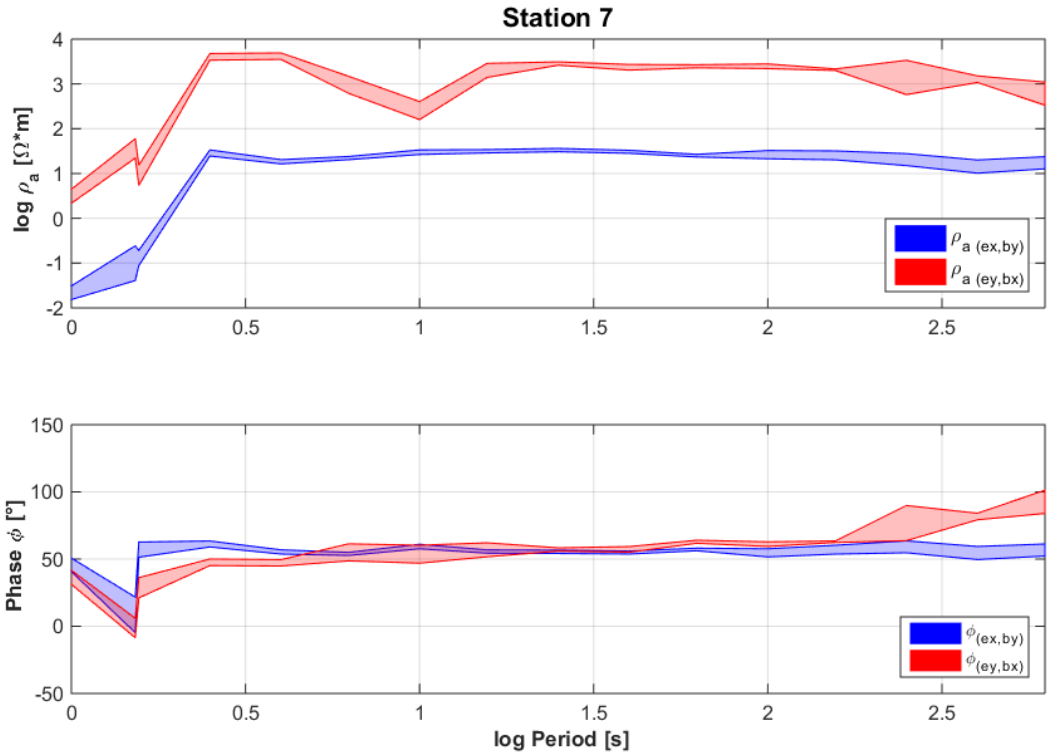

Figure 6.14: Apparent resistivity and phase - Station 7

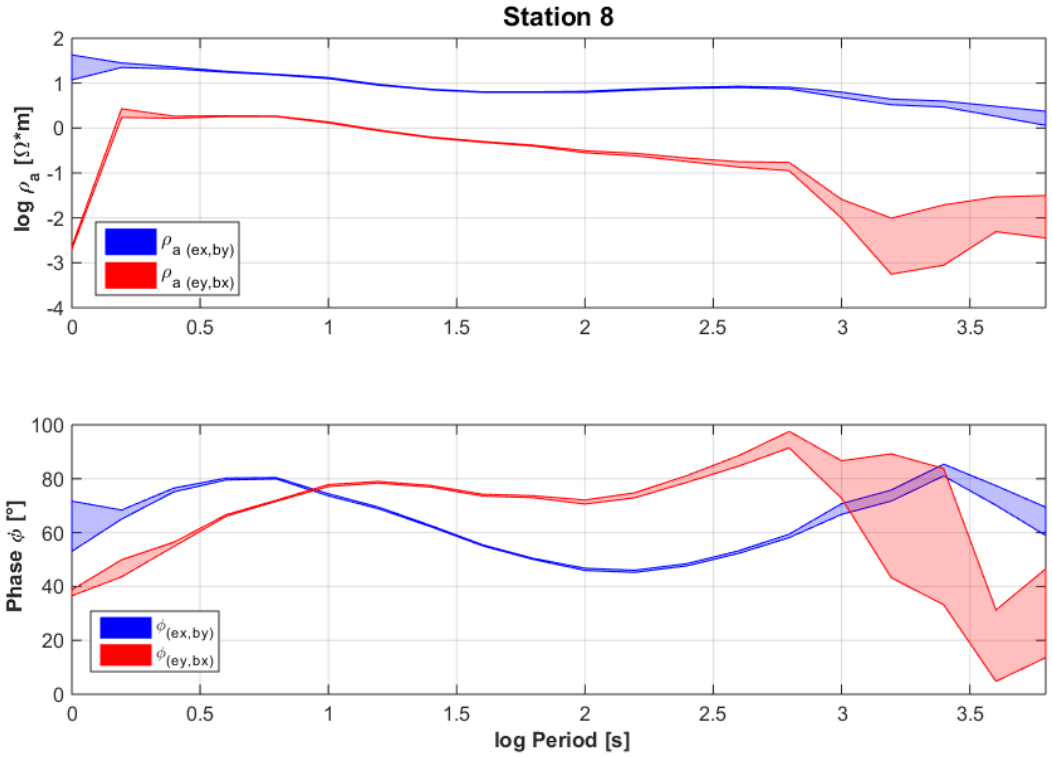

Figure 6.15: Apparent resistivity and phase - Station 8

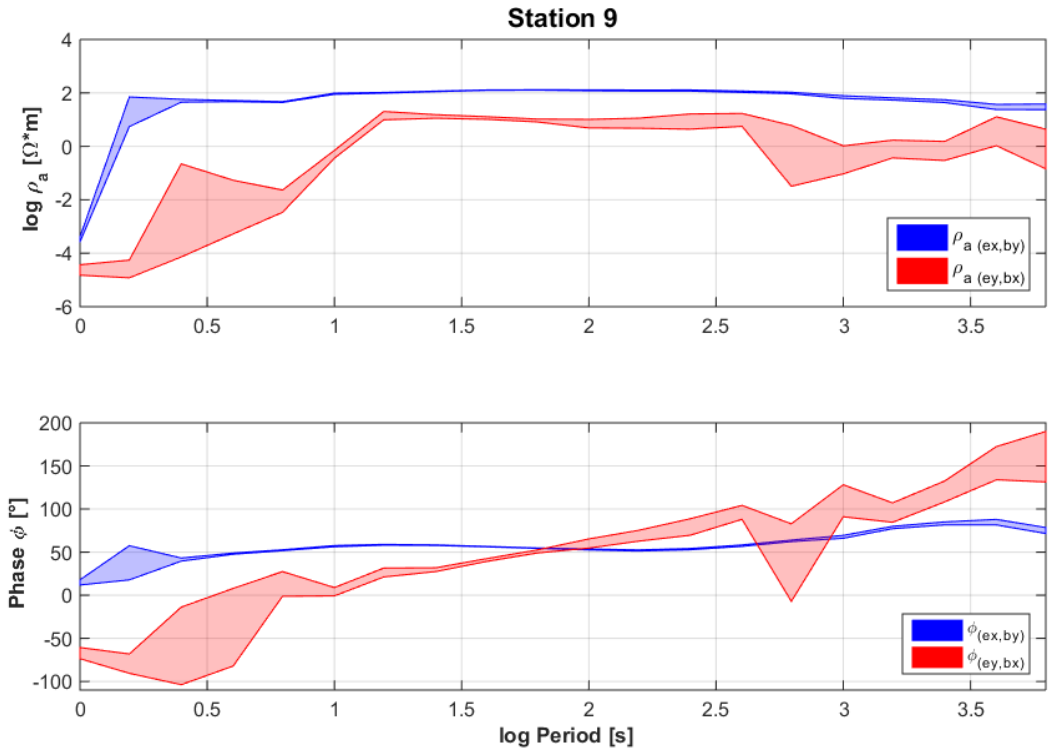

Figure 6.16: Apparent resistivity and phase - Station 9

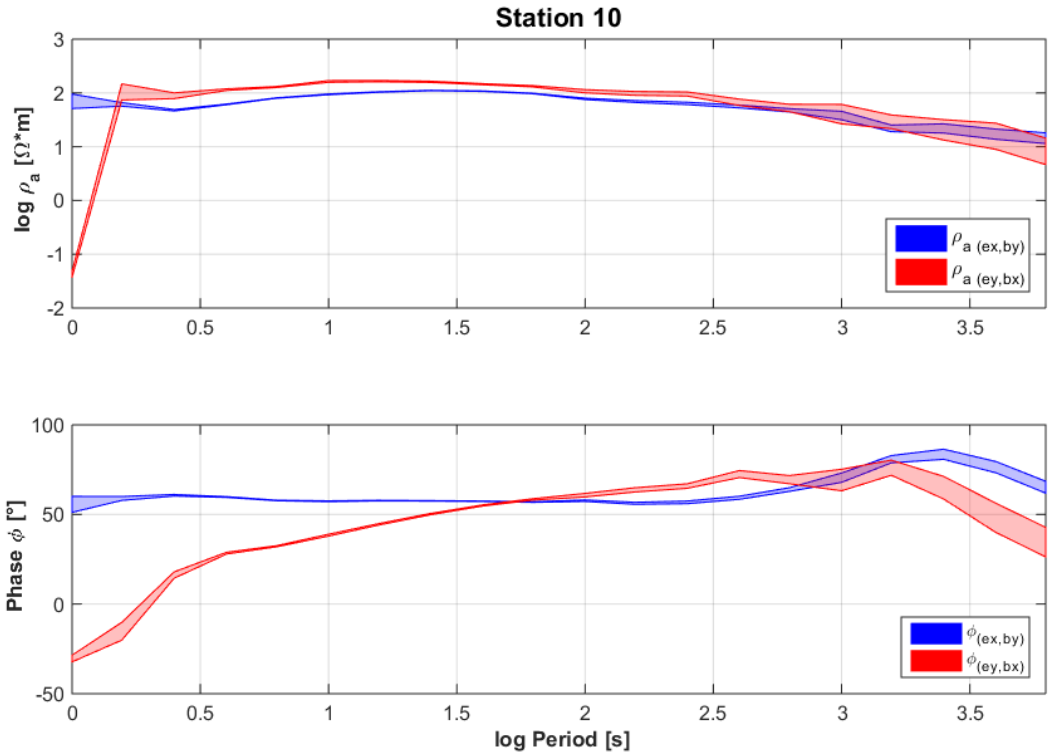

Figure 6.17: Apparent resistivity and phase - Station 10

The induction arrows for all stations are displayed in Fig. 6.18 and 6.19. The real induction arrow illustrates where a conductivity contrast is present, by pointing away from the conductive material. In the following, only description of the real induction arrows will be included.
Station 1 has at periods before $10^{1.8}$ s conductivity to the east of the station, and hereafter the induction arrows rotate counter clockwise indicating conductivity to the north west, ending with a north direction. Rotation in the induction arrows with period is often an indication of more complex three dimensional structures [Ritter, 2007]. Station 2 has almost no induction arrows at low periods and small arrows which grow to approximately 0.3 and a north west direction. A constant direction in induction arrows indicates that the subsurface at this location is two dimensional, however at low periods where no induction arrows are present indicates a one dimensional subsurface [Ritter, 2007]. Similar behaviour is seen at station 3, but with the conductivity located towards north. Small variation in low periods and after $10^{1.5}$ s the arrows slowly turn more north, north west. Similar to station 1, station 4 has a rotation in the induction arrows with period. However, it is a clockwise rotation beginning at north west and ending in a west direction. Station 5 has a clockwise rotation from north to south, with largest induction arrows of 0.8. At station 6 the induction arrows begin with conduction towards east, rotate over south and ends west. Station 7 has in the lowest periods conduction to the south west, and hereafter conduction to the north west. Station 9 and 10 are similar with conductive material to the north west. The arrows are larger at station 10 in the lower periods and almost zero at station 9.

The phase tensors for station 1 - 3 and 6 - 10 are displayed in Fig. 6.20. At all the stations the subsurface is two or three dimensional, since the length of the axes are different from each other. There are at a few periods phase tensors which are displaying

a one dimensional behaviour where the length of the axes are similar. For example at station 1 the phase tensors display three dimensional behaviour at low periods, but as the period increases the phase tensors change towards a more one dimensional behaviour in the second longest period. Similar one dimensionality is also visible at station 9 around $10^{1.5}$ and $10^{3.5}$ s.

Above the different transfer functions have been described, though without any conclusions of how the subsurface might be described from this data. Since the data has not been sorted by a selection criterion, any interpretation should be made with caution. It might not be the true subsurface displayed in the transfer functions, but also parts from other source fields which might be near. However, these transfer functions can be used for comparison with data that have been sorted and selected, as for example the transfer functions from the multiple station processing discussed in the next section.

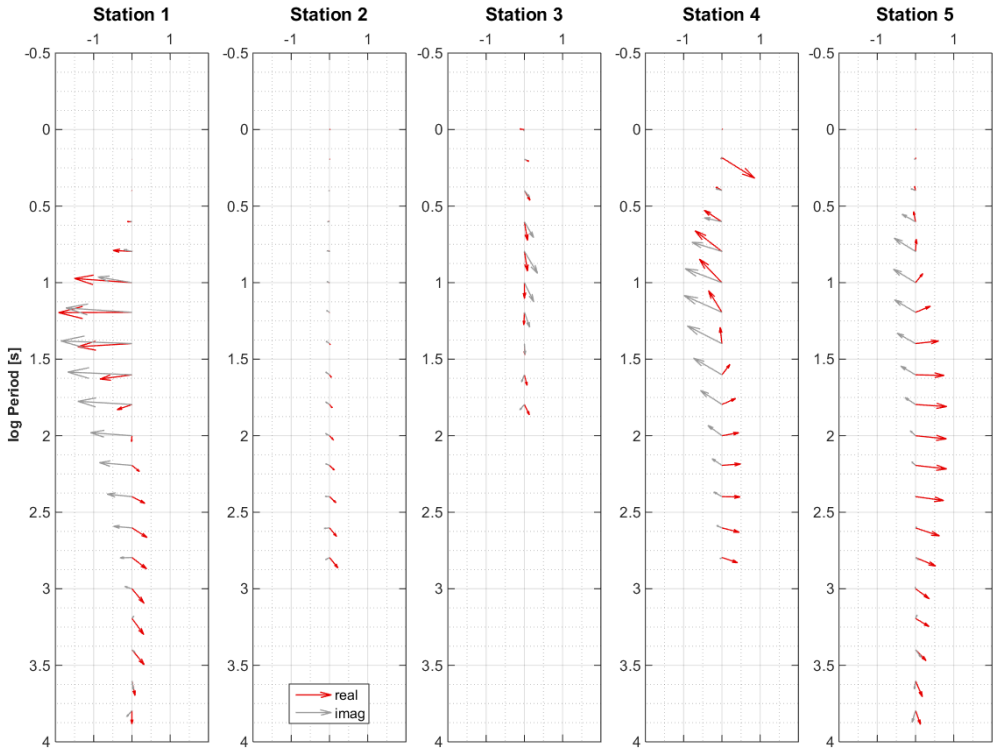

Figure 6.18: Induction arrows, station 1 - 5. The real induction arrows point away from conductive material, where a rotation in the direction with period indicates a three dimensional subsurface. Geographical north (up).

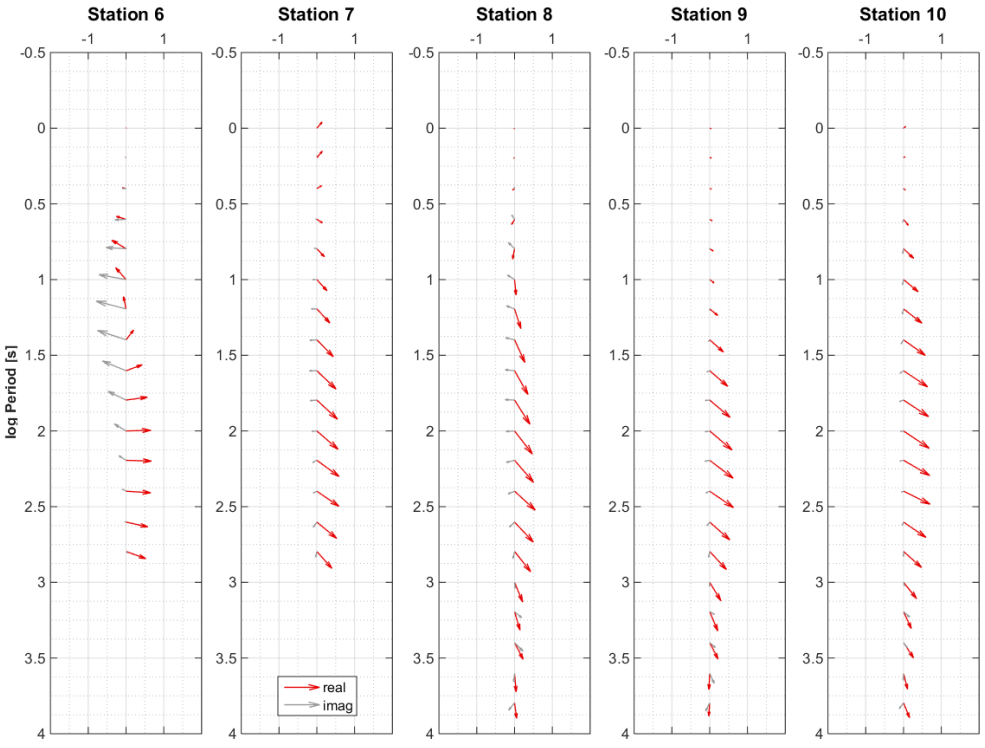

Figure 6.19: Induction arrows, station 6 - 10. The real induction arrows point away from conductive material, where a rotation in the direction with period indicates a three dimensional subsurface. Geographical north (up).

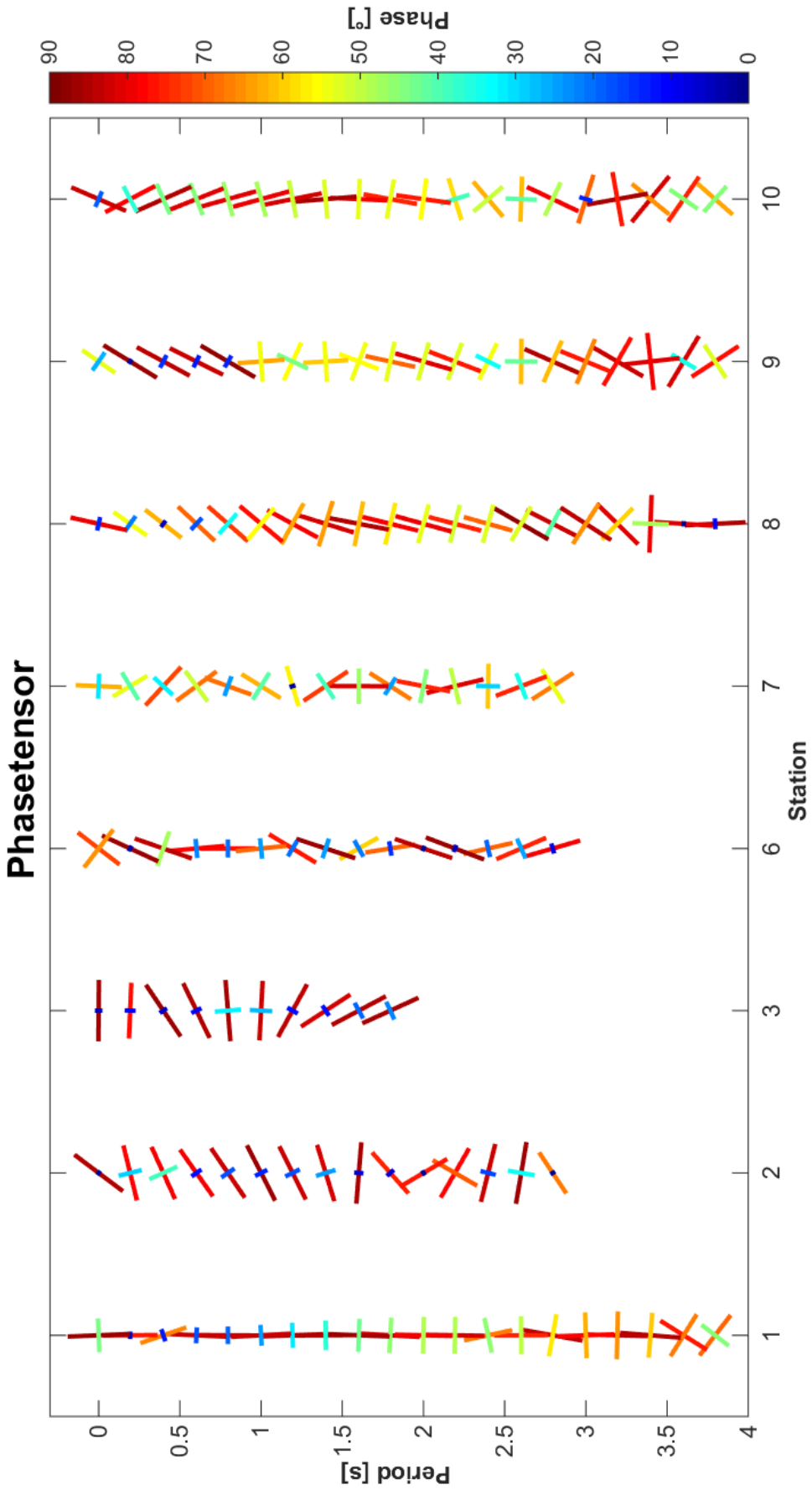

Figure 6.20: Phase tensor for station 1 - 3 and 6 - 10. Phase tensors with different axes length illustrate a multidimensional subsurface. Geographical north (up).

6.2 Multiple station processing results

The EGstart software presented in sec. 5.3.2 uses the multivariate estimation in sec. 5.2.3, and has been used in different set ups to test its usability on the magnetotelluric data set collected in this project. Three set ups are presented in this section; (1) Station 1, 8, 9 and 10 are analysed with the time intervals fixed to one hour for all target periods, with the largest being 55.215 s. (2) The same four stations are analysed, with flexible time intervals depending on the target period, with the largest being 1746.04 s. (3) All ten stations are analysed with flexible time intervals, with the largest being 810.439 s, however only the magnetic data is evaluated. Finally, the different results are compared and discussed.

Only four stations have been used in the first two set ups, due to the lack of simultaneously recording time in the electrical fields for the other stations. As seen in Fig. 4.4 in chapter 4, station 1, 8, 9 and 10 have a considerable recording time that overlaps. In the same figure it also shows that all stations have magnetic fields which overlap and therefore it is possible to perform the third set up with all stations.

The time series are in EGstart divided into time intervals of one hour, where time interval no. 1 is the first time interval of 1 hour and time interval no. 100 is the 100th hour.

6.2.1 Analysis with fixed time intervals

With the eigenvalue problem in the multivariate estimation, it is possible to detect if more than two dominating eigenvalues are present in the data when analysing station 1, 8, 9 and 10 together. Fig. 6.21 and 6.22 illustrate the second and third largest eigenvalues at all time intervals and all periods, respectively. There are clear time dependent variations in the second eigenvalue, which illustrates that the magnetic fields are changing in time, as expected, because of fluctuations in the source fields. However, the third eigenvalue is also showing time dependent variations. For a perfect plane wave, as the magnetotelluric method assumes, the third eigenvalue would be zero in all time intervals and in all periods. There are several time intervals where the third eigenvalue is similar in strength to the second eigenvalue, which indicates that there are other sources present than the plane wave.

These variations are visible in the eigenvalues, but also in the transfer functions. An example is the induction arrows for seven time intervals, no. 268 to no. 274, in Fig. 6.23 for station 8 and Fig. 6.24 for station 10. Each column of induction arrows represents the data from one time interval. There are clear differences in the induction arrows depending on the time interval, which can lead to false interpretations of the data if not discovered and handled with care.

Therefore, the data in the time intervals are sorted, and with the criteria described in eqn. 5.24 the best time intervals are selected. For this analysis, the 20% time intervals with the highest EV-index are chosen. The EV-index illustrates which time intervals have the largest ratio between the second and the third eigenvalues, but also takes into account that the third eigenvalue should be low. A weighted median of these selected eigenvalues is calculated, and the result is displayed in Fig. 6.25. There is a significant separation between the second and third eigenvalue for all periods, though

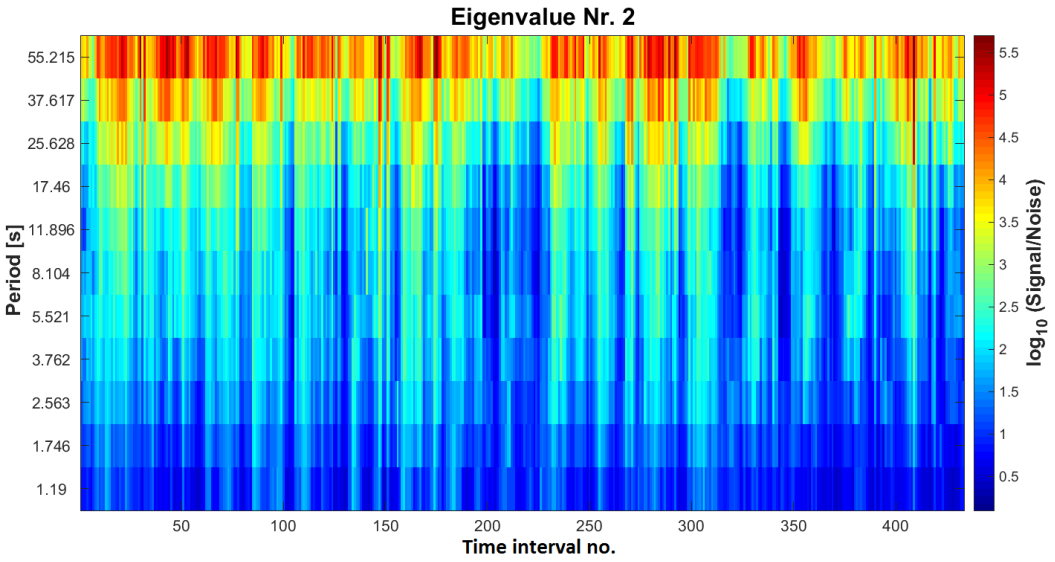

Figure 6.21: Second largest eigenvalue for all time intervals, with fixed time intervals. The time intervals are displayed along the x-axis and the target periods along the y-axis. The colour scale illustrates the value of the eigenvalue, the signal to noise ratio. The time series begin on 20th September 2013 19:29:04 UT.

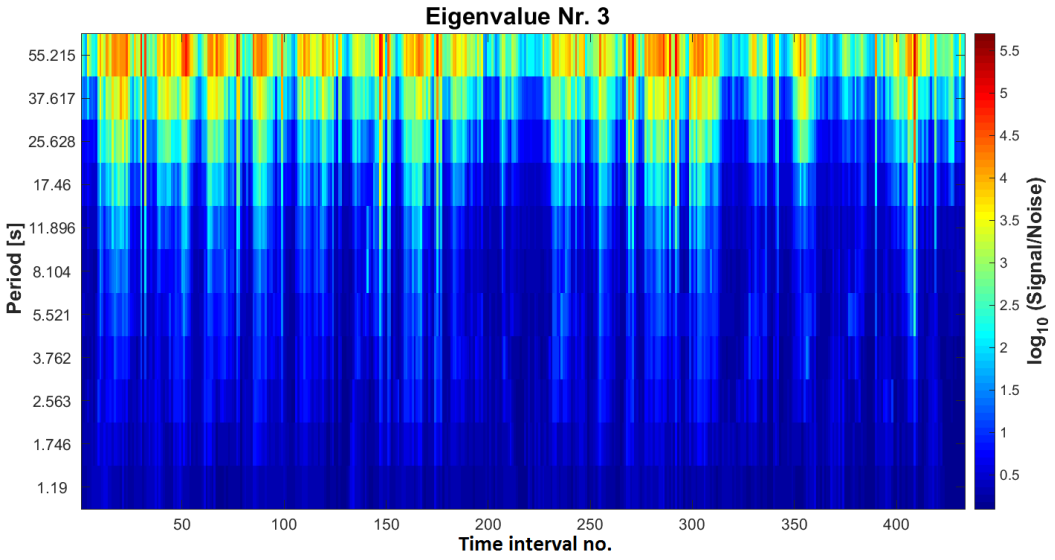

Figure 6.22: Third largest eigenvalue for all time intervals, with fixed time intervals. The time intervals are displayed along the x-axis and the target periods along the y-axis. The colour scale illustrates the value of the eigenvalue, the signal to noise ratio. The time series begin on 20th September 2013 19:29:04 UT.

smaller at long periods than short periods. Comparing these median eigenvalues to the eigenvalues of a single time interval, no. 286 in Fig. 6.27, there is a significant difference in the separation. In time interval no. 286 there are many large eigenvalues at all periods, and not two dominating. Other time intervals can, however, give very different results. Fig. 6.28 illustrate the single best time intervals, which is significantly different than time interval no. 286. However, it is also slightly different from the 20%

selection. The best time interval is not used in the analysis, but instead the 20% is used in order ensure both a good result at same time as improving the data amount. The advantage of a large amount of data is that small outliers or variations from the mean signal will not affect the response noticeably.

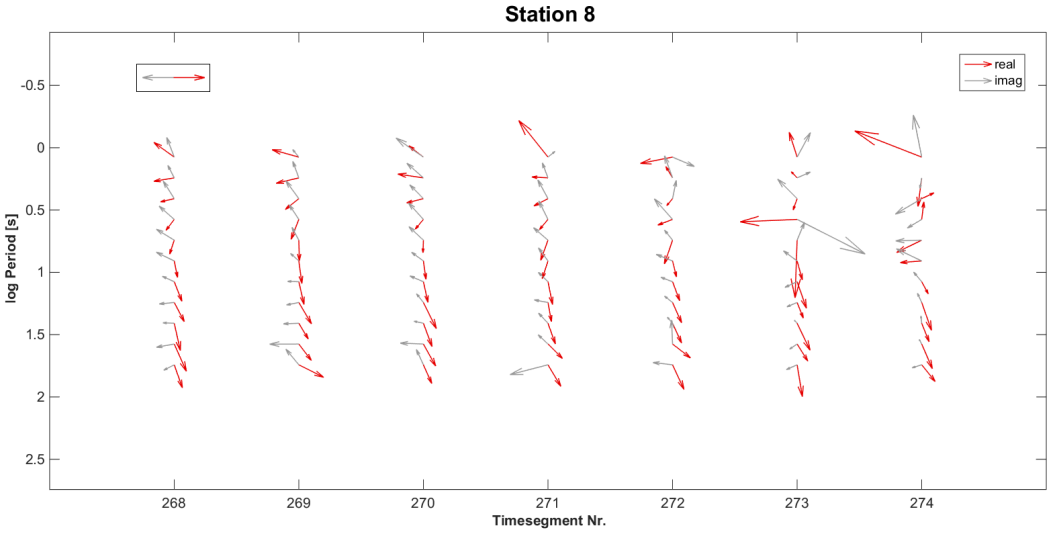

Figure 6.23: Induction arrows of station 8 for seven time intervals, no. 268 to no. 274. Geographical north (up).

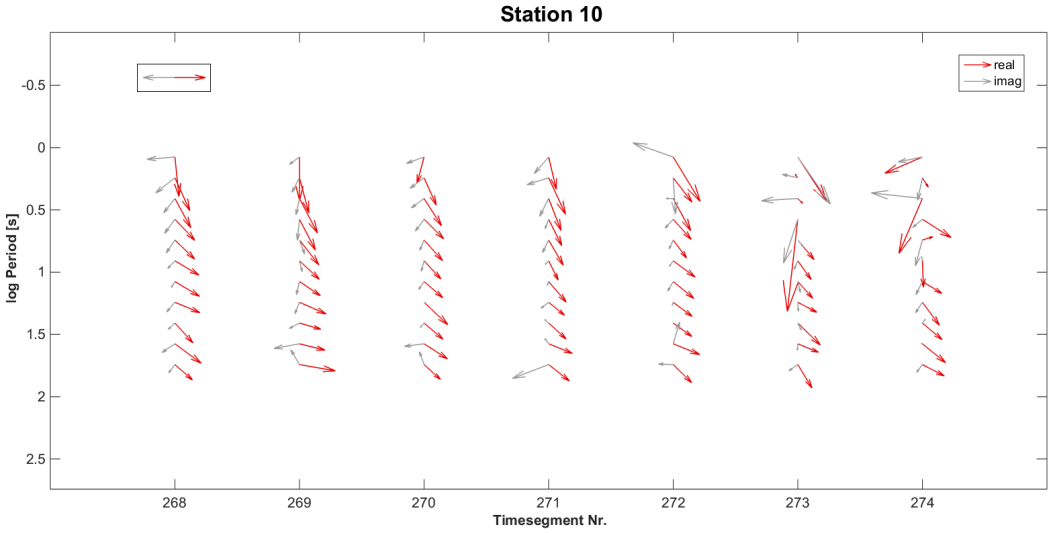

Figure 6.24: Induction arrows of station 10 for seven time intervals, no. 268 to no. 274. Geographical north (up).

The amount of time intervals included in the median result was set to 20%, as mentioned above. However, selecting a smaller percentage, will not improve the results considerably. Fig. 6.29 and 6.30 illustrate the eigenvalues when only the top 10% are selected. Comparing with Fig. 6.25 and 6.26, they are almost identical and all the eigenvalues selected are within the same range. The shaded areas in Fig. 6.26 and 6.30 illustrate the area wherein the different eigenvalues included in the 20%, are located.

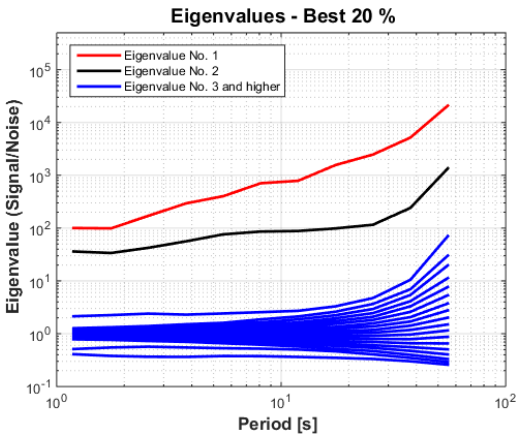

Figure 6.25: The weighted median eigenvalues of the selected 20% best time intervals, with fixed time interval.

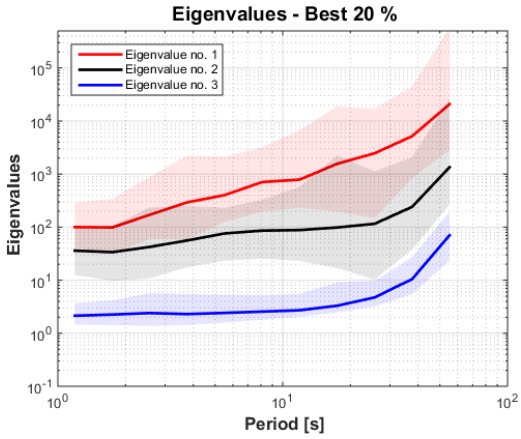

Figure 6.26: The weighted median eigenvalues of the selected 20% best time intervals, with fixed time interval. The shaded areas are the range wherein the 20% best time intervals are located.

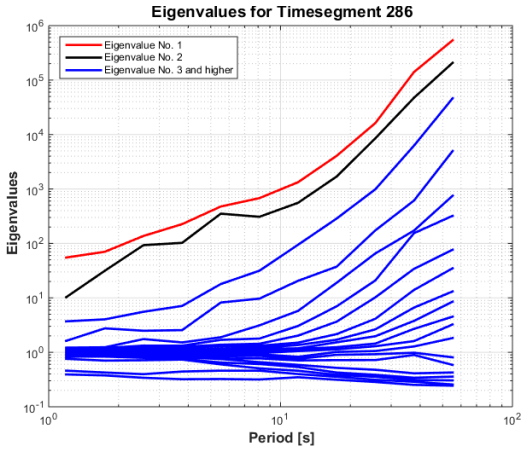

Figure 6.27: Eigenvalues for time interval no. 286.

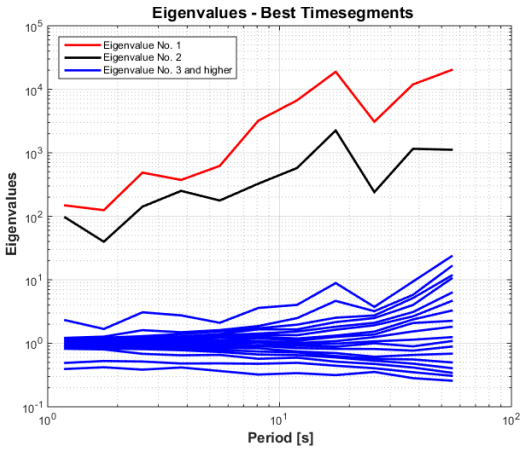

Figure 6.28: Eigenvalues for the best time interval.

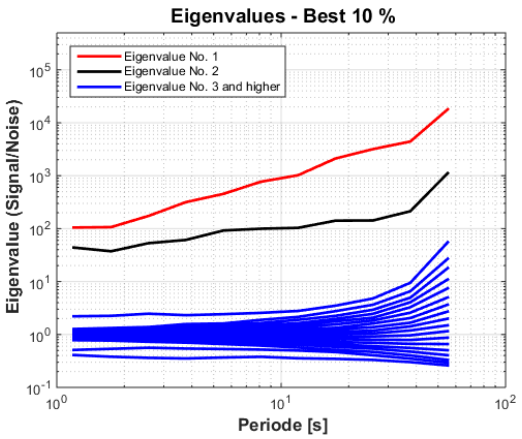

Figure 6.29: The median eigenvalues of the selected 10% best time intervals, with fixed time interval.

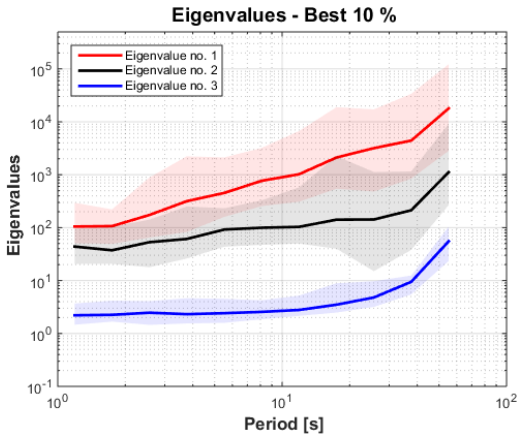

Figure 6.30: The median eigenvalues of the selected 10% best time intervals, with fixed time interval. The shaded areas are the range wherein the 10% best time intervals are located.

Description of transfer functions

Based on the impedance tensor, the apparent resistivity ρ_a and impedance phase ϕ are calculated for station 1, 8, 9 and 10. The corresponding off diagonal elements are displayed in Fig. 6.31 - 6.34, respectively. Note, that the presented values are given in the geomagnetic reference frame, which is defined by a declination of 32° W at the measurement area [National Geophysical Data Center, 2016]. The induction arrows, which are a representation of the tipper $\mathbf{T}$, and the phase tensors, also a representation of the impedance tensor, are displayed in the geographical reference frame and illustrated in Fig. 6.35 and 6.36.

Beginning with the description of station 1, the apparent resistivities $\rho_{a\ (e_y,b_x)}$ and $\rho_{a\ (e_x,b_y)}$ in Fig. 6.31 illustrates a split in all periods, where $\rho_{a\ (e_y,b_x)}$ have the highest values. The split minimizes as the periods increase. A similar pattern is visible in the impedance phases, where $\phi_{(e_y,b_x)}$ has a phase above 50° and $\phi_{(e_x,b_y)}$ below. The split is largest in the short periods and smallest in long periods. A split between the impedance phases indicates that the subsurface is multidimensional, and a split in the apparent resistivities can indicate static shift. The split in the short periods might be explained by an anisotropic layer at shallow depths if it is a general pattern at many stations. However, in this project, it is more likely to be caused by nearby fjords. The effect of fjords will be discussed in sec. 7.1.

At station 8, the apparent resistivities have a similar parallel split, which indicates static shift caused by small near surface anomalies. The impedance phases behave differently. There is a split between the two phases, which implies a multi-dimensional subsurface, since $\phi_{(e_x,b_y)}$ and $\phi_{(e_y,b_x)}$ experience a different subsurface. However, $\phi_{(e_x,b_y)}$ has the highest value in the short periods, but at $10^{0.9}$ s there is phase shift so $\phi_{(e_x,b_y)}$ decrease and $\phi_{(e_y,b_x)}$ becomes largest for the longer periods.

The split in the resistivities is also visible at station 9, where $\rho_{a\ (e_x,b_y)}$ has the largest values over the whole period range, up to $10^2\ \Omega m$. The corresponding phase, $\phi_{(e_x,b_y)}$,

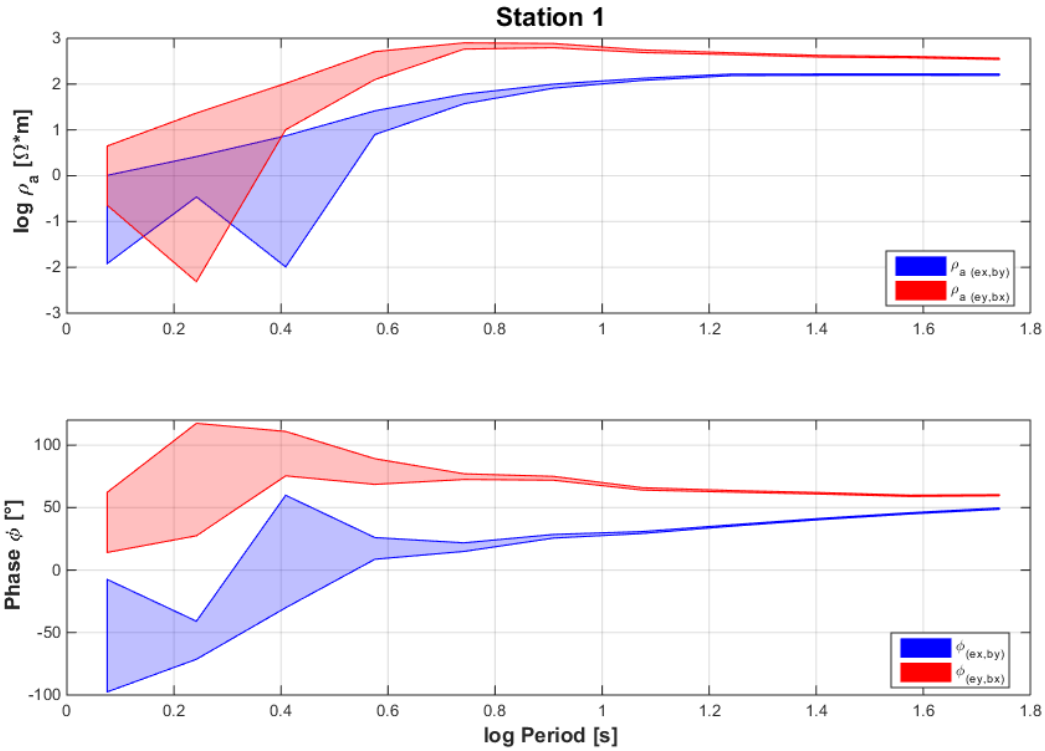

Figure 6.31: Apparent resistivity and phase - station 1 - fixed time interval.

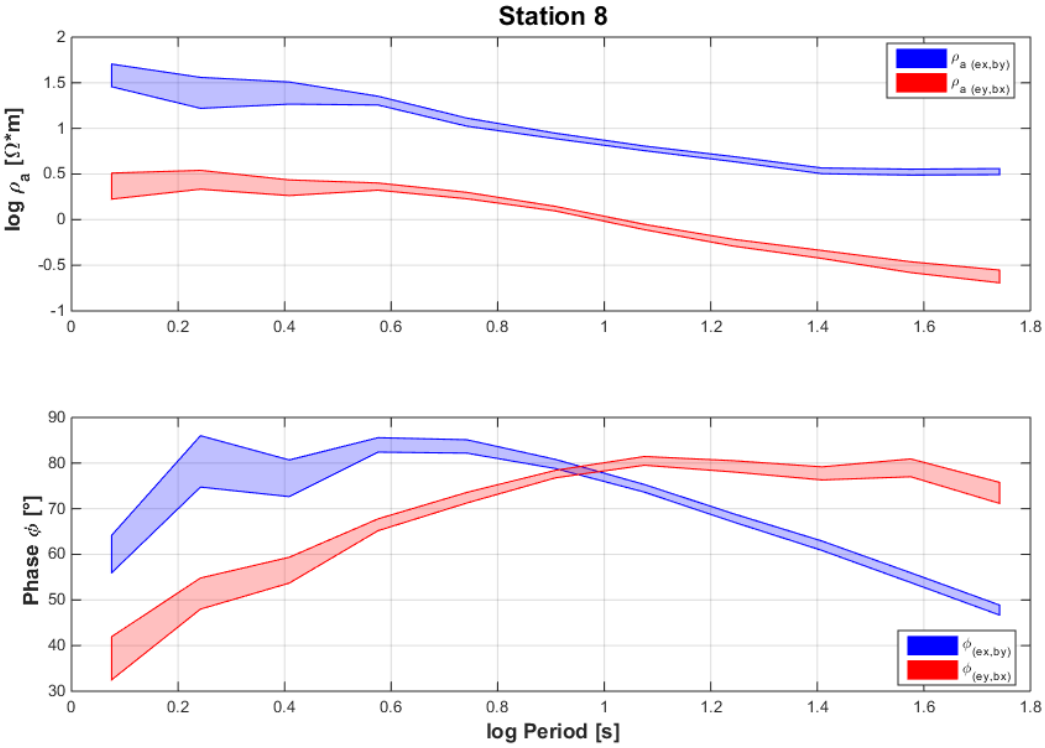

Figure 6.32: Apparent resistivity and phase - station 8 - fixed time interval.

behaves almost constantly around 50°, whereas $\phi_{(e_y,b_x)}$ seems unstable with large error margins, however with an increasing trend from -75° to 50°. The error margins on $\rho_{a\ (e_y,b_x)}$ are also large, which might result from poor data.

At station 10 there is a small split in the resistivities at the short periods, where after they follow each other steadily around $10^2\ \Omega m$. The impedance phases, however, illustrate a split which is largest in the short periods and diminishes at the longest period. This can indicate a top layer with anisotropy and a deeper isotropic layer. However, the phases can also depart from each other again at periods outside our period range, so it is important to be careful with the conclusions when approaching the boundaries of the period range.

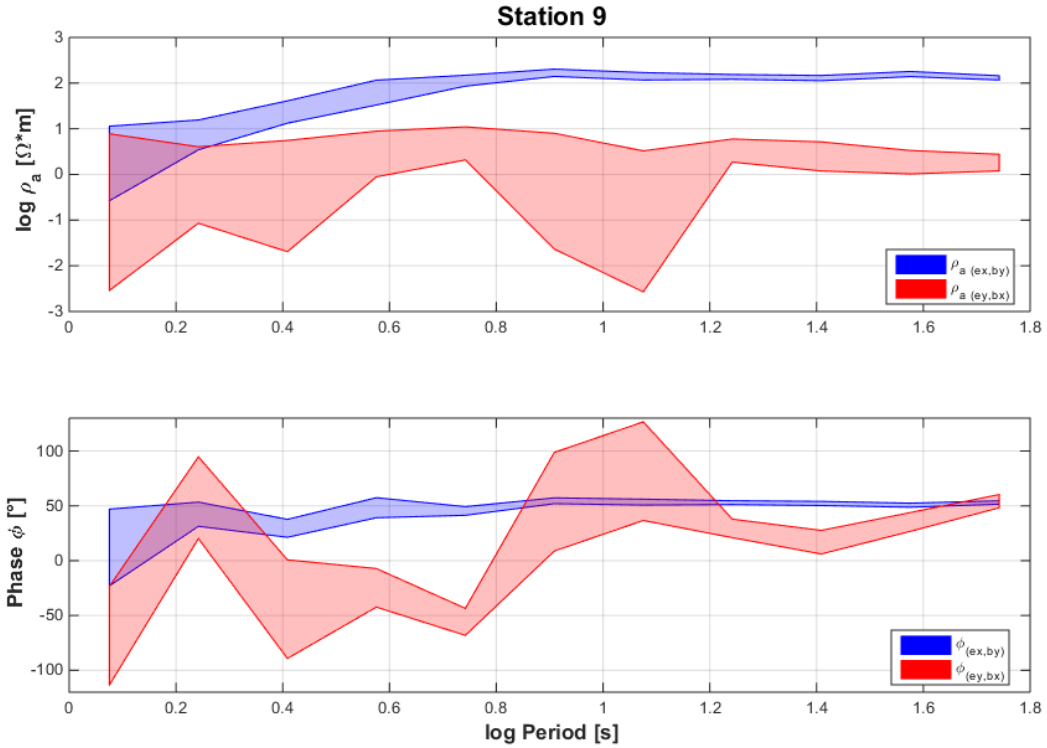

Figure 6.33: Apparent resistivity and phase - station 9 - fixed time interval.

The induction arrows are illustrated in Fig. 6.35, with the Wiese convention [Wiese, 1962], where the real induction arrows point away from good conductors. In the situation where the subsurface is two dimensional, the arrows will be perpendicular to the strike direction. Both the real and imaginary induction arrows are illustrated in red and grey, respectively. Station 1 has large real induction arrows with conductive material to the east for periods larger than $10^{0.5}$ s. Hereon after, the amplitude decreases when the period increases. The imaginary induction arrows, however, point in the same direction as the real arrows for periods larger than $10^{0.5}$ s. This indicates that the subsurface is three dimensional. For a pure two dimensional subsurface, the imaginary induction arrow will point opposite of the real induction arrow. The large induction arrows can be a sign of a multidimensional subsurface. However, as we will see later in sec. 7.1, a station at the shoreline of a fjord will have large induction arrows similar to those at station 1. At station 8, the real induction arrows begin with a conductor to the east in the short periods and rotate counter clockwise as the period increases, to end

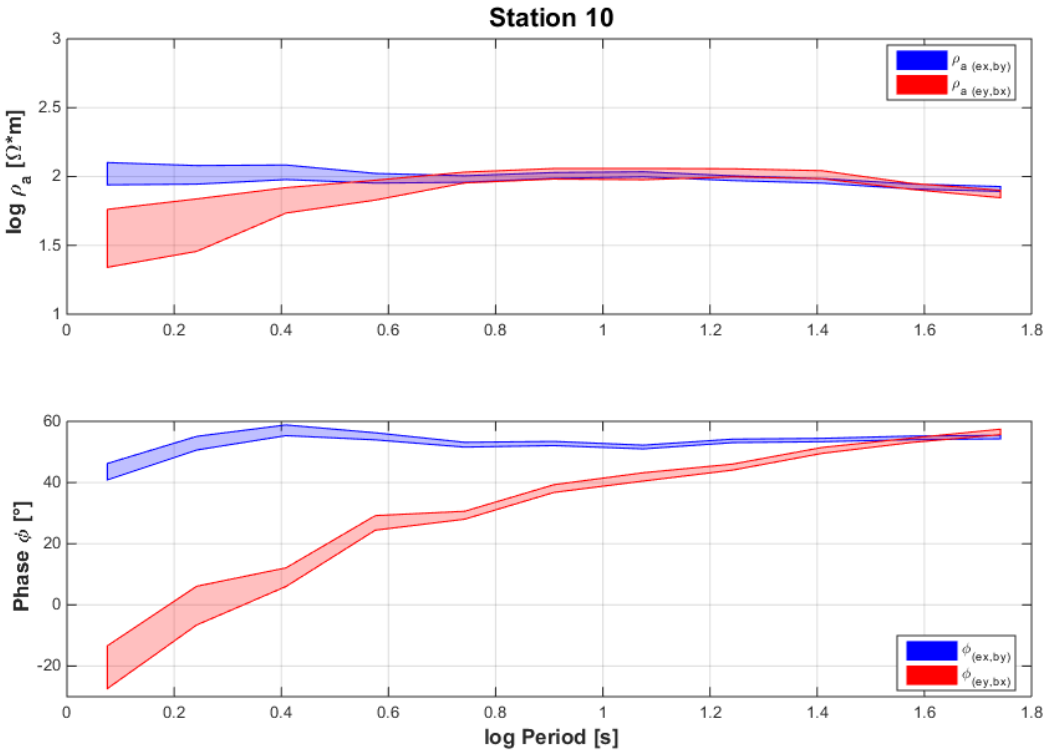

Figure 6.34: Apparent resistivity and phase - station 10 - fixed time interval.

at north west. The imaginary induction arrows are beginning with an orientation away from south and turning counter clockwise towards east. However, at no point are they parallel to the real induction arrows, which indicate the subsurface is three dimensional. The general direction of the induction arrows at station 9 is with a conductor to the north west, however there are small unstable variations in the shorter periods which change the direction slightly. The imaginary arrows are changing in directions at almost all periods, with no general movement. It can be three dimensionality or simply that the selected data is affected by noise which makes it unstable and one must be careful when interpreting. The real induction arrows at station 10 begin to the north and continue with a slight counter clockwise rotation to end north west. The imaginary arrows are orientated east or north east, but never parallel to the real induction arrows, again indicating a three dimensional subsurface.
There is a general direction in the longer periods for station 8, 9 and 10, indicating a conductor to the north west, and by studying the location of the four stations in Fig. 4.2, the ocean is within 20 - 50 km of the stations, in the north west direction. This can be a cause of the orientation of the arrows, since the ocean is to the west, but also includes the Disko bay just north of the stations. This is not seen at station 1, however the stations are set up in a large fjord system, which might affect the induction arrows the same way as the ocean does. This effect from the fjord system on induction arrows is investigated in sec. 7.1.

The phase tensors are illustrated in Fig. 6.36, which is a different representation of the information contained in the impedance tensor. All four impedance tensor elements are included in the calculation of the phase tensor, see sec. 3.3, and are illustrated by ϕ_{min}, ϕ_{max}, β and α. In the phase tensor there are clear indications of a multidimensional

subsurface at all four stations, which is visible when the two phase tensor axes have different length.

To distinguish if the subsurface is two or three dimensional, it is useful to visualise the phase tensor together with the induction arrows. If the induction arrows do not align with one of the phase tensor axes, the subsurface is likely three dimensional.

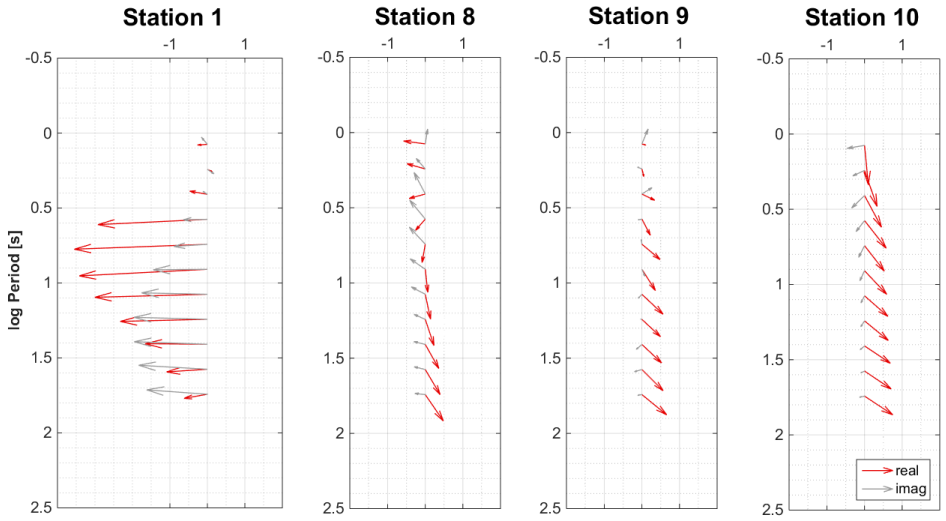

Figure 6.35: Induction arrows for station 1, 8, 9 and 10, with fixed time interval. Geographical north (up).

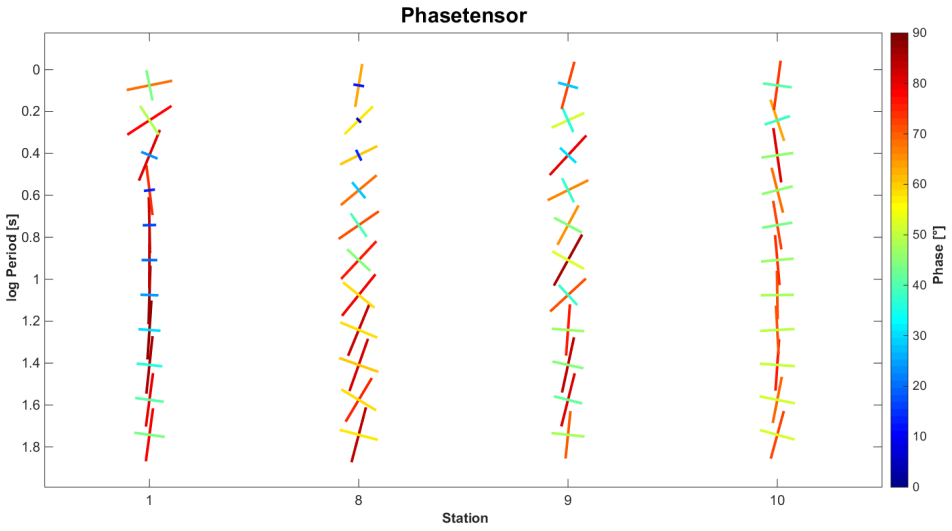

Figure 6.36: Phase tensor for station 1, 8, 9 and 10, with fixed time interval. Geographical north (up).

Fig. 6.37 illustrate the induction arrows and phase tensors at the four different stations on a satellite image, for periods of 1.2 s and 55 s. By just comparing the phase tensor and the corresponding induction arrows, the indications is that the subsurface is three dimensional. However, there is a complex network of fjords penetrating the landscape around the stations. At 1.2 s, the real induction arrows are displaying a behaviour pointing away from the nearby fjord. For a closer look at the stations near the shoreline, Fig. C.1 illustrate a zoom of the nearby area. The phase tensor also align

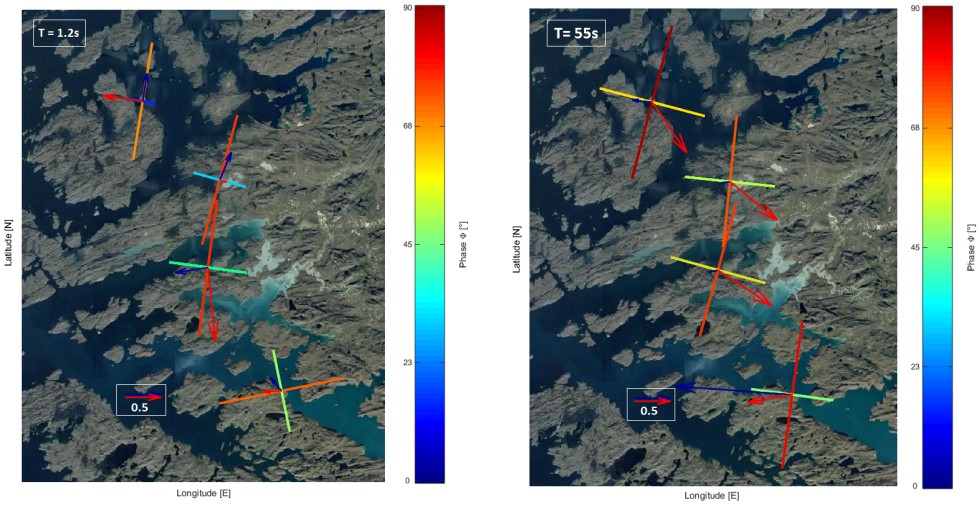

Figure 6.37: Induction arrows and phase tensor on satellite image, 1 s and 55 s. Satellite images from Google Earth, IBCAO, U.S. Geological Survey and DigitalGlobe [2016].

with the shoreline at 1.2 s. At 55 s, the induction arrows have changed direction to point away from north west at three of the stations, the direction of the ocean. It can be that the ocean influences the induction arrows and not the phase tensors. If the induction arrows and the phase tensors are affected by different structures, it is useful to use the skew angle of the phase tensor to determine three dimensionality instead, see Fig. 6.38. When the axes are of different lengths and the skew angle in non zero, the subsurface is three dimensional, which is visible in all periods at station 8 and 10. Station 1 and 9 have both have both two and three dimensionality in the period range. Two dimensionality is present when the skew angle is zero and the axes are of different lengths. In chapter 7 the effect of fjords on induction arrows are discussed and the

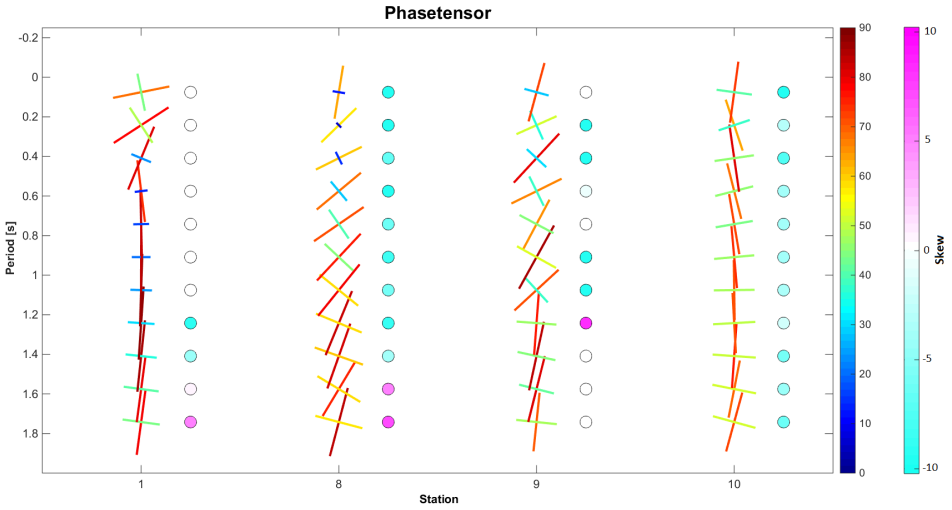

Figure 6.38: Phase tensor and skew for station 1, 8, 9 and 10, with fixed time interval. If the skew is different from 0 and the axes are of different lengths, the subsurface is 3D. Geographical north (up).

difference to the effect on the phase tensors.

6.2.2 Analysis with flexible time intervals

Since the eigenvalue analysis is performed on each target period and each time interval individually, the time intervals can be of different length, depending on the target period. Short periods need shorter time intervals than longer periods, as described in sec. 5.1.1.

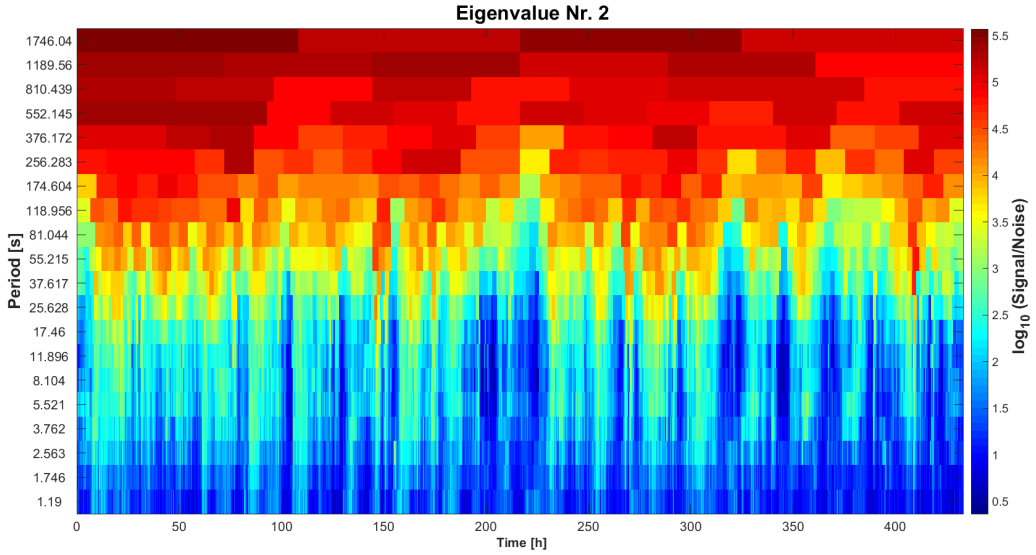

Figure 6.39: Second largest eigenvalue for all time intervals, with flexible time intervals. The time intervals are displayed along the x-axis and the target periods along the y-axis. The colour scale illustrates the value of the eigenvalue, the signal to noise ratio. The time series begin on 20th September 2013 19:29:04 UT.

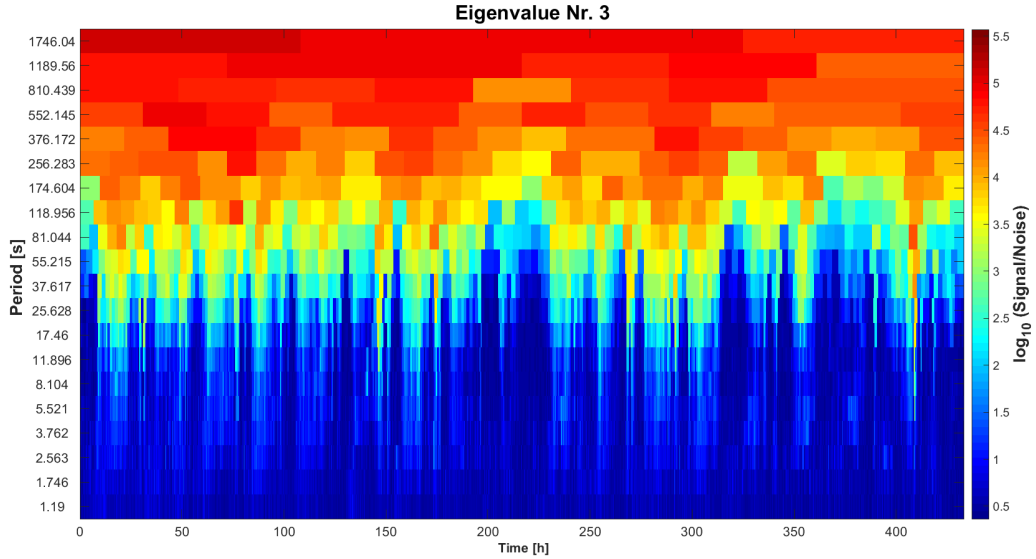

Figure 6.40: Third largest eigenvalue for all time intervals, with flexible time intervals. The time intervals are displayed along the x-axis and the target periods along the y-axis. The colour scale illustrates the value of the eigenvalue, the signal to noise ratio. The time series begin on 20th September 2013 19:29:04 UT.

The analysis is performed on the same four stations as in sec. 6.2.1, and should therefore present similar results within the same period range, however the maximum period evaluated in this analysis is larger, 1746.04 s.

The second and third eigenvalue for each time interval is displayed in Fig. 6.39 and 6.40. The change in time interval size is visible with the different box sizes at different periods. There are clear changes in the values depending on the time interval, and especially in the long periods the third eigenvalue can be of similar size as the second eigenvalue. The short periods have a larger difference between the two eigenvalues, which was also the scenario in the previous analysis. When selecting the 20% time intervals with the highest EV-index, see sec. 5.3.2, and calculating the median hereof, the resulting eigenvalues take the form as depicted in Fig. 6.41. At periods below $10^{1.5}$ s, there are only two dominating eigenvalues which corresponds with the source field being a plane wave. However, at periods larger than $10^{1.5}$ s, the third and higher eigenvalues increase and illustrate that at longer periods other source fields than a plane wave contribute to the data.

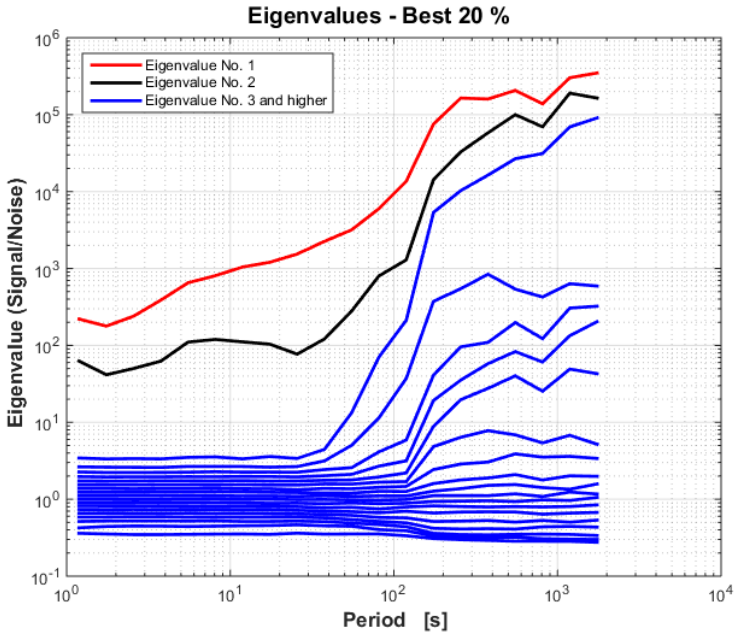

Figure 6.41: The weighted median eigenvalues of the selected 20% best time intervals, with flexible time interval.

It is not possible to know if the data from the plane wave is limited to the two dominating eigenvalues alone or distributed over all large eigenvalues together with the contributions from other sources, either source fields or noise, as explained in sec. 5.2.3.

Description of transfer functions

The impedance tensor is calculated from the data belonging to the two dominating eigenvalues and the corresponding apparent resistivity and impedance phase are displayed in Fig. 6.42 - 6.45. Up until $10^{1.5}$ s there are only two dominating eigenvalues, so the interpretation of the transfer functions would represent the subsurface alone. At higher periods, one must be careful since it is not certain that the transfer functions

describe the subsurface or other external source fields. However, the impedance phases behave similar to the result from the fixed time interval analysis in Fig. 6.31 - 6.34, at periods before $10^{1.5}$ s. There are a few small differences close to 10^{0} s in the apparent resistivities, but this is in the magnetotelluric dead band where the strength of the electric and magnetic field is generally lower.

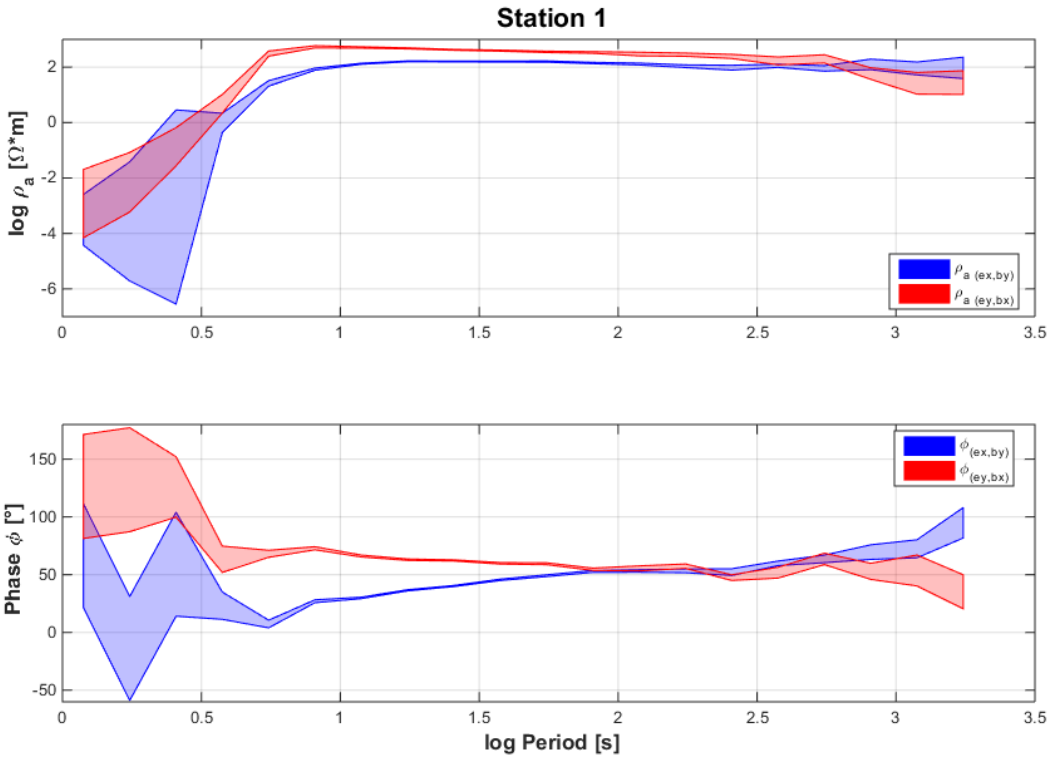

Figure 6.42: Apparent resistivity and phase - Station 1

After $10^{1.5}$ s, where it is questionable if the results describe the subsurface alone, the apparent resistivity and phase behave smoothly and continue the behaviour already set at lower periods. This is the situation at all four stations, see Fig. 6.42 - 6.45. At station 1, the apparent resistivities continue the small split and are located at an almost constant value of 10^{2} Ωm. The impedance phases also continue the behaviour, with a split which minimises and becomes stable around 50° from $10^{2} - 10^{2.5}$ s. The apparent resistivities have a split, at station 8, which continues and increases slightly with longer periods. The impedance phases also maintain the split at longer periods, after the phase shift at 10^{1} s.

At station 9, the resistivities increase in the shortest periods up to 10^{2} Ωm for $\rho_{a\ (e_x,b_y)}$ and $10^{0.5}$ Ωm for $\rho_{a\ (e_y,b_x)}$ where they maintain these values at longer period. The impedance phases are similar, with an increase in the shortest periods which settles around 50°, increasing slightly at the longest periods. A similar situation is present at station 10, where both apparent resistivities follow each other, though without a split, and only to deviate from each other at the longest periods. The phases are split in periods shorter than $10^{1.5}$ s, where after they follow each other at approximately $60°$. The induction arrows of the analysis are presented in Fig. 6.46. The results are identical to the results of the analysis where the time intervals have a fixed length, Fig. 6.35, until $10^{1.8}$ s. At station 8, 9 and 10 the induction arrows in the long periods follow the

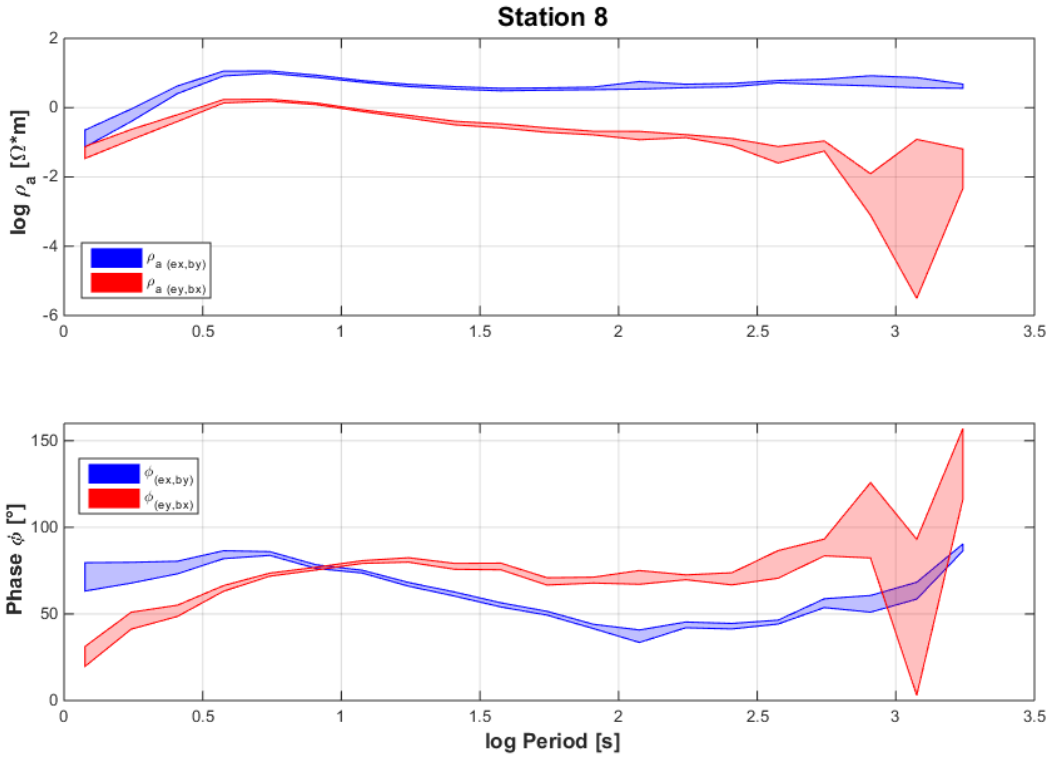

Figure 6.43: Apparent resistivity and phase - Station 8

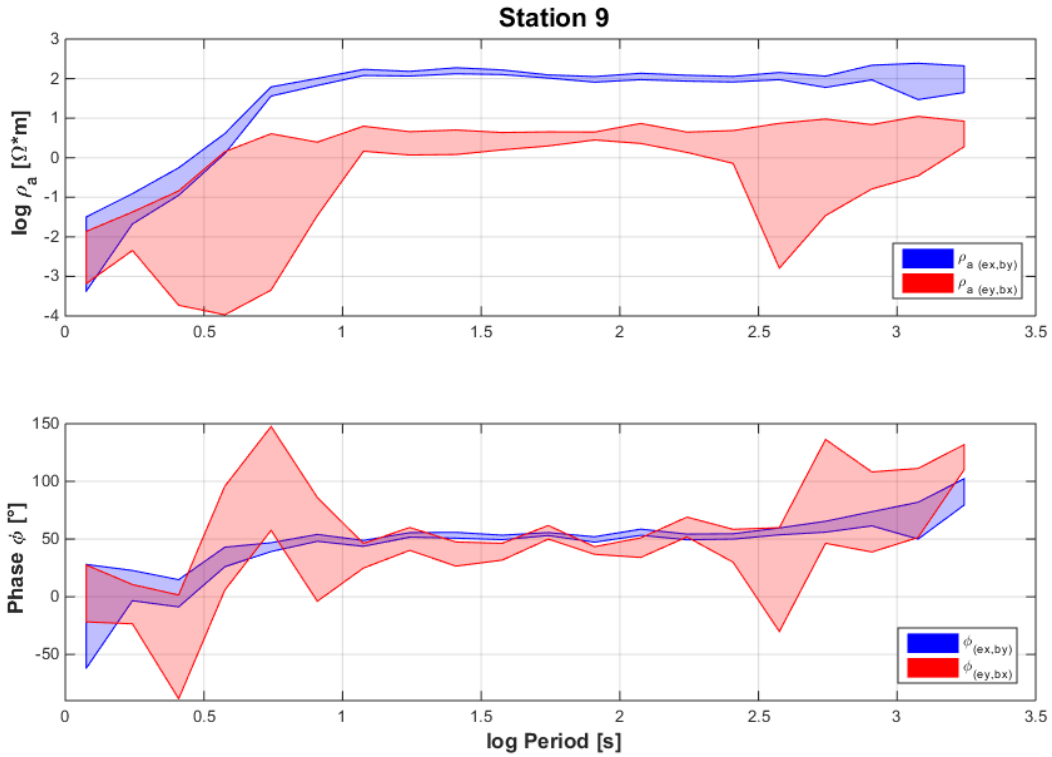

Figure 6.44: Apparent resistivity and phase - Station 9

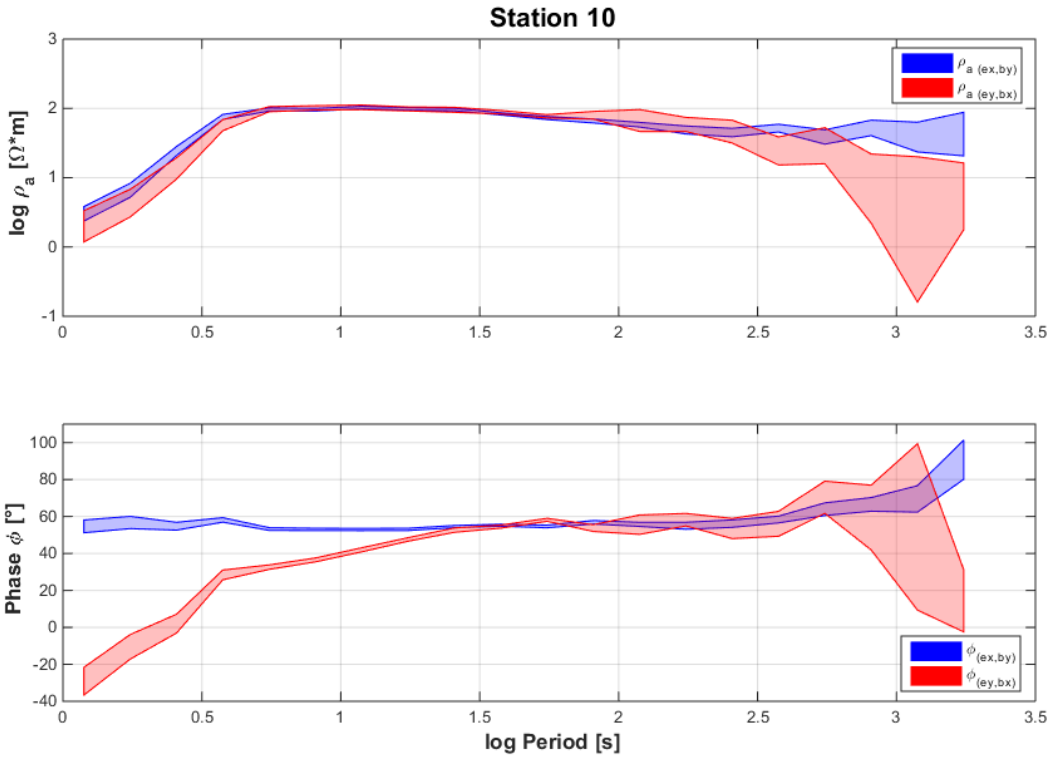

Figure 6.45: Apparent resistivity and phase - Station 10

same direction as the periods before them. Station 1 has a counter clockwise rotation in the real induction arrows with increasing periods, however at the longest periods the induction arrows have the same orientation as the three other stations.

A similar behaviour is displayed in the phase tensors, see Fig. 6.47, where the longer periods follow the pattern of the periods before with a few variations in the longest period. Station 10 has more variations in periods longer than $10^{1.5}$ s, than the other three stations.

It is interesting to see that the behaviour of the induction arrows and phase tensors in the longer periods are not deviating drastic from the behaviour of around $10^{1.5}$ s, which seems to be the boundary where other sources than the plane wave begins to be included in the data, as seen in Fig. 6.41. Whether it is a description of the subsurface or a non-uniform source field like the polar electrojet, is hard to determine. At the long periods in the induction arrows, the real induction arrow are almost identical at all four stations, which can be an indication, that either the subsurface is the same at that approximate depth, or they all experience the same contribution from the polar electrojet. All stations are within 40 km of each other, so a similar subsurface is a possibility, however the effect of the polar electrojet might also be similar. The polar electrojet is confined in a band in the north - south direction, as explained in sec. 2.2, however its location moves north and south during a substorm event, therefore not necessarily affecting the stations equally.

More investigation into the transfer functions at long periods is needed to conclude if this is a representation of the subsurface, the polar electrojet, other sources or a mixture. One way could be to compare with the single station processing result, however with

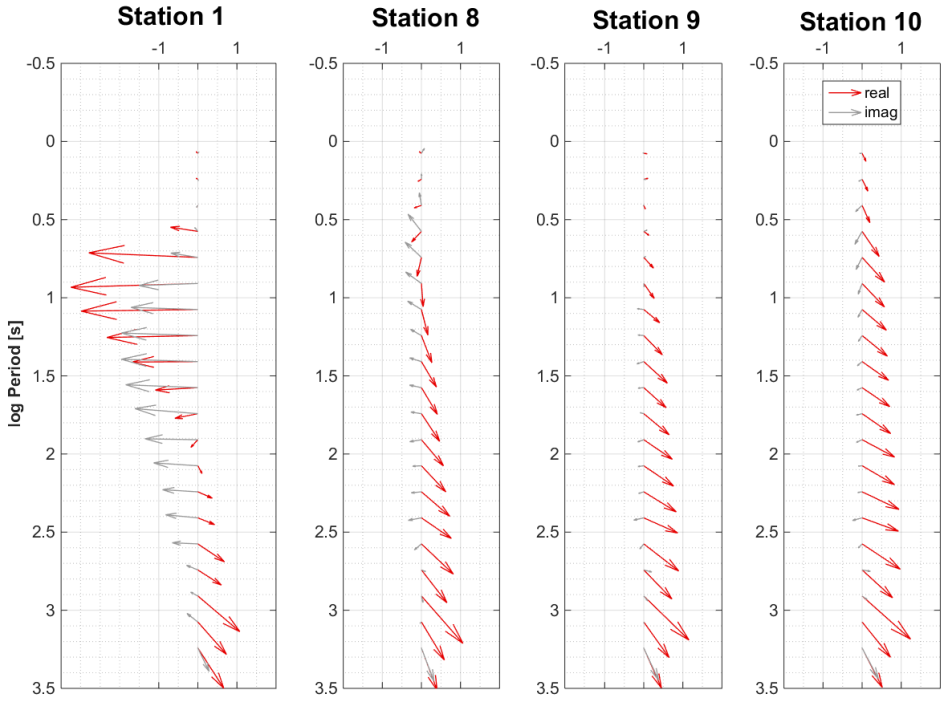

Figure 6.46: Induction arrows for station 1, 8, 9 and 10, with flexible time interval. Geographical north (up).

a careful selection of the time intervals to assure good data quality. If conducting a new measurement in Greenland, or similar Arctic locations, longer time series could possibly ensure time intervals with longer periods than $10^{1.5}$ s, which has a smaller third eigenvalue than is the situation in this investigation.

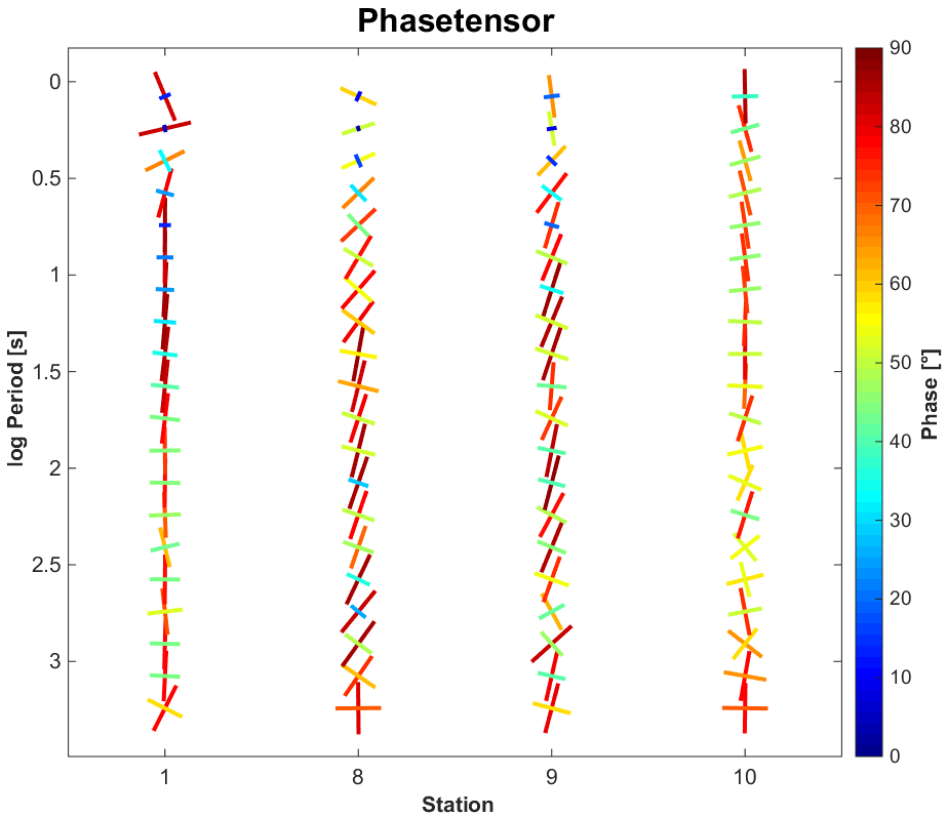

Figure 6.47: Phase tensor for station 1, 8, 9 and 10, with flexible time interval. Geographical north (up).

6.2.3 Analysis with flexible time intervals - only magnetic data

When only considering magnetic measurements, all 10 stations can be analysed together, since they have overlapping time series. EGstart is used with flexible time intervals, on the magnetic data of the 10 stations. The transfer functions are only displayed as the inductions arrows, since the impedance tensor is only available when electric fields are included in the analysis.

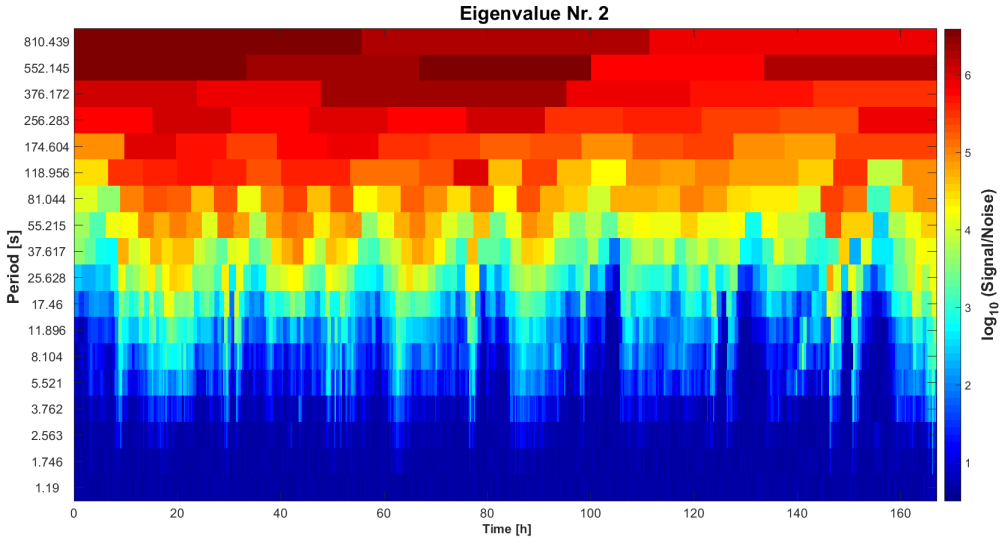

Figure 6.48: Second largest eigenvalue for all time intervals, in the magnetic analysis. The time intervals are displayed along the x-axis and the target periods along the y-axis. The colour scale illustrates the value of the eigenvalue, the signal to noise ratio. The time series begin on 20th September 2013 19:29:04 UT.s

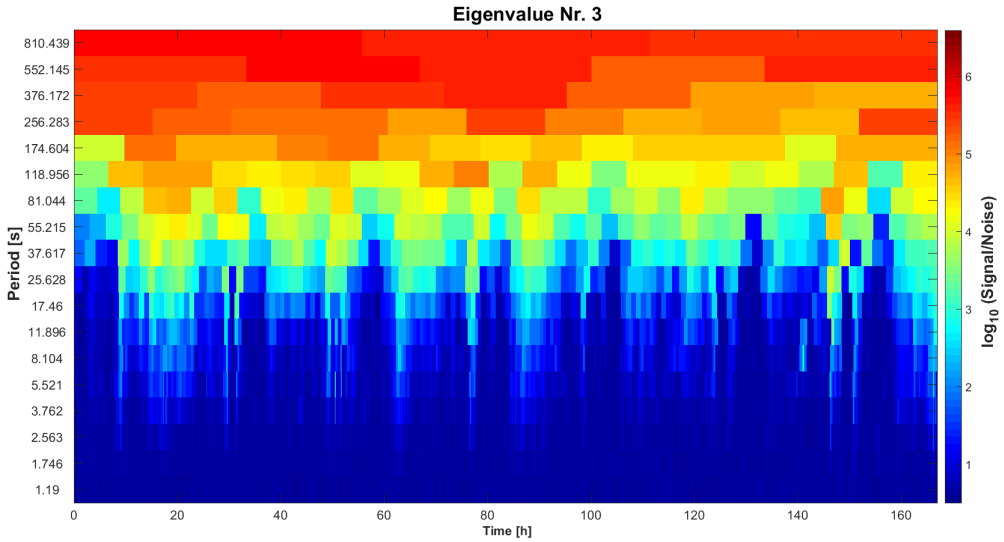

Figure 6.49: Third largest eigenvalue for all time intervals, in the magnetic analysis. The time intervals are displayed along the x-axis and the target periods along the y-axis. The colour scale illustrates the value of the eigenvalue, the signal to noise ratio. The time series begin on 20th September 2013 19:29:04 UT.s

However, the magnetic field measurements are continuous at all 10 stations for a longer period than the electric fields since all the stations have magnetic data between 20. - 27. August 2013. The eigenvalue analysis can therefore be conducted for all stations, however the result will only consists of the induction arrows, since the impedance tensor requires both electric and magnetic data to be measured simultaneously.

The comparison of the second and third largest eigenvalue in Fig. 6.48 and 6.49, shows similar results as the previous analyses in the long periods, however the third eigenvalue seems to be closer to the second eigenvalue even in the lower periods. For a better view, the median of the time intervals with the 20% highest EV-index are illustrated in Fig. 6.50.

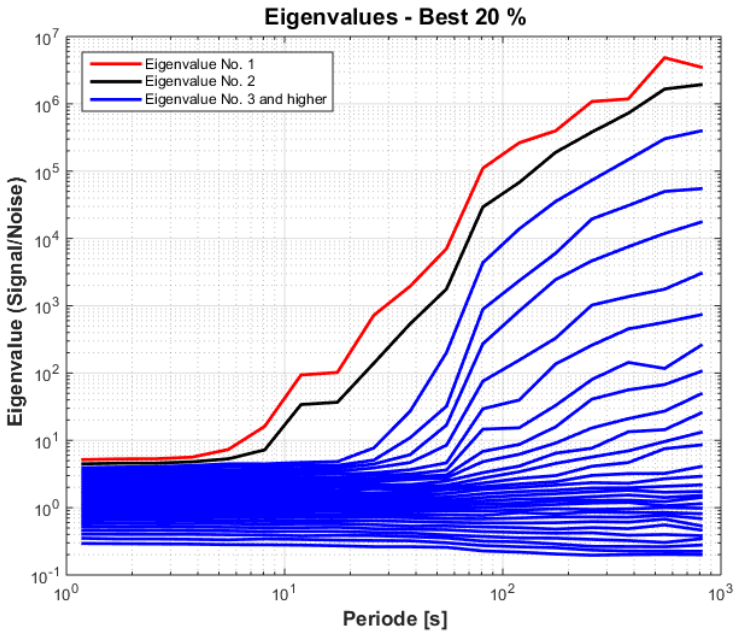

Figure 6.50: The weighted median eigenvalues of the selected 20% best time intervals, with flexible time interval in the magnetic analysis.

The signal to noise ratio is very low in the low periods for all 30 eigenvalues, compared to the previous analyses, and there are more than two dominating eigenvalues in almost all periods. Between 10^1 s and $10^{1.6}$ s there are two eigenvalues which are high compared to the other eigenvalues. This indicates that there are several sources present in the longer periods which were not present in the previous analysis. However, this analysis includes more stations which can affect the outcome. If one station has poor data it can result in a bad eigenvalue analysis since all stations are compared and therefore influence each other.

Description of transfer functions

Even though there are no dominating eigenvalues in almost all periods, the resulting induction arrows display a consistent behaviour with period without too much scatter, see Fig. 6.51 - 6.52. Again at station 1, there are large induction arrows around 10^1 s with a rotation of direction when the period increase, indicating a three dimensional subsurface. Station 2 has almost no induction arrows, an indication of a one dimensional

subsurface or at least a subsurface with very small conductivity contrasts. Station 3 contains large induction arrows in the short periods and smaller with depth. However, there is also a slight scatter in some periods. Station 4 illustrates large induction arrows before 10^1 s, where after they rotate from pointing away from south east to settle at a west direction. The imaginary arrows do not undergo a rotation, but have a constant direction towards south east. Most induction arrows at station 5 are orientated away from west, with a few pointing away from south in the shorter periods. Station 6 has a similar behaviour as station 4, though with shorter arrows. Station 7, 8, 9 and 10 have a general behaviour with arrows pointing away from west, though station 8 has a few arrows in the south direction around 10^1 s.

At all stations the induction arrows are approximately zero in periods lower than $10^{0.5}$ s, which can be explained by the extremely low signal to noise ratio also seen in the eigenvalues, Fig. 6.50.

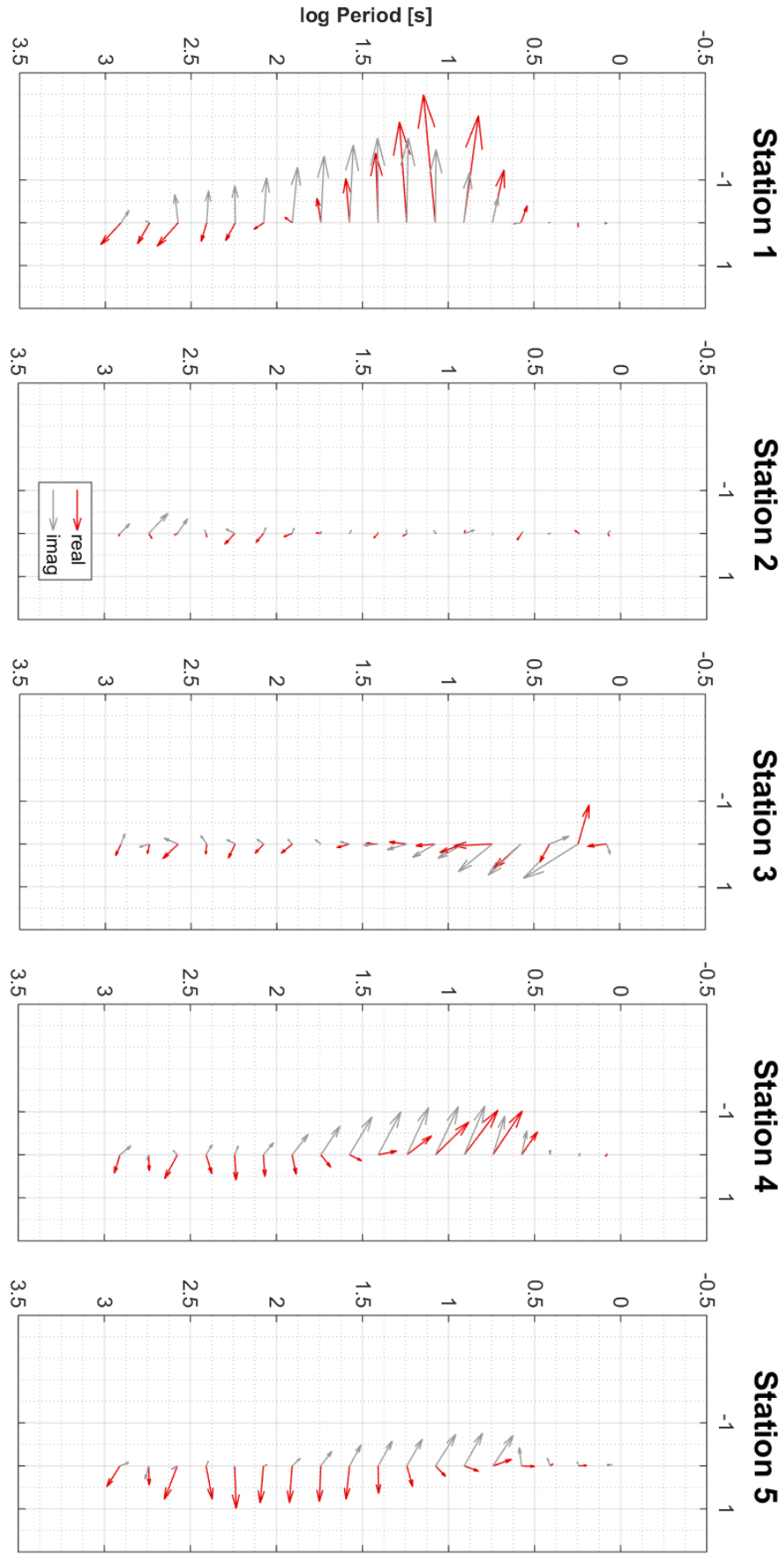

Figure 6.51: Induction arrows station 1 - 5. Geographical north (up).

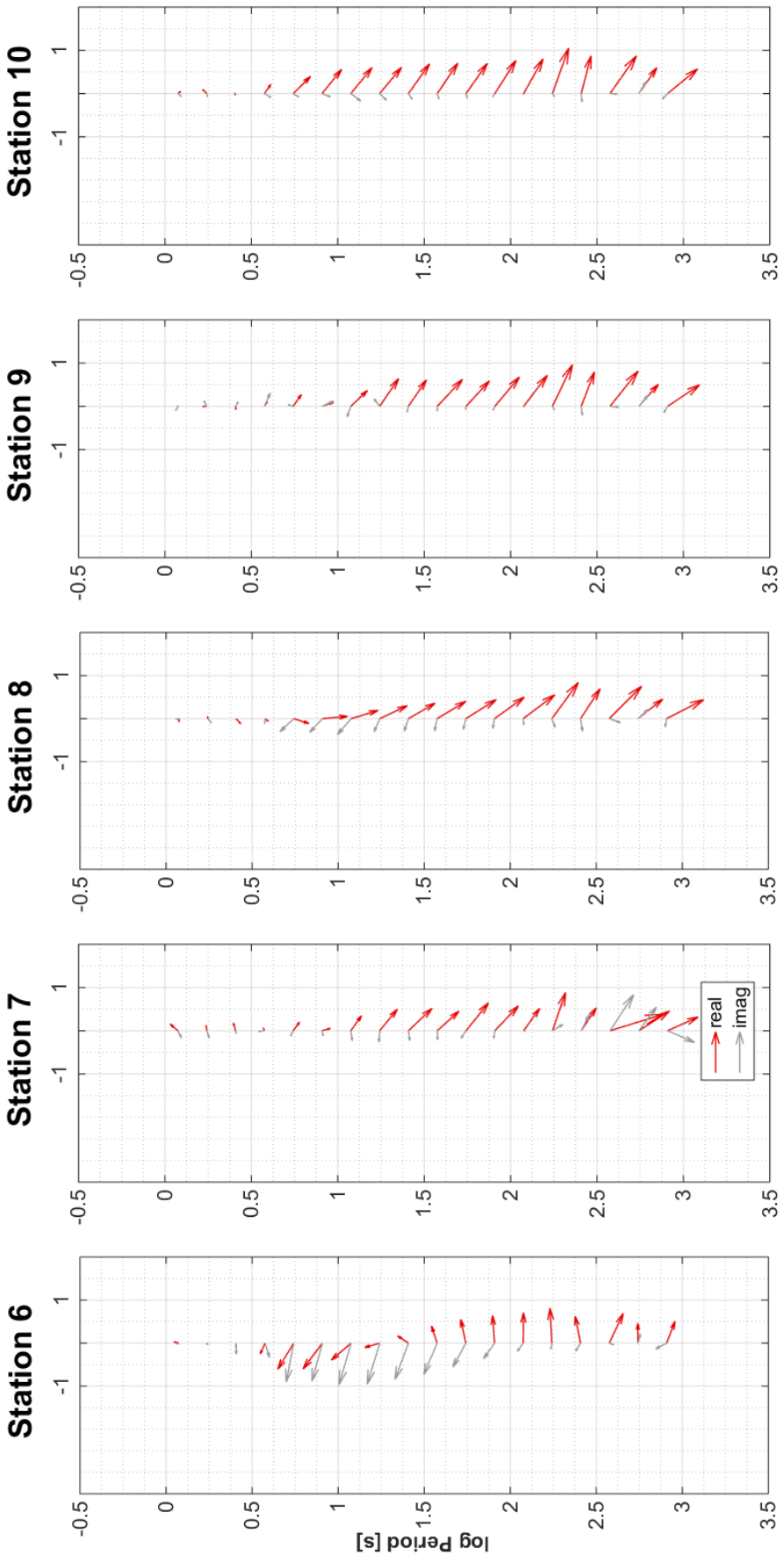

Figure 6.52: Induction arrows station 6 - 10. Geographical north (up).

6.3 Comparison

The two first sections of this chapter have presented the result obtained using two processing techniques, one set of results by a single station robust processing and three sets of results from a multiple station processing. These results with respect to each other will be discussed in the following section, beginning by comparing the three results of the multiple station processing, and afterwards comparing the results of the two processing techniques.

Comparing Fig. 6.31 - 6.36 when the time intervals are fixed, with Fig. 6.42-6.47 where they are flexible, the apparent resistivities and impedance phases illustrate the same pattern at periods shorter than $10^{1.5}$ s. However, the results in the shortest periods around 1 s differs, since these periods are within the dead band these variations can be a result of a low signal. The induction arrows are also showing almost identical results. However, at station 8 in the shortest periods there is a stronger contrast to the east in the result from the fixed time intervals than from the flexible time interval. The short periods have generally smaller induction arrows in the flexible time intervals. The phase tensors behave also identical, with exception of the shortest periods.
These two methods are expected to produce similar results since the processing scheme is identical, but the time intervals are different. The differences occur in the short periods, where the method with the flexible time intervals can select very narrow time intervals compared to the method with the fixed time intervals. However, both methods select from the criteria of the EV-index and thereby ensure the best ratio between the eigenvalues.

The third method, where only the magnetic fields have been used for the analysis, including all 10 stations, the induction arrows again show almost identical behaviour as the two previous methods, for the stations included in all three methods, station 1, 8, 9 and 10. The results in the shortest periods are again almost zero, but at longer periods the results have the same behaviour. This result is more surprising since the eigenvalues in Fig. 6.50 are extremely low in the short periods and in the longer periods are there several large eigenvalues. When there are more than two dominating eigenvalues in the data, the fear is that the data contain both information about the subsurface and about other sources, which can be artificial noise or in our situation likely the polar electrojet. The signal from the subsurface is not necessarily isolated to the two dominating eigenvalues, and therefore is the interpretation of the transfer functions from these eigenvalues something which must be performed with care. However, in this situation where the induction arrows are almost identical even though there are multiple strong eigenvalues, it could indicate that the subsurface contribution is located in the two strongest eigenvalues.

Comparing the transfer functions from the single station processing and the multiple station processing, the results are very similar. However, we do not know if both represent the subsurface or both results represent a mix of subsurface and other sources. The periods less than $10^{1.5}$ s are where the multiple station processing with fixed time intervals has two dominating eigenvalues, but their transfer functions are similar to the transfer functions of the single station processing. This could indicate that a selection in these periods might not be as important as for other periods and that the standard robust processing or multivariate processing is sufficient. However, the multiple station processing with fixed time intervals secures a better result in the short

periods, with a higher signal to noise ratio. At longer periods it is more uncertain if any of the results is actually representative of the subsurface alone, since the multiple station processing has several large eigenvalues, and the single station processing shows variation with time in the impedance tensor, see e.g. Fig. 6.3. More investigations have to be performed to see if any of the methods represent the true subsurface. Previous research has shown that robust processing without data editing, can reduce the effect of a non-uniform source field if the data is not strongly contaminated, when dealing with data collected in the polar regions [Garcia et al., 1997]. However, Jones and Spratt [2002] found that robust processing where all data, measured in the polar regions, are included fails to describe the subsurface. Therefore caution must always be taken, when evaluating data from polar regions. The multiple station processing must undergo further investigations to ensure if it actually can be usable at longer periods for data collected in polar regions. This might be the situation if the two highest eigenvalues contain the subsurface response alone, even though there are several large eigenvalues, as in the analysis with the magnetic data from all 10 stations.

Chapter 7

Forward Modelling

The transfer functions presented in chap. 6 represent a specific subsurface volume. To estimate the true resistivity structures, forward modelling of the observed transfer functions has been performed and available information has been included as a priori information in the model. Additionally, a model study of fjords' impact on induction arrows is presented, from which important information can be deduced for the observed data modelling. The modelling is performed with a combination of COMSOL Multiphysics [v. 4.4, 2015] and MATLAB [R2013a, 2015] through a LiveLink connection for the data modelling and with COMSOL Multiphysics [v. 5.1, 2015] for the fjord model study.

COMSOL is a 3D simulation and modelling software. For the model construction a Cartesian coordinate system (x, y, z), with x and y spanning the horizontal plane and z is the height, positively upwards, is used. The Finite Element Method is used for solving the partial differential equations, such as Maxwell's equations presented in chapter 3. The finite element method approximate the partial differential equations with discrete solutions at selected points in the model [Brenner and Scott, 2007].

To set up a model in COMSOL Multiphysics [2015], three main steps are required. Construct a geometry, build a mesh and apply the boundary conditions to the model. These steps will be explained in the following section. First, a simple geometric model is build as seen in Fig. 7.1, which consists of two boxes. The top box, (1), represents the air above the surface and the bottom box (2) describes the subsurface. The dimensions of the box are set to approximately 3 - 4 times the skin depth of the evaluated period, to avoid boundary problems, as explained later. In each box a 3D tetrahedral mesh is defined, which consists of a finite amount of elements, grid cells, that are linked though discrete points, nodes. In these nodes, the partial differential equations are solved, and in between the points the values are linearly interpolated. The grid cells are tetrahedrals and differ in size de-

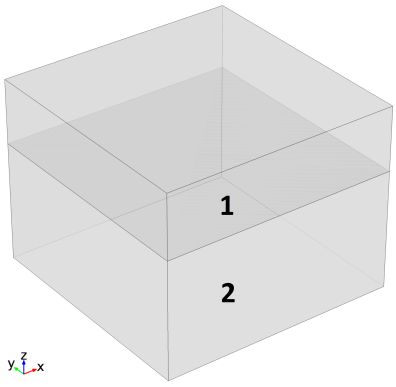

Figure 7.1: Geometric model set up. (1) isolating air box, and (2) box containing the subsurface.

pending on their location. The mesh is fine close to the investigation area, and coarser towards the outermost boundaries.

A magnetic source field is applied to the model volume, which consists of two orthogonal polarisations. From these polarisations, the total model response is calculated. Depending on the polarisation direction, the boundary conditions for the sides of the model volume are a perfect electric conductor parallel, and a perfect magnetic conductor orthogonal to the polarisation direction of the magnetic field, see Fig. 7.2. These settings allow the fields to be continuous at the boundaries.

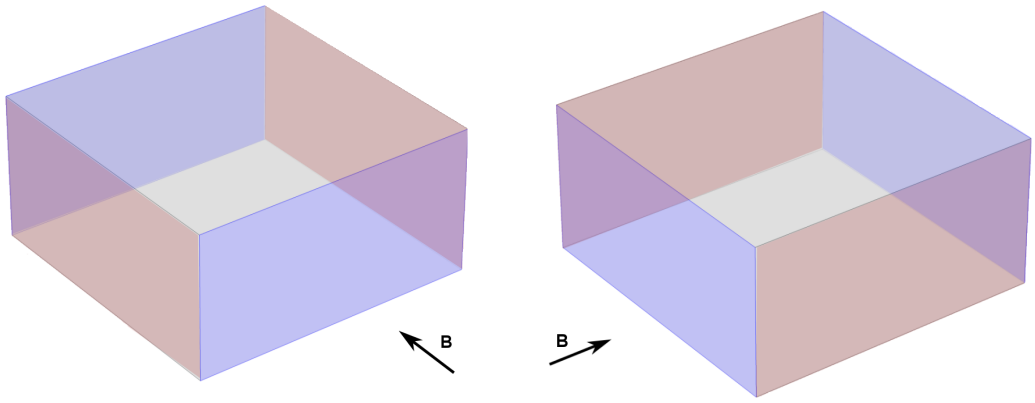

Figure 7.2: Boundary conditions of the sides of the model volume. The boundary conditions are perfect electric conductor parallel and a perfect magnetic conductor orthogonal to the polarisation direction of the magnetic field.

The uppermost boundary of the model volume is set to be a *scatter boundary*, at which the source plane wave magnetic field is defined. The bottom boundary is an *Impedance boundary*, which has a resistivity equal to the resistivity of the background set in the subsurface box, see Fig. 7.1, $\rho = \rho_{bg}$.

7.1 Model study

Oceans can have a large impact on magnetotelluric transfer functions [Fischer, 1979; Parkinson, 1959]. The area of the magnetotelluric fieldwork presented in this project, is penetrated by large fjord systems reaching over 100 km inland, see Fig. 4.2. These fjords are connected to the ocean and hence contain seawater. A model study has been conducted, to investigate how the seawater in such a fjord affects the induction arrows on land.

The modelled fjord is set in a the geometric model as depicted in Fig. 7.3, where the size and location of the fjord is fixed in all evaluated periods. It has a total length of 29 km, the part of the fjord in the x direction is 20 km and the bended part of the fjord is 9 km. Several models are created in this study, one model for each decade. The width and length of the fjord is fixed in each model, so that the responses of the fjord can be compared. The dimensions in Fig. 7.3 represent one of these models, with a width of 2 km and a depth of 200m, at the period of 1 s. The position of ocean at the end of the fjord is fixed so the two objects are always connected, however the ocean expands when the model changes and increases its dimensions. It expands together with the

background box in the directions away from the fjord. The height of the ocean box is set to 2 km.

Besides the fjord, the model consists of a background box wherein the other objects are embedded, such as a top layer containing a cylinder with a fine mesh close to the area of interest. These objects depend on the period that is evaluated. For each decade, the model is resized depending on the highest period within the decade, T_{max}, and the highest resistivity in the model, ρ_{max}. The background box has a width, height and length equal to three times the skin depth, δ, of the highest period and highest resistivity, $3 \cdot \delta_{max}$, as given in eqn. 3.27. The top layer has the same dimensions in width and length, but the height is set to be 5000 m. The high resolution cylinder in the centre of the model, has a radius of $1 \cdot \delta_{max}$ and a height of 5000 m. On top of the geometric model, visible in Fig. 7.3, an air box is located to avoid any boundary effects close to the area of interest, as in Fig. 7.1. The resistivity of the fjord and ocean is $0.25\ \Omega m$, the background, top layer and high resolution cylinder have a resistivity of $500\ \Omega m$ and the air box on top is set to be isolating with a resistivity of $10^7\ \Omega m$.

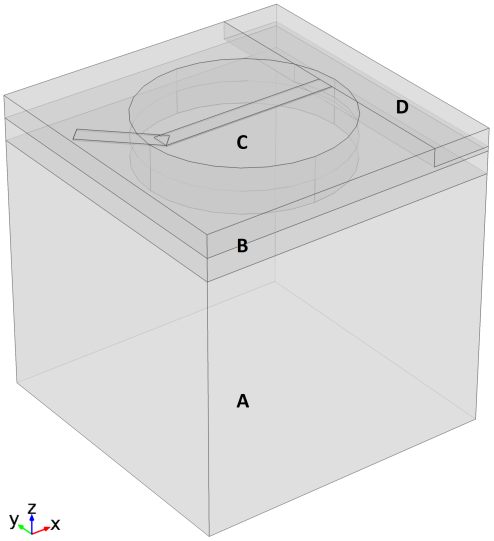

Figure 7.3: Geometric model volume used in model study, for the period of 1 s. (A) Background, (B) top layer (C) high resolution cylinder and (D) ocean box attached to the fjord.

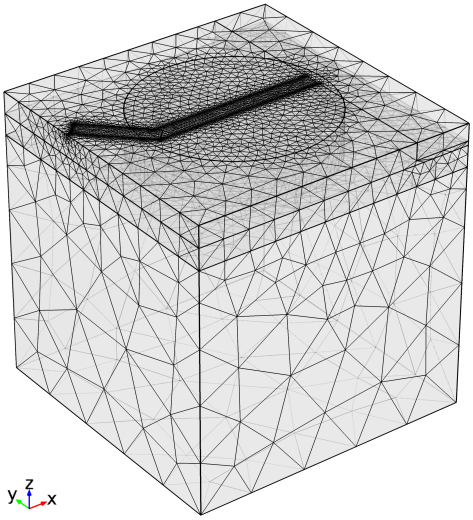

Figure 7.4: Mesh in the model volume, for the period of 1 s.

The mesh generated for this model study depends on the object. The modelled fjord has a very fine mesh, the cylinder has a fine mesh and further away from the fjord the mesh will be coarsening towards the boundaries of the model volume. The boundaries of each tetrahedral in the different objects are displayed in Tab. C.1 in App. C.1.

In the first approach, a bended fjord with and without connection to the ocean is investigated [Lauritsen et al., 2015]. Moreover, it is investigated how the impact changes depending on the geometry of the fjord. COMSOL Multiphysics [2015, v. 5.1] has been used to perform the modelling as explained in the beginning of the chapter. The model fjord has a rectangular cross section as depicted in Fig. 7.5, with a resistivity of 0.25 Ωm for the seawater, 500 Ωm for the background geology and 10^7 Ωm for the air

above. The width and the depth of the fjord varies in the different set ups.

Fig. 7.6 illustrate a bended fjord with a width of 2 km and a depth of 200 m. It is isolated with no connection to the ocean, and evaluated in the three different periods of 1 s, 10 s and 100 s. The background colour represents the magnitude of the tipper.The strongest tipper magnitude and therefore the largest induction arrows are concentrated along the shoreline, but especially on the inside of the bend. The induction arrows are illustrated in the Wiese convention [Wiese, 1962], thus pointing away from conducting zones. The induction arrows along the shoreline are with large values above 1 at 1 s, which is the limit that is normally expected from geology [Williams and Rodriguez, 2001]. At longer periods, the tipper magnitude decreases and becomes negligible at 100 s. However, if the fjord is not isolated but connected to the ocean, the effect on the induction arrows changes drastically. Fig. 7.7 illustrate an identical bended fjord as in Fig. 7.6, but with a connection to the 2 km deep ocean. At 1 s, the largest tipper magnitude has shifted closer to the ocean, with the highest value being twice as large as the value in the bend, where the value is similar to the value in the previous situation without the ocean. The main difference between the two scenarios can be observed along the shoreline. The tipper magnitude and induction arrows are very large all along the shoreline, whereas for the fjord without the ocean, it decreases when moving away from the bend. For the period of 10 s, the magnitude is approximately the same in the bend as without the ocean, but the induction arrows are larger. When moving to longer periods, 100 s, the induction from the fjord is completely disguised in the induction originating from the ocean. It is clear from this investigation that the induction from a fjord is very high in low periods, and it can transverse further into a larger fjord system when connected to the ocean. This induction originates from currents being channelled from the ocean into the fjord [Jones, 1983; Simpson and Bahr, 2005], as seen in Fig. 7.8. The induction arrows along the shoreline, far from the ocean are caused by the transition from highly conducting sea water to the resistive land. Contrary, at the entrance of the fjord the electric currents induced in the seawater are strongly distorted. They act as a line current at the surface of the earth producing a high ratio of the vertical to the horizontal magnetic field according to Ampères law eqn. 3.5.

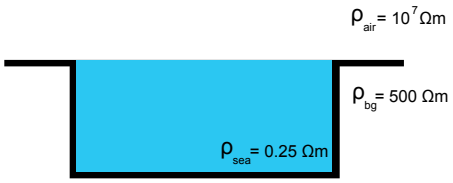

Figure 7.5: Cross section of the fjords and resistivity of the seawater, background and air.

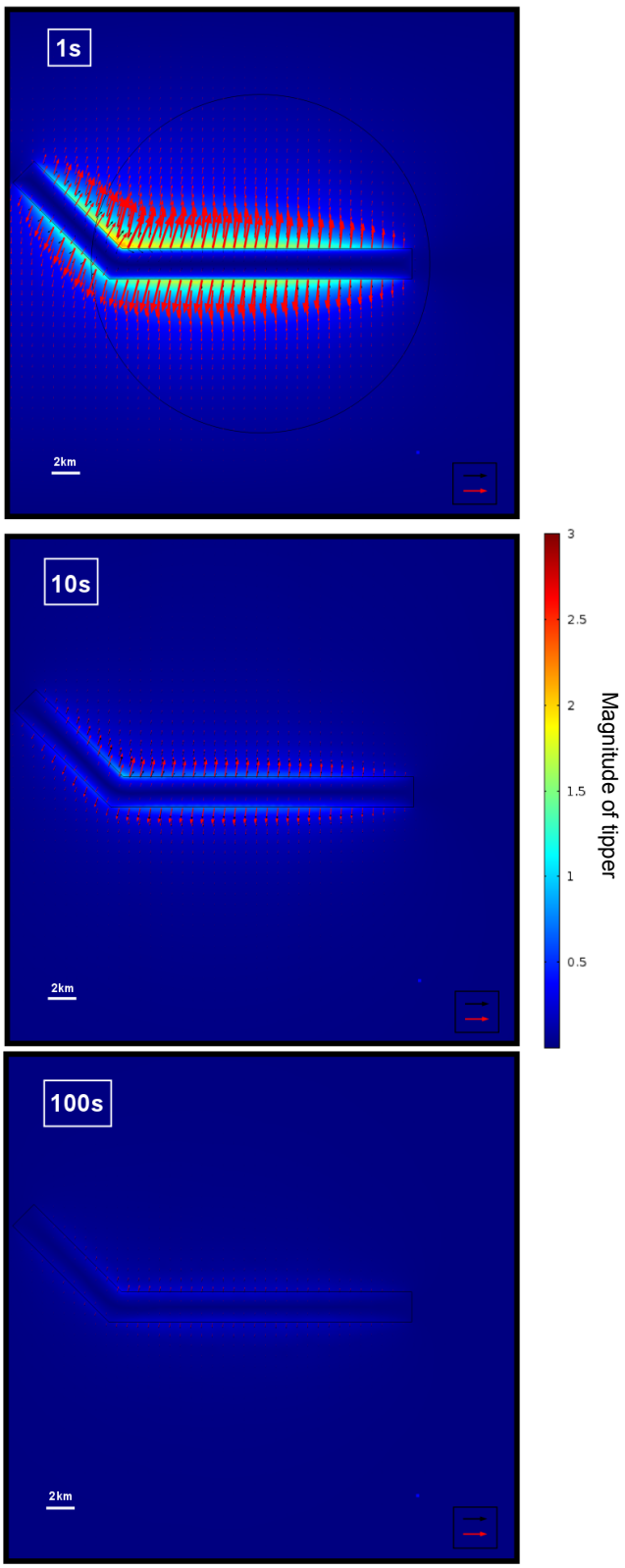

Figure 7.6: 2 km wide and 200 m deep fjord without connection to the ocean (plane view). Real (red) and imaginary (black) induction arrows. A unit vector is placed for scale in the bottom right corner. The colour scale illustrates the total magnetic field.

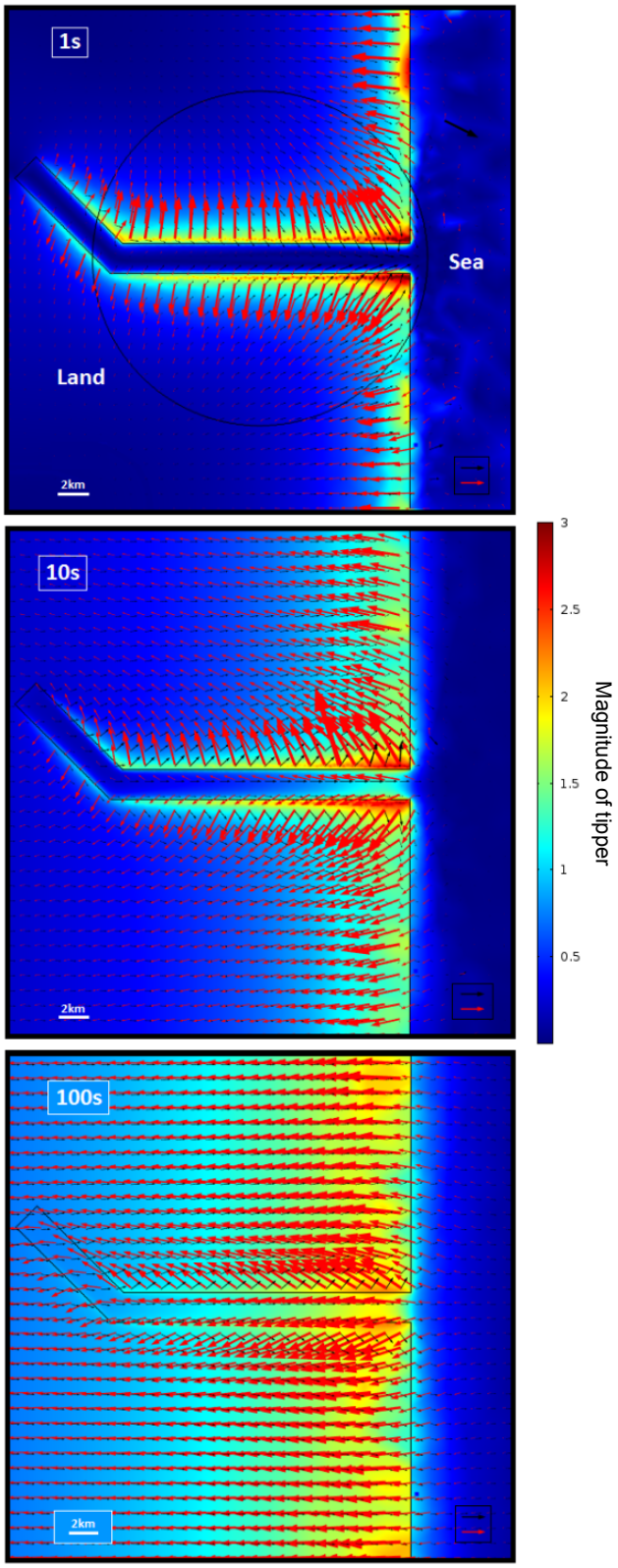

Figure 7.7: 2 km wide and 200 m deep fjord with connection to the ocean (plane view). Real (red) and imaginary (black) induction arrows. A unit vector is placed for scale in the bottom right corner. The colour scale illustrates the magnitude of the tipper.

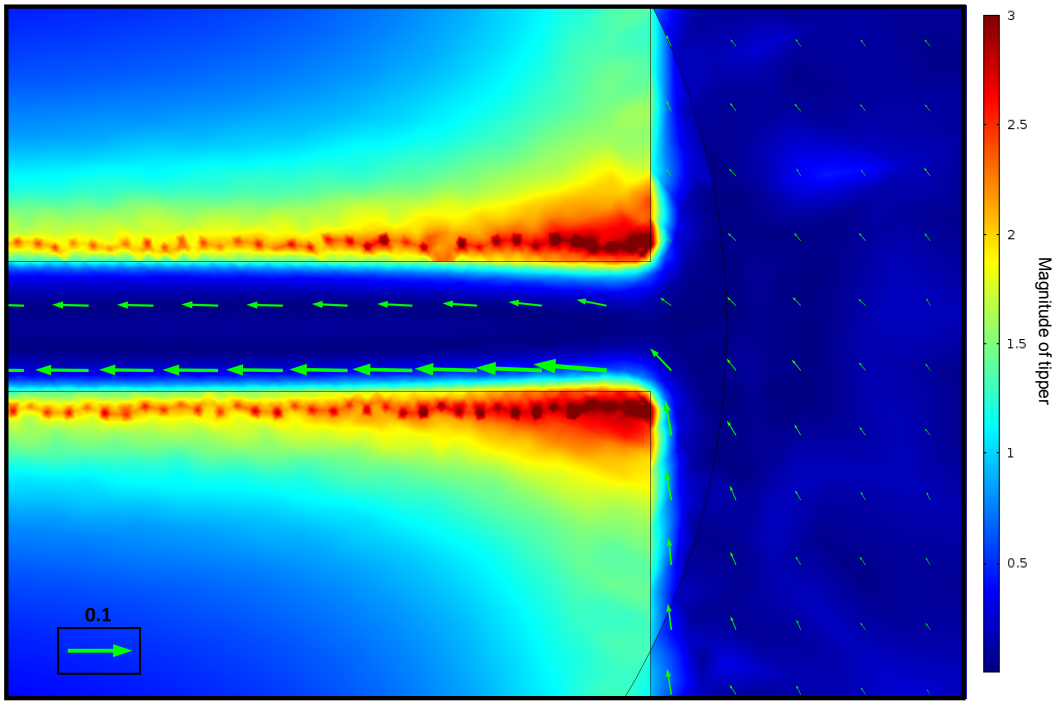

Figure 7.8: Currents (green arrows) channelled from the ocean into a fjord are greatly increased in magnitude. This illustrate the fjord in Fig. 7.7, zoomed in. A scale is visible in the bottom left corner.

The connection to the ocean is important when determining the impacts from fjords, however the geometry of the fjord can also have an effect. Fig. 7.7 - 7.11 illustrate four different geometries, the first being the already studied fjord of 2 km width and 200 m depth. The other geometries are compared to this first set up and discussed.

The geometry of the four different fjords are specified below, and they are evaluated in the three different periods 1 s, 10 s and 100 s:

- Fig. 7.7 illustrate a bended fjord with a cross section 2 km wide and 200 m deep.
- Fig. 7.9 illustrate a bended fjord with a cross section 2 km wide and 500 m deep.
- Fig. 7.10 illustrate a bended fjord with a cross section 10 km wide and 200 m deep.
- Fig. 7.11 illustrate a basin of 10 km width and 200 m depth connected to the ocean via a narrower fjord of 2 km width and 200 m depth.

The overall behaviour of the induction arrows for all the different fjords, are as described for Fig. 7.7, where at 1 s the contribution from the ocean is only noticeable at the shoreline very close to the ocean, but along the fjord the channelling of currents from the ocean into the fjord give rise to large induction arrows. Increasing the period to 10 s, the channelling along the shoreline of the fjord decreases, but the effect from the ocean increases in areas where there before were almost no induction arrows. For 100 s the channelling in the fjord is diminished considerable and the contribution from the

ocean is dominating. However, depending on the geometry this description might vary slightly. Fig. 7.9 illustrates a similar fjord as Fig. 7.7, with a modified depth of 500 m. The tipper magnitude along the fjord is lower for the period of 1 s and 10 s compared to the fjord with a depth of 200 m, but almost indistinguishable at 100 s where the contribution from the ocean is dominating. If the width of the fjord is extended to 10 km and the depth is kept at 200 m, as illustrated in Fig. 7.10, the induction arrows are again large in the corner towards the ocean and the tipper magnitude is now larger than in the fjord of 2 km width. However, the behaviour is still similar, with the channelling of currents decreasing along the shore line away from the ocean. Often the fjord does not have a similar width everywhere, which can change the channelling impact, as seen in Fig. 7.11. This fjord has a larger seawater basin of 10 km width to the left and the ocean to the right. The induction arrows are still largest near the ocean, but they are large all along the narrower fjord until the basin. Even at the corner to the basin the induction arrows are larger than at the middle of the narrow fjord. This illustrates that the effect is maintained almost constant along the narrow fjord, due to the presence of a seawater basin at the opposite end of the fjord.

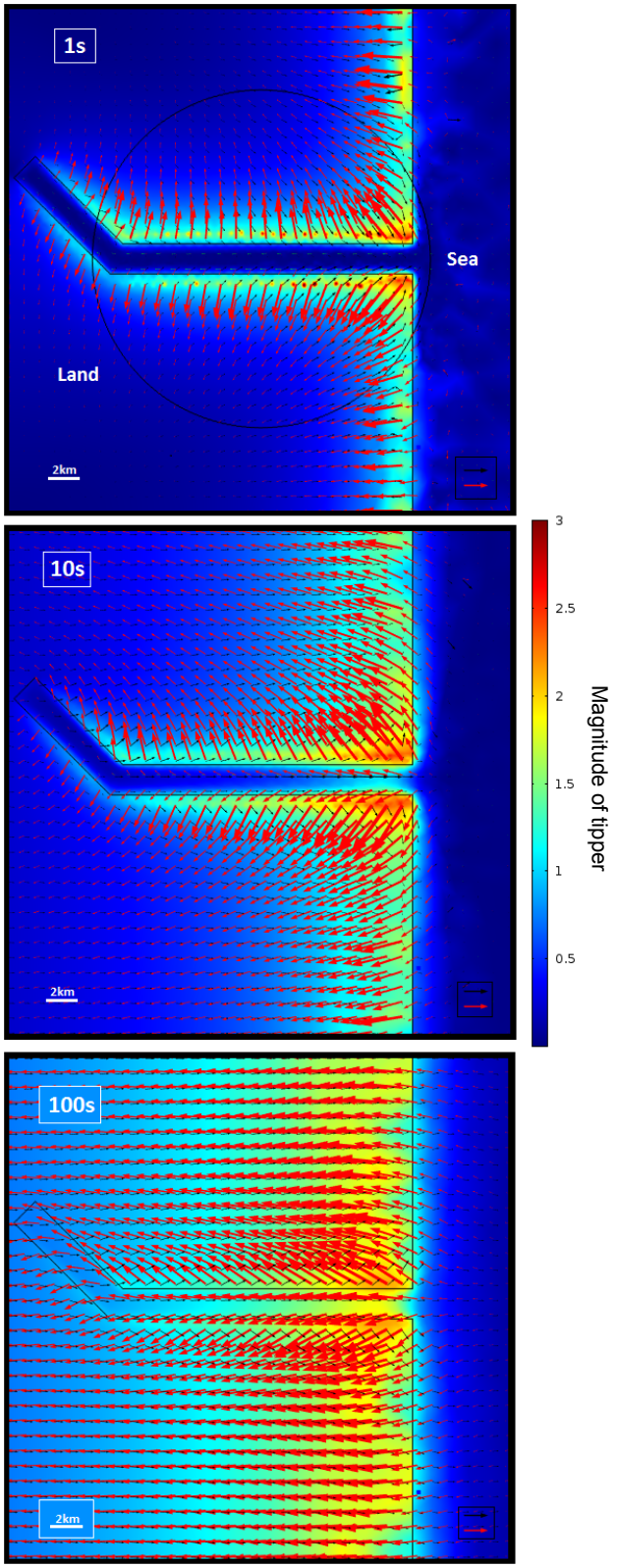

Figure 7.9: 2 km wide and 500 m deep fjord with connection to the ocean (plane view). Real (red) and imaginary (black) induction arrows. A unit vector is placed for scale in the bottom right corner. The colour scale illustrates the magnitude of the tipper.

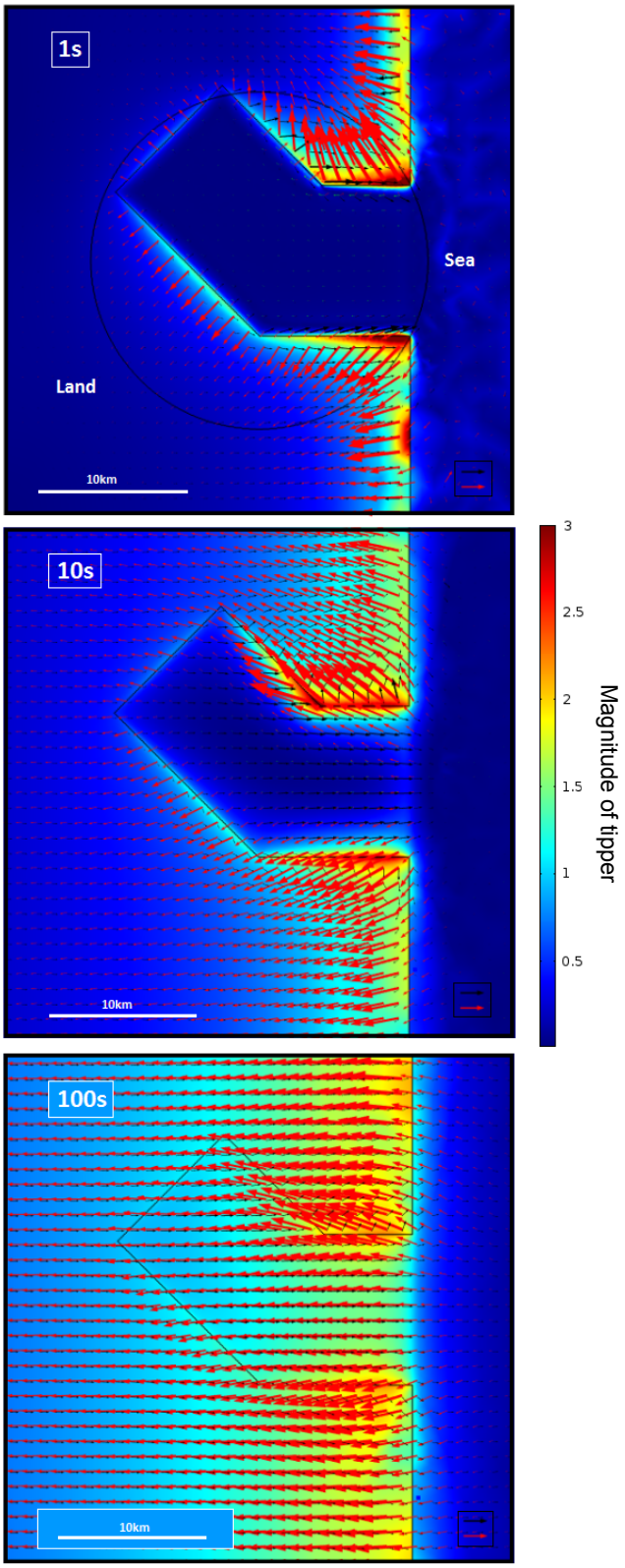

Figure 7.10: 10 km wide and 200 m deep fjord with connection to the ocean (plane view). Real (red) and imaginary (black) induction arrows. A unit vector is placed for scale in the bottom right corner. The colour scale illustrates the magnitude of the tipper.

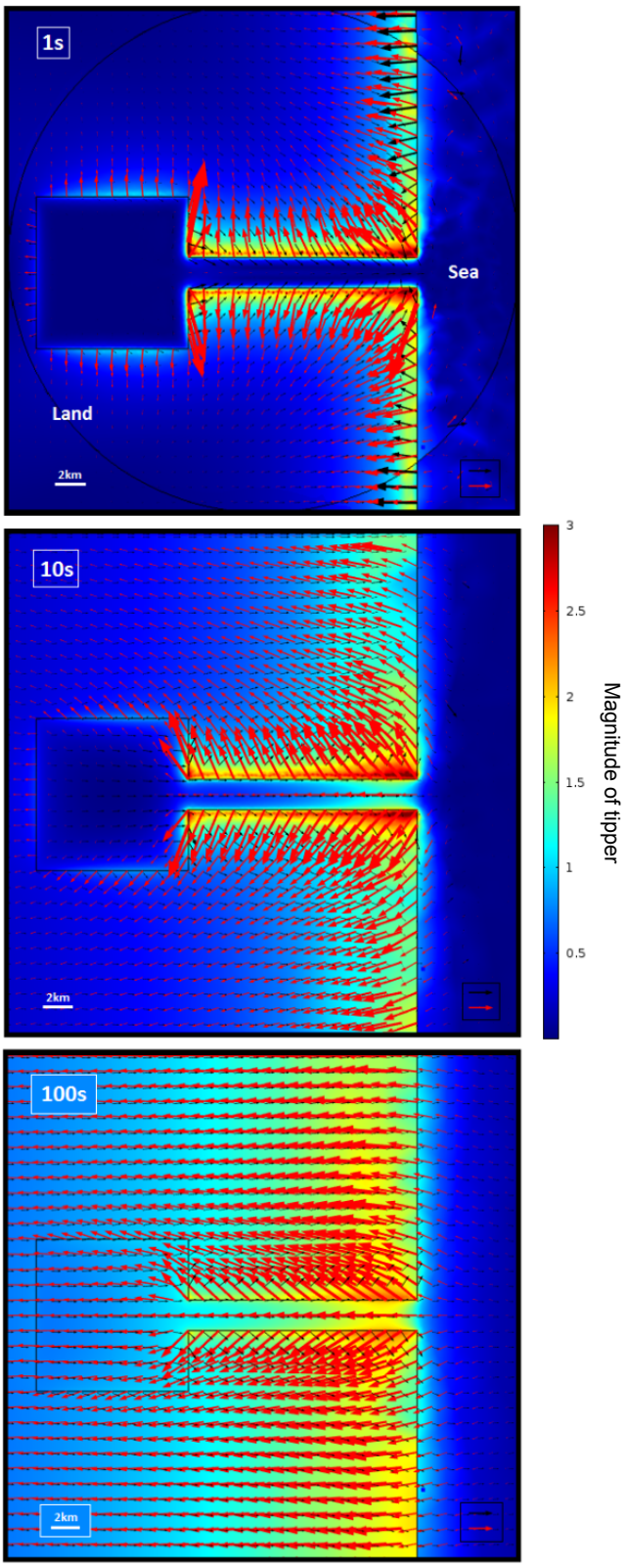

Figure 7.11: 10 km and 2 km wide fjord with a depth of 200 m, with connection to the ocean (plane view). Real (red) and imaginary (black) induction arrows. A unit vector is placed for scale in the bottom right corner. The colour scale illustrates the magnitude of the tipper.

7.2 Ocean and fjord modelling

The three dimensional forward modelling of the measuring area is performed with the software "MT3D" developed at Frankfurt University [Löwer, 2014], which uses a combination of COMSOL Multiphysics [v. 4.4, 2015] and MATLAB [R2013a, 2015] through a LiveLink connection.

The geometric model for this forward modelling is similar to that of Fig. 7.1. The subsurface box contains three concentric half spheres as illustrated in Fig. 7.12. The size of the box and the half spheres depend on the skin depth, δ, of the highest resistivity, ρ_{max}, and the lowest resistivity, ρ_{min} in the model, for the evaluated period. For each period and each station, a new model is created. ρ_{max} and ρ_{min} can be determined from the resistivity distribution in the constructed model, or can be set manually to receive a specific geometric size for the model volume. In this model they were set manually to, $\rho_{max} = 1000\ \Omega m$ and $\rho_{min} = 10\ \Omega m$, to ensure the model is large enough when including the ocean bathymetry and to account for small conductive anomalies beneath the investigated area. [Cembrowski, 2016, personal conversation]. The subsurface box has a width and length of $6 \cdot \delta_{max}$ and a height of $3 \cdot \delta_{max}$. The three half spheres have a radius of δ_{min} for the inner sphere (1), $3 \cdot \delta_{min}$ for the second sphere (2), and $1.5 \cdot \delta_{max}$ for the outermost sphere (3) [Löwer, 2014]. A tetrahedral mesh is defined within the model volume with a fine mesh in the center and coarsening towards the boundaries of the volume, see Fig, 7.13. The size of the tetrahedral elements are dependent of the maximum and minimum skin depths, and their maximum element size and growth rate are shown in Tab. C.2 in App. C.1.

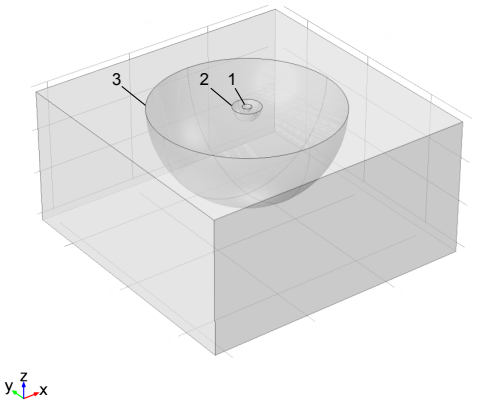

Figure 7.12: Geometric model volume of the forward modelling.

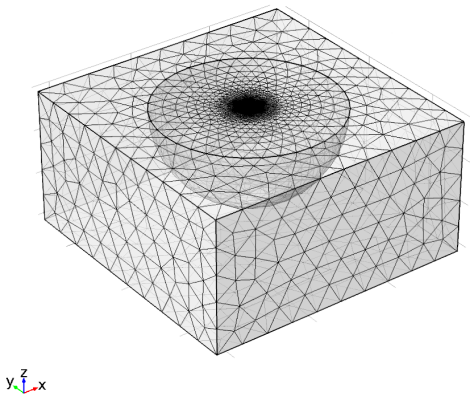

Figure 7.13: Mesh of the forward modelling.

An a priori resistivity model is constructed by defining the resistivity values on a fixed number of support points. The resistivities of the values of the support points are linearly interpolated onto the mesh of the model volume. Outside the spheres a constant background resistivity is ascribed to the mesh. The forward modelling is then performed for each period and each station or location for the geometrical scheme mentioned above.

The oceans are conductivity anomalies whose dimensions and resistivities are well known and can therefore be included in the model as a priori information. The bathymetry of

the ocean was supplied by GEBCO world map, IOC, IHO and BODC [2003]. Instead of varying ocean depths and a constant resistivity of 0.25 Ωm, the oceans are set to 2 km depth near the coastline to account for the shallow seawater and to 10 km far away from the coast, due to computational reasons. To keep the true conductance of the oceans, the resistivity varies depending on the true ocean depth.
Besides including the ocean in the a priori model, several anomalies representing the fjord system of the measuring area are also included. They are also included via a fine grid of support points along the edges of the shoreline and interpolated onto the mesh of the subsurface model. Since no bathymetry or similar data is available, the geometry of the fjords is estimated from satellite images via Google Earth. The depth of the fjords is unknown, since no depth measurement has been performed in this area, and are therefore set to a constant depth of 200 m.

Based on the results from the model study in sec. 7.1, which illustrate the effect of fjords on transfer functions, the fjord system of the measuring area was, as well as the ocean, incorporated into the model. Fig. 7.14 - 7.16 illustrate the resistivity model of the ocean and fjords, at two periods, 1.2 s and 55 s, which is the shortest and longest period evaluated in the EGstart analysis with fixed time intervals.

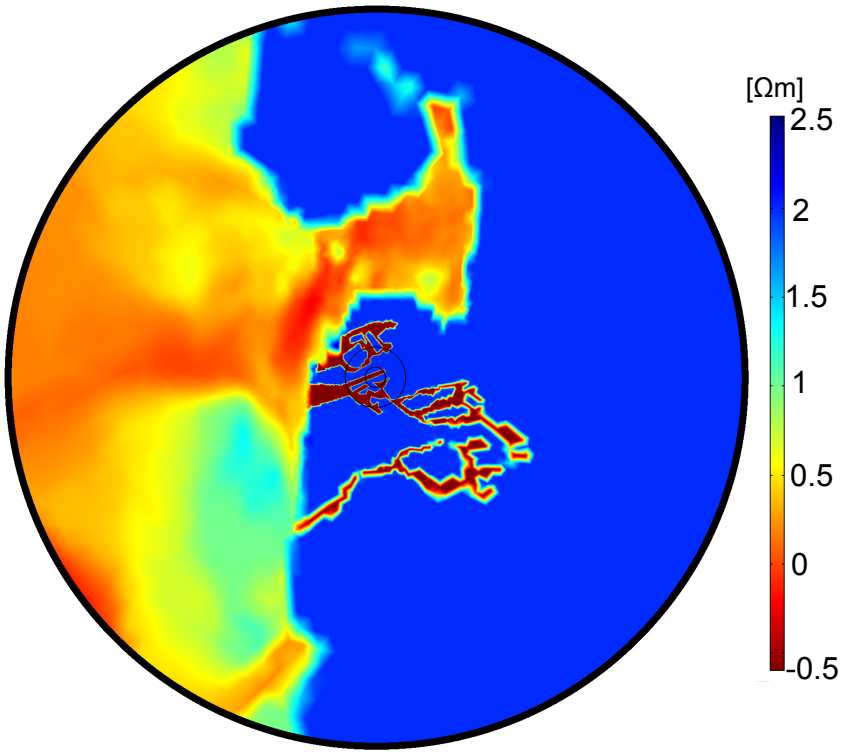

Figure 7.14: Resistivity model centred at station 10, for period 55 s, inside the three half spheres. Blue represent resistive material, whereas red represent conductive material. Presented in Lauritsen et al. [2015] in reversed colour scale.

Even with this simple model with a homogeneous subsurface and only the ocean and fjords to affect the transfer functions, the apparent resistivities and impedance phases are complex, see Fig. 7.17 - 7.20. The following transfer functions are displayed in the same reference frames as the results in sec. 6, where the apparent resistivity and impedance phase are visible in the geomagnetic reference frame, and the induction arrows and phase tensors are displayed in the geographical reference frame.

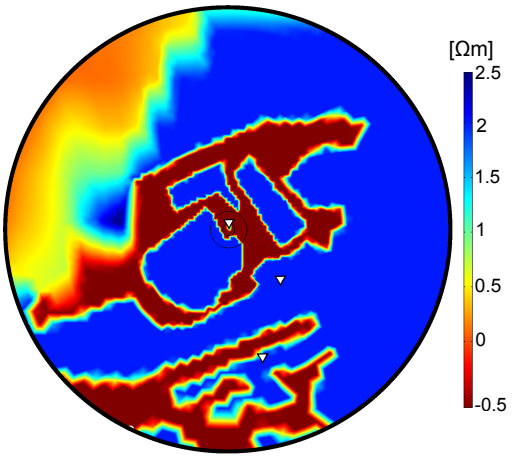

Figure 7.15: Resistivity model centred at station 8, for period 1.2 s, inside the three half spheres. Blue represent resistive material, whereas red represent conductive material. The triangles indicate the location of station 8, 9 and 10 (from North to South).

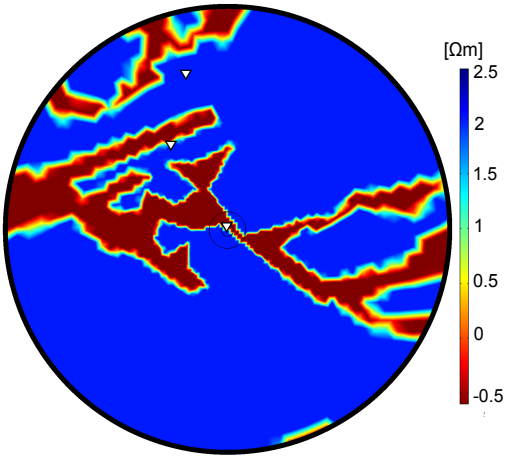

Figure 7.16: Resistivity model centred at station 1, for period 1.2 s, inside the three half spheres. Blue represent resistive material, whereas red represent conductive material. The triangles indicate the location of station 9, 10 and 1 (from North to South).

In all the resistivities and phases there are a split, which is expected with stations located extremely close to a resistivity contrast, though the split is larger at some stations then others. Station 1 has a narrow split in the resistivities and the phases beginning with a split of 25° and ends with a $< 5°$ split at $10^{3.2}$ s with phase values of approximately 45°. An explanation could be the very narrow fjord model, as seen in Fig. 7.16, where the phases is in the short periods detects the close fjord and in the longer periods they detects the homogeneous background with a resistivity of 100 Ωm. Station 8 has a large split in the resistivities, which is consistent with the large body of water in its vicinity, see Fig. 7.15. In this model, station 9 is located at some distance to the water, see Fig. 7.15 and 7.16. This can explain the narrow split between the resistivities. The location in the true world is on the shoreline of a fjord, see for example Fig. C.1, however, the fjord model has been insufficient to capture the true fjord geometry close to station 9. This is seen in the phases, which vary very slightly around 45° in the short periods, illustrating a 1D subsurface, but splitting from each other in the longer periods when they detect the fjord. Similar to station 1, a narrow split is visible at station 10 which decrease until the longest period, where the resistivities are near the value of the background resistivity of 100 Ωm. The phases have a small split varying between 12° and 2°. There are a few data points in the resistivities and phases which differs drastically from the neighbouring data points, for example both resistivities at station 1 around 10^2 s. This is caused by numerical problems, where the mesh is to coarse at longer periods to resolve the narrow fjords. Similar data points are visible in station 8 and 10.

The impact of the fjords is also clearly visible in the induction arrows. As illustrated in Fig. 7.21 at station 1, the induction arrows can become extremely large when the station is at the shoreline of a fjord, which confirms the result from the model study in

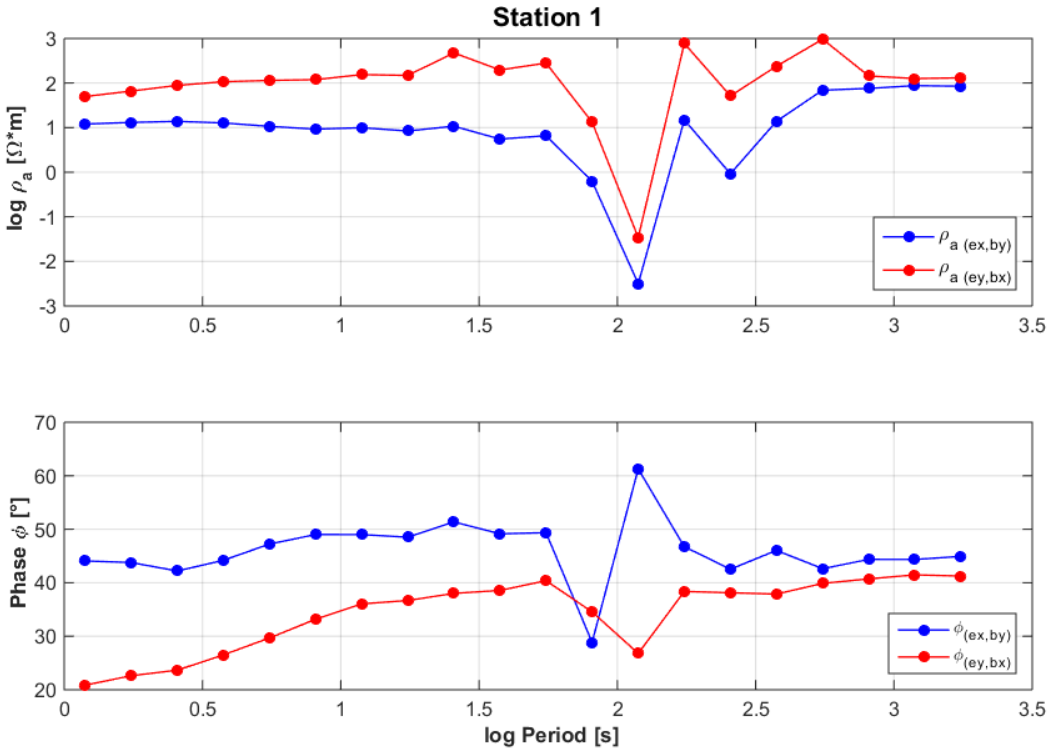

Figure 7.17: Apparent resistivity and phase - Station 1 - bathymetry and fjord model. They have been rotated and are displayed in the geomagnetic reference frame.

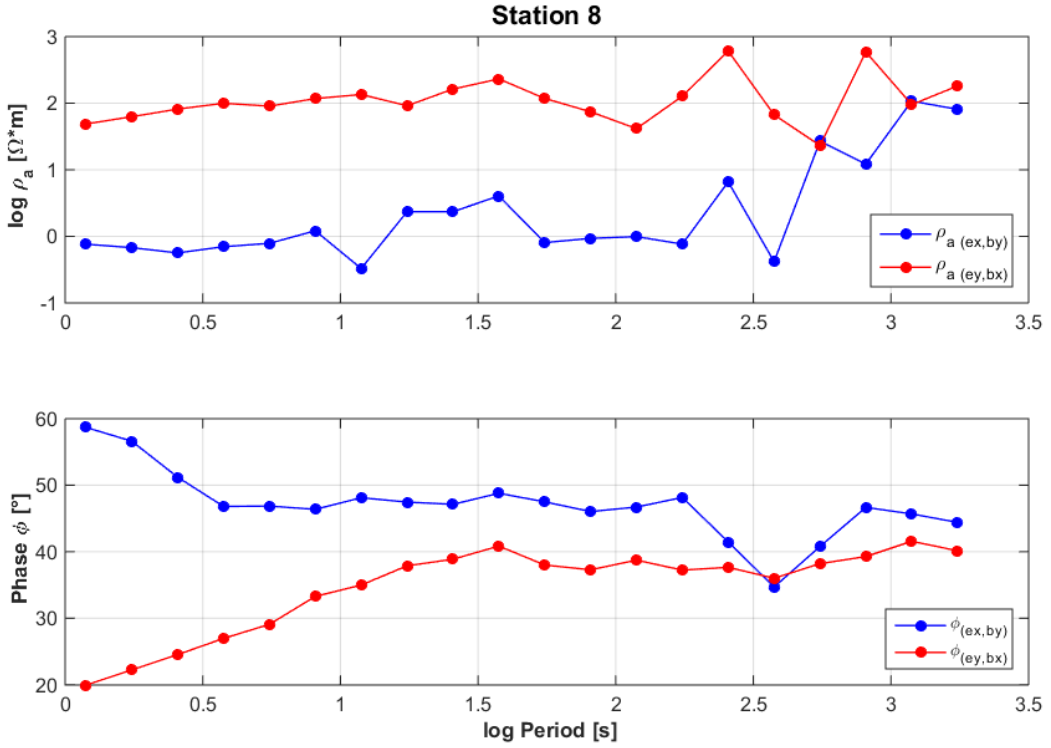

Figure 7.18: Apparent resistivity and phase - Station 8 - bathymetry and fjord model. They have been rotated and are displayed in the geomagnetic reference frame.

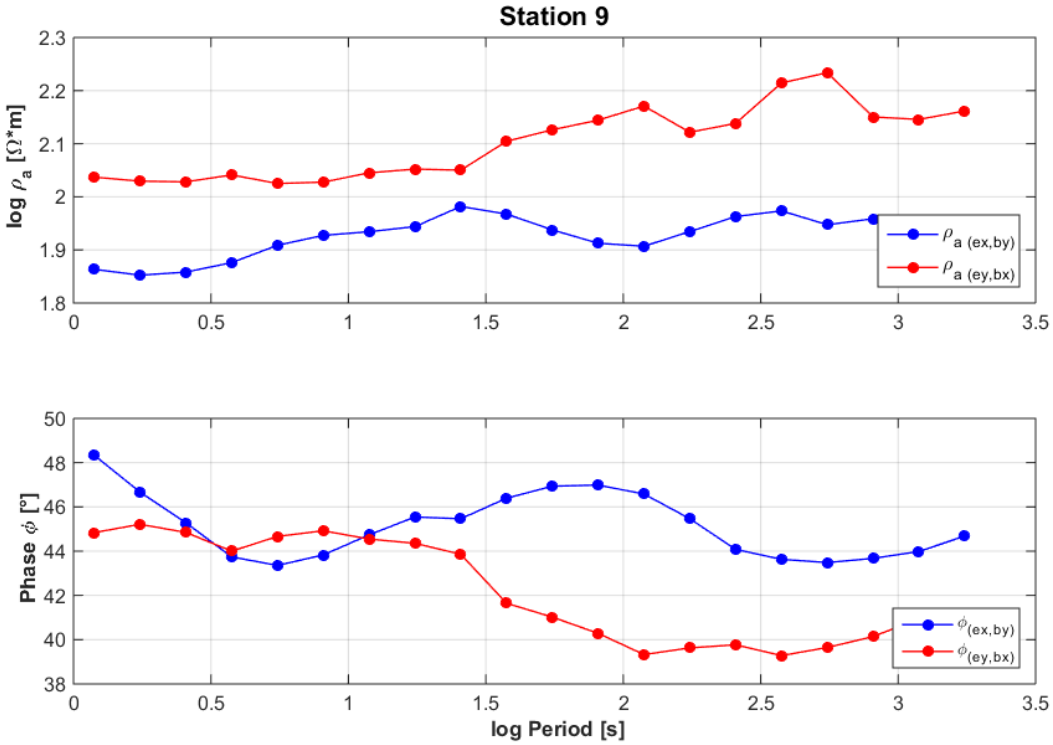

Figure 7.19: Apparent resistivity and phase - Station 9 - bathymetry and fjord model. They have been rotated and are displayed in the geomagnetic reference frame.

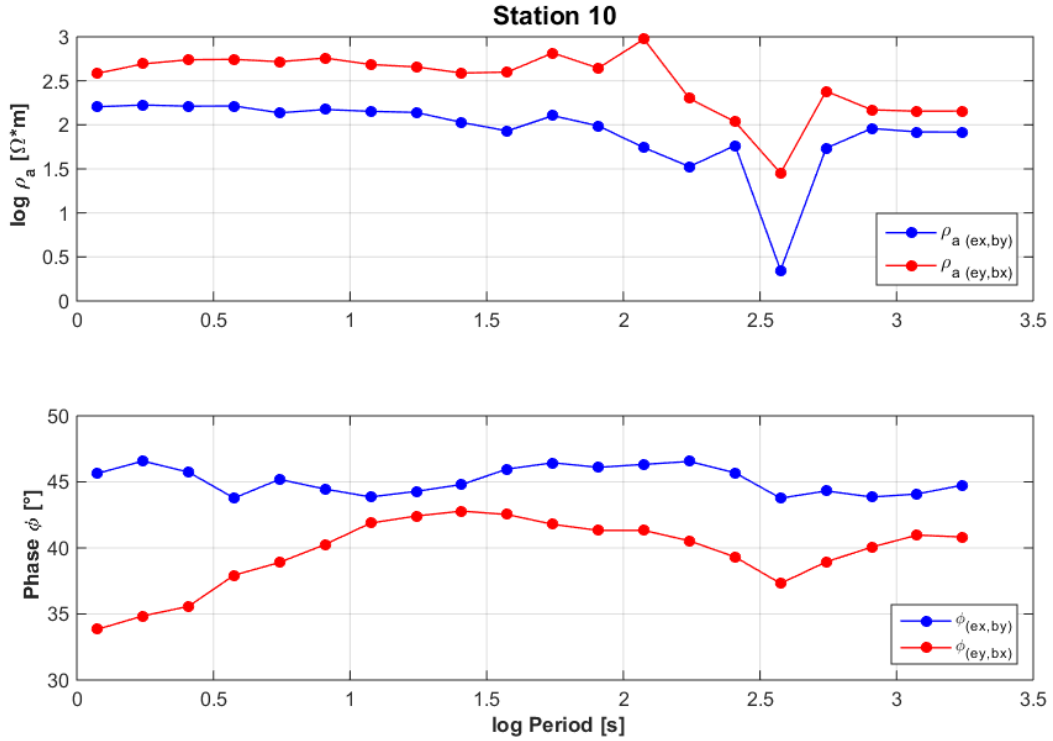

Figure 7.20: Apparent resistivity and phase - Station 10 - bathymetry and fjord model. They have been rotated and are displayed in the geomagnetic reference frame.

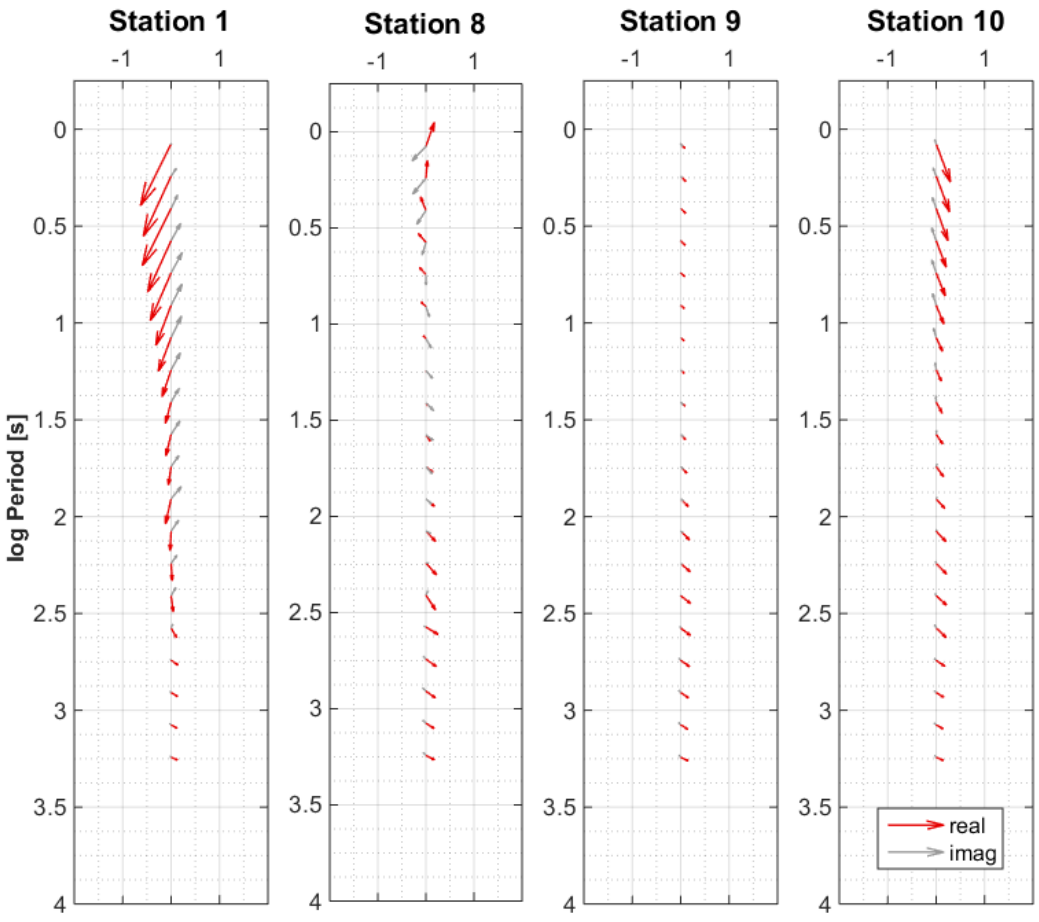

Figure 7.21: Induction arrows - model - Station 1, 8, 9 and 10. Geographical north (up).

sec. 7.1. The arrows at station 8 are smaller than at station 1, which can be explained by the water on both sides of the station. For longer periods the arrows diminish since there is a larger distance to a vertical conductivity contrast. Station 9 is in this model located some distance from the shoreline of the fjord, which explains the small induction arrows. Similar pattern is visible at station 10, though with larger arrows in the short periods since the location is closer to the fjord.

The phase tensors, in Fig. 7.22, are very homogeneous for the long periods, which is consistent with a one dimensional subsurface. In the short periods, especially at station 1 and 8, the subsurface is 2D or 3D, which originates from the close proximity of the fjords. At station 9 and 10, the phase tensors are not as distinct multidimensional, however this is consistent with the induction arrows at these stations, where the imaginary and real arrows are parallel.
To distinguish if the phase tensors illustrate a 2D or 3D subsurface, the skew, β, is also illustrated in Fig. 7.22. The skew confirms a 3D subsurface in the short periods at station 1, 9 and 10, and 2D at station 8, which originates from the nearest fjords. In the longest periods, the subsurface is also confirmed 1D.

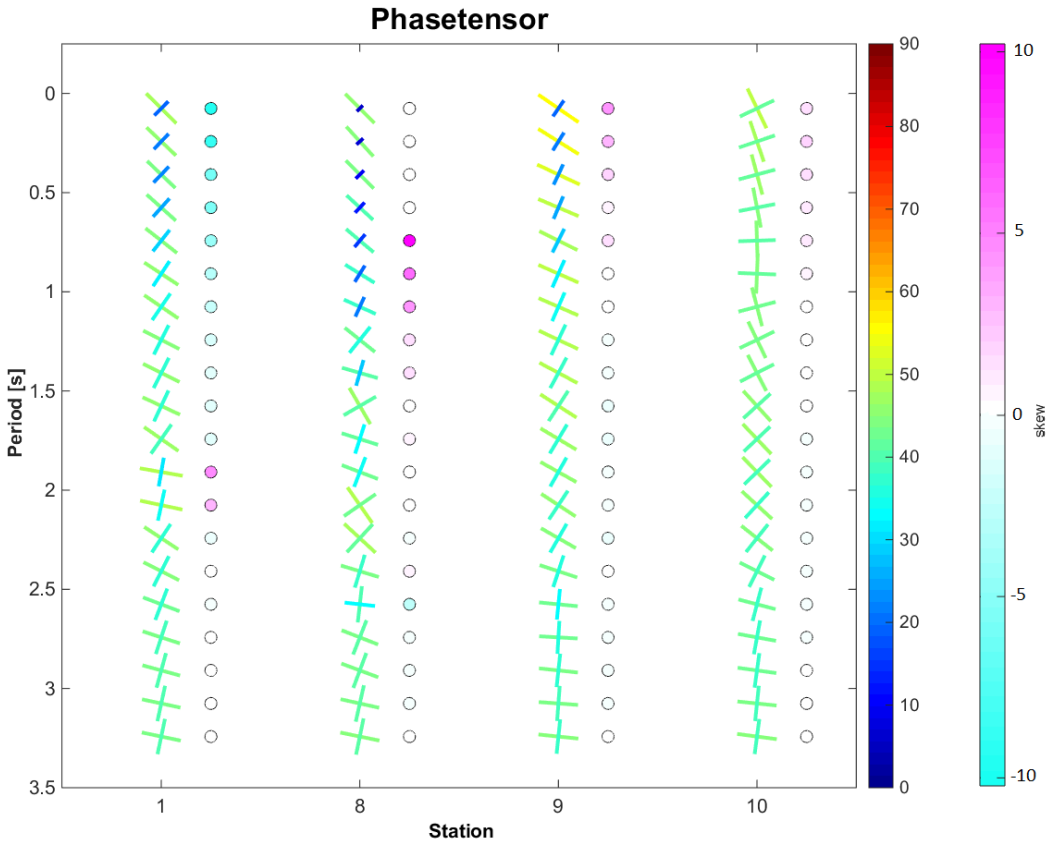

Figure 7.22: Phase tensor and skew - model - Station 1, 8, 9 and 10. Geographical north (up).

7.3 Comparison with processed data

The results of the EGstart analysis with fixed time windows, which was the best result, will be compared with the result of the forward modelling. The apparent resistivities and impedance phases in both the observed data and in the forward modelling are displayed in the geomagnetic coordinate system, where the forward model results have been rotated.
Both results, Fig. 6.31 - 6.34 and Fig. 7.17 - 7.20, show a split between the apparent resistivities which is caused by the nearby fjord, which is dominating the result. Comparing the induction arrows and phase tensors between the model and data is different. Here, the induction arrows and phase tensors of the observed data are rotated. Station 1 in Fig. 6.35 (observed data) and Fig. 7.21 (modelled data) illustrate extremely large induction arrows. These arrows are caused by the narrow fjord close to the station. The observed induction arrows at station 8, Fig. 6.35, illustrate a rotation from the short periods to the longer periods. This coincide well with the geography of the location of station 8, which is located on a small island with a large body of water to the east, see for example the satellite images in Fig. C.1. The water to the east affects the induction arrows more in the shortest periods. With increasing period, the induction volume increases and the seawater around station 8 affects the induction arrows, resulting in the observed rotation. The rotation with period in the model, is not identical to the observed data, however this can be explained by the simple model compared to the complex reality. The models of station 9 and 10 have the same direction in the induction arrows as the observed data. The arrows are larger in the observed data than the model, but as also discussed earlier, the fjord is closer to station 9 in reality than in the forward model. The phase tensors and skew display a large difference between the observed and modelled data, with dominant 3D effects at all periods and stations in the observed data. The modelled data, however, only illustrate 3D effects in the short periods of station 1 and 8, but with different phase tensor orientations than the modelled data, and at longer periods they describe the one dimensionality of the homogeneous half space.

There are no information of fjord depth and bathymetry in the fjord system where the measurements took place, which makes it difficult to model the correct conditions. Besides the missing depths, the modelling of the fjords geometry at sea level is difficult due to the complexity of the fjord system and due to limitations of the used mesh at longer periods. This missing information can be an explanation of the difference between the observed data and the modelled data, which however has similar traits that confirms that the majority of the information contained in e.g. the induction arrows originates from the nearby fjords. This indicates that the fjords are strongly affecting the inductions arrows, but not the phase tensor, which might then contain information about the geology in the area of study.

Chapter 8

Conclusion and outlook

The main objective of this project was to investigate the geological structures of the crust in the area between the towns of Aasiaat and Kangerlussuaq, located within the Naqssugtoqidian orogen in west Greenland. Different challenges are connected with magnetotelluric field work in a location such as Greenland, with the close proximity of the polar electrojet and the conductive seawater in the ocean and fjords. An eigenvalue analysis method has been tested, for its usability in isolating data with the least influence from the polar electrojet and other noise sources. At the same time the influence of the conductive ocean has been modelled, thereby determining its effect on the different transfer functions. However, in this process it was discovered that the fjord systems located in this area can have a large impact as well. These conductive fjords were included in the modelling of the observed data, in order to determine their impact in the measurement area. The modelled induction arrows were heavily dominated by the ocean and fjords, which unfortunately means that a response originating from geology would be masked by this signal. The modelled induction arrows coincide well with the observed inductions arrows, emphasising that it will be difficult to determine the response from the geology. The observed phase tensors does, however, illustrate a different response than the modelled phase tensors, which might indicate that they are not as heavily influenced by the ocean and fjords, and thereby can describe the subsurface. No model was found to explain the behaviour of the observed phase tensors.

The multiple station processing technique included in EGstart, is useful in selecting data with the least influence from other sources. When using the fixed time intervals, the data quality improved in the short periods close to 1 s, compared to the flexible time intervals and robust processing technique. For periods longer than 55 s, where EGstart with flexible time intervals was used, the induction arrows from the two largest eigenvalues seems to be consistent with the expectations of the induction arrows from the ocean, indicating that they describe the subsurface and not a non-uniform source field. However, more investigations is needed to confirm if this is always the situation.

The model study illustrates the high impact nearby fjords can have on the transfer functions. The impact changes depending on the geometry of the fjord, where in periods of 1-100 s, deep fjords are less inductive than shallow, wide fjords are more inductive than narrow, and a fjord between two water basins is more inductive than a single fjord with one water basin. Therefore, it is important to model the geometry of the fjords as accurately as possible to ensure the correct model response. When

including this knowledge into the forward modelling of the observed data, most of the response displayed in the induction arrows are clearly originating from the nearby fjords. The modelled induction arrows are not identical to the observed, however the general trend is the same. Since there are no information regarding the water depth and geometry of the fjords, except satellite images, it complicates a correct modelling. The area of the survey has not been prioritised in this regard due to its remoteness and it is of no importance strategically or commercially at the moment. If this information becomes available in the future the fjords could be modelled more accurately, and the model response might describe the observed data better. However, not only the lack of information about the fjords is an issue, but the modelling of very accurate fjords might also be a challenge in the numerical modelling.

The modelled phase tensors on the other hand, display a different response than the observed data, which indicates that it is not as sensitive to the impacts of fjords, and therefore might describe the subsurface beneath. However, no forward model was found which matched the observed response. It could, however, be worth trying to perform an inversion to see if a reasonable result can be obtained, matching the observed data response.

For future long period magnetotelluric investigations in Greenland, it is important to select a measuring area at a good distance to fjords and ocean. And if possible, as with al magnetotelluric field works, regularly inspect the stations to ensure minimal loss of data, due to animal interference or failure of equipment. This can be a challenge, since the locations are best reached by helicopter or long hikes, due to limited infrastructure. A less challenging location would be the ice cap, however other circumstances can make it difficult. Magnetotelluric measurements on the ice have been a success before, as seen in Wannamaker et al. [2004]. Regarding the influence of non-uniform source fields in the ionosphere, the EGstart software should be tested on other data sets with longer time series, located within the polar regions. Preferably with a large distance between the outer stations in the profile/array, since the stations then might be affected differently by the polar electrojet. The issue is to determine the response originating from this non-uniform source and to remove it from the data.

Bibliography

Alken, P., Maus, S., Richmond, A., and Maute, A. (2011). The ionospheric gravity and diamagnetic current systems. *Journal of Geophysical Research: Space Physics*, 116(A12). A12316.

Bahr, K. (1988). Interpretation of the magnetotelluric impedance tensor: regional induction and local telluric distortion. *Journal of Geophysics*, pages 119–127.

Baumjohann, W. and Treumann, R. A. (2012). *Basic Space Plasma Physics*. Imperial College Press, revised edition.

Berdichevsky, M., Dmitriev, V., and Pozdnjakova, E. (1998). On two-dimensional interpretation of magnetotelluric soundings. *Geophysical Journal International*, 133(3):585–606.

Booker, J. R. (2014). The magnetotelluric phase tensor: a critical review. *Surveys in Geophysics*, 35(1):7–40.

Brenner, S. and Scott, R. (2007). *The mathematical theory of finite element methods*. Springer Science & Business Media, 3rd edition.

Bridgwater, D., Austrhelm, H., Hansen, B., Mengel, F., Pedersen, S., and Winter, J. (1990). The Proterozoic Nagssugtoqidian mobile belt of southeast Greenland: A link between the eastern Canadian and Baltic shields. *Geoscience Canada*, 17(4):305–310.

Cagniard, L. (1953). Basic theory of magneto-telluric method of geophysical prospecting. *Geophysics*, 18:605–635.

Caldwell, T. G., Bibby, H. M., and Brown, C. (2004). The magnetotelluric phase tensor. *Geophysical Journal International*, 158(2):457–469.

Cembrowski, M. (2016). Personal conversation.

Chapman, S. and Bartels, J. (1940a). *Geomagnetism*, volume 1. Clarendon Press, Oxford.

Chapman, S. and Bartels, J. (1940b). *Geomagnetism*, volume 2. Clarendon Press, Oxford.

Chatfield, C. (2004). *The analysis of time series: an introduction*. CRC press.

Chave, A. D. and Weidelt, P. (2012). *The theoretical basis for electromagnetic induction, in The Magnetotelluric Method: Theory and Practice, edited by A. D. Chave and A. G. Jones*, chapter 2, pages 19–49. Cambridge University Press, UK.

COMSOL Multiphysics (2015). COMSOL AB, Stockholm, Sweden. www.comsol.com.

Connelly, J. N. and Mengel, F. C. (2000). Evolution of archean components in the paleoproterozoic nagssugtoqidian orogen, west greenland. *Geological Society of America Bulletin*, 112(5):747–763.

Dahl-Jensen, T., Holbrook, W. S., Hopper, J. R., Kelemen, P. B., Larsen, H. C., Detrick, R., Bernstein, S., and Kent, G. (1997). Seismic investigation of the east greenland volcanic rifted margin. *Geol. Greenl. Surv. Bull*, 176:50–54.

Davis, T. N. and Sugiura, M. (1966). Auroral electrojet activity index AE and its universal time variations. *Journal of Geophysical Research*, 71(3):785–801.

Egbert, G. D. (1997). Robust multiple-station magnetotelluric data processing. *Geophysical Journal International*, 130(2):475–496.

Egbert, G. D. and Booker, J. R. (1986). Robust estimation of geomagnetic transfer functions. *Geophysical Journal of the Royal Astronomical Society*, 87(1):173–194.

Engels, M. (1997). *Untersuchungen zur elektromagnetischen Induktion in Grönland*. PhD thesis, University of Göttingen. (in German).

Engels, M., Korja, T., and the BEAR Working Group (2002). Multisheet modelling of the electrical conductivity structure in the Fennoscandian shield. *Earth, planets and space*, 54(5):559–573.

Fischer, G. (1979). Electromagnetic induction effects at an ocean coast. In *Proceedings of the IEEE*, volume 67. 7.

Forsberg, R. (1986). Gravity measurements in Jameson Land and neighbouring parts of East Greenland; Meddelser om Grønland. *Geoscience*, 15:24.

Garcia, X., Chave, A. D., and Jones, A. G. (1997). Robust processing of magnetotelluric data from the auroral zone. *Journal of geomagnetism and geoelectricity*, 49(11/12):1451–1468.

Garcia, X. and Jones, A. G. (2002). Atmospheric sources for audio-magnetotelluric (AMT) sounding. *Geophysics*, 67(2):448–458.

GEBCO world map, IOC, IHO and BODC (2003). Centenary edition of the gebco digital atlas. Intergovernmental Oceanographic Commission and the International Hydrographic Organization as part of the General Bathymetric Chart of the Oceans, British Oceanographic Data Centre, Liverpool, U.K. www.gebco.net.

Geological Survey of Denmark and Greenland (2016). www.geus.dk.

GFZ - German Research Centre for Geosciences (2016). http://www.gfz-potsdam.de/en/kp-index/. [Online; accessed 30/6-2016].

GFZ GIPP (2015). Geophysical Instrument Pool Potsdam (GIPP). http://www.gfz-potsdam.de/en/section/geophysical-deep-sounding/infrastructure/geophysical-instrument-pool-potsdam-gipp/instruments/gipp-mt/. GFZ Potsdam, Germany, [Online; accessed 8/12-2015].

Google Earth and DigitalGlobe (2016a). Greenland. (12/7-2012) 68°10'46.82"N, 52°31'38.49"W, DigitalGlobe 2016. https://www.google.com/earth/. [accessed 09/09-2016].

Google Earth and DigitalGlobe (2016b). Greenland. (24/8-2009) 68°28'16.72"N, 52°55'21.61"W, DigitalGlobe 2016. https://www.google.com/earth/. [accessed 09/09-2016].

Google Earth and DigitalGlobe (2016c). Greenland. (24/8-2009) 68°23'31.14"N, 52°42'41.25"W, DigitalGlobe 2016. https://www.google.com/earth/. [accessed 09/09-2016].

Google Earth and DigitalGlobe (2016d). Greenland. (24/8-2009) 68°18'13.11"N, 52°44'40.06"W, DigitalGlobe 2016. https://www.google.com/earth/. [accessed 09/09-2016].

Google Earth, IBCAO, U.S. Geological Survey and DigitalGlobe (2016). Greenland. (13/8-2015) 68°20'26.26"N, 52°46'22.62"W, IBCAO, U.S. Geological Survey, DigitalGlobe 2016. https://www.google.com/earth/. [accessed 11/09-2016].

Griffiths, D. J. (1999). *Introduction to Electrodynamics*. Prentice Hall International, Inc., 3rd edition.

Groom, R. W. and Bahr, K. (1992). Corrections for near surface effects: decomposition of the magnetotelluric impedance tensor and scaling corrections for regional resistivities: a tutorial. *Surveys in Geophysics*, 13(4-5):341–379.

Gubbins, D. and Herrero-Bervera, E., editors (2007). *Encyclopedia of geomagnetism and paleomagnetism*. Springer Netherlands.

Häuserer, M. (2010). *Magnetotellurik in der Rwenzori Region im Westen Ugandas: Ein anisotropes 3D Modell*. PhD thesis, Goethe University Frankfurt am Main, Germany.

Hautot, S. and Tarits, P. (2016). Joint MT-Gravity iinversion in a complex geological environment: Example of western Greenland margin. Poster at the 23rd Electromagnetic Induction Workshop.

Heincke, B., Chen, J., Riisager, P., Kolb, J., and Jørgensen, A. F. (2015). 2-D magnetotelluric experiment to investigate the Nassugtoqidian orogeny in South-East Greenland. In *EGU General Assembly Conference Abstracts*, volume 17, page 6720.

Henriksen, N. (2008). *Geological History of Greenland*. Geological Survey of Denmark and Greenland (GEUS).

Henriksen, N., Higgins, A., Kalsbeek, F., and Pulvertaft, T. (2009). Greenland from archaean to quaternary. *Geological Survey of Denmark and Greenland Bulletin*, 18:207–214.

Hering, P. (2015). Magnetotellurische Messungen im Westerwald - Eine Studie zur Detektion und Minimierung von anthropogenen Rauschsignalen. Master's thesis, Goethe University Frankfurt am Main, Germany. (in German).

Hering, P., Junge, A., Lauritsen, N., and Löwer, A. (2015). Multivariate processing of magnetotelluric data - comparison and interpretation of measurement results from the Westerwald (Germany). In *Protokoll über das 26. Schmucker-Weidelt-Kolloquium für elektromagnetische Tiefenforschung in Dassel, Germany, Deutsche Geophysikalische Gesellschaft*, volume 26.

Hjelt, S., Korja, T., Kozlovskaya, E., Lahti, I., Yliniemi, J., et al. (2006). Electrical conductivity and seismic velocity structures of the lithosphere beneath the Fennoscandian Shield. *Geological Society, London, Memoirs*, 32(1):541–559.

Hopper, J. R., Lizarralde, D., and Larsen, H. C. (1998). Seismic investigations offshore South-East Greenland. *Geology of Greenland Survey Bulletin*, 180:145–151.

Huber, P. J. (1981). *Robust statistics*. John Wiley & Sons, New York, NY.

Jacobs, J. A., editor (1991a). *Geomagnetism*, volume 3. Academic press.

Jacobs, J. A., editor (1991b). *Geomagnetism*, volume 4. Academic press.

Johansson, Å. (2009). Baltica, Amazonia and the SAMBA connection - 1000 million years of neighbourhood during the Proterozoic? *Precambian Research*, 175:221–234.

Jones, A. (1983). The problem of current channelling: A critical review. *Geophysical surveys*, 6(1):79–122.

Jones, A. G. (1993). Electromagnetic images of modern and ancient subduction zones. *Tectonophysics*, 219(1-3):29–45.

Jones, A. G. (2012). *Distortion of magnetotelluric data: its identification and removal, in The Magnetotelluric Method: Theory and Practice, edited by A. D. Chave and A. G. Jones*, chapter 6, pages 219–302. Cambridge University Press, UK.

Jones, A. G. and Spratt, J. (2002). A simple method for deriving the uniform field MT responses in auroral zones. *Earth, Planets and Space*, 54(5):443–450.

Jones, F. W. and Price, A. T. (1970). The perturbations of alternating geomagnetic fields by conductivity anomalies. *Geophysical Journal International*, 20(3):317–334.

Junge, A. (1992). Erweiterte Auswerteverfahren in Göttingen. In *Tagungsband, 14. Kolloquium Elektromagnetische Tiefenforschung in Borkheide, Germany, Deutsche Geophysikalische Gesellschaft,*. (in German).

Junge, A. (1994). Induzierte erdelektrische Felder-neue Beobachtungen in Norddeutschland und im Bramwald, Habilitation thesis, (in German).

Kato, Y. and Kikuchi, T. (1950a). On the phase difference of Earth current induced by the changes of the Earth's magnetic field.(part 1). *Science reports of the Tohoku University. Ser. 5, Geophysics*, 2(2):139–141.

Kato, Y. and Kikuchi, T. (1950b). On the phase difference of Earth current induced by the changes of the Earth's magnetic field.(part 2). *Science reports of the Tohoku University. Ser. 5, Geophysics*, 2(2):142–145.

Keller, G. V. and Frischknecht, F. C. (1966). *Electrical Methods in Geophysical Prospecting*. Pergamon Press Ltd.

Korja, T., Engels, M., Zhamaletdinov, A. A., Kovtun, A. A., Palshin, N. A., Smirnov, M. Y., Tokarev, A. D., Asming, V. E., Vanyan, L. L., Vardaniants, I. L., and BEAR Working Group (2002). Crustal conductivity in Fennoscandia - a compilation of a database on crustal conductance in the Fennoscandian shield. *Earth, Planets and Space*, 54(5):535.

Kother, L. (2012). A magnetotelluric study around Kangerlussuaq, West Greenland. Master's thesis, University of Copenhagen, Denmark.

Kother, L. (2016). Personal conversation.

Lahti, I., Korja, T., Kaikkonen, P., and Vaittinen, K. (2005). Decomposition analysis of the BEAR magnetotelluric data: implications for the upper mantle conductivity in the Fennoscandian shield. *Geophysical Journal International*, 163(3):900–914.

Larsen, H. and Jakobsdóttir, S. (1988). Distribution, crustal properties and significance of seawards-dipping sub-basement reflectors off E Greenland. *Geological Society, London, Special Publications*, 39(1):95–114.

Lauritsen, N. L. B., Hering, P., Junge, A., Matzka, J., and Olsen, N. (2015). 3D MT modelling in west Greenland considering the influence of fjord systems and ocean. In *Protokoll über das 26. Schmucher-Weidelt-Kolloquium für Elektromagnetische Tiefenforschung in Dassel, Germany, Deutsche Geophysikalische Gesellschaft*.

Löwer, A. (2014). *Magnetotellurische Erkundung geologischer Grossstrukturen des südwestlichen Vogelsberges mit anisotroper, dreidimensionaler Modellierung der Leitfähigkeitsstrukturen*. PhD thesis, Goethe University Frankfurt am Main, Germany. (in German).

MATLAB (2015). The MathWorks, Inc. *Natick, Massachusetts, United States*, 4:382.

Maus, S. and Lühr, H. (2006). A gravity-driven electric current in the Earth's ionosphere identified in CHAMP satellite magnetic measurements. *Geophysical research letters*, 33(2). L02812.

McPherron, R. (1991). *Physical processes producing magnetospheric substorms and magnetic storms, in Geomagnetism Vol. 4, edited by J. Jacobs*, chapter 7, pages 593–739. Academic Press Ltd., London, England.

Mengel, F., van Gool, J., Krogstad, E., and the 1997 field crew (1998). Archaean and Palaeoproterozoic orogenic processes: Danish Lithosphere Centre studies of the Nagssugtoqidian orogen, West Greenland. *Geological Survey of Denmark and Greenland Bulletin*, 180:100–110.

Menvielle, M. and Berthelier, A. (1991). The K-derived planetary indices: Description and availability. *Reviews of Geophysics*, 29(3):415–432.

Menvielle, M., Rossignol, J., and Tarits, P. (1982). The coast effect in terms of deviated electric currents: a numerical study. *Physics of the Earth and Planetary Interiors*, 28(2):118–128.

National Geophysical Data Center (2016). `http://www.ngdc.noaa.gov/geomag-web/`. [Online; accessed 26/7-2016].

Nolasco, R., Tarits, P., Filloux, J. H., and Chave, A. D. (1998). Magnetotelluric imaging of the Society Islands hotspot. *J. Geophys. Res.*, 103(B12):30287–30309.

Olsen, N. (2007). Natural sources for electromagnetic induction studies. In *Encyclopedia of Geomagnetism and Paleomagnetism*, pages 696–700. Springer.

Olsen, N. and Stolle, C. (2016). Geomagnetic signatures from sources internal and external of the Earth: An overview. Under review.

Osipova, I., Hjelt, S., and Vanyan, L. (1989). Source field problems in northern parts of the Baltic shield. *Physics of the earth and planetary interiors*, 53(3-4):337–342.

Parkinson, W. D. (1959). Directions of rapid geomagnetic fluctuations. *Geophysical Journal of the Royal Astronomical Society*, 2(1):1–14.

Parkinson, W. D. and Jones, F. W. (1979). The geomagnetic coast effect. *Reviews of Geophysics*, 17(8):1999.

Pirjola, R. (1992). On magnetotelluric source effects caused by an auroral electrojet system. *Radio Science*, 27(4):463–468.

Priestley, M. B. (1981). *Spectral analysis and time series*. Academic press.

Ramberg, H. (1949). On the petrogenesis of the gneiss complexes between Sukkertoppen and Christianshaab, West Greenland. *Meddelelser fra Dansk Geologisk Forening*, 11:312–327.

Rasmussen, T. M., Roberts, R. G., and Pedersen, L. B. (1987). Magnetotellurics along the Fennoscandian Long Range profile. *Geophysical Journal International*, 89(3):799–820.

Rikitake, T. (1951). Changes in Earth current and their relation to the electrical state of the Earth's crust. *Bulletin of the Earthquake Research Institute, University of Tokyo*, 29:271–276.

Ritter, O. (2007). Induction arrows. In *Encyclopedia of Geomagnetism and Paleomagnetism*, pages 412–413. Springer Netherlands.

Santos, F. M., Nolasco, M., Almeida, E. P., Pous, J., and Mendes-Victor, L. A. (2001). Coast effects on magnetic and magnetotelluric transfer functions and their correction: application to MT soundings carried out in SW Iberia. *Earth and Planetary Science Letters*, 186(2):283–295.

Schmucker, U. (1973). Regional induction studies: a review of methods and results. *Physics of the Earth and Planetary Interiors*, 7(3):365–378.

Schmucker, U. (1985). *Sources of the geomagnetic field*, chapter 4.1, pages 31–73. Landolt-Börnstein, Berlin-Heidelberg: Springe-Verlag. New-Series, 5/2b.

Schmucker, U. (1987). Substitute conductors for electromagnetic response estimates. *Pure and Applied Geophysics*, 125(2-3):341–367.

Schmucker, U. and Weidelt, P. (1975). Electromagnetic induction in the earth. *Lecture Notes, Aarhus Univ., Denmark*.

Simpson, F. and Bahr, K. (2005). *Practical Magnetotellurics*. Cambridge University Press, UK.

Sokolova, E. Y., Varentsov, I. M., BEAR Working Group, et al. (2007). Deep array electromagnetic sounding on the Baltic Shield: External excitation model and implications for upper mantle conductivity studies. *Tectonophysics*, 445(1):3–25.

Sugiura, M. (1964). Hourly values of equatorial Dst for the IGY. *Pergamon Press, Oxford*, 35(9).

Swift, C. M. (1967). *A magnetotelluric investigation of an electrical conductivity anomaly on the southwestern United States*. PhD thesis, Massachusetts Institute of Technology.

Telford, W. M., Geldart, L. P., and Sheriff, R. E. (1990). *Applied geophysics*, volume 1. Cambridge university press, 2nd edition.

Tikhonov, A. N. (1950). On determining electrical characteristics of the deep layers of the Earth's crust. *Doklady*, 73:295–297.

van Gool, J. A., Alsop, G. I., Árting, U. E., Garde, A. A., Knudsen, C., Krawiec, A. W., Mazur, S., Nygaard, J., Piazolo, S., Thomas, C. W., et al. (2002). Precambrian geology of the northern Nagssugtoqidian orogen, West Greenland: mapping in the Kangaatsiaq area. *Geology of Greenland Survey Bulletin*, 191:13–23.

Varentsov, I. M., Sokolova, E. Y., Martanus, E., Nalivaiko, K., et al. (2003). System of electromagnetic field transfer operators for the bear array of simultaneous soundings: methods and results. *IZVESTIIA PHYSICS OF THE SOLID EARTH C/C OF FIZIKA ZEMLI-ROSSIISKAIA AKADEMIIA NAUK*, 39(2):118–148.

Viljanen, A. (1996). Source effect on geomagnetic induction vectors in the Fennoscandian auroral region. *Journal of geomagnetism and geoelectricity*, 48(7):1001–1009.

Viljanen, A. (2012). *Description of the magnetospheric/ionospheric sources, in The Magnetotelluric Method: Theory and Practice, edited by A. D. Chave and A. G. Jones*, chapter 3B, pages 96–121. Cambridge University Press UK.

Viljanen, A., Pirjola, R., and Hákkinen, L. (1993). An attempt to reduce induction source effects at high latitudes. *J. geomagn. geoelec*, 45(9):817–831.

Wait, J. R. (1954). On the relation between telluric currents and the Earth's magnetic field. *Geophysics*, 19(2):281–289.

Wannamaker, P. E., Stodt, J. A., Pellerin, L., Olsen, S. L., and Hall, D. B. (2004). Structure and thermal regime beneath the south pole region, East Antarctica, from magnetotelluric measurements. *Geophysical Journal International*, 157(1):36–54.

Weidelt, P. (1972). The inverse problem of geomagnetic induction. *Zeitschrift für Geophysik*, 38:257–289.

Weidelt, P. and Chave, A. D. (2012). *The magnetotelluric response function, The Magnetotelluric Method: Theory and Practice, edited by A. D. Chave and A. G. Jones*, chapter 4, pages 122–162. Cambridge University Press UK.

Weigel, W., Flüh, E., Miller, H., Butzke, A., Dehghani, G., Gebhardt, V., Harder, I., Hepper, J., Jokat, W., Kläschen, D., et al. (1995). Investigations of the East Greenland continental margin between 70 and 72 N by deep seismic sounding and gravity studies. *Marine Geophysical Researches*, 17(2):167–199.

Wiese, H. (1962). Geomagnetische Tiefentellurik Teil II: die Streichrichtung der Untergrundstrukturen des elektrischen Widerstandes, erschlossen aus geomagnetischen Variationen. *Geofisica pura e applicata*, 52(1):83–103.

Williams, J. M. and Rodriguez, B. D. (2001). Magnetotelluric data across the battle mountain-Eureka and Carlin trends, North of Eureka, Nevada. Technical report, U.S. Department of the Interior, U.S. Geological Survey.

Winch, D. (2007). Periodic external fields. In *Encyclopedia of Geomagnetism and Paleomagnetism*, pages 809–816. Springer.

World Data Center for Geomagnetism, Kyoto (2016). `http://wdc.kugi.kyoto-u.ac.jp/dstae/index.html`. [Online; accessed 30/6-2016].

Appendix A

Processing

A.1 Bivariate elements of Z and T

Bivariate estimation of Z_{xx}, Z_{yx}, Z_{yy} and T_y.

$$Z_{xx} = \frac{\langle E_x B_x^* \rangle \langle B_y B_y^* \rangle - \langle E_x B_y^* \rangle \langle B_y B_x^* \rangle}{\langle B_x B_x^* \rangle \langle B_y B_y^* \rangle - |\langle B_x B_y^* \rangle|^2} \tag{A.1}$$

$$Z_{yx} = \frac{\langle E_y B_x^* \rangle \langle B_y B_y^* \rangle - \langle E_y B_y^* \rangle \langle B_y B_x^* \rangle}{\langle B_x B_x^* \rangle \langle B_y B_y^* \rangle - |\langle B_x B_y^* \rangle|^2} \tag{A.2}$$

$$Z_{yy} = \frac{\langle E_y B_y^* \rangle \langle B_x B_x^* \rangle - \langle E_y B_x^* \rangle \langle B_x B_y^* \rangle}{\langle B_x B_x^* \rangle \langle B_y B_y^* \rangle - |\langle B_x B_y^* \rangle|^2} \tag{A.3}$$

$$T_y = \frac{\langle B_z B_y^* \rangle \langle B_x B_x^* \rangle - \langle B_z B_x^* \rangle \langle B_x B_y^* \rangle}{\langle B_x B_x^* \rangle \langle B_y B_y^* \rangle - |\langle B_x B_y^* \rangle|^2} \ . \tag{A.4}$$

Appendix B

Processing results

B.1 Impedance tensor elements for each hour of each day

B.1.1 Station 8, Z_{yx}

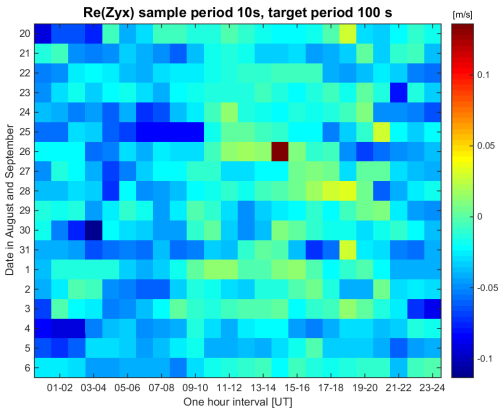

Figure B.1: $\Re(Z_{yx})$ for station 8 at period 100 s. The y axis is the date in August and September of the measurement, the x axis is divided into one hour intervals from 00-24 UT.

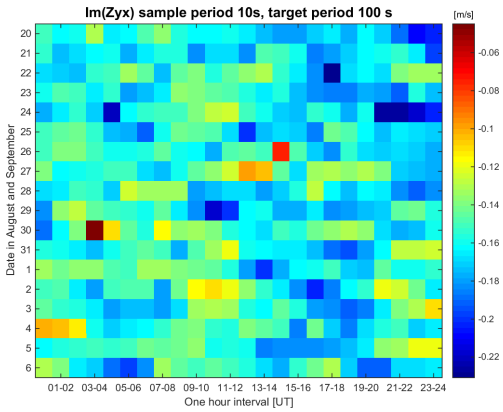

Figure B.2: $\Im(Z_{yx})$ for station 8 at period 100 s. The y axis is the date in August and September of the measurement, the x axis is divided into one hour intervals from 00-24 UT.

B.1.2 Station 8, Z_{xx}

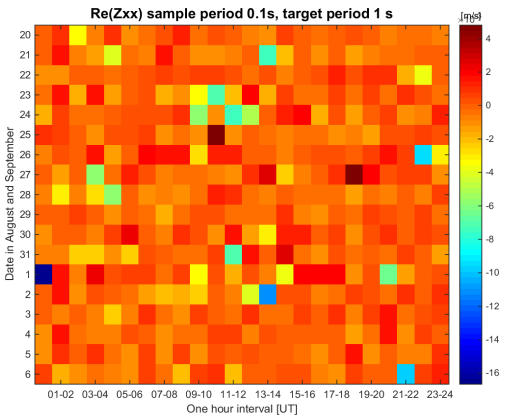

Figure B.3: $\Re(Z_{xx})$ for station 8 at period 1 s. The y axis is the date in August and September of the measurement, the x axis is divided into one hour intervals from 00-24 UT.

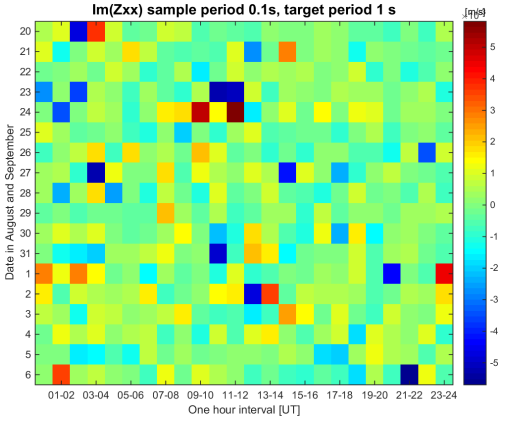

Figure B.4: $\Im(Z_{xx})$ for station 8 at period 1 s. The y axis is the date in August and September of the measurement, the x axis is divided into one hour intervals from 00-24 UT.

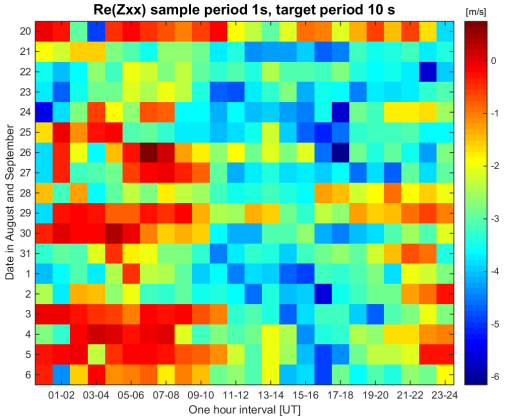

Figure B.5: $\Re(Z_{xx})$ for station 8 at period 10 s. The y axis is the date in August and September of the measurement, the x axis is divided into one hour intervals from 00-24 UT.

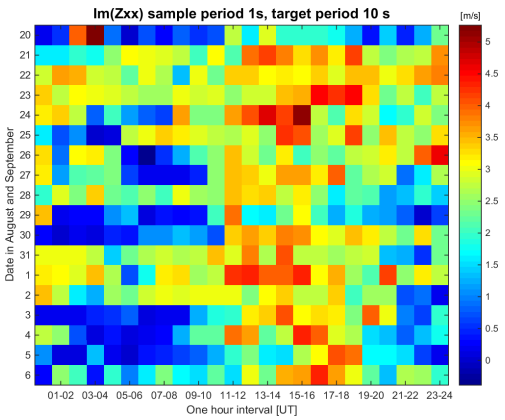

Figure B.6: $\Im(Z_{xx})$ for station 8 at period 10 s. The y axis is the date in August and September of the measurement, the x axis is divided into one hour intervals from 00-24 UT.

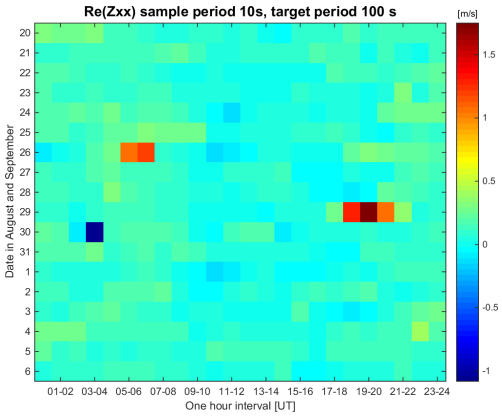

Figure B.7: $\Re(Z_{xx})$ for station 8 at period 100 s. The y axis is the date in August and September of the measurement, the x axis is divided into one hour intervals from 00-24 UT.

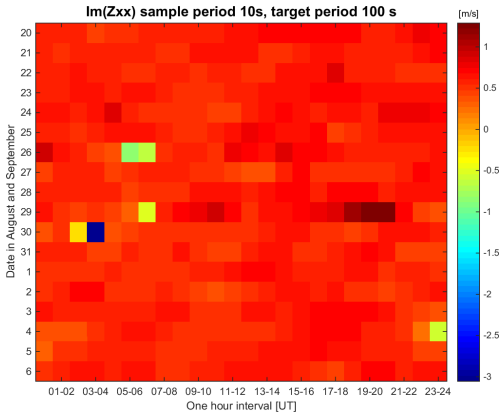

Figure B.8: $\Im(Z_{xx})$ for station 8 at period 100 s. The y axis is the date in August and September of the measurement, the x axis is divided into one hour intervals from 00-24 UT.

B.1.3 Station 8, Z_{xy}

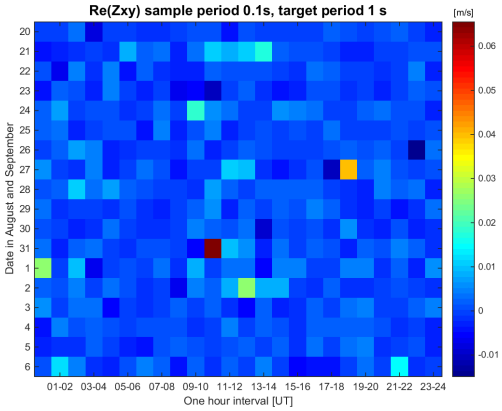

Figure B.9: $\Re(Z_{xy})$ for station 8 at period 1 s. The y axis is the date in August and September of the measurement, the x axis is divided into one hour intervals from 00-24 UT.

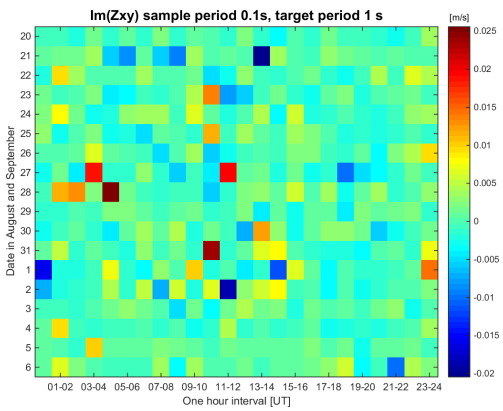

Figure B.10: $\Im(Z_{xy})$ for station 8 at period 1 s. The y axis is the date in August and September of the measurement, the x axis is divided into one hour intervals from 00-24 UT.

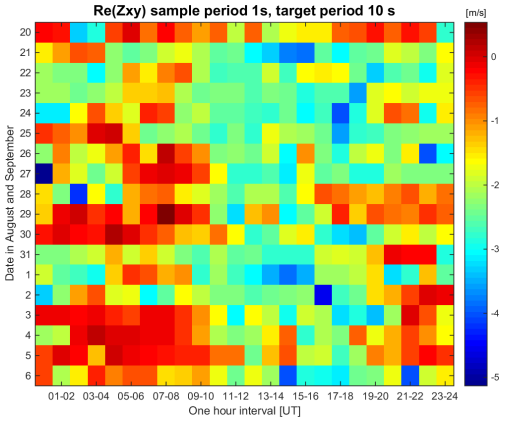

Figure B.11: $\Re(Z_{xy})$ for station 8 at period 10 s. The y axis is the date in August and September of the measurement, the x axis is divided into one hour intervals from 00-24 UT.

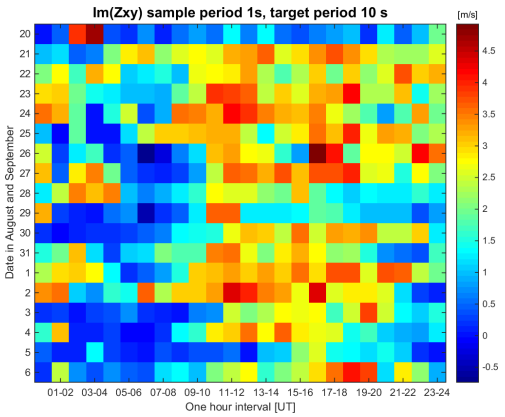

Figure B.12: $\Im(Z_{xy})$ for station 8 at period 10 s. The y axis is the date in August and September of the measurement, the x axis is divided into one hour intervals from 00-24 UT.

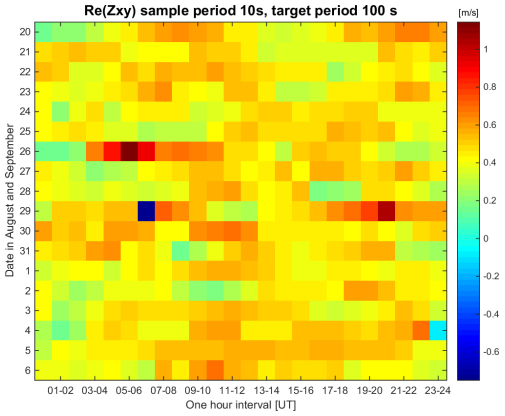

Figure B.13: $\Re(Z_{xy})$ for station 8 at period 100 s. The y axis is the date in August and September of the measurement, the x axis is divided into one hour intervals from 00-24 UT.

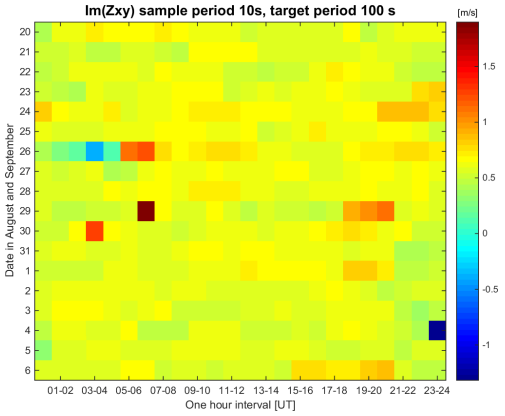

Figure B.14: $\Im(Z_{xy})$ for station 8 at period 100 s. The y axis is the date in August and September of the measurement, the x axis is divided into one hour intervals from 00-24 UT.

B.1.4 Station 8, Z_{yy}

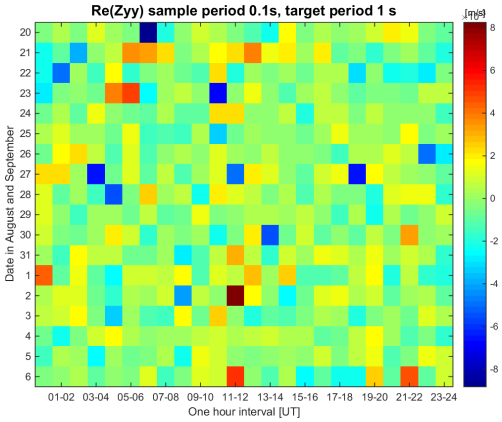

Figure B.15: $\Re(Z_{yy})$ for station 8 at period 1 s. The y axis is the date in August and September of the measurement, the x axis is divided into one hour intervals from 00-24 UT.

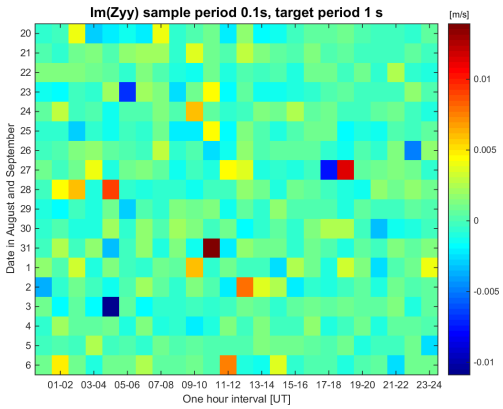

Figure B.16: $\Im(Z_{yy})$ for station 8 at period 1 s. The y axis is the date in August and September of the measurement, the x axis is divided into one hour intervals from 00-24 UT.

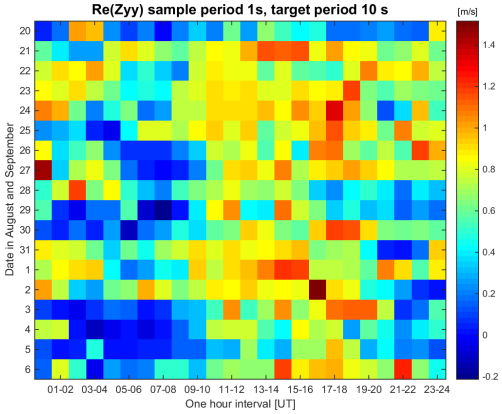

Figure B.17: $\Re(Z_{yy})$ for station 8 at period 10 s. The y axis is the date in August and September of the measurement, the x axis is divided into one hour intervals from 00-24 UT.

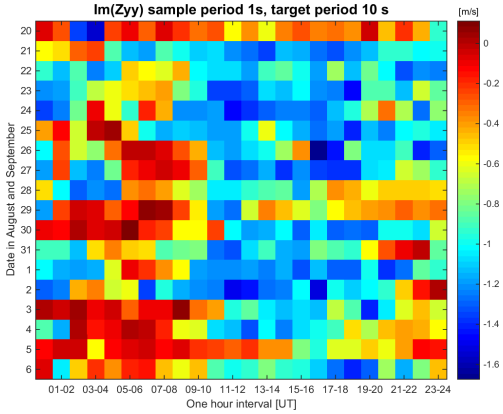

Figure B.18: $\Im(Z_{yy})$ for station 8 at period 10 s. The y axis is the date in August and September of the measurement, the x axis is divided into one hour intervals from 00-24 UT.

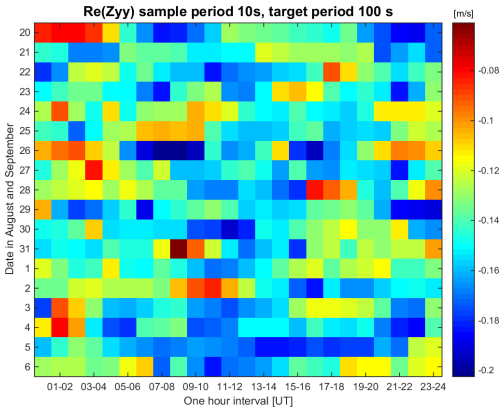

Figure B.19: $\Re(Z_{yy})$ for station 8 at period 100 s. The y axis is the date in August and September of the measurement, the x axis is divided into one hour intervals from 00-24 UT.

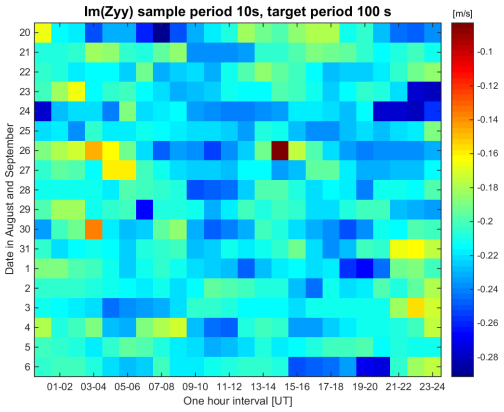

Figure B.20: $\Im(Z_{yy})$ for station 8 at period 100 s. The y axis is the date in August and September of the measurement, the x axis is divided into one hour intervals from 00-24 UT.

B.1.5 Station 10, Z_{yx}

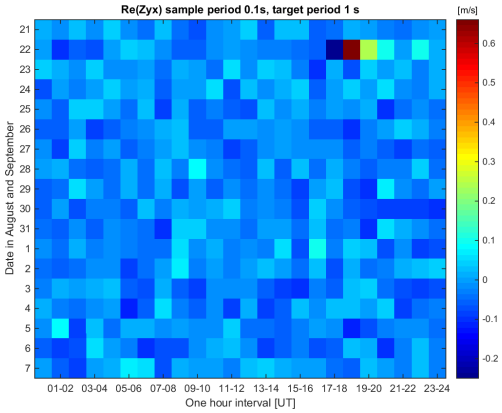

Figure B.21: $\Re(Z_{yx})$ for station 10 at period 1 s. The y axis is the date in August and September of the measurement, the x axis is divided into one hour intervals from 00-24 UT.

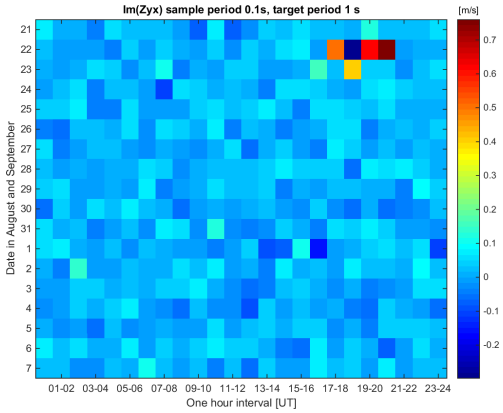

Figure B.22: $\Im(Z_{yx})$ for station 10 at period 1 s. The y axis is the date in August and September of the measurement, the x axis is divided into one hour intervals from 00-24 UT.

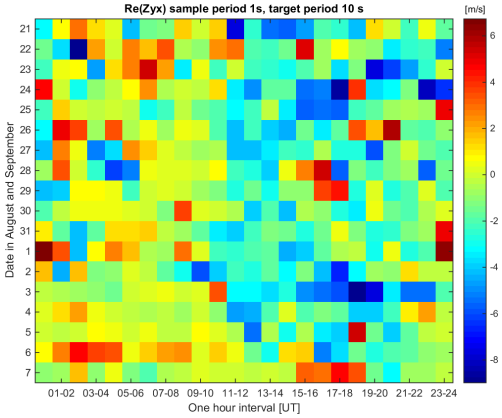

Figure B.23: $\Re(Z_{yx})$ for station 10 at period 10 s. The y axis is the date in August and September of the measurement, the x axis is divided into one hour intervals from 00-24 UT.

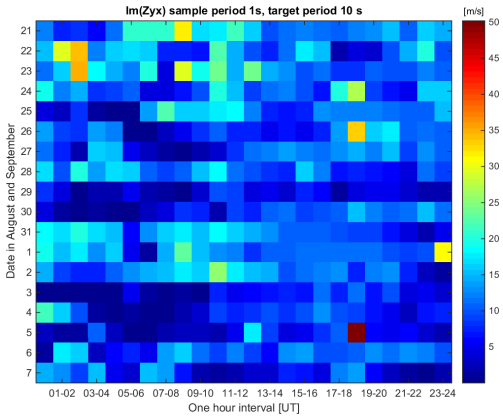

Figure B.24: $\Im(Z_{yx})$ for station 10 at period 10 s. The y axis is the date in August and September of the measurement, the x axis is divided into one hour intervals from 00-24 UT.

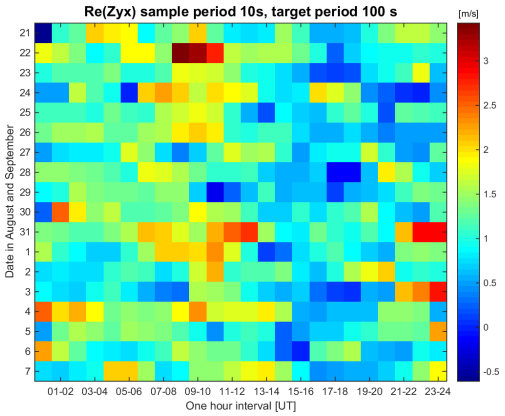

Figure B.25: $\Re(Z_{yx})$ for station 10 at period 100 s. The y axis is the date in August and September of the measurement, the x axis is divided into one hour intervals from 00-24 UT.

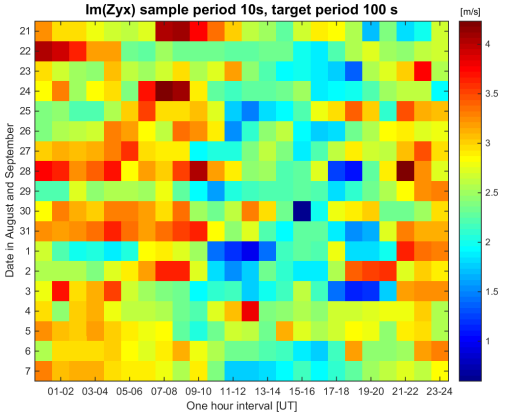

Figure B.26: $\Im(Z_{yx})$ for station 10 at period 100 s. The y axis is the date in August and September of the measurement, the x axis is divided into one hour intervals from 00-24 UT.

B.1.6 Station 10, Z_{xx}

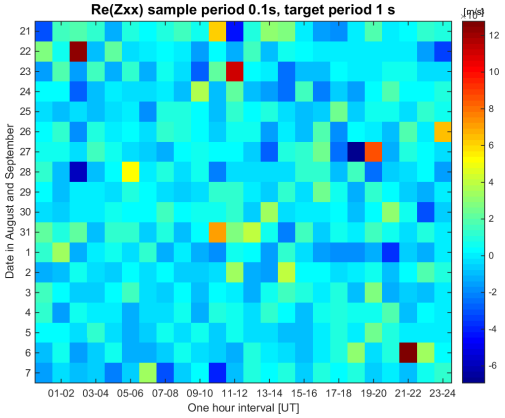

Figure B.27: $\Re(Z_{xx})$ for station 10 at period 1 s. The y axis is the date in August and September of the measurement, the x axis is divided into one hour intervals from 00-24 UT.

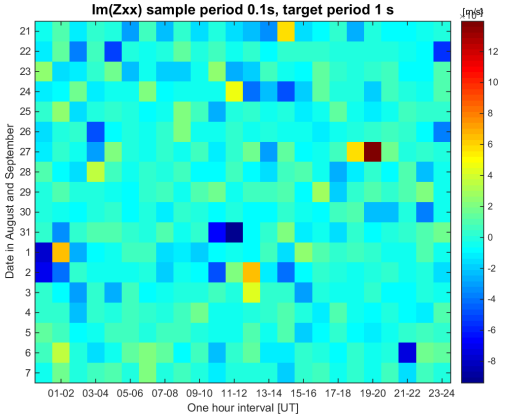

Figure B.28: $\Im(Z_{xx})$ for station 10 at period 1 s. The y axis is the date in August and September of the measurement, the x axis is divided into one hour intervals from 00-24 UT.

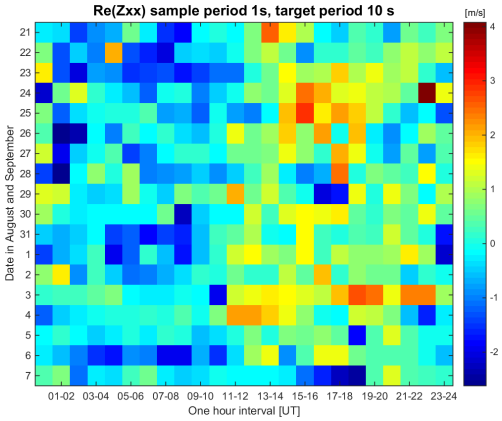

Figure B.29: $\Re(Z_{xx})$ for station 10 at period 10 s. The y axis is the date in August and September of the measurement, the x axis is divided into one hour intervals from 00-24 UT.

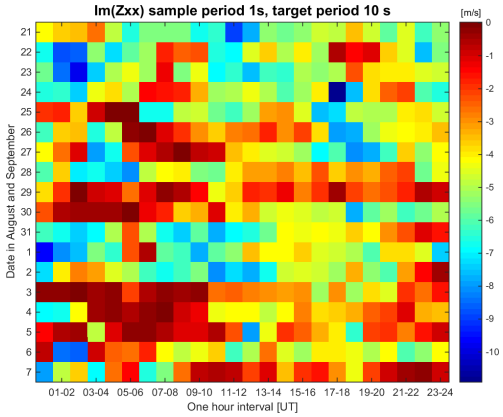

Figure B.30: $\Im(Z_{xx})$ for station 10 at period 10 s. The y axis is the date in August and September of the measurement, the x axis is divided into one hour intervals from 00-24 UT.

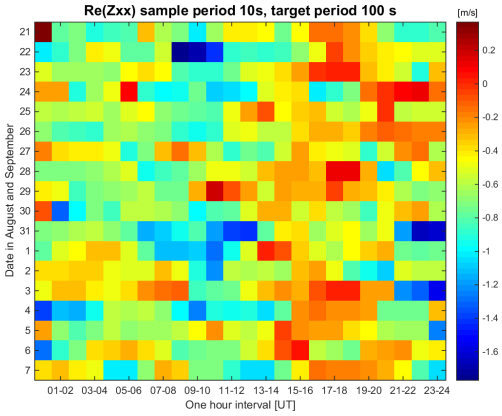

Figure B.31: $\Re(Z_{xx})$ for station 10 at period 100 s. The y axis is the date in August and September of the measurement, the x axis is divided into one hour intervals from 00-24 UT.

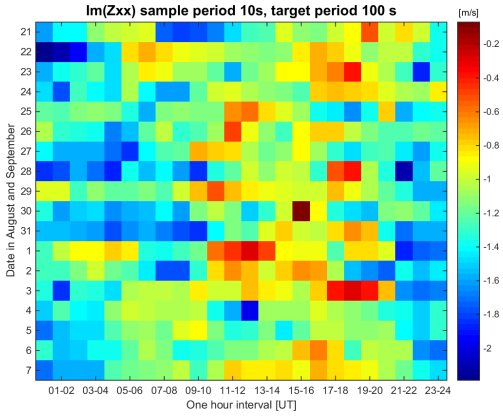

Figure B.32: $\Im(Z_{xx})$ for station 10 at period 100 s. The y axis is the date in August and September of the measurement, the x axis is divided into one hour intervals from 00-24 UT.

B.1.7 Station 10, Z_{xy}

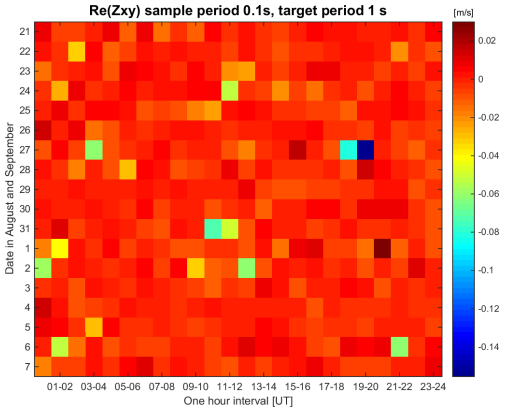

Figure B.33: $\Re(Z_{xy})$ for station 10 at period 1 s. The y axis is the date in August and September of the measurement, the x axis is divided into one hour intervals from 00-24 UT.

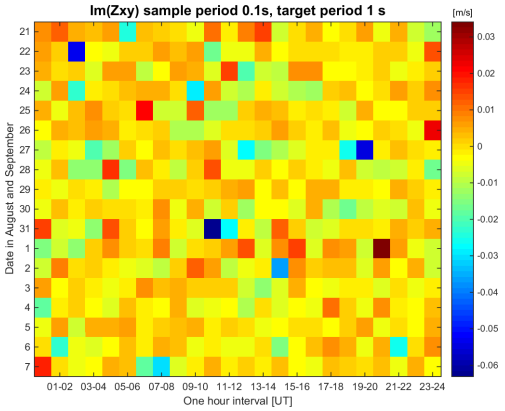

Figure B.34: $\Im(Z_{xy})$ for station 10 at period 1 s. The y axis is the date in August and September of the measurement, the x axis is divided into one hour intervals from 00-24 UT.

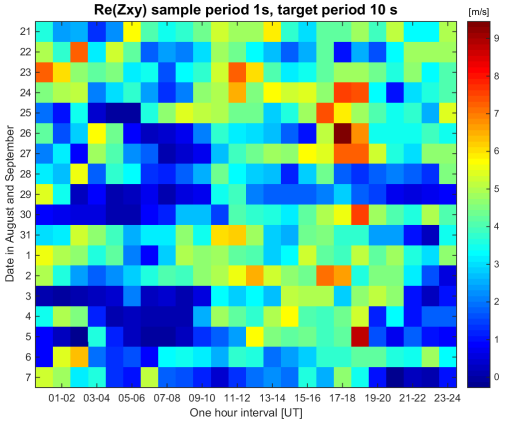

Figure B.35: $\Re(Z_{xy})$ for station 10 at period 10 s. The y axis is the date in August and September of the measurement, the x axis is divided into one hour intervals from 00-24 UT.

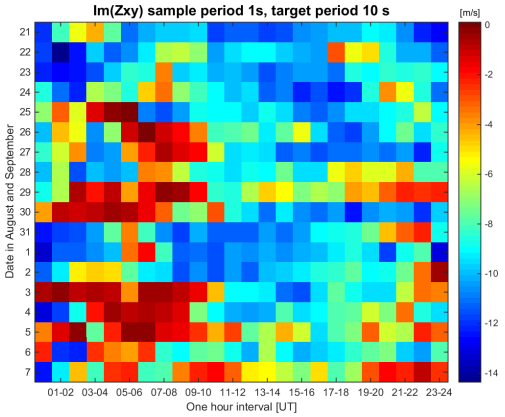

Figure B.36: $\Im(Z_{xy})$ for station 10 at period 10 s. The y axis is the date in August and September of the measurement, the x axis is divided into one hour intervals from 00-24 UT.

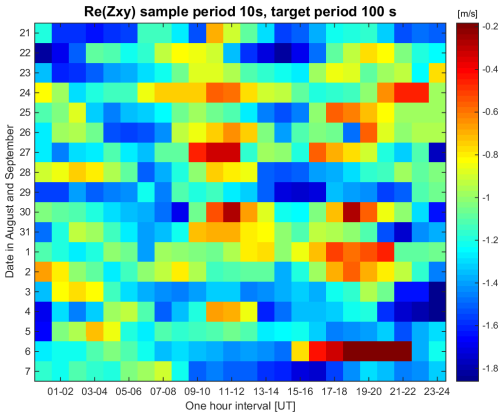

Figure B.37: $\Re(Z_{xy})$ for station 10 at period 100 s. The y axis is the date in August and September of the measurement, the x axis is divided into one hour intervals from 00-24 UT.

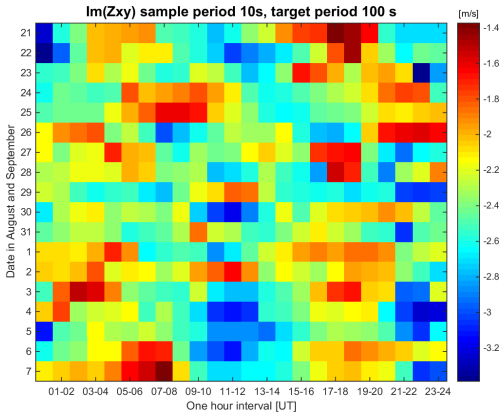

Figure B.38: $\Im(Z_{xy})$ for station 10 at period 100 s. The y axis is the date in August and September of the measurement, the x axis is divided into one hour intervals from 00-24 UT.

B.1.8 Station 10, Z_{yy}

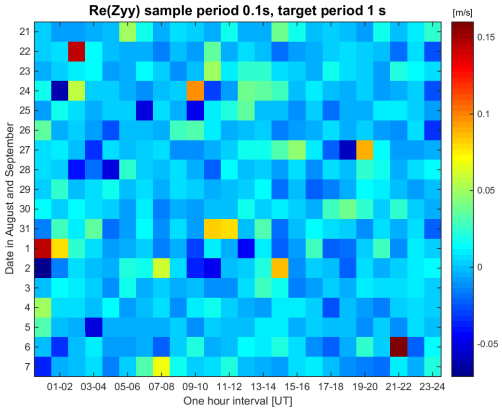

Figure B.39: $\Re(Z_{yy})$ for station 10 at period 1 s. The y axis is the date in August and September of the measurement, the x axis is divided into one hour intervals from 00-24 UT.

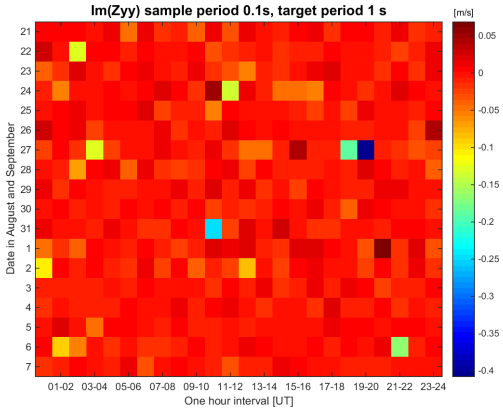

Figure B.40: $\Im(Z_{yy})$ for station 10 at period 1 s. The y axis is the date in August and September of the measurement, the x axis is divided into one hour intervals from 00-24 UT.

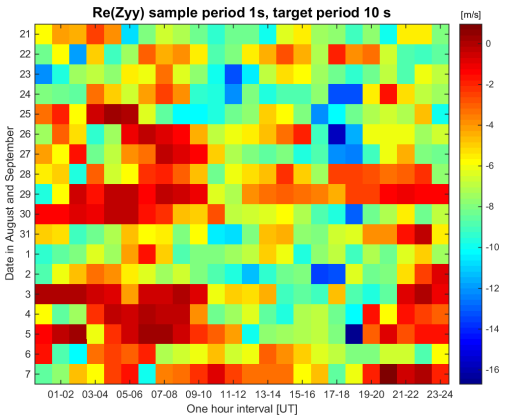

Figure B.41: $\Re(Z_{yy})$ for station 10 at period 10 s. The y axis is the date in August and September of the measurement, the x axis is divided into one hour intervals from 00-24 UT.

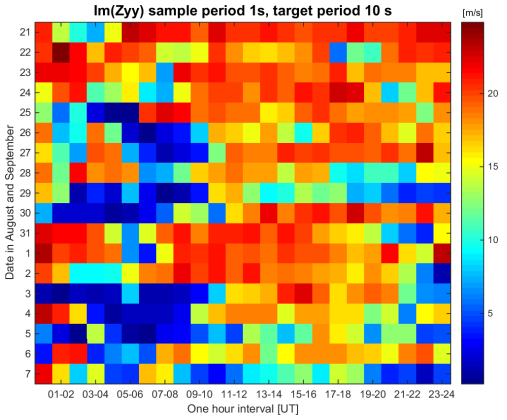

Figure B.42: $\Im(Z_{yy})$ for station 10 at period 10 s. The y axis is the date in August and September of the measurement, the x axis is divided into one hour intervals from 00-24 UT.

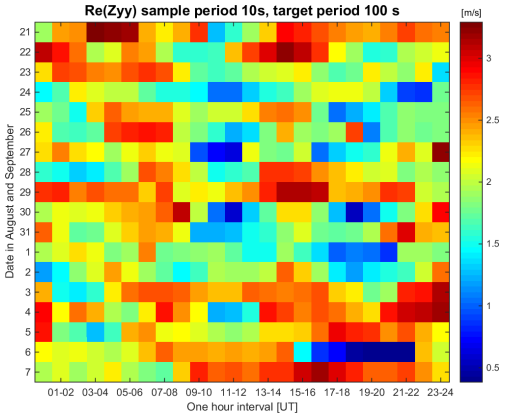

Figure B.43: $\Re(Z_{yy})$ for station 10 at period 100 s. The y axis is the date in August and September of the measurement, the x axis is divided into one hour intervals from 00-24 UT.

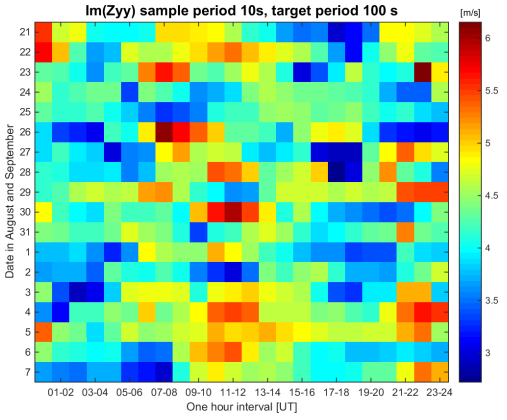

Figure B.44: $\Im(Z_{yy})$ for station 10 at period 100 s. The y axis is the date in August and September of the measurement, the x axis is divided into one hour intervals from 00-24 UT.

Appendix C

Modelling

C.1 Meshing

The boundary conditions of the tetrahedral in the COMSOL Multiphysics [2015] model used for the model study presented in sec. 7.1.

Object	Max. element size	Min. element size	Max. element growth rate
Fjord and ocean	21300	50	–
High res. cylinder	$max(\delta/10, radius/10)$	$max(\delta/20, radius/10)$	–
Top layer	$max(\delta/10, 3 \cdot \delta/10)$	$max(\delta/20, 3 \cdot \delta/40)$	1.50
Background	$0.7 \cdot \delta$	$\delta/20$	2.00
Air*	$13400 - 42400$	$2410 - 7640$	1.85

Table C.1: Element size for mesh in model study. (*) The air box uses COMSOL Multiphysics [2015] predefined mesh, *Extra coarse*, which depend on the size of the whole model. The values in the table represent the values for the smallest model and the values for the largest model.

The boundary conditions of the tetrahedral in the COMSOL Multiphysics [2015] model used for the forward modelling of the magnetotelluric field work data presented in sec. 7.2.

Object	Max. element size	Min. element size	Max. element growth rate
Sphere 1	$0.1 \cdot \delta_{min}$	–	–
Sphere 2	$0.5 \cdot \delta_{max}$	–	1.1
Sphere 3	–	–	1.2
Background	–	–	1.2

Table C.2: Element size for mesh in the forward model.

C.2 Location of station 1, 8, 9 and 10

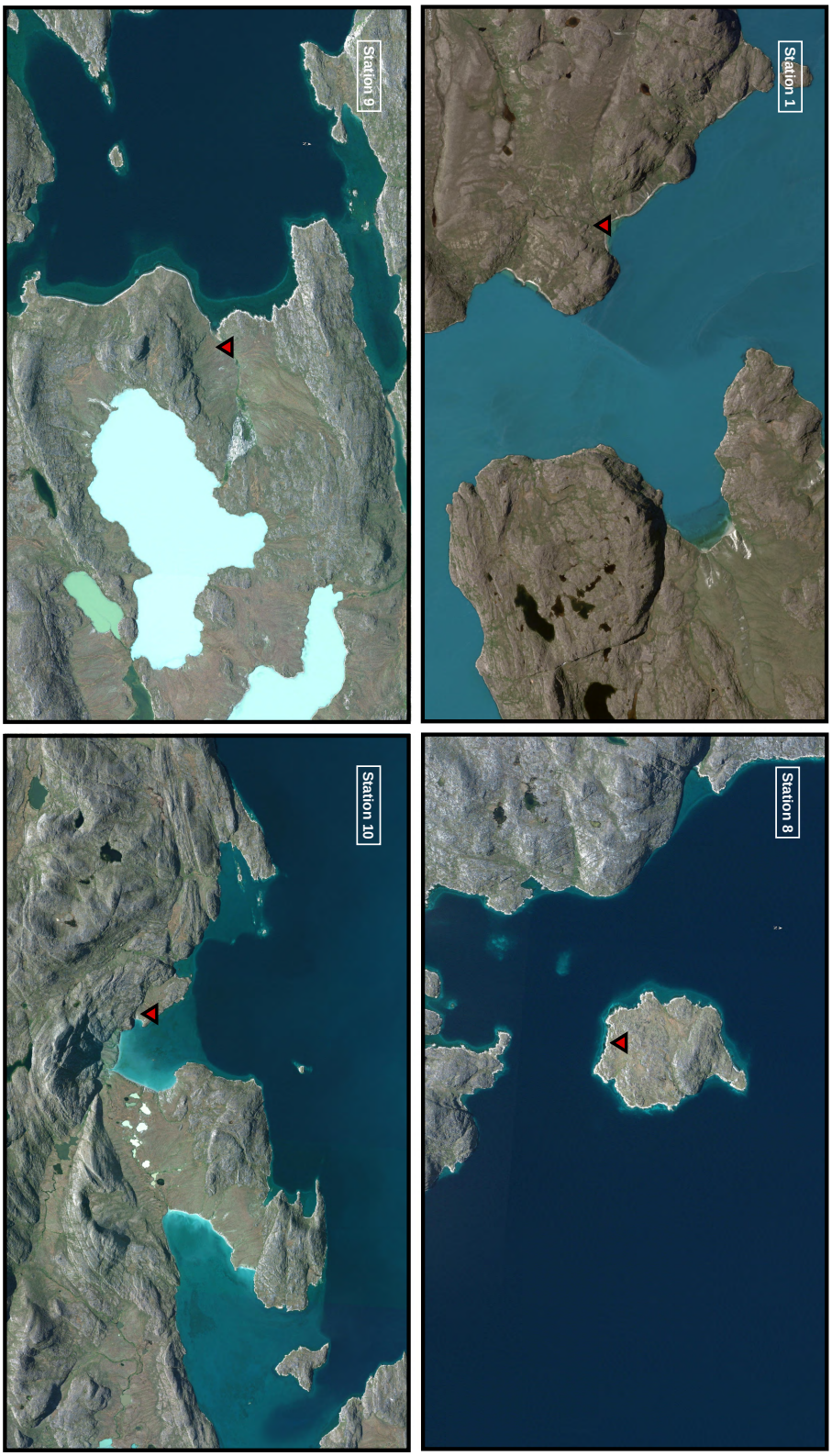

Figure C.1: Satellite images of station 1 [Google Earth and DigitalGlobe, 2016a], 8 [Google Earth and DigitalGlobe, 2016b], 9 [Google Earth and DigitalGlobe, 2016c] and 10 [Google Earth and DigitalGlobe, 2016d].

Appendix D

Publications and list of conference contributions

In the following are listed my contributions to different conferences and workshops during my Ph.D study, and finally, the extended abstract published in connection with the EMTF conference in 2015.

The 22rd Electromagnetic Induction Workshop (EMIW):

Lauritsen, N. L. B., Matzka, J., Löwer, A., Junge, A., Rasmussen, T. M., Olsen, N., *A Magnetotelluric study in North-west Greenland*, Poster, 2014

75. Jahretagung der DeutschenGeophysikalischen Gesellschaft (DGG):

Lauritsen, N. L. B., Matzka, J., Löwer, A., Junge, A., Rasmussen, T. M., Olsen, N., *Magnetotelluric study of the lithosphere in West Greenland*, Poster, 2015

International Union of Geodesy and Geophysics, 26th General assembly (IUGG):

Lauritsen, N. L. B., Matzka, J., Löwer, A., Junge, A., Rasmussen, T. M., Olsen, N., *3D Modelling in West Greenland Considering the Influence of Polar Electrojet, Ocean and Geology*, Oral, 2015

Lauritsen, N. L. B., Matzka, J., Löwer, A., Junge, A., Rasmussen, T. M., Olsen, N., *Magnetotelluric study of the lithosphere in West Greenland*, Poster, 2015

26. Schmucker-Weidelt Kolloquium für Elektromagnetische Tiefenforschung (EMTF):

Lauritsen, N. L. B., Hering, P., Junge, A., Löwer, A., Matzka, J., Olsen, N., *3D Modelling in West Greenland Considering the Influence of Polar Electrojet and Ocean*, Oral, 2015

Hering, P., Junge, A., **Lauritsen, N. L. B.**, Löwer, A., *A multivariate processing scheme for magnetotelluric data based on a new eigenvalue selection criterion*, Poster, 2015

The 23rd Electromagnetic Induction Workshop (EMIW):

Lauritsen, N. L. B., Hering, P., Junge, A., Löwer, A., Matzka, J., Olsen, N., *3D MT Modelling in West Greenland Considering the Influence of Polar Electrojet and Fjord systems*, Poster, 2016

Lauritsen, N. L. B., Hering, P., Junge, A., Löwer, A., Matzka, J., Olsen, N., *Model study of the impact of fjords on induction arrows*, Poster, 2016

Hering, P., Junge, A., **Lauritsen, N. L. B.**, *Multivariate evaluation of magnetotelluric data-processing methods and practical application*, Poster, 2016

3D MT Modelling in West Greenland Considering the Influence of Fjord Systems and Ocean.

N. L. B. Lauritsen[1], P. Hering[2], A. Junge[2], J. Matzka[3], and N. Olsen[1]

[1]*DTU Space, Technical University of Denmark, Denmark*
[2]*Institue of Geosciences, Goethe Universität Frankfurt am Main, Germany*
[3]*GFZ Potsdam, Germany*

Introduction

Collecting magnetotelluric data in Greenland give rise to different challenges. Here we investigate one of the challenges, how a fjord system connected to the ocean can affect induction arrows around the fjord, by numerical simulations for periods of 1s, 10s and 100s. The results are induction arrows from a magnetotelluric data set collected in West Greenland in the summer 2013, with stations along the shoreline of the fjords between the towns of Kangerlussuaq and Aasiaat, see Figure 1. The setup consisted of 10 LMT stations on a 100 km profile with equipment kindly supplied by the GIPP at GFZ Potsdam (2015).

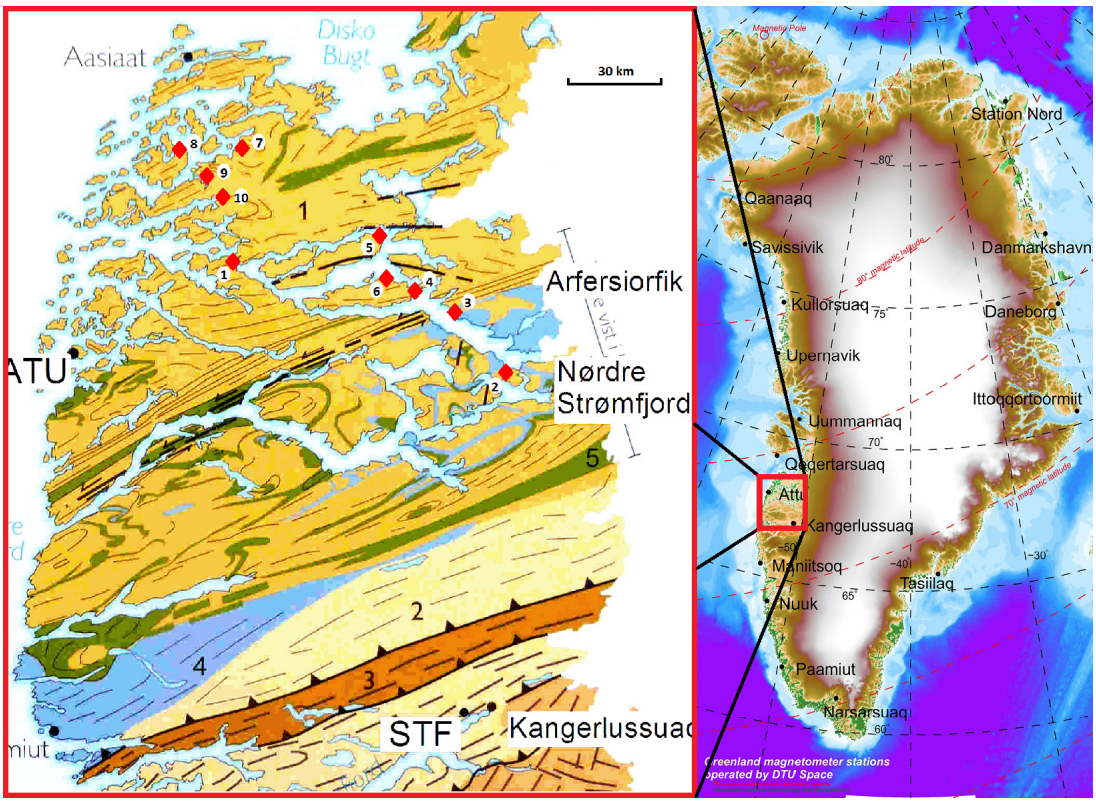

Figure 1: Left Red diamonds indicate the locations of the 10 stations at Arfersiorfik fjord. Geological map from van Gool in Henriksen (2008). **Right** Red square indicates the left-side maps location together with permanent DTU Space magnetometer stations.

Model study: the impact of fjords on MT transfer functions

We have conducted a model study with a simplified bended fjord, with or without connection to the ocean, to investigate how seawater of the fjord affects the induction arrows along the shoreline. The COMSOL Multiphysics v. 5.2 (2015) software is used to perform the modeling. The cross section of the fjord is set to a rectangle, 2 km width and 200 m depth.
Figure 2, left column, illustrates a fjord with no connection to the ocean, with the three panels presenting induction arrows for periods of 1s, 10s or 100s. The background color displays the magnitude of the induction, with the highest induction concentrated along the shoreline, but especially on the inside of the bend of the fjord. The real part of the induction arrows, illustrated as red arrows in Figure 2, will point away from conductive material (Wiese convention). Focusing first on the period of 1s, it is clear that the arrows along the shoreline (not towards the ends) are larger than 1, which is the maximum limit we normally expect from geology. For longer periods, 10s and 100s, the magnitude decreases fast and is negligible at long periods. Therefore, the induction caused by the fjord is most distinct for short periods, when the station is located very close to the shoreline.

The induction arrows change if the fjord is connected to the ocean. Figure 2, right column, illustrates thisfor periods 1s, 10s and 100s. Focusing on the period of 1s, the largest magnitude of the induction has shifted closer to the ocean, however the highest value is twice as large as in the bend. The magnitude in the bend is approximately the same value as in the situation without the ocean, but the difference is along the shoreline. The magnitude and the real induction arrows are very large all along the shoreline, whereas for the fjord without an ocean it decreases when moving away from the bend.
For the period of 10s, the magnitude is approximately the same in the bend, but the real induction arrows are larger. Induction from the fjord is completely disguised in the induction originating from the ocean, for the period of 100s,.
The induction from a fjord is therefore very high in low and medium periods and it can transverse further into a big fjord system when connected to the ocean, because of currents channeling.

Comparison with observations

The results of the model study illustrates the importance of modeling fjords in the vicinity of stations. The area of the magnetotelluric survey from West Greenland is traversed with a complex fjord system, see Figure 1. We have therefore tried to model the fjord system to account for the effect. As the bathymetry of the fjord system is not currently known different depths were tested and an average value of 100 m was selected.
Additionally, the model also consists of a model of the ocean created with the bathymetry from GEBCO world map (2014).
Figure 3 illustrates the model with a background resistivity of 100Ωm and a resistivity of the water (fjord and ocean) of 0.25Ωm. The induction arrows from this model are illustrated in Figure 4 together with the data response for three stations, station 8, 9 and 10 in the survey, see location in Figure 1.

Both station 9 and 10 illustrate a transition between conductive and resistive material to the north west of their location, which in the long periods is boundary to the ocean and for shorter periods is boundary to the fjord. The model responses agree with the data, the arrows

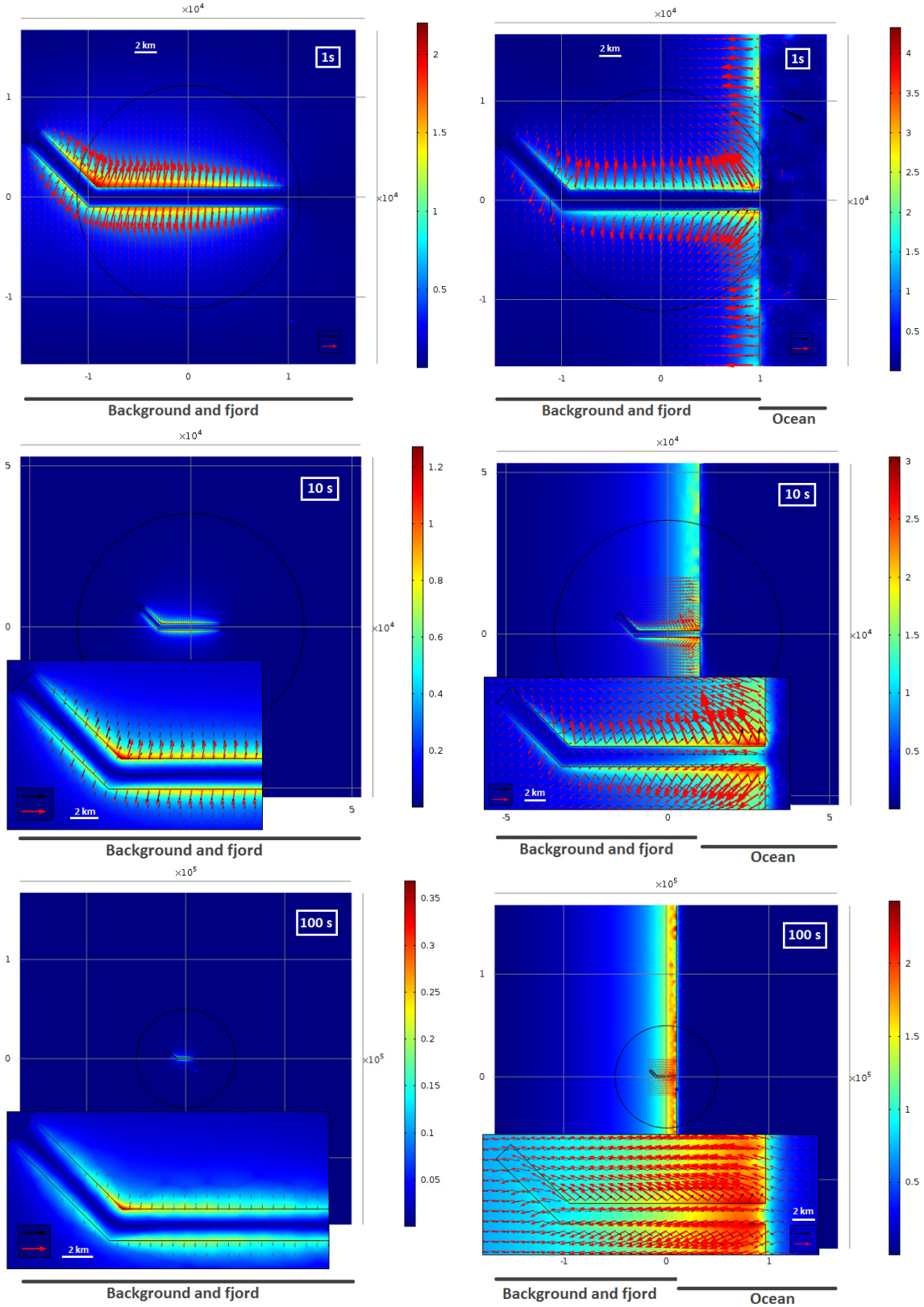

Figure 2: Left Models of a closed fjord, and **Right** model of a fjord connected to an ocean, for three different periods 1s, 10s and 100s. The color represents the magnitude of the total magnetic field and the red (black) arrows represents the real (imaginary) induction arrow. The four bottom figures display a zoom in of the fjord. Scale shown by unit arrows in each figure.

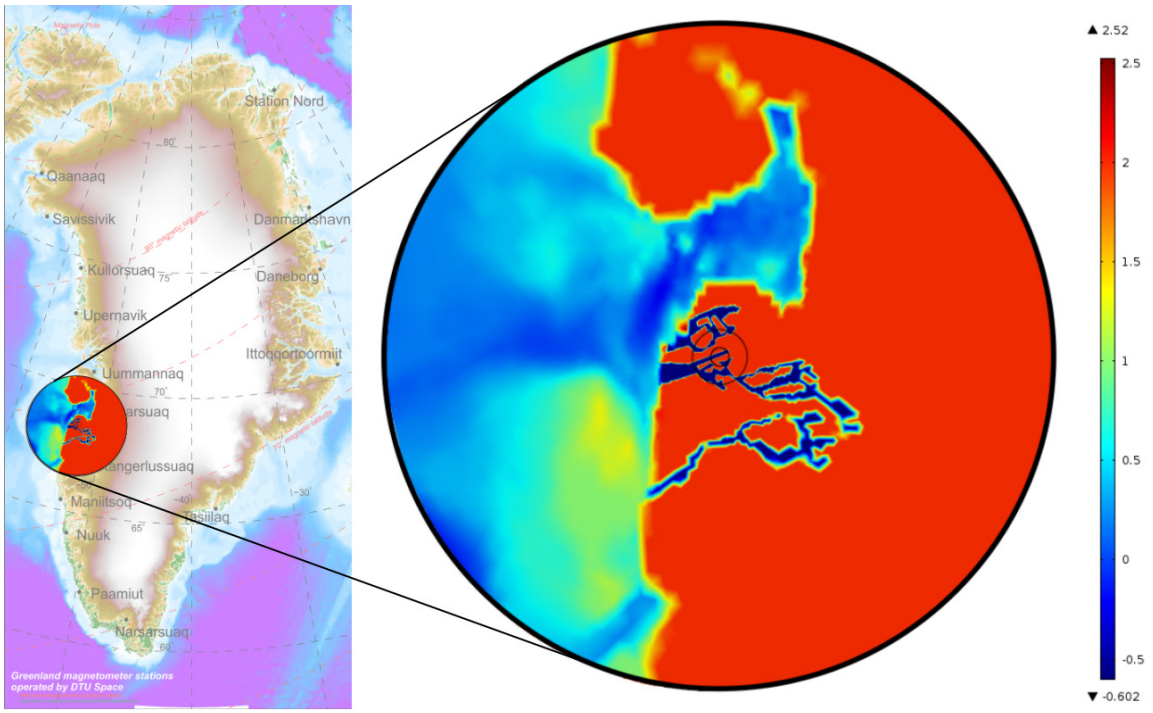

Figure 3: Left The resistivity distribution of the model located in its geographical surroundings. **Right** A close-up of the resistivity of the model, with a background resistivity of 100Ωm.

have the same direction in the real part, although not the same magnitude. Station 8 behaves differently, it illustrates a boundary between conductive and resistive material to the east in short periods and to the north west in long periods, with a smooth transition in between. This is present both in the data and the model. This can be explained by the location of station 8, which is on a small island within the fjord. There is a larger water area to the east and a large island to the west, which explains the rotation of the arrows with period.
Even though the model and data differ from each other with respect to the direction, they reveal the same pattern.

The model consists only of a homogeneous background, ocean and fjords and does not include any geological bodies. The considerable contribution originating from the ocean and fjords has to be considered definitely when explaining the observed data by conductivity models. To achieve a reasonable data fit shaping the fjord in the model as truly as possible is important.

References

COMSOL Multiphysics v. 5.2. (2015). COMSOL AB, Stockholm, Sweden. (`www.comsol.com`)

GEBCO world map. (2014). (www.gebco.net)

GFZ Potsdam. (2015). *Geophysical Instrument Pool Potsdam (GIPP)*. http://www.gfz-potsdam.de/en/section/geophysical-deep-sounding/infrastructure/geophysical-

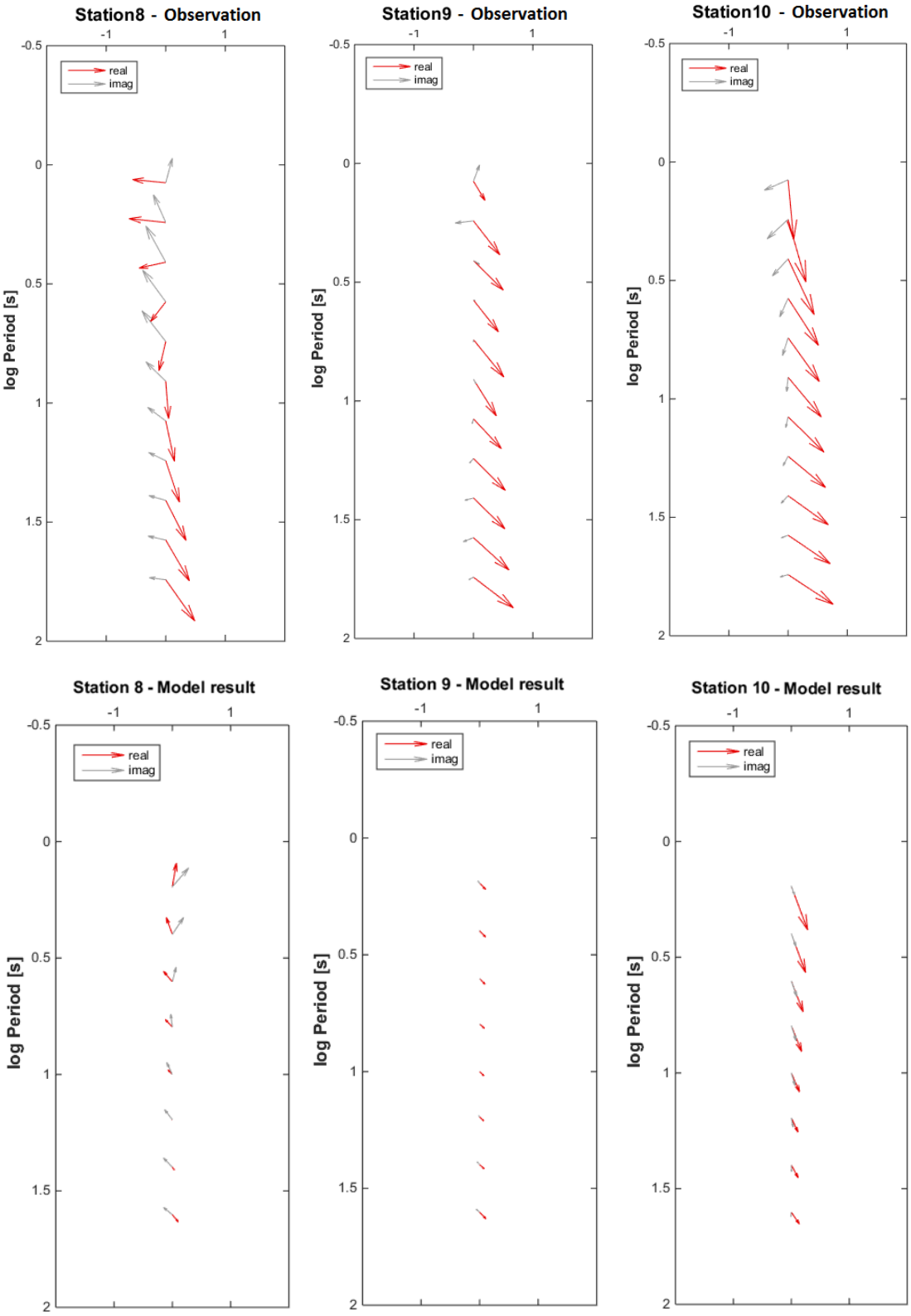

Figure 4: Observed (Top) and model (Bottom) induction arrows of station 8, 9 and 10.

instrument-pool-potsdam-gipp/instruments/gipp-mt/. ([Online; accessed 08-December-2015])

Henriksen, N. (2008). *Geological History of Greenland*. Geological Survey of Denmark and Greenland (GEUS).

Nynne Louise Berthou Lauritsen

Magnetotelluric investigation in West Greenland

DTU Space - National Space Institute
Technical University of Denmark

Diplomvej 371
2800 Kongens Lyngby
Tlf. +45 45259500

www.space.dtu.dk
ISBN 978-87-91694-33-2

DTU